Modelling and numerical simulation of metastable two-phase flows

Marco de Lorenzo

université PARIS-SACLAY

NNT : 2018SACLX029

Thèse de doctorat

Modélisation et Simulation Numérique des Ecoulements Diphasiques Métastables

Thèse de doctorat de l'Université Paris-Saclay
préparée à l'Ecole Polytechnique

École doctorale n°579 : sciences mécaniques et énergétiques, matériaux et géosciences (SMEMAG)
Spécialité de doctorat: mécanique des fluides

Thèse présentée et soutenue à Palaiseau, le 28 mai 2018, par

Marco De Lorenzo

Composition du Jury :

Rémi Abgrall Professeur, Université de Zurich	Rapporteur
Ray A. Berry Distinguished Staff Scientist/Engineer, Idaho National Laboratory	Rapporteur
Daniel Fuster Chargé de Recherches, Institut Jean Le Rond d'Alembert	Examinateur
Marc Massot Professeur, Ecole Polytechnique	Président
Pierre Ruyer Ingénieur Chercheur, Institut de Radioprotection et de Sûreté Nucléaire	Examinateur
Philippe Lafon Ingénieur Chercheur HDR, Electricité de France	Directeur de thèse
Marica Pelanti Maître de Conférences, Ecole Nationale de Techniques Avancées	Co-encadrant
Yann Bartosiewicz Professeur, Université Catholique de Louvain	Co-encadrant

To Michele, Paul & Philippe

ACKNOWLEDGEMENTS

The writing and completion of this Dissertation would not have been possible without the contribution, support and guidance of a few very special people. After three fantastic years spent in a new Country, working with new people and engaged on such an exciting task, the writing of the acknowledgments seems more complicated than writing the entire thesis. I will begin by thanking the jury members of my defense, then my colleagues and my friends.

I would first like to thank the reviewers of this thesis, Prof. Rémi Abgrall and Dr. Ray A. Berry, to have read and commented it. I am particularly grateful to Dr. Berry for the many technical and grammatical corrections proposed and for having traveled from the USA to attend to my PhD defense. Then, I thank the jury members, Dr. Pierre Ruyer and Dr. Daniel Fuster, for the many interesting questions and its president, Prof. Marc Massot for having coordinated the dissertation and the debate.

I would like to thank my PhD supervisor, Dr. Philippe Lafon, who has put his valuable experience and wisdom at my disposal. It has been a greatly enriching experience to me to work under his guidance. He has been supportive but he has given me the freedom to pursue various projects without objection. He has been much more than a PhD supervisor; he has been a mentor, a guidance, a colleague and a friend. His teachings have gone far beyond the two-phase flow domain, ranging from politics to demography and from history to geography and I am so grateful.

I would like to thank my co-advisors, Prof. Marica Pelanti and Prof. Yann Bartosiewicz, that helped me to learn many valuable things and to better explain and valorize my work. I must also thank my *'extra'* co-advisor, Dr. Jean-Marie Seynhaeve, for his stimulating questions and constructive criticisms that were always more challenging.

I would like to thank my EDF colleagues: Dr. Léonard Antoinat, Dr. Frédéric Daude, David Iampietro, Dr. Hippolyte Lochon and, a CEA colleague, Pascal Galon, for the interesting debates had during the last three years but, above all, the many positive and negative criticisms that motivated me to improve my work.

I will forever be thankful to my former internship students, Michele Di Matteo and Alessandro Pantano, for their huge support. Without their daily contribution this PhD thesis would be poorer and less relevant. I tried to teach you as many things as I could; many of them were probably wrong or incomplete but I am very happy that you both are now working in the research domain. During his internship, Michele has also been one of my flatmates and I will never forget the nights and the weekends spent coding the steam-water tables and accompanied by *bonne barbaque*, 'nduja, camembert and wine. This experience has strengthened our former friendship and I am very happy

to have such a great friend.

Trois ans à Paris m'ont donné la possibilité de rencontrer beaucoup d'amis et de vivre de très beaux moments qui resteront gravés dans ma mémoire. Je remercie mon professeur d'arts martiaux, Frédéric Payet, pour sa passion et pour tout ce qu'il m'a appris dans la vie et dans le sport. Je remercie Julie Adjiman, Élodie Ricou, Francesco Bettonte, Aurélien Joly, Silun Zhang, Jingya Li, Célia Giraudeau, Jérôme Delplace pour leur amitié et leur encouragement. Je remercie très spécialement Marie Dzamba pour son soutien et sa présence inconditionnelle.

Je remercie tous mes colocs pour les beaux moments vécus ensemble: Riad Othman, Antoine Poret, Federica Tognon, Omar Hseine et, surtout, Paul Vincent, mon plus cher ami.

Ringrazio anche i miei amici di sempre: Daniele Gigliotti, Francesco Tocco, Lorenzo Niccoli, Lorenzo Petracca e Valentina Columbro. Inoltre, sono particolarmente riconoscente verso Nancy Prestanicola che mi ha reso una persona migliore ed uno studente appassionato durante i molti anni trascorsi insieme.

Infine, un ringraziamento speciale va alla mia famiglia, che è il mio punto di riferimento. Grazie per avermi educato, instruito e di avermi incessantemente incoraggiato e sostenuto in tutti questi anni. Se sono arrivato alla fine di questo cammino, è solo grazie a voi.

SCIENTIFIC PRODUCTION OF THIS THESIS

Peer-reviewed articles

- De Lorenzo M., Lafon Ph., Seynhaeve J.-M., Bartosiewicz Y., 2017, *Benchmark of Delayed Equilibrium Model (DEM) and Classic Two-Phase Critical Flow Models against Experimental Data. Int. J. Multiphase Flow*, Vol. 92, 112-30.

- De Lorenzo M., Lafon Ph., Di Matteo M., Pelanti M., Seynhaeve J.-M., Bartosiewicz Y., 2017, *Homogeneous Two-Phase Flow Models and Accurate Steam-Water Table Look-up Method for Fast Transient Simulations. Int. J. Multiphase Flow*, Vol. 95, 199-219.

- De Lorenzo M., Pelanti M., Lafon Ph., 2018, *HLLC-type and path-conservative schemes for a single-velocity six-equation two-phase flow model: a comparative study. Applied Mathematics and Computation*, Vol. 333C, 95-117.

- De Lorenzo M., Lafon Ph., Pelanti M., 2018, *A hyperbolic phase-transition model with non-instantaneous EoS-independent relaxation procedures.* Submitted to *Journal of Computational Physics*.

- Fang Y., De Lorenzo M., Lafon Ph., Poncet S., Bartosiewicz Y., 2018, *An Accurate and Efficient Look-up Table Equation of State for Two-phase Compressible Flow Simulations of Carbon Dioxide. Industrial & Engineering Chemistry Research*, Vol. 57(22), 7676-7691.

- De Lorenzo M., Lafon Ph., Pelanti M., Pantano A., Di Matteo M., Bartosiewicz Y., Seynhaeve J.-M., 2018, *A hyperbolic phase-transition model coupled to tabulated EoS for metastable two-phase flows.* Submitted to *Computer & Fluids*.

Presentations at international conferences

- De Lorenzo M., Lafon Ph., Bartosiewicz Y., Seynhaeve J.-M., 2016, *Physical and Numerical Investigations for the Development of a New Experimental Facility for Studying Blowdown Phenomena.* Proc. *ICONE24*, Charlotte, North Carolina, USA.

- Fang Y., De Lorenzo M., Lafon Ph., Poncet S., Bartosiewicz Y., Hakim N., 2018, *Fast And Accurate CO2 Properties Calculation Algorithm For Massive Numerical Simulations Of Supersonic*

Two-phase Ejectors. 17th International Refrigeration and Air Conditioning Conference, West Lafayette, Indiana, USA.

- De Lorenzo M., Pelanti M., Lafon Ph., 2018, *Non-instantaneous relaxation procedures with arbitrary equation of state for modeling liquid-vapor flows with phase transition. ECCOMAS 2018: 7th European Conference on Computational Fluid Dynamics (ECFD 7)*, Glasgow, UK.

TABLE OF CONTENTS

Page

Table of Contents **vii**

List of Tables **xi**

List of Figures **xiii**

Introduction **1**

Resumé en français **9**

I Mathematics and physics of metastable two-phase flows **13**

1 Physical features of metastability **15**

1.1 Pure phase diagram 15

1.2 Equations of state and thermodynamic potentials 18

1.3 Saturation curve 20

1.4 Stability, metastability and instability 20

1.4.1 Metastable water 21

1.4.2 Spinodal curve 23

1.5 Metastable fluids in nature and in industry 23

2 Mathematical features of two-phase flow models **25**

2.1 Introduction to two-phase flows 25

2.1.1 Averaging methods and diffused interface technique 26

2.1.2 Computational methods for two-phase flow 27

2.2 Averaged two-phase flow models 28

2.3 Hierarchy of the two-phase flow models 29

2.3.1 The seven-equation model 31

2.3.2 The single-pressure six-equation model 33

2.3.3 The single-velocity six-equation model 34

2.3.4 The five-equation model 35

2.3.5 The four-equation model 36

2.3.6 The homogeneous equilibrium model 38

2.4 Comparison of the speed of sound of two-phase flow models 39

II Classical models and accurate equations of state 41

3 Steady-state metastable flows: the flashing 43

3.1 Introduction 45
3.2 Mathematical Characteristics of Critical Flows 48
3.3 Balance Equations of the Models 49
3.3.1 Balance Equations of the Homogeneous Equilibrium Model 49
3.3.2 Balance Equations of Non-Homogeneous Equilibrium Models 49
3.3.3 Balance Equations of Homogeneous Non-Equilibrium Models 50
3.3.4 Balance Equations of the Delayed Equilibrium Model 51
3.4 Speed of Sound of the Models 52
3.4.1 Speed of Sound of the Homogeneous Equilibrium Model 53
3.4.2 Critical Mass Flux of the Moody Model 54
3.4.3 Speed of Sound of the Henry-Fauske Model 55
3.4.4 Speed of Sound of the Delayed Equilibrium Model 56
3.5 Calculation of the Critical Mass Flux 57
3.5.1 Calculation of the Critical Mass Flux with Homogeneous Equilibrium Model and Moody Model 57
3.5.2 Calculation of the Critical Mass Flux with Henry-Fauske Model 58
3.5.3 Calculation of the Critical Mass Flux with Delayed Equilibrium Model 58
3.6 Comparison against Experimental Data 63
3.6.1 Critical Two-Phase Flow Through Long Tubes 65
3.6.2 Critical Two-Phase Flow Through Short Nozzles 68
3.6.3 Critical Two-Phase Flow Through Slits 71
3.7 Benchmark on other Critical Flow Data and Quantitative Analysis 73
3.8 Conclusions 75
3.9 Appendix 3.A: Condition of Critical Mass Flux of Moody Model 77

4 Transient metastable flows and steam-water tables 79

4.1 Introduction 81
4.2 Homogeneous two-phase flow models 83
4.2.1 Homogeneous Equilibrium Model 84
4.2.2 Homogeneous Relaxation Model 86
4.3 Steam-water EoS for two-phase models 89
4.3.1 Use of a simple caloric EoS 89
4.3.2 Use of an iterative algorithm for an accurate EoS 90
4.3.3 Look-up table interpolation 91
4.4 IAPWS-IF97 and the representation of the liquid spinodal curve 91
4.4.1 Spinodal and saturation curve for water 93

4.5 Look-up table method for thermodynamic properties evaluation on the *e-v* diagram . 95
4.5.1 Grid Construction on e-v diagram and bicubic interpolation 96
4.5.2 Bicubic interpolation 98
4.5.3 Derivatives calculation from bicubic splines 102
4.6 Numerical simulations of steam-water transients 103
4.6.1 Mass transfer for the HRM 104
4.6.2 Steam-water transients 105
4.6.3 Waterhammer 111
4.7 Conclusions 115
4.8 Appendix 4.A: HEM - Speed of sound using IAPWS-IF97 116
4.9 Appendix 4.B: HRM - Speed of sound using IAPWS-IF97 118
4.10 Appendix 4.C: Iterative algorithms for the IAPWS-IF97 119
4.11 Appendix 4.D: Derivatives of IAPWS-IF97 for the Bicubic Interpolation 119

III The single-velocity six-equation two-phase flow model 123

5 Riemann solvers: a comparative study 125
5.1 Introduction 126
5.2 The six-equation single-velocity two-phase flow model 129
5.3 Nonconservative terms of the six-equation model 130
5.3.1 Numerical treatment of the nonconservative terms 132
5.4 Numerical solution methods 133
5.4.1 Hyperbolic operator 133
5.4.2 Pressure relaxation operator 144
5.5 Test problems 145
5.5.1 Water cavitation tube problem 146
5.5.2 Dodecane liquid-vapor shock tube problem: shock in pure vapor 148
5.5.3 Dodecane liquid-vapor shock tube problem: shock in the mixture 149
5.6 Conclusions 152
5.7 Appendix 5.A: Matrices of the 6-equation single-velocity two-phase flow model 154
5.8 Appendix 5.B: Model System Eigenstructure 155

6 EoS-independent relaxation procedures 157
6.1 Introduction 158
6.2 Six-equation single-velocity two-phase flow model 160
6.3 Equations of state and thermodynamic quantities 161
6.4 Physical modeling of the relaxation processes 164
6.4.1 Pressure relaxation 166
6.4.2 Temperature relaxation 169
6.4.3 Mass transfer 170
6.5 Numerical solution methods 172

6.5.1 Hyperbolic operator . . . 173
6.5.2 Relaxation operators . . . 175
6.6 Equilibrium recovery test . . . 176
6.7 1-D numerical tests . . . 179
6.7.1 Water cavitation problem with the stiffened gas EoS . . . 180
6.7.2 Water cavitation test with the IAPWS-IF97 EoS . . . 181
6.7.3 Evaporation-condensation shock tube test with the IAPWS-IF97 EoS . . . 183
6.7.4 Evaporation shock tube test with the IAPWS-IF97 EoS . . . 185
6.8 2-D numerical test . . . 188
6.9 Conclusions . . . 189
6.10 Appendix 6.A: Semi-analytic relaxations . . . 190
6.10.1 Appendix 6.A.1: Semi-analytic temperature relaxation . . . 190
6.10.2 Appendix 6.A.2: Semi-analytic Gibbs free enthalpy relaxation . . . 191
6.11 Appendix 6.B: Irreversibility of the relaxation procedures . . . 191
6.11.1 Appendix 6.B.1: Irreversibility of the pressure relaxation process . . . 191
6.11.2 Appendix 6.B.2: Irreversibility of the temperature relaxation process . . . 192
6.11.3 Appendix 6.B.3: Irreversibility of the mass transfer process . . . 193
6.12 Appendix 6.C: Well-posedness of the relaxation procedures . . . 193

7 A six-equation single-velocity model with tabulated EoS 197
7.1 Introduction . . . 198
7.2 Six-equation single-velocity two-phase flow model . . . 199
7.2.1 Homogeneous hyperbolic portion of the model . . . 199
7.2.2 The complete model for phase transition . . . 200
7.3 Look-up table algorithm for liquid and vapor EoS . . . 201
7.3.1 The e-v diagram for water . . . 201
7.3.2 Extension to vapor metastable states . . . 202
7.3.3 A bicubic interpolation method . . . 204
7.4 Numerical solution methods . . . 206
7.4.1 Hyperbolic operator . . . 206
7.4.2 Relaxation operators . . . 208
7.5 Numerical simulations of fast depressurizations . . . 211
7.6 Conclusions . . . 215

Conclusions and perspectives 217

Bibliography 221

List of Tables

Table **Page**

3.1 DEM model 52
3.2 Mean error for critical mass flux predictions 75
3.3 Mean error for critical pressure predictions 75
3.4 Standard deviation for critical mass flux predictions 76
3.5 Standard deviation for critical pressure predictions 76

6.1 Parameters for the Stiffened Gas EoS for liquid and vapor water (first test) 181
6.2 Parameters for the Stiffened Gas EoS for liquid and vapor water (second test) 181

List of Figures

Figure **Page**

0.1 Schematic of a Pressurized Water Reactor (PWR). 3
0.2 Illustration of a Loss of Coolant Accident in a PWR. 3

1.1 p-T diagram for pure water 16
1.2 p-v diagram for pure water 17
1.3 Stability, metastability and instability 21
1.4 p-T diagram for pure water with metastable states 22
1.5 T-v diagram for pure water with metastable states 24

2.1 Two-phase flow patterns 26
2.2 Hierarchy of two-phase flow models 30
2.3 Celerity of two-phase flow models 39

3.1 Speed of sound in vapor-liquid water of the critical models. 53
3.2 Schematic example of a critical trajectory in the phase space 61
3.3 Benchmarks of HEM and Moody (1965) on Super Moby Dick long tubes 64
3.4 Benchmarks of Henry-Fauske (1971) and DEM on Super Moby Dick long tubes 65
3.5 Pressure and void fraction profiles in SMD test section: $20\,bar$ 67
3.6 Pressure and void fraction profiles in SMD test section: $120\,bar$ 68
3.7 Benchmarks of HEM and Moody (1965) on Super Moby Dick, short tubes 69
3.8 Benchmarks of Henry-Fauske (1971) and DEM on Super Moby Dick, short tubes 70
3.9 Pressure and void fraction profiles in SMD short test section: 20 bar 72
3.10 Benchmarks of HEM, Moody (1965), Henry-Fauske (1971) and DEM on John et al. 74
3.11 Benchmarks of HEM, Moody (1965), Henry-Fauske (1971) and DEM on all data 77

4.1 Isobaric curve on the T-v diagram 84
4.2 Mixture speed of sound for water for HEM, HRM and Wood's relation 87
4.3 Region subdivision of the IAPWS-IF97 on the p-T diagram 92
4.4 Metastable domain on the e-v and p-T planes 94
4.5 Trend of spinodal curves on the p-T diagram 95
4.6 Isotherms on the p-v diagram 96
4.7 Thermodynamic diagram e-v 97
4.8 Thermodynamic diagram e-v 98
4.9 Grid of nodes in the physical domain and in the transformed one 99

4.10 Distribution of the relative error with the look-up table method . . . 101
4.11 Pressure evolution in the Bartak's experiment . . . 105
4.12 Schematic of Super Canon experimental facility . . . 106
4.13 Assessment of HEM and HRM on a Super Canon experiment (15 MPa, 573.15 K) . . . 107
4.14 Comparison using different correlations for Θ (15 MPa, 553.15 K) . . . 108
4.15 Comparison using different correlations for Θ (15 MPa, 573.15 K) . . . 109
4.16 Comparison using different correlations for Θ (15 MPa, 593.15 K) . . . 110
4.17 Pressure history of Simpson's waterhammer experiment . . . 112
4.18 Schematic of the injection test . . . 113
4.19 Temporal evolutions at points A and B . . . 114
4.20 Magnification of the temporal evolutions . . . 115

5.1 Sketch of the phasic volume fraction increasing along z . . . 132
5.2 Numerical results for the water cavitation test with $|u| = 2\,m/s$ . . . 146
5.3 Mesh convergence study on the water cavitation test with initial velocity $|u| = 2\,m/s$ . . . 147
5.4 Efficiency study on the water cavitation test $|u| = 2\,m/s$ . . . 147
5.5 Numerical results for the water cavitation test with $|u| = 500\,m/s$ . . . 148
5.6 Numerical results for the dodecane liquid-vapor shock tube . . . 149
5.7 Numerical results for the dodecane liquid-vapor shock tube . . . 150
5.8 Benchmark test against the Saurel et al. [232] shock relations . . . 151
5.9 Numerical results for the dodecane liquid-vapor shock tube with Glimm's method . . . 152
5.10 Numerical results for the dodecane liquid-vapor shock tube . . . 153

6.1 Sound speed of two-phase flow models . . . 162
6.2 T-v diagram of water . . . 163
6.3 Time evolution of properties during the pressure relaxation step . . . 176
6.4 Time evolution of properties during the temperature relaxation step . . . 177
6.5 Time evolution of properties during the chemical relaxation step . . . 177
6.6 Evolution on the $T - v$ diagram . . . 178
6.7 Numerical results for the water cavitation test with $|u| = 0.2\,m/s$ . . . 179
6.8 Numerical results for the water cavitation test with $|u| = 2\,m/s$ . . . 180
6.9 Numerical results of the water cavitation test with the IAPWS-IF97 EoS . . . 182
6.10 Numerical results of evaporation-condensation test with the IAPWS-IF97 EoS . . . 184
6.11 Numerical results of evaporation test with the IAPWS-IF97 EoS . . . 186
6.12 Pressure field of the 2D test . . . 187
6.13 Chemical disequilibrium field of the 2D test . . . 188
6.14 Trend of the partial derivatives $\frac{\partial F_i^p}{\partial y_j}(\mathbf{y})$ . . . 194
6.15 Trend of the partial derivatives $\frac{\partial F_i^T}{\partial y_j}(\mathbf{y})$ . . . 194

7.1 Liquid and vapor water on the e-v diagram . . . 202
7.2 Phasic pressures, temperatures and speeds of sound on the e-v diagram. . . . 203
7.3 Speed of sound and temperature profiles on the vapor spinodal curve. . . . 204

7.4 Grid of nodes in the physical domain and in the transformed one 205
7.5 Schematic of Super Canon experimental facility 210
7.6 Pressure evolution in the Bartak's experiment 211
7.7 Assessment on a Edwards-O'Brien experiment (1500 $Psia$, 544 K) 213
7.8 Assessment on a Super Canon experiment (15 MPa, 593.15 K) 214

INTRODUCTION

Metastable two-phase flows are involved in many industrial fields as well as in natural phenomena. In the nuclear energy industrial domain, metastable two-phase flows should be taken into account in the study of hypothetical safety accidents. Within Pressurized Water Reactors (PWRs), under nominal conditions, the coolant is a single-phase liquid water, which may transform into a two-phase mixture during accidental transients. Moreover, liquid and vapor may be in *thermodynamic disequilibrium*, thus, one or both phases are in metastable conditions.

In the nuclear domain, as well as in other industrial contexts, the correct simulation of those flows is of paramount importance for enhancing the safety of the system. In fact, numerical simulations are expected to provide accurate information about the mechanical efforts both on the nuclear fuel and other reactor components. Nevertheless, the analysis of the metastable two-phase flows is very challenging, and the complexity of simulating two-phase flows is higher compared to single-phase flows. In fact, for the simulation of metastable two-phase flows, there are three main difficulties: (i) the presence of a continuously moving interface that separates the two fields, (ii) the interphase transfers, and, (iii) the compressibility of both phases.

The separating interface is the locus of the discontinuities in the fluid properties. In the case of *phase-transitions*, this interface may also disappear due to the complete water vaporization or condensation. This feature additionally increases the complexity of modeling these phenomena.

At the interface, mass, momentum and energy exchanges take place. In phase transitions the exchanges are driven by complex mechanisms and by the thermodynamic disequilibrium between the phases. Those interfacial exchanges strongly affect the transport phenomena.

For a complete description of certain phenomena, phases must be considered as *compressible fluids*. On one hand, this choice is necessary for representing *wave motion phenomena*. On the other hand, it renders the numerical modeling even more difficult because it introduces a strong coupling between the various physical aspects as convection, wave propagation and interphase transfers, requiring appropriate methods for their mathematical solvability.

From an industrial point of view, currently, for the safety analysis of PWRs, those complex flows are described using simple models. But they are not altogether satisfactory because they do not take into account the thermodynamic disequilibrium between liquid and vapor water phases. To improve the accuracy of the numerical simulations of nuclear safety accidents, a more complete methodology is desired.

Today several computational codes are able to take into account the presence of metastable phases [24, 203, 220], however, most of them are based on an ill-posed mathematical model [254]. In the last two decades, more advanced models for metastable two-phase flows have appeared

[200, 231, 233, 283]. These are mathematically more consistent than the metastable models of the past since they have the very important feature of being hyperbolic. In nuclear industry, the transition towards these hyperbolic models has recently started [64, 221] and this thesis belongs to this path.

The purpose of this Ph.D. thesis is to develop a modern and time-efficient model for the analysis of metastable two-phase flows, and to couple it with realistic energy and mass transfer terms, together with accurate water properties.

To achieve that, we followed a progressive path. It starts with the use of classical two-phase flow models and accurate thermodynamic properties of water. Then, it focuses on the numerical aspects of a more elaborate two-phase model for metastable flows. And, finally, it couples the accurate thermodynamic methods to the elaborate two-phase flow model.

The final product of this work is a hyperbolic model for metastable two-phase flows that uses novel techniques for the calculation of interfacial transfers and up-to-date algorithms for steam-water properties. Moreover, it is computationally affordable for use in industrial configurations.

These novel techniques for the calculation of interfacial transfers are the main scientific contribution of this Ph.D. thesis. They allow combining today's *state-of-art in numerical modeling* with *up-to-date thermodynamics for real fluids*. Furthermore, this methodology is time-efficient for industrial purposes.

Given the specificity of the phenomena analyzed in this thesis, the focus is on liquid and vapor water in phase transitions. However, the modeling and the numerical procedures here developed are general and may apply to different contexts.

Industrial context

This thesis, realized at the R&D department of EDF (Électricité de France), aims at studying new modeling and simulation approaches for the analysis of accidental transients occurring in nuclear power plants. EDF owns many Pressurized Water Reactors (see Fig. 0.1), therefore, the accidental scenarios studied in this work are the *Loss of Coolant Accident (LOCA)*, *waterhammers* and *steam explosions*.

The LOCA is a hypothetical scenario and is one of the Design Basis Accidents (DBA) of nuclear power plants. It represents a sudden rupture of the primary fluid flow circuit and its depressurization (see Fig. 0.2). According to the primary system breach size, we refer to Large-Break LOCA, Small-Break LOCA or to slits. The first two represent severe hypothetical accidents of nuclear power plants. In such scenarios, the water of the primary system comes out through the break and vaporizes. This complex accident involves many physical phenomena and various components of the nuclear power plant.

In this thesis, the attention is only drawn to the two-phase phenomena *at the breach*, for both fast transient and stationary aspects. For the stationary aspects, Large-Break LOCA, Small-Break LOCA and slits are analyzed, whereas, for the case of the fast depressurization, the primary circuit is considered to have a full circumferential break (also called double-ended guillotine break).

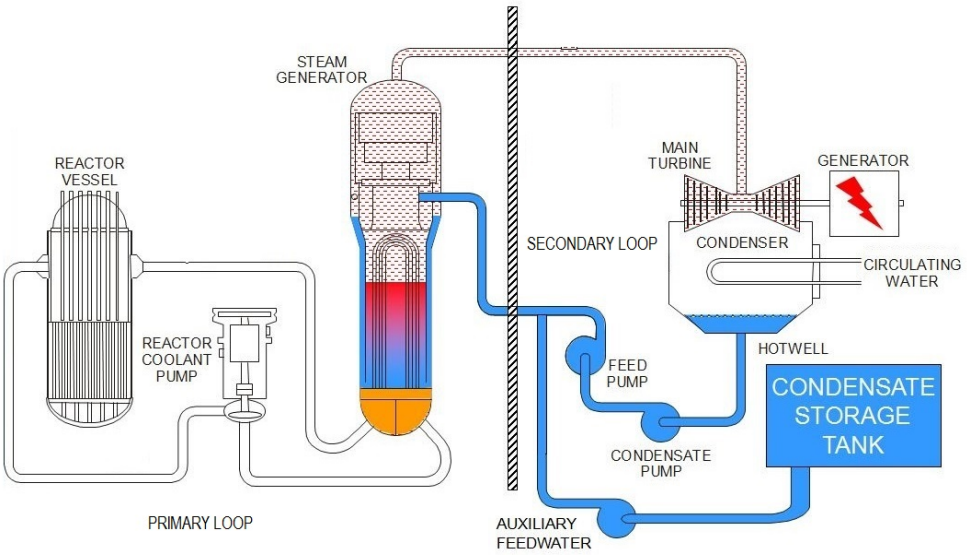

FIGURE 0.1. Schematic of a Pressurized Water Reactor (PWR). Source: Nuclear Regulatory Commission (NRC).

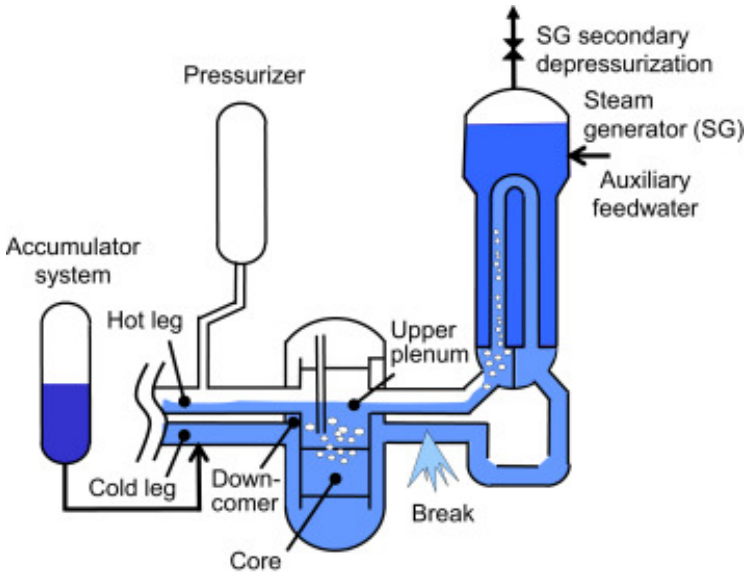

FIGURE 0.2. Illustration of a Loss of Coolant Accident in a PWR. Source: [257].

As concerns the fast transient aspects, if a rupture suddenly occurs in the primary system of a PWR, a depressurization wave originates at the breach and propagates upstream into the circuit. When it arrives into the reactor pressure vessel, it hits the core and it could mechanically damage the nuclear fuel and the safety and control equipment (control rods, etc.). An accurate analysis of the rarefaction wave, and of the fluid-structure interaction, can provide more precise information about the mechanical effects the core components are subjected to. At EDF, currently, these simulations are performed with the EUROPLEXUS code using an equilibrium model [105]. EUROPLEXUS code [101] is owned by the Commissariat à l'Energie Atomique et aux Energies Alternatives (CEA) and

the Joint Research Centre (JRC) of the European Union.

For the quasi-stationary aspects, it is important to evaluate the discharge rate of the coolant inventory through the breach because it influences the depressurization rate of the primary system, the pressurization of the reactor containment, etc. Establishing an accurate evaluation of the coolant discharge rate at the breach allows a better design of the safety systems of the nuclear power plant.

The other fast transients we are interested in are the waterhammers and the steam explosions. Waterhammer is a pressure surge occurring in the circuits of the power plant. This wave propagation phenomenon can be triggered by the sudden closure/opening of a valve, by condensation of vapor pockets, etc. Steam explosion is the interaction between two components at very different temperatures. Specifically, the temperature of the hot component is higher than the saturation temperature of the cold one. In the nuclear industry, steam explosion may occur during a severe reactor accident when the molten fuel comes into contact with the coolant water or, in a mildly form, during a Reactivity-Initiated Accident (RIA).

The common feature of all these phenomena is the presence of two-phase water in which phases may be in thermodynamic disequilibrium. Then, phases can be in metastable states, that means, the persistence of a phase into the stability domain of another phase. Furthermore, except for the analysis of the stationary flow at the breach, all the others are *wave dominant phenomena* in two-phase water.

Modeling approach

The analysis of the physical phenomena can be carried out by means of an empirical, mathematical or a hybrid approach. For the metastable two-phase flows, an empirical approach is necessary for the understanding of the complex interfacial mechanisms or the thermodynamic properties of real fluids. But the drawbacks of a full empirical approach stems in its narrow validity range and in the difficulty to describe the spatial and time evolution of the flow.

On the contrary, mathematical modeling helps to generalize the two-phase flows and allows treatment of a large number of physical phenomena using the same numerical tools. For instance, the same system of equations can be used to describe solid explosives, shock propagation into solid alloys, fast liquid-vapor phase transition, etc. But a methodology fully based on a mathematical approach is not able to correctly take into account some specific phenomena or the accurate fluid properties.

To balance the drawbacks of those approaches, a hybrid empirical-mathematical approach is used in this work. The mathematical modeling of the two-phase flows is the basis of our approach, however, water properties and interfacial exchanges are based on empirical laws. These laws are already present in the literature and are based on experimental data.

The system of equations analyzed in this work are the *Homogeneous Equilibrium Model (HEM)* [136], the *Homogeneous Relaxation Model (HRM)* [28] and the *single-velocity six-equation two-phase flow model* [234].

These models are always used in their conservative forms because the physical phenomena

analyzed may also include shock waves, that is, property discontinuities in the fluid flow. In fact, for smooth solutions, all formulations are equivalent, but, for solutions containing shock waves, nonconservative formulations give incorrect shock solutions. Then, these systems of governing equations must be closed with an Equation of State (EoS) to calculate the thermodynamic properties as a function of the system conservative variables.

For water, because accurate analytical EoS for this purpose are not available yet, we adopt an efficient and very accurate algorithm to calculate water properties when the independent variables of the EoS are the density and the specific internal energy. This algorithm is based on the IAPWS-IF97 EoS formulation [273] that is very accurate and able to account for metastable states. The water properties described by this EoS are stored on a tabulated $e-v$ diagram of water. Then, a bicubic interpolation is performed on this domain in order to accurately calculate the thermodynamic properties.

For the HEM, liquid and vapor are at full equilibrium then they are at saturation condition, therefore, during a phase transition, mass and energy transfers are dictated by the equilibrium conditions. For the HRM, the liquid is metastable and the vapor is at saturation, then the mass transfer must be modeled separately using an appropriate phase transition model. The single-velocity six-equation two-phase flow model describes the case of phases at velocity equilibrium but full thermodynamic disequilibrium for which the mass and energy transfer need to be defined. For both the hyperbolic transport equation and for the mass-energy exchange terms, we use the steam-water look-up method mentioned above.

To ascertain the correctness of our algorithms, several *verifications* have been systematically performed. The steam-water look-up method has been compared to the original IAPWS-IF97 showing a very low numerical error in terms of pressure, temperature and speed of sound. The numerical schemes for the hyperbolic systems have been verified comparing them to exact solutions, when available. The equilibrium states of the relaxation algorithms have been compared to the equilibrium conditions given by the IAPWS-IF97. Finally, to show the physical consistency of the numerical procedures and of the modeling approach, several *validations* have been done against the available experimental data.

Outline of the thesis

The thesis is composed of seven chapters divided into three parts. Four chapters are articles published or under review, therefore, a simple and didactic part was added to introduce the reader to the metastable two-phase flows. This is done in Part I which is composed of two chapters. Chapter 1 introduces elementary concepts of the thermodynamics of real fluids, phase diagrams, equations of state and stability-metastability-instability. Chapter 2 describes the mathematical aspects of the two-phase flows, the necessity of averaging transport equations, the mathematical characteristics of two-phase flow models and the existence of a hierarchy of these models based on the equilibrium assumptions.

The following chapters, which are papers either published or under review, are preceded by

a brief introduction. The order of the chapters represents the *chronological order of the papers*, which also shows the research path followed during the Ph.D. thesis. Each chapter represents a supplementary step towards a complete and coherent analysis of the metastable two-phase flows. The introductions that precede each chapter serve to describe the industrial needs of each work and show the links with the previous and next chapters.

Part II discusses the stationary and transient metastable flows using classical two-phase flow models and state-of-art equations of state. It is composed of two chapters, representing research articles published in the *International Journal of Multiphase Flow*.

Chapter 3 is about the stationary metastable two-phase flow at the breach in the event of a LOCA. Here, we compare Delayed Equilibrium Model (DEM), Homogeneous Equilibrium Model, Moody (1965) [184] and Henry-Fauske [125] models to experimental data containing a sample range in excess of 450 conditions to determine an appropriate benchmark. This analysis has been carried out for both critical mass flux and critical pressure evaluations.

Chapter 4 deals with the fast transient metastable two-phase flows as rapid depressurizations, waterhammers and steam explosions. The aim of this paper is to show an efficient and very accurate algorithm to calculate water properties when the independent variables are the density, ρ and the specific internal energy e. For a given thermodynamic pair (ρ, e), we wish to obtain the corresponding pressure, temperature and speed of sound. The main purpose is to couple this algorithm to two-phase flow models in their conservative form. To reach this goal, thermodynamic properties shall be tabulated on the e-v thermodynamic diagram. These developments are based on the recent works of Kunick et al. [133]. The obtained algorithm is then coupled to two common two-phase flow models, the Homogeneous Equilibrium Model and the Homogeneous Relaxation Model, and their numerical simulations are compared to experimental data showing the very good performance of our computational approach.

Part III is devoted to the single-velocity six-equation two-phase flow model and its use for the numerical simulation of fast transients. It is composed of three chapters that describe the evolution in numerics and modeling for the final use of this two-phase flow model, fully coupled to the proposed steam-water tables, for the simulation of fast depressurizations.

In Chapter 5 we make a comparison of different numerical schemes for several test cases, including cavitation problems and shock tubes. The main difference between these schemes stems from their differing numerical treatments of the nonconservative terms. Further, an efficiency study for first and second order schemes is also presented. Attention is drawn to the numerical resolution of the homogeneous portion of this model, hence, the equation of state used throughout this chapter is an analytic one allowing comparison of the numerical results to the exact solutions.

In Chapter 6 new non-instantaneous EoS-independent relaxation procedures are proposed for the treatment of phase transition cases. These new procedures are tested from both thermodynamic and numerical points of view. In particular, we show that, starting from a metastable mixture, they are able to recover the correct full equilibrium state.

We also show that these new relaxation procedures converge to instantaneous equilibrium simulations when the characteristic equilibrium recovery times tend to zero. Here the single-velocity six-equation two-phase flow model is coupled to the IAPWS-IF97 equation of state. This chapter is

the cornerstone for the use of the single-velocity six-equation model in industrial contexts.

Chapter 7 presents the steam-water tables extended to the vapor metastable domain and the coupling of the look-up table method to the single-velocity six-equation model for the calculation of phasic properties. Here, the hyperbolic solver of the six-equation model as well as the non-instantaneous EoS-independent relaxation procedures use the steam-water tables for an accurate description of fast depressurizations.

Resumé en français

Cette thèse de doctorat s'intéresse aux écoulements diphasiques métastables typiques de certains transitoires accidentels qui pourraient intervenir dans les centrales nucléaires. Ces phénomènes sont difficiles à traiter en raison de la complexité topologique de l'écoulement, des transferts entre phases et du couplage fort entre les caractéristiques thermodynamiques et les aspects mathématiques. Les méthodes aujourd'hui en usage dans l'industrie ne décrivent pas complètement la complexité de ces écoulements car elles s'appuient sur des modèles trop simples. En fait ces méthodes ne prennent pas en compte le déséquilibre thermo-chimique entre l'eau liquide et sa vapeur. Par ailleurs, les méthodes hyperboliques proposées récemment dans la littérature pour la simulation des écoulements métastables ne peuvent pas être appliquées dans l'industrie car elles utilisent des lois d'état simples qui ne sont pas adaptées pour les calculs industriels. Le but de cette thèse est de développer une nouvelle approche qui couple les méthodes hyperboliques modernes à des équations d'état précises.

Le premier chapitre est consacré à une introduction à la physique et à la thermodynamique des fluides métastables. On présente d'abord les concepts élémentaires à propos du diagramme de phase en se concentrant sur le mélange liquide-vapeur. Puis les concepts de degrés de liberté et de potentiels thermodynamiques sont introduits. Pour aborder le concept de métastabilité c'est l'approche phénoménologie basée sur la thermodynamique des milieux continus qui est utilisée ici. Enfin, l'importance de la métastabilité est discutée pour différents phénomènes existants dans la nature ou dans l'industrie. Bien que les analyses conduites dans ce chapitre soient valables pour n'importe quel fluide, une attention particulière est bien sûr accordée à l'eau.

Le second chapitre est dédié à introduire les principaux concepts mathématiques qui seront nécessaires par la suite. Tout d'abord on introduit les principales caractéristiques des écoulements diphasiques. Les complexités physiques et mathématiques des écoulements diphasiques sont notamment discutées ainsi que les conséquences en terme de difficultés numériques pour la simulation de tels écoulements. Dans ce cadre, les équations de conservation des écoulements diphasiques sont le plus souvent moyennées. D'autre part, de nombreuses techniques numériques existent si bien qu'il est nécessaire de clairement préciser quelles approches seront utilisées afin de bien définir le contexte numérique de la thèse. Ensuite on donne des éléments d'information mathématiques pour les écoulements diphasiques compressibles et leurs équations d'état et on décrit les modèles d'écoulements diphasiques les plus communs ainsi que la hiérarchie existant entre eux en fonction du degré de déséquilibre autorisé entre phases. Les différentes formulations de la vitesse du son associée à ces modèles sont finalement analysées.

Le troisième chapitre s'intéresse aux modèles de débit critique diphasique. En effet, l'analyse de

sûreté des réacteurs PWR en cas d'APRP dépend de la capacité à évaluer le débit de fuite du liquide de refroidissement à la brèche. A cause de la grande différence de pression entre l'eau primaire et le bâtiment réacteur, le débit massique est bloqué à la brèche. Sous ces conditions, les déséquilibres mécanique et thermodynamique entre phases ne sont pas assurés. Une théorie générale pour le débit critique diphasique n'est pas encore disponible. Cependant, des modèles sont capables de fournir des évaluations précises à la fois des débits critiques et des pressions critiques, comme le modèle DEM (Delayed Equilibrium Model) dont il est principalement question ici. On montre comment intégrer le système d'équations du modèle DEM en couplant une méthode de Runge-Kutta classique à l'algorithme Possible-Impossible pour l'écoulement, ce qui donne une procédure de résolution assez simple sans recourir à des schémas numériques sophistiqués. Puis les quatre modèles DEM, HEM (Homogeneous Equilibrium Model), Moody (1965) et Henry-Fauske (1971) sont comparés aux données expérimentales disponibles. Plus de 450 conditions expérimentales sont ainsi utilisées couvrant notamment des configurations différentes de type «tuyau long», «tuyau court» et «fissures». Le modèle DEM donne finalement les meilleurs résultats.

Le quatrième chapitre est consacré aux écoulements transitoires métastables et aux tables thermodynamiques pour l'eau et sa vapeur. En effet, le système des équations de conservation doit être fermé à l'aide d'une équation d'état afin de calculer la pression en fonction des variables conservatives. Pour l'eau, des équations d'état analytiques suffisamment précises ne sont pas encore disponibles. On propose ici un algorithme efficace et précis pour calculer les propriétés de l'eau quand les variables indépendantes de la loi d'état sont la densité et l'énergie interne spécifique. Cet algorithme utilise la formulation IAPWS-IF97 pour la loi d'état de l'eau et sa vapeur, et une méthode de tabulation s'appuyant sur une interpolation bicubique. La métastabilité dans le domaine liquide est étendue jusqu'à la spinodale. La loi d'état ainsi définie est couplée à deux modèles diphasiques classiques : le modèle HEM (Homogeneous Equilibrium Model) et le modèle HRM (Homogeneous Relaxation Model). Ils sont utilisés pour simuler des problèmes de dépressurisation rapide, de coups de bélier et d'injection d'énergie. Les comparaisons avec des données expérimentales montrent les bonnes performances des algorithmes proposés.

Le cinquième chapitre présente une étude comparative de différents solveurs de Riemann dans le cadre de l'intégration du modèle diphasique à six équations et une vitesse avec relaxations instantanées. La littérature montre l'efficacité de ce modèle pour la simulation d'écoulements complexes incluant des processus de vaporisation et de cavitation. On présente ici l'analyse de différents schémas numériques pour ce modèle en se concentrant sur l'intégration des termes non-conservatifs présents dans les équations d'énergie phasiques. Deux nouvelles méthodes sont proposées : un *path-conservative* schéma de type HLLC basé sur la théorie de Dal Maso – Le Floch – Murat et un schéma de type HLLC généralisé basé sur un solveur de Riemann de type Siliciu. Ce dernier schéma présente l'importante propriété de préserver la positivité aux états intermédiaires des quantités conservées. On utilise aussi deux autres schémas proposés dans la littérature qui sont dérivés des solveurs de Riemann Osher et HLLEM. On compare ces schémas sur différents cas-tests dont des cas de cavitation et des tubes à choc. Les résultats numériques montrent que les différentes méthodes qui correspondent à différents traitements numériques des termes non conservatifs donnent des résultats similaires et précis sauf, comme attendu, pour les chocs diphasiques aux très

grands rapports de pression.

Le sixième chapitre développe un modèle hyperbolique avec transition de phase, avec de nouvelles procédures de relaxation instantanées et indépendantes de la loi d'état. Dans ce cadre, les deux phases initialement à différentes pressions, températures et potentiels chimiques sont supposées être amenées vers les conditions d'équilibre grâce à trois processus successifs de relaxation. Tout d'abord, un processus mécanique s'applique à la relaxation des pressions phasiques, puis un processus thermique pilote le transfert de chaleur sensible entre les phases à différentes températures et enfin un processus chimique est responsable du transfert de masse. Le modèle à six équations et une vitesse est composé de six équations avec termes source qui autorisent la description de mélanges avec déséquilibre thermodynamique complet. La partie homogène du système d'équations est résolue à l'aide d'un schéma volume fini à l'ordre deux qui utilise un solveur de Riemann de type HLLC. Les termes source qui modélisent les processus de relaxation sont intégrés séparément sous la forme de trois systèmes d'équations différentielles ordinaires. La contribution majeure de ce travail concerne la capacité de décrire le temps de retard pour le retour à l'équilibre, l'indépendance par rapport à la loi d'état de l'ensemble du processus numérique et la possibilité de prendre en compte la morphologie de l'écoulement en utilisant l'aire interfaciale entre phases.

Le septième chapitre est consacré à l'application des différents développements des chapitres précédents : modèle diphasique à six équations et une vitesse, tables thermodynamiques métastables pour l'eau et sa vapeur, solveurs de Riemann et enfin nouvelles procédures de relaxation. Le cas test retenu est représentatif des problèmes de dépressurisation rapide comme en situation d'APRP. Le modèle fournit des résultats en très bonne correspondance avec les données expérimentales notamment en ce qui concerne les effets métastables.

Le produit final de ce travail de thèse est un nouveau modèle pour l'analyse industrielle des écoulements diphasiques métastables qui associe de nouvelles techniques pour le calcul des transferts entre les phases et des propriétés de l'eau et de sa vapeur. De plus, cette approche est d'un coût abordable pour les configurations industrielles. Les méthodes développées dans cette thèse ont été systématiquement vérifiées avec des solutions exactes et validées en utilisant des données expérimentales de la littérature

Part I

Mathematics and physics of metastable two-phase flows

CHAPTER 1

PHYSICAL FEATURES OF METASTABILITY

This first chapter is devoted to a bibliographic introduction to thermodynamics and to the physics of metastable fluids. It starts with elementary concepts about the *phase diagram* of a pure fluid focusing on the liquid-vapor mixtures. It introduces also the basic thermodynamic concepts of degrees of freedom and the thermodynamic potentials. Then the equations of state are briefly discussed and the concepts of stability and equilibrium are introduced. About the metastability, the so called *phenomenological* approach is used here because it is based on the continuum thermodynamics. Then the chapter ends with a discussion on the importance of the metastability in both nature and industry. Even though the thematics treated in this chapter are valid for any pure fluid, particular attention will be devoted to water due to the industrial context of this thesis.

1.1 Pure phase diagram

A pure phase can exist under different states of aggregation. For instance water, at atmospheric pressure, according to its temperature, can be *solid*, *liquid* or *vapor*. A phase diagram allows to schematize such information. In Fig. 1.1, the p-v-T and the p-T diagrams for pure water are reported. Referring to Fig. 1.1(b), the red lines are the loci of two-phase equilibrium and delimit the stability domains of the three phases.

More precisely, the melting curve indicated by TM continues indefinitely to the highest pressure. Conversely, the vapor-liquid curve indicated by TC terminates at the critical point C. Beyond this point, we speak about the *supercritical domain* where fluctuations becomes important and vapor and liquid can be no longer distinguished, therefore, we refer at it as *supercritical fluid*.

Water is a very particular matter with many anomalies. For instance, the negative slope of the melting curve means that the density of the solid is lower than the one of the liquid. Or the liquid density maximum at 277.13 K, that is one of the most famous anomalies of water [255]. At low temperature, the isothermal compressibility factors k_T and the isobaric specific heat c_p increase

(a)

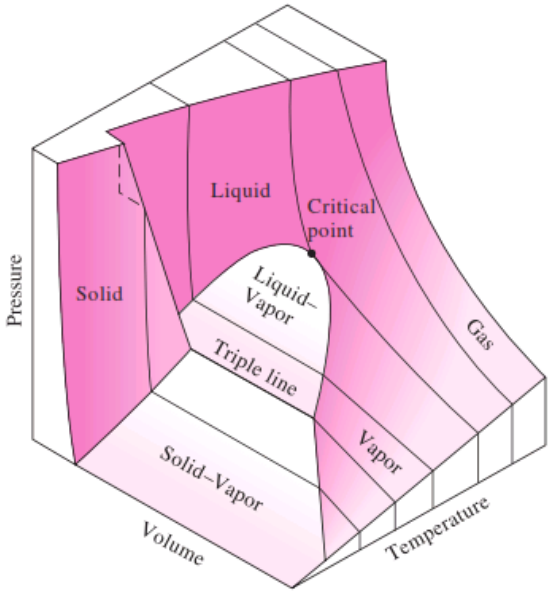

(b)

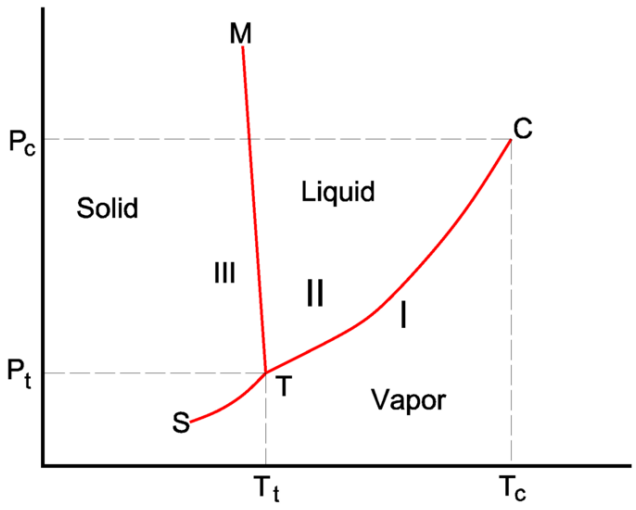

FIGURE 1.1. (a) *p-v-T* and (b) *p-T* diagrams for pure water. Sources: http://sounak4u.weebly.com/properties-of-pure-substance.html and https://commons.wikimedia.org/wiki/File:Clausius-Clapeyron_phase_diagram.png.

when the temperature decreases [73, 210], that is untypical for a liquid. Further, the specific heat of water is extremely elevated. Many other unusual properties make water a complicate matter in thermodynamics, therefore, to well approximate its behavior, complex equations of state are needed. For this reason, this thesis fully relies on the state-of-art equations of state IAPWS-95 [272] and IAPWS-IF97 [273], based on a large database of experimental data.

As visible from Fig. 1.1 two remarkable points exist in the water phase diagram. One is the

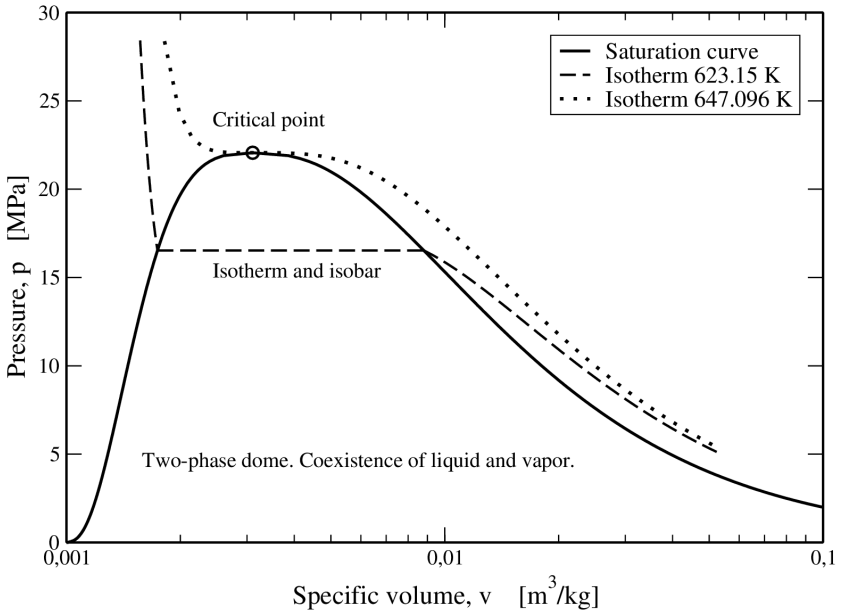

FIGURE 1.2. p-v diagram for pure water. Realized using IAPWS-IF97 EoS.

triple point T, where the three phases coexist and the fluid properties are [272]:

$$T_{tr} = 273.16\ K, \quad p_{tr} = 0.6117 \cdot 10^{-3}\ MPa.$$

The properties at the triple point are very well known. Since the 5^{th} International Conference on the Properties of Steam in London in 1956, it has been taken as reference state, thus the specific internal energy and the specific entropy of the saturated liquid triple point are set equal to zero:

$$e_{tr} = 0\ kJ/kg, \quad s_{tr} = 0\ kJ/kg/K.$$

The second one is the critical point C [272]:

$$T_{cr} = 647.096\ K, \quad p_{cr} = 22.064\ MPa, \quad \rho_{cr} = 322\ kg/m^3.$$

Concerning the *degrees of freedom* (Gibbs rule) of the matter, when only a single phase is present, the internal equilibrium is said to be *divariant*, that is the degrees of freedom are two. This means that to know the properties of the matter, two variables must be fixed, for instance pressure and temperature. When two phases are present and are in equilibrium (along the red lines of Fig. 1.1(b)), the system in *univariant*, that is, one degree of freedom, thus pressure and temperature are correlated. The critical and the triple points are fixed once for all, then the system is said to be *invariant*.

Given that this thesis deals with metastable fluids, as we will see in Chapter 2, phases can be divariant also in a mixture when phases are not in equilibrium.

The study of the liquid-vapor mixtures lying along the *vaporisation curve*, going from the triple point to the critical point, is the main topic of this thesis. For completeness, let us say also that the vaporization curve is also called in the literature as the *saturation curve*, the *vapor-pressure curve* or the *coexistence curve*. This curve is depicted in Fig. 1.2 on the p-v plane, where the vaporisation

curve becomes a *dome*. In Fig. 1.2, two isotherms are also shown: the one corresponding to 623.15 K and the critical one. Here we can see that in the saturation dome, when phase are in thermal equilibrium, the isotherms are also isobars due to the univariance of the equilibrium two-phase mixtures discussed above. Nevertheless this is not the case for mixtures of metastable phases.

Regarding the critical isotherm, it is the one that admits a horizontal tangent and an inflexion point, defining the end of the vaporisation curve. Mathematically, at the critical point:

$$\left(\frac{\partial p}{\partial v}\right)_T = 0, \qquad \left(\frac{\partial^2 p}{\partial v^2}\right)_T = 0, \tag{1.1}$$

and

$$\left(\frac{\partial T}{\partial s}\right)_p = 0, \qquad \left(\frac{\partial^2 T}{\partial s^2}\right)_p = 0. \tag{1.2}$$

On the $p-T$ diagram, the liquid-vapor transitions are accompanied by volume (but also entropy) discontinuities. For this reason they are usually called *first order phase transitions*[1]. The latter is a segment on the p-v diagram and is called *binodal curve*. The liquid-vapor transition at the critical point is not accompanied by a volume or entropy discontinuities but is called *second order phase transitions* because of the mathematical characteristic of this point (see Eqs. (1.1) and (1.2)). In this thesis we are mainly focused on first order phase transitions.

1.2 Equations of state and thermodynamic potentials

From the previous section it was stated that a single-phase system has two degrees of freedom. Therefore one needs to know two variables, together with a corresponding equation of state, to identify the thermodynamic state of the system.

The equation of state is a thermodynamic equation relating state variables and describes the physical conditions of the matter. This thermodynamic relation is usually constructed using thermodynamic potentials describing the equilibrium behavior of a system. They are: the *internal energy*, e, the *Helmholtz free energy*, f, the *enthalpy*, h, and the *Gibbs free energy*, g. The latter will be also called *Gibbs free enthalpy*. These potentials are related each other by the following algebraic relations:

$$\begin{aligned} f &= e - Ts, \\ h &= e + pv, \\ g &= h - Ts, \end{aligned} \tag{1.3}$$

where s is the specific entropy. Thanks to the thermodynamic potentials, the *complete EoS* take the form of

$$e(s,v), \qquad f(T,v), \qquad g(T,p), \qquad h(s,p). \tag{1.4}$$

Here the complete EoS are expressed in natural variables, that is, a set of appropriate variables that allow to compute the other thermodynamic potentials by partial differentiation. Therefore, no

[1] Ehrenfest proposed that the order of the transition is given by the lowest-order derivative of the Gibbs energy that is discontinuous at the transition. Entropy and volume are first order derivatives of the Gibbs energy.

other relations are needed to describe the thermodynamic behavior of the matter. In Chapter 2 we will see that compressible flow models require an equation of state in the form

$$p(\rho, e). \tag{1.5}$$

This is an *incomplete EoS* and needs additional relations to define, for instance, the temperature [63, 181]. Moreover, an incomplete EoS can not determine a corresponding complete EoS [181]. In this thesis, the incomplete EoS are replaced by iterative or a look-up table inversion of a reference complete EoS.

Referring to the thermodynamic potentials, their differentials are:

$$\begin{aligned} de &= \ \ Tds - pdv, \\ df &= -sdT - pdv, \\ dh &= \ \ Tds + vdp, \\ dg &= -sdT + vdp. \end{aligned} \tag{1.6}$$

The first is called *Gibbs relation* and is the fundamental equation of classical thermodynamics. In this context, Legendre transformations are a useful tool to pass from a potential to another one, see [4, 285] for further details. From those, together with the symmetry property of the second derivatives, one can obtain the *Maxwell's relations*:

$$\begin{aligned} \left(\frac{\partial T}{\partial v}\right)_s &= -\left(\frac{\partial p}{\partial s}\right)_v = +\frac{\partial^2 e}{\partial s \partial v}, \\ \left(\frac{\partial T}{\partial p}\right)_s &= +\left(\frac{\partial v}{\partial s}\right)_p = +\frac{\partial^2 h}{\partial s \partial p}, \\ \left(\frac{\partial s}{\partial v}\right)_T &= +\left(\frac{\partial p}{\partial T}\right)_v = -\frac{\partial^2 f}{\partial T \partial v}, \\ \left(\frac{\partial s}{\partial p}\right)_T &= -\left(\frac{\partial v}{\partial T}\right)_p = -\frac{\partial^2 g}{\partial T \partial p}. \end{aligned} \tag{1.7}$$

These relations will be extensively used for the calculation of the partial derivatives $\left(\frac{\partial}{\partial v}\right)_e$ and $\left(\frac{\partial}{\partial e}\right)_v$ needed for the water properties tabulation on the e-v plane. And they will be also useful to express more easily certain derivatives in the analysis of the relaxation of the thermodynamic disequilibrium.

Let us define also some thermodynamic properties that are used in the following. The specific heats at constant volume and pressure are

$$c_v = \left(\frac{\partial e}{\partial T}\right)_\rho = T\left(\frac{\partial s}{\partial T}\right)_\rho, \qquad c_p = \left(\frac{\partial h}{\partial T}\right)_p = T\left(\frac{\partial s}{\partial T}\right)_p. \tag{1.8}$$

The isothermal and isentropic compressibility factors are

$$k_T = \frac{1}{\rho}\left(\frac{\partial \rho}{\partial p}\right)_T, \qquad k_s = \frac{1}{\rho}\left(\frac{\partial \rho}{\partial p}\right)_s. \tag{1.9}$$

The coefficient of thermal expansion is

$$\beta = -\rho\left(\frac{\partial \rho}{\partial T}\right)_p. \tag{1.10}$$

The previous properties are also called direct measurable quantities and may be related by two identities

$$\frac{k_s}{k_T} = 1 - \frac{\beta^2 T}{\rho c_p k_T} = \frac{c_v}{c_p}. \tag{1.11}$$

Alongside with the phasic measurable quantities, two dimensionless parameters will be also used in the following. The adiabatic exponent γ and the Grüneisen coefficient Γ:

$$\gamma = \frac{1}{\rho p}\left(\frac{\partial^2 e}{\partial v^2}\right)_s = \frac{1}{p k_s}, \qquad \Gamma = \frac{1}{\rho}\left(\frac{\partial p}{\partial e}\right)_\rho = \frac{\beta}{c_v k_T}. \tag{1.12}$$

A paramount variable in compressible flows is the isentropic speed of sound. It is defined as

$$c = \sqrt{\frac{1}{\rho k_s}}. \tag{1.13}$$

1.3 Saturation curve

Along the saturation curve (or vaporization curve), the phase are in full thermodynamic equilibrium:

$$\begin{aligned} p_l &= p_v, \\ T_l &= T_v, \\ g_l &= g_v, \end{aligned} \tag{1.14}$$

where subscripts l and v indicate, respectively, the liquid phase and the vapor one, and where g denotes the Gibbs free enthalpy. The conditions expressed in Eq. (1.14) are also called *Maxwell criterion* [179].

Since the system is univariant, a dependency $p_{sat}(T)$, or $T_{sat}(p)$, exists. For instance, to construct the relation $p_{sat}(T)$ we apply the Gibbs-Duhem equation (see Eq. 1.6) between the two saturated states. Since it is an isotherm, this reduces to:

$$g_v - g_l = \int_{p_l}^{p_v} v dp. \tag{1.15}$$

Then, the saturation curve, $p_{sat}(T)$, can be constructed by requiring the vanishing of Eq. (1.15). Other methods exist to construct the saturation curve. However, in the case of water, the IAPWS-IF97 provides a suitable basic equation that relates saturation pressure and temperature.

1.4 Stability, metastability and instability

In this section a brief introduction to the concepts of stability, metastability and instability is given. Although it must not be considered as fully exhaustive. To learn more about this subject, the author suggests [43, 73] for a rigorous thermodynamic approach and [41] for a graphical and effective understanding.

To briefly introduce these concepts, it is useful to make the classical analogy reported in Fig. 1.3. It depicts the trend of a potential energy with respect to an arbitrary abscissa and the state of the system is represented by a sphere that can roll to a lower potential energy to reach its equilibrium.

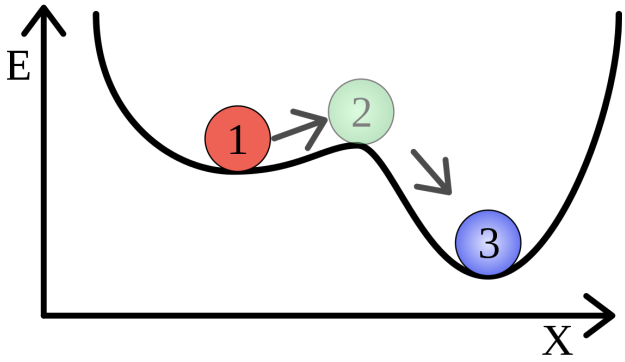

FIGURE 1.3. Concepts of *stability*, *metastability* and *instability*. Source: https://en.wikipedia.org/wiki/Metastability, drawing made by Georg Wiora (Dr. Schorsch).

The red sphere represents the metastable state, the green one the instable state and the blue the stable state of equilibrium of the system. Referring to thermodynamics, the potential energy is the Gibbs free enthalpy and the abscissa could be the specific volume.

The equilibrium state of the system corresponds to the absolute minimum of the Gibbs energy [43, 73] however another minimum exist, that is a relative minimum, and is where the red sphere lies. Let us consider now a liquid-vapor phase transition. The abscissa of the metastable state is the one of the liquid that is obviously lower than the one of the vapor, represented by the blue sphere. The equilibrium phase of the system would be the vapor one, however the fluid is initially a metastable liquid. In order to reach the equilibrium, it needs to overcome an *energy barrier* (the bump on the top of which the green sphere is located). Then it needs a high enough perturbation.

In other words, a metastable system, when subject to small perturbation does not evolve into another state; however, when the perturbation is higher than a certain activation value, it does. On the contrary, a stable system remains in its state no matter the perturbation. Finally, the instable state evolves to another state if subject to arbitrarily small perturbations.

1.4.1 Metastable water

In this work we refer to the metastability as: *the persistence of a phase into the stability domain of another phase*. For instance Fig. 1.4 shows the existence of metastable subcooled vapor in the subcooled liquid domain and the metastable superheated liquid in the superheated vapor domain. Obviously, the lifetime of a metastable phase is limited since a stable phase is always going to appear sooner or later. Moreover, the deeper the metastability of a phase, the shorter its lifetime is [73, 245].

In real systems, the fluids are never pure, suspended impurities exist, the container walls have irregularities, etc. These facilitate the nucleation of a new phase preventing the fluid to reach a deep metastable state. They simply decrease the energy barrier discussed above, needed to activate the nucleation mechanisms. This means that the higher the purity of a fluid, the higher is the possibility to reach a deep metastable state.

In the case of liquid water, experimentally, one can observe the *supercooled water*, the *superheated water* and the *tensile water*. The first is the case of water staying in liquid form below its solidification

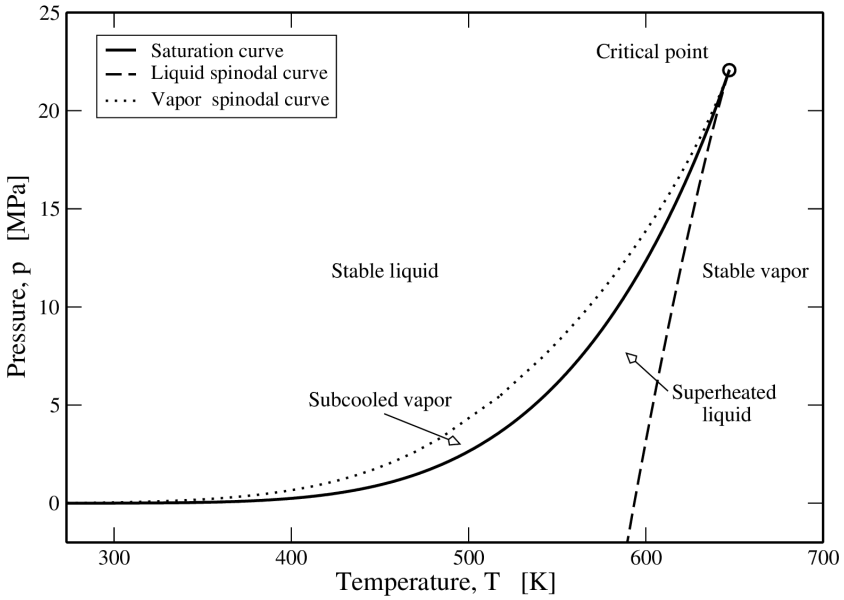

FIGURE 1.4. p-T diagram of water. The plot has been realized using the IAPWS-IF97.

temperature, for instance [73, 138]. The second is liquid water at a temperature higher than the boiling temperature (or, equivalently, at a pressure lower than the saturation pressure) and is the case on which this work is focused on. Some experimental evidences of superheated water are reported in [8, 32, 246]. The superheated water could also reach negative pressures, that is the fluid is able to make a tensile strength on its container walls, for this reason it is also called *tensile* [73, 131]. The vapor can be metastable too, as in the case of the *subcooled vapor*, i.e. vapor at a temperature lower than the condensation one.

A good reference for the experimental procedures to obtain metastable water and their limits is [99].

There are two approaches to the phase stability: the *microscopic* and the *phenomenological* ones. The first is based on statistical mechanics. The second is based on the continuum thermodynamics and is more suitable for macroscopic systems, therefore, the more appropriate for our industrial purposes. A remarkable difference between the two approaches is that following the microscopic approach, there is not a sharp transition from metastability to instability. The spinodal is not a mathematical and physical locus, rather, an approximation.

For the *phenomenological* approach we start analyzing the phase stability of an isolated system. From thermodynamics, it is well known that an isolated system attains a maximum value of entropy at equilibrium [43]. Hence, the criteria for equilibrium and stability can be expressed as:

$$\begin{aligned} &\delta S = 0 && \textit{criterion of equilibrium}, \\ &\delta^n S < 0, \quad \text{for the smallest } n \text{ at which } \delta^n S \neq 0 && \textit{criterion of stability}, \end{aligned} \tag{1.16}$$

where δS and $\delta^n S$ are a shorthand way of representing the terms of successive order. For instance, for $S = S(e,v)$:

$$\delta S = \left(\frac{\partial S}{\partial e}\right)_v de + \left(\frac{\partial S}{\partial v}\right)_e dv. \tag{1.17}$$

Further developments of the last criterion of Eq. (1.16) provide two conditions which ensure the stability of a system:

$$\begin{aligned} c_v > 0 \qquad & \textit{criterion of thermal stability}, \\ \left(\frac{\partial p}{\partial v}\right)_T < 0 \qquad & \textit{criterion of mechanical stability}. \end{aligned} \tag{1.18}$$

If both are satisfied, the system is *intrinsically stable*. Both the equilibrium and the metastable phase are intrinsically stable, however, the latter remains in this condition only for a finite time interval. When the thermal fluctuations and the molecular vibrations drive the system to the equilibrium conditions, provoking vaporisation (for the superheated liquid) or condensation (for the subcooled vapor), the metastable phase disappears.

1.4.2 Spinodal curve

The criterion of thermal stability shown in (1.18) is always satisfied, whereas the fulfillment of the mechanical stability criterion is not always ensured. For instance, cubic EoS, such as the van der Waals EoS, satisfy the mechanical stability condition until the so-called spinodal line. The spinodal line seems to indicate the separation between the unstable domain from the stable/metastable one, however, it is just an artifact of equations of state describing both the liquid and the vapor phase.

In equilibrium thermodynamics phase transition occurs at saturation conditions, on the contrary, in real systems an isothermal pressure change would very likely carry the state point into the metastable domain. The deeper the metastability reached, the higher is the probability for the phase change to occur. The spinodal curve is the limit beyond which phase change has already occurred.

The liquid and vapor spinodal lines connect all the minima of the isotherms (*liquid spinodal*) and all the maxima (*vapor spinodal*) closest to the associated side of the saturation curve within the saturation dome. At these minima and maxima points isotherms have zero slope (see Fig. 1.5), hence, spinodal lines mark the location from where the mechanical stability condition is violated.

Using the IAPWS-IF97 as EoS, we reveal in the following that the spinodal corresponds to positive values of the pressure until $T \approx 593.50\,K$. Below this temperature, the limit of mechanical stability corresponds to negative pressures. This is the domain of the *tensile water* [49, 73, 131, 132, 143, 170, 245, 284], however this is out of interest in this thesis.

1.5 Metastable fluids in nature and in industry

Pure water and aqueous solutions are often in metastable conditions, both in nature and industry, nonetheless, these conditions of the matter are often ignored. For this reason, this section enumerates and briefly discusses the main fields in which metastable states exist.

In geology, the water is often metastable in the soil due to capillarity [206] or in the deep earth's crust [243]. Metastable states are common in regions of high thermal fluxes (volcanic regions and magmas [259], geysers [215], etc.), therefore, many research papers on metastability come from the geophysics and geochemistry journals. Evidently, this is not restricted to the planet Earth, in fact, metastable aqueous solutions are believed present in the hyper-arid environments of Mars [182, 183].

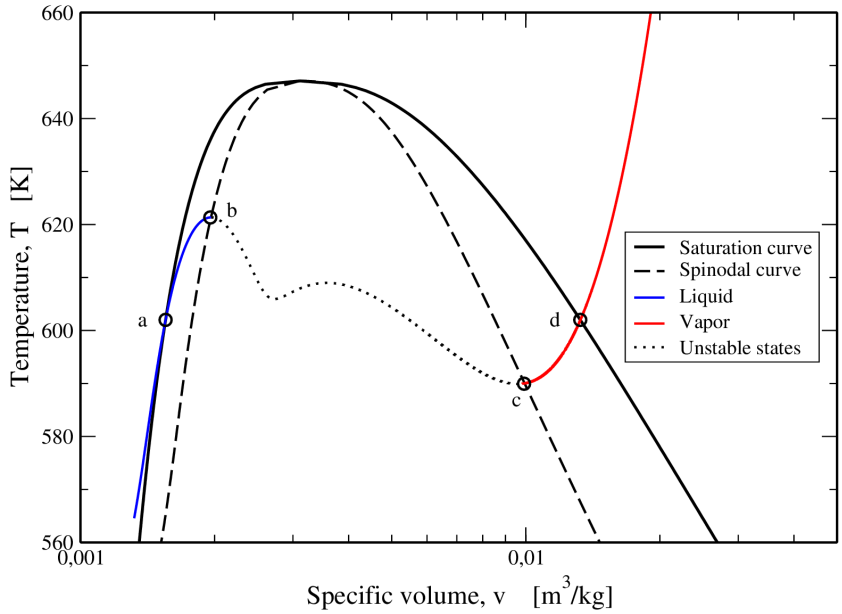

FIGURE 1.5. T-v diagram of water. The plot has been realized using the IAPWS-IF97. Here we can see the saturation curve, the spinodal curve ($(\partial p/\partial v)_T = 0$) and an isobaric curve (i.e. $p = 12.7 MPa$). The latter has been divided in three portions: the blue one represents the liquid states, the red one denotes the vapor states and the black dotted curve refers to the unstable states that connect the previous ones. Going rightwards along the isobaric curve, up to point (a) water is liquid in a stable state, from (a) to (b) water is a metastable liquid, from (b) to (c) the fluid is in unstable conditions, from (c) to (d) water is in metastable vapor conditions and, starting from point (d), the vapor is stable.

In biology, the metastable states, especially the supercooled ones, play a fundamental role for the life of cells, microorganisms, etc. An interesting discussion is reported in the introductory chapter of [73].

Another relevant field in which we can find metastable water is in plant physiology. In fact, an aqueous solution, called *sap*, becomes tensile in reaching the tops of trees. The fact that water reaches negative pressures inside the trees is known at least from the 19^{th} century [73]! Many of the EoS for the negative pressure domain have been developed to simulate such a phenomenon.

As concerns industry, metastability is often synonym of accident. In industrial processes, metastable states typically appear due to fast depressurizations or to energy injection. As already discussed, the industrial context of this thesis is the one of the hypothetical nuclear accidents involving metastable two-phase flows. However, the same phenomena could be encountered in many industrial process or chemical factories. For example, in beer or sparkling drinks production sites, paper factories, in the metallurgy for cooling the melting metals, in petroleum engineering (LNG), etc.

Some of them are fully stationary as the critical two-phase flow through a safety valve or a breach of a pipe. Some others are highly non-stationary phenomena, like fast depressurizations, waterhammers or energy injection. Those kinds of phenomena are separately addressed respectively in Chapters 3 and 4.

CHAPTER 2

MATHEMATICAL FEATURES OF TWO-PHASE FLOW MODELS

This chapter introduces many concepts that will be necessary for the following. An introduction to the main features of the two-phase flows is given in 2.1. Here the physical and mathematical complexities of the two-phase flows are discussed. These complexities translate into numerical difficulties for the computational simulation of such flows. To overcome them, the balance laws for two-phase flows are often *averaged* [137]. Further, many computational techniques exist, then it is important to well specify the numerical approaches that will be used in order to give the precise numerical context to this thesis. Section 2.2 gives some mathematical information about compressible multiphase flows and their equations of state. Section 2.3 describes the most common two-phase flow models and the hierarchy existing according to the disequilibria allowed between phases. To each of these models corresponds a different formulation of the two-phase speed of sound. For the homogeneous models, a comparison is given in Section 2.4.

2.1 Introduction to two-phase flows

Two-phase flow phenomena are involved in many industrial fields as well as in nature. One can mention *power systems* as conventional or nuclear power plants, *process systems* as distillation units or chemical reactors, *heat transfer systems* as heat exchangers, evaporators and condensers, *biological systems* as the cardiovascular or the respiratory systems, *other natural phenomena* as volcanic jets or clouds formations. The two-phase flows arising from such a variety of systems are very different from many viewpoints: the phases involved (gas-liquid, gas-solid, liquid-solid), the flow regime, the kind of interactions between the phases, etc.

Two-phase flows are widely more complicated than single-phase ones. For instance, single-phase flows are generally categorized as laminar, transitional and turbulent. Whereas, for two-phase flows, plenty of *flow regimes* (or *flow patterns*) exist and their categorization is not often the same from one textbook to another.

At the beginning, the analysis of the two-phase flows was somewhat *empirical* and widely based

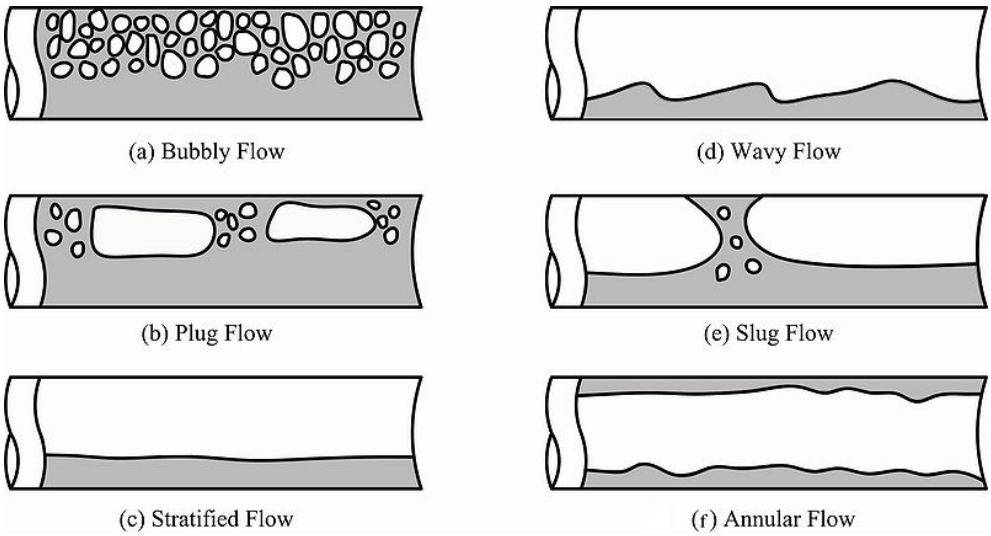

FIGURE 2.1. Two-phase flow patterns for a liquid-vapor mixture. Source: http://www.thermalfluidscentral.org/encyclopedia/.

on experimental correlations. Hence, its validity was constrained by the test setup, the experimental range investigated, etc. Due to the large number of fields and applications of two-phase flows, one can imagine that a large number of tests were done and a lot of correlations exist. Some good references for this kind of approach are [39, 43, 58, 278].

Later, there was a shift from the empirical approaches to the *mathematical modeling*. This allowed the improvement of the prediction of the dynamical behavior of two-phase flows and to unify many fields and phenomena that were previously treated by separate empirical approaches. In fact, very different phenomena could be analyzed using the same mathematical and numerical tools. Some references for the mathematical modeling of two-phase flows are [136, 145].

This thesis is based on the latter approach, however, due to the difficulties to treat some phenomena, correlations are also used. For instance to model the pressure losses in a two-phase flow (cf. Chapter 3) or to quantify the characteristic time of thermodynamic equilibrium recovery (cf. Chapter 4).

2.1.1 Averaging methods and diffused interface technique

In a two-phase flow, two media (or *fields*) with different properties flow together. The two fields must be disjoint, therefore, they cannot be two gases. An interface separates the two fields, hence, this is the locus of the discontinuities of fluid properties. The interfaces are multiple, topologically complicated and their shape depends on the flow pattern (see Fig. 2.1). Moreover, interfaces move, deform and may interact in time and in space. In phase-transition flows, they may also disappear.

These features make us understand that the mathematical and computational treatment of such complicated and time-dependent interfaces is not easy at all. For the feasibility of the numerical treatment of two-phase flows, those *sharp interfaces* are replaced by *diffused interfaces*. In other words, some details of the flow are suppressed in order to obtain easier systems of equations for the numerical treatment.

Mathematically, this involves the *averaging* of the field properties. Generally, we speak about time averaging but also spatial and statistical averaging techniques exist. Standard references are [76, 86, 136], however, those topics are discussed in any multiphase flow textbook, a concise one is reported in Chapter 8 of [213].

The system of equations obtained must be seen as a macroscopic formulation that is continuous across the interfaces, eliminating the fluid properties discontinuity across them and making both phases coexisting continua [137]. Those systems are composed by *field balance equations* describing mass, momentum and energy conservation complemented by *constitutive equations* and *interfacial transfer terms* that describe momentum transfer, thermo-chemical transfers, wall friction, etc.

Thanks to averaging, complicated interfaces are absorbed into the volume fraction variables: α_k. In fact, in two-phase flow analysis, the volume fractions, α_k, and the interfacial area, A_{int}, are two fundamental first-order geometrical parameters and they are closely related to the flow regime [137].

In Chapters 3 and 4 of Part II, the interfacial area is not used because the two phases are considered as a homogeneous mixture and interfacial exchanges are not modeled. However, in Chapter 6, new relaxation procedures are proposed in order to correlate the interfacial exchanges to the interfacial area.

2.1.2 Computational methods for two-phase flow

The great heterogeneity of two-phase flows and its presence in many industrial fields has led to the development of several computational techniques. A reference book describing the most important ones is [213]. Due to the presence of many computational methods, it is important to specify the kind of techniques employed for this thesis.

As mentioned above, two-phase flows are very complicated due to the presence of complex interfaces. For very simple flows, the averaging procedure is not necessary and Navier-Stokes equations may be solved for each phase. This requires an interface tracking method as marker functions or connected marker particles.

When the flows become more complex, the direct solution of the Navier-Stokes equations would be too expensive from a computational point of view, therefore, the expedient is the solution of the averaged equations aforementioned. For a general flow pattern, the two most important techniques for the numerical solution of averaged equations are *segregated methods* [20, 161, 198] and *coupled methods* [24, 220, 221, 231, 247, 252, 262].

For the first approach, the balance equations are solved sequentially. This idea comes from the SIMPLE method, widely used in the single-phase CFD. For the second approach, the equations of the system are simultaneously solved, hence, they are strictly coupled. Evidently, the latter is the only one suitable for fast transient calculations and/or for the analysis of flows in which phases have very strong interactions. This is the case of the industrial context of this thesis: a strong coupling between the conservation equations, strong interactions between phases and the simulation of fast transients. Therefore, only coupled methods are used in the following.

The systems of Partial Differential Equations (PDEs) are solved using the Finite Volume Method where the flux across the interfaces between adjacent finite volumes is calculate using Riemann

Solvers [116, 264]. From the computational point of view, the main works in the literature of two-phase flow on which this thesis is based are [112, 200, 231, 233, 234, 262, 263, 283].

The only exception to this approach is Chapter 3. Here the stationary metastable critical flows are analyzed, therefore, the time dependency of the balance equations is removed. The latter become Ordinary Differential Equations (ODEs) that are solved in a more classic fashion using Runge-Kutta ODE solvers.

2.2 Averaged two-phase flow models

Considering the macroscopic approach aforementioned, phases can be simultaneously present in a volume domain, for instance the cell mesh of the computational domain. This is also called *interpenetrating continua hypothesis*. Several two-phase flow models exist, their classification is given in the next section. Here a brief introduction of their mathematical properties is given.

Considering for simplicity the 1D case, the averaged two-phase flow models can be generally written as

$$\partial_t \mathbf{U} + \partial_z \mathbf{F}(\mathbf{U}) + \mathbf{B}(\mathbf{U})\, \partial_z \mathbf{U} = \mathbf{b}, \qquad z \in \mathbb{R}, \quad t \in \mathbb{R}^+, \tag{2.1}$$

where $\mathbf{U} \in \Omega_U \subset \mathbb{R}^n$ is the state vector and Ω_U is the phase-space. Given that the industrial context of this thesis includes also shock waves, conservative forms of the balance equations are always preferred. In fact, for smooth solutions all formulations are equivalent. However, for solutions containing shock waves, non-conservative formulations give incorrect shock solutions [264]. Therefore, $\mathbf{U}$ is the vector of the conservative variables, that is, its components are *physically conserved quantities* as mixture (or phasic) mass, momentum and total energy. The only exception is the volume fraction of one of the two species. Sometimes, for sake of simplicity, it is included into the vector $\mathbf{U}$, however, it is not a conservative quantity.

The conservative part of the system is contained in the nonlinear flux vector $\mathbf{F} = \mathbf{F}(\mathbf{U})$, and the nonconservative terms, if present, are expressed in the nonconservative product $\mathbf{B}(\mathbf{U})\partial_z \mathbf{U}$. Unfortunately, for some two-phase flow models, the homogeneous portion of Eq. (2.1) is not a system of conservation laws. This is the case when the matrix of nonconservative terms $\mathbf{B}(\mathbf{U}) \neq 0$. Due to the nonconservative form of the equations, the standard notion of *weak solution* in the sense of distributions does not apply. More precisely, because of the nonconservative term, $\mathbf{B}(\mathbf{U})\partial_z \mathbf{U}$, and the fact that products of distributions are not defined by the theory of distributions [239], it is not possible to rigorously define the notion of weak solution and it is not possible to derive Rankine-Hugoniot jump conditions. Moreover, for this kind of two-phase flow models, the uniqueness of solutions can not be guaranteed in the presence of discontinuities.

Alternatively, the PDE (2.1) can be cast in its quasi-linear form

$$\partial_t \mathbf{U} + \mathbf{A}(\mathbf{U})\, \partial_z \mathbf{U} = \mathbf{b}, \tag{2.2}$$

where the matrix

$$\mathbf{A}(\mathbf{U}) = \frac{\partial \mathbf{F}}{\partial \mathbf{U}} + \mathbf{B}(\mathbf{U}) \tag{2.3}$$

includes both the conservative and the nonconservative terms. The term $\frac{\partial \mathbf{F}}{\partial \mathbf{U}}$ is the Jacobian of the nonlinear flux. The system is hyperbolic if $\mathbf{A}(\mathbf{U})$ has only real eigenvalues and a full set of linearly

independent eigenvectors exists. The eigenvalues are

$$\lambda_1 \leq \lambda_2 \leq ... \leq \lambda_n, \qquad \lambda_i \in \mathbb{R}. \tag{2.4}$$

To close system (2.1), one or two equations of state are needed. In fact, according to the kind of disequilibria existing between the two phases, system (2.1) may require a single equation of state for the mixture equilibrium pressure:

$$p = p(\rho, e, ...) \tag{2.5}$$

where the mixture density and internal energy are:

$$\begin{aligned} \rho &= Y_1 \rho_1 + Y_2 \rho_2, \\ e &= Y_1 e_1 + Y_2 e_2, \end{aligned} \tag{2.6}$$

$Y_k = \alpha_k \rho_k / \rho$ being the phasic mass fractions.

Other models require two separate equations of state, one per phase:

$$p_k = p_k(\rho_k, e_k), \qquad k = 1,2. \tag{2.7}$$

The latter case relies upon the *principle of phase separation* [87]. That is, the thermodynamic properties of one phase do not depend on the thermodynamic state of the other constituent.

Coming back to Eq. 2.1, the vector $\mathbf{b}$ accounts for the source terms. They can be: heat source, wall friction, thermo-chemical interfacial transfers, momentum transfer, etc. In Chapter 3, source terms will account for the macroscopic effect of heat transfer, wall shear stress, gravitational force and mass transfer. In Chapter 4, the source terms are the mass transfer for the Homogeneous Relaxation Model (HRM) and the volumetric energy injection (for the simulation of a steam explosion). In Chapter 6, the source terms will serve to model the transfers between phases in a less macroscopic way. In fact, the component of $\mathbf{b}$ are used to describe the volume-energy transfer due to the pressure disequilibrium between phases and the interfacial thermal and chemical transfers due to, respectively, temperature and Gibbs enthalpy disequilibria. Despite the paramount importance they have in the two-phase flow analysis, in this chapter they will be neglected to focus on the mathematical features of the convective portion of the system of equations. Therefore, throughout this chapter, $\mathbf{b} = 0$.

2.3 Hierarchy of the two-phase flow models

Different models describing two-phase flows are available in the literature. Here we consider compressible flow models that belong to the class stemming from the Baer–Nunziato model [12]. Models in this class differ primarily in the level of non-equilibrium between the two phases that they are able to take into account.

Each phase is described by five variables, therefore ten variables describe a two-phase flow [254]:

$$\alpha_k,\ p_k,\ T_k,\ g_k,\ u_k, \qquad k = 1,2. \tag{2.8}$$

The volume fractions α_k indicate the amount of space occupied by each phase and are constrained by the following volume saturation condition:

$$\alpha_1 + \alpha_2 = 1. \tag{2.9}$$

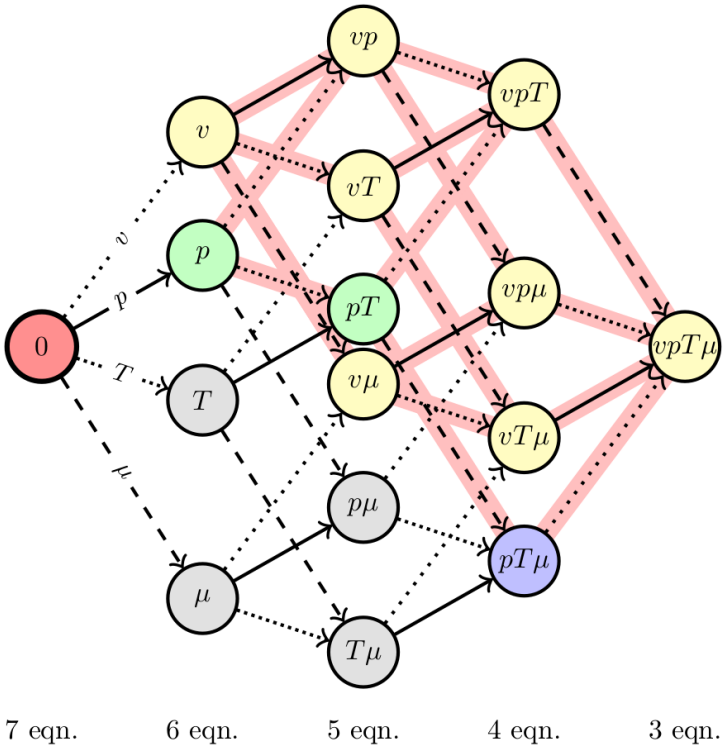

FIGURE 2.2. Four-dimensional hypercube representing the hierarchy of two-phase flow models. Parallel edges correspond to the same relaxation processes, and vertexed (circles) represent the models of the hierarchy. Arrows indicate the instantaneous relaxation processes needed to reach the pressure (p), temperature (T), chemical (μ) and velocity (v) equilibria. For instance, the 0 model represents the seven-equation model of [12], the v model is the single-velocity six-equation model used in Part III, and $vpT\mu$ denotes the homogeneous equilibrium model. The *homogeneous models*, that is, the models assuming that phases move at the same velocity, are represented by yellow circles. Source: [171].

Further, as discussed in Section 1.1, each phase has two degrees of freedom, hence an EoS relates one variable to the two others, for instance $g_k = g_k(p_k, T_k)$. From these considerations, the degrees of freedom are, at the maximum, seven. Then, seven partial differential equations are required to describe a two-phase flow in full disequilibrium.

Adding some equilibrium hypothesis reduces the number of equations required and those models are called: *reduced models*. Finally, compressible two-phase flow models span from the seven equation model (Baer–Nunziato 1986) to the Homogeneous Equilibrium Model (HEM). The former allows pressure, temperature, Gibbs enthalpy and velocity disequilibria between phases, whereas, the latter assumes phases are in full equilibrium.

Then there exist a hierarchy of the compressible two-phase flow models according to the allowed disequilibria. A practical scheme to understand this hierarchy is reported in Fig. 2.2. Referring to this figure, the hierarchy is represented by means of a four-dimensional hypercube where each circle represents a two-phase flow model and edges denote the relaxation processes. In particular, parallel edges correspond to the same relaxation processes. This representation of the hierarchy of

two-phase flow models is due to Linga [171].

The 0 model represents the seven-equation model of [12], where phases are in full disequilibrium. Proceeding from left to right, equilibria are added, up to the full equilibrium model, the HEM, here denoted as $vpT\mu$. Reduced models of the 7-eq. model can be obtained using the Chapman-Enskong developments [54, 189], as done in [155].

The *homogeneous models*, that is, the models assuming that phases move at the same velocity, are represented by yellow circles. More details about the mathematical properties of these models and their speed of sound are reported in [54, 176]. Except for a comparative study in Chapter 3, all the models considered in this thesis belong to the subhierarchy of the homogeneous models.

The model indicated as p is the single-pressure six-equation model and, among the various models of the hierarchy, it is the most employed in engineering. It is very popular notwithstanding its well-known ill-posedness, due to the loss of hyperbolicity on a large part of the phase-space [24, 178, 254, 262, 263], that may lead to numerical difficulties.

Evidently, not all models represented in Fig. 2.2 are of practical use in engineering because some rely on unrealistic hypothesis. To explain better this affirmation, let us assume that there exist characteristic times of the equilibrium recovery processes for pressure Θ^p, temperature Θ^T, velocity Θ^u and Gibbs enthalpy Θ^μ disequilibria. Labois, in Chapter 1 of [155], analyses the orders of magnitude of these characteristic times and he found that

$$\Theta^p \ll \Theta^u \ll \Theta^T \ll \Theta^\mu. \tag{2.10}$$

About those characteristic time evaluations, see also [30, 119, 139, 205, 205].

This analysis indicates that the pressure relaxation process is much faster than the velocity relaxation one, that, in turn, is faster than the thermal relaxation process. And the latter is faster than the chemical relaxation process. This means that the model indicated as $vT\mu$, for instance, considers that phases are in thermodynamic equilibrium, they move at the same velocity, however, they have different phasic pressure. This is clearly in contrast with Eq. (2.10).

In the following the most important two-phase flow models are discussed. The reduced models are not formally derived from the seven equation model, because this practice, by now, is well known for the two-phase flow domain. The next section is intended to be a discussion about the reduced models and their physical and mathematical properties.

For a comprehensive discussion about all the various models, one can refer to [139, 155, 176, 178, 254].

2.3.1 The seven-equation model

The most complete among the compressible two-phase flow model is the seven equation model of Baer–Nunziato (1986) [12], sometimes called Non-Equilibrium Model (NEM). It allows a full disequilibrium between phases. In fact pressure, temperature, Gibbs enthalpy and velocity of the phases are not in equilibrium.

In 1D, the homogeneous portion of the system of equations is

$$\begin{cases} \partial_t \alpha_1 + u_{int}\partial_z \alpha_1 = 0, \\ \partial_t(\alpha_1\rho_1) + \partial_z(\alpha_1\rho_1 u_1) = 0, \\ \partial_t(\alpha_2\rho_2) + \partial_z(\alpha_2\rho_2 u_2) = 0, \\ \partial_t(\alpha_1\rho_1 u_1) + \partial_z(\alpha_1\rho_1 u_1^2 + \alpha_1 p_1) - p_{int}\partial_z \alpha_1 = 0, \\ \partial_t(\alpha_2\rho_2 u_2) + \partial_z(\alpha_2\rho_2 u_2^2 + \alpha_2 p_2) - p_{int}\partial_z \alpha_2 = 0, \\ \partial_t(\alpha_1\rho_1 E_1) + \partial_z[\alpha_1(\rho_1 E_1 + p_1)u_1] - p_{int}u_{int}\partial_z \alpha_1 = 0, \\ \partial_t(\alpha_2\rho_2 E_2) + \partial_z[\alpha_2(\rho_2 E_2 + p_2)u_2] - p_{int}u_{int}\partial_z \alpha_2 = 0, \end{cases} \tag{2.11}$$

where p_{int} and u_{int} are, respectively, the interfacial pressure and velocity.

The system has seven real eigenvalues:

$$\lambda_1 = u_{int}, \quad \lambda_2 = u_1 - c_1, \quad \lambda_3 = u_1, \quad \lambda_4 = u_1 + c_1, \quad \lambda_5 = u_2 - c_2, \quad \lambda_6 = u_2, \quad \lambda_7 = u_2 + c_2. \tag{2.12}$$

They have not been enumerated to give $\lambda_i \leq \lambda_{i+1}$ as stated in (2.4). The fields associated with the $\lambda_{3,6}$ are linearly degenerate (LD) whereas the ones associated to the $\lambda_{2,4,5,7}$ are genuinely non linear (GNL). See [116, 168, 264] for more information about LD and GNL fields. The field associated with $\lambda_1 = u_{int}$ can be LD or GNL according to the choice of the interfacial velocity. Therefore, this choice greatly impacts the mathematical properties of (2.11), then, the numerical strategy for its discretization.

For instance, if u_{int} is chosen in order to have a LD-field associated with λ_1, the volume fractions will not change across shock waves, therefore, the nonconservative terms will be inactive across the shocks. This avoids numerical difficulties in the discrete treatment of those terms. To understand better the numerical discretization of nonconservative products, see Section 5.3.1.

An analysis of the couple interfacial pressure and velocity which ensures that the field associated to λ_1 be LD and that enforces the entropy inequality is given in [61]. Some other authors have preferred physically-based choices of p_{int} and u_{int}, with the duty of dealing with nonconservative products, for instance in [231].

As already stated, the phases are in full thermodynamic disequilibrium, that is

$$p_1 \neq p_2, \qquad T_1 \neq T_2, \qquad u_1 \neq u_2, \qquad g_1 \neq g_2. \tag{2.13}$$

To close system (2.11), two decoupled equations of state are needed:

$$p_k = p_k(\rho_k, e_k), \qquad k = 1,2. \tag{2.14}$$

The 7-equation model has become popular a few decades later than the spreading of the single-pressure six-equation model. The idea of introducing an extra equation with respect to the single-pressure six-equation model, was initially introduced by [190, 196, 197, 217] in order to allow the pressure disequilibrium and to avoid the ill-posedness of the single-pressure six-equation model (see next paragraph). Baer–Nunziato [12], simplified and generalized this idea neglecting the inertial effects for the void fraction evolution.

Since then, this model is quite popular especially for the deflagration to detonation analysis of explosives, then, reactive granular multiphase mixtures. Also thanks to the work of Abgrall, Saurel and their co-workers [231], this model has become popular for simulating one-component multiphase flow transients as cavitations, etc.

Currently it is the reference model of the under development RELAP-7 code [221] and has been integrated in the fast dynamics code EUROPLEXUS [64, 71, 173–175] for the analysis of steam-water fast transients as waterhammers, etc.

2.3.2 The single-pressure six-equation model

The single-pressure six-equation model (p in Fig. 2.2) is certainly the most used two-phase flow model, at least in the nuclear safety and thermal hydraulics domain.

Up to now it is reference model of several codes: CATHARE [24], NEPTUNE_CFD [203], RELAP-5 [220], TRAC [252], WAHA [262, 263]. Notwithstanding with its mathematical problems, it has demonstrated to be robust and accurate for a great number of situations. But, due to its ill-posedness, it is less suitable for dominant wave motion phenomena.

In 1D, the homogeneous portion of the system of equations is

$$\begin{cases} \partial_t(\alpha_1\rho_1) + \partial_z(\alpha_1\rho_1 u_1) = 0, \\ \partial_t(\alpha_2\rho_2) + \partial_z(\alpha_2\rho_2 u_2) = 0, \\ \partial_t(\alpha_1\rho_1 u_1) + \partial_z(\alpha_1\rho_1 u_1^2 + \alpha_1 p) - p\,\partial_z\alpha_1 = 0, \\ \partial_t(\alpha_2\rho_2 u_2) + \partial_z(\alpha_2\rho_2 u_2^2 + \alpha_2 p) - p\,\partial_z\alpha_2 = 0, \\ \partial_t(\alpha_1\rho_1 E_1) + \partial_z[\alpha_1(\rho_1 E_1 + p)u_1] + p\,\partial_t\alpha_1 = 0, \\ \partial_t(\alpha_2\rho_2 E_2) + \partial_z[\alpha_2(\rho_2 E_2 + p)u_2] + p\,\partial_t\alpha_2 = 0. \end{cases} \tag{2.15}$$

This model can not be cast in a conservative form, then, the uniqueness of solutions can not be guaranteed in the presence of discontinuities. Further, it is not hyperbolic [31, 36, 115, 254], thus, mathematically, it presents an ill-posed initial value problem in the sense of Hadamard [122]. This means that the solution does not probably depend continuously on the initial data [42].

Several authors have added extra terms to make the system conditionally or inconditionally hyperbolic [209], for example adding a virtual mass term in the momentum equation [85] or using an interfacial pressure [24, 62]. The latter term has a physical meaning when the flow is stratified, otherwise, it is just a mathematical trick to ensure hyperbolicity on a large portion of the phase-space.

The system eigenvalues and their nature do depend on the hyperbolization technique used. An analysis of eigenstructure of this model is given in [262]. Similarly to system (2.11), two eigenvalues are equal to the phasic velocities: $\lambda_1 = u_1$, $\lambda_2 = u_2$ and the fields associated are LD. The other four eigenvalues are functions of the phasic densities, velocities, celerities and volume fractions. The fields associated are GNL.

Phases are in thermodynamic disequilibrium, moving at different velocity but at the same pressure, that is

$$p_1 = p_2 = p, \qquad T_1 \neq T_2, \qquad u_1 \neq u_2, \qquad g_1 \neq g_2. \tag{2.16}$$

Since the application domain of this model is not the one of the wave propagation phenomena, alternative forms, not expressed in conservative variables, are often used in the codes. Thus, the EoS used can be rather different. A popular way to rewrite system (2.15) in a nonconservative form is:

$$\mathbf{C}\,\partial_t \mathbf{W} + \mathbf{D}\,\partial_z \mathbf{W} = 0, \tag{2.17}$$

where the vector of the independent variables is $\mathbf{W} = (p, a, u_1, u_2, e_1, e_2)^T$ or $\mathbf{W} = (p, a, u_1, u_2, h_1, h_2)^T$, according to the code, thus, to close system (2.17), the EoS needed are:

$$\rho_k = \rho_k(p, e_k), \qquad k = 1,2, \tag{2.18}$$

or

$$\rho_k = \rho_k(p, h_k), \qquad k = 1,2. \tag{2.19}$$

This makes one understand why most of the steam-water libraries are arranged on the $p-e$ thermodynamic plane [44] or on the $p-h$ one [156, 218, 280].

When the formulation with the conservative variables reported in system (2.15) is used for numerical purposes as done in [262], to close the system, one needs:

$$p = p(\alpha_1\rho_1, \alpha_2\rho_2, e_1, e_2), \qquad \alpha_k = \alpha_k(\alpha_1\rho_1, \alpha_2\rho_2, e_1, e_2). \tag{2.20}$$

Due to the pressure equality assumption, and the fact that the void fraction is not known *a priori*, the EoS require often an iterative procedure (unless simple analytic EoS are used), that is computationally expensive [262].

2.3.3 The single-velocity six-equation model

The single-velocity six-equation model is indicated by the circle v in Fig. 2.2. It represents the most complete among the subhierarchy of the homogeneous two-phase flow models and it is the subject of Part III of this thesis.

In the homogeneous models, phases evolve at the same velocity. This leads to a much simpler wave pattern, in fact, all the homogeneous models have the same wave pattern of the single-phase gas dynamics Euler equations. Notwithstanding to the similar wave pattern, the mathematical and physical properties of the homogeneous models are very different according to the thermodynamical disequilibria allowed between the phases.

In 1D, the homogeneous portion of the single-velocity six-equation model is

$$\begin{cases} \partial_t \alpha_1 + u\partial_z \alpha_1 = 0, \\ \partial_t(\alpha_1\rho_1) + \partial_z(\alpha_1\rho_1 u) = 0, \\ \partial_t(\alpha_2\rho_2) + \partial_z(\alpha_2\rho_2 u) = 0, \\ \partial_t(\rho u) + \partial_z(\rho u^2 + \alpha_1 p_1 + \alpha_2 p_2) = 0, \\ \partial_t(\alpha_1\rho_1 E_1) + \partial_z[\alpha_1(\rho_1 E_1 + p_1)u] + \Sigma(\mathbf{U}, \partial_z \mathbf{U}) = 0, \\ \partial_t(\alpha_2\rho_2 E_2) + \partial_z[\alpha_2(\rho_2 E_2 + p_2)u] - \Sigma(\mathbf{U}, \partial_z \mathbf{U}) = 0. \end{cases} \tag{2.21}$$

The nonconservative terms in the phasic total energy equations are

$$\Sigma(\mathbf{U}, \partial_z \mathbf{U}) = -u\left[Y_2 \partial_z(\alpha_1 p_1) - Y_1 \partial_z(\alpha_2 p_2)\right]. \tag{2.22}$$

These terms are non-zero if $u \neq 0$ and if $Y_1 Y_2 \neq 0$, that is, the fluid is a mixture containing both species moving at non-zero velocity. The presence of nonconservative terms does not guarantee the uniqueness of solutions in the presence of discontinuities. This problem is analyzed and discussed in Chapter 5.

The eigenvalues of the system are

$$\lambda_1 = u - c_{6eq}, \qquad \lambda_{2,3,4,5} = u, \qquad \lambda_6 = u + c_{6eq}, \tag{2.23}$$

where the speed of sound is

$$c_{6eq} = \sqrt{Y_1 c_1^2 + Y_2 c_2^2}. \tag{2.24}$$

The single-velocity six-equation model allows all the thermodynamic disequilibria:

$$p_1 \neq p_2, \qquad T_1 \neq T_2, \qquad u_1 = u_2 = u, \qquad g_1 \neq g_2. \tag{2.25}$$

To close system (2.21), two decoupled equations of state are needed:

$$p_k = p_k(\rho_k, e_k), \qquad k = 1,2. \tag{2.26}$$

This full thermodynamic decoupling is very important for our purpose of using accurate steam-water properties in an efficient way.

This model has initially appeared in [139] as an intermediated step to obtain the celebrated 5-eq. model of Kapila et al. [139]. Then it was proposed by Saurel et al. [234] for computational purposes and it was later reformulated by Pelanti & Shyue in [200] to ensure *mixture-energy-consistency* at the discrete level.

Considering the characteristic times of the equilibrium recovery reported in (2.10), it could seem physically wrong to consider the pressure disequilibrium under the assumption of velocity equilibrium. However, in this thesis, the single-velocity six-equation model will be always coupled to instantaneous or quasi-instantaneous pressure relaxation terms in order to use it as an alternative way for solving directly the five-equation model of [139]. This is motivated by its greater robustness of numerical approximations with respect to the Kapila's 5-equation model in relation to positivity preservation of the volume fraction.

Further information about the nonconservative terms of this model and their numerical treatment are given in Chapter 5. The proposition of new relaxation procedures coupled to system (2.21) is discussed in Chapter 6.

2.3.4 The five-equation model

The five-equation model under discussion is the one represented by the circle vp in Fig. 2.2. In the following, it will be sometimes called: *Kapila's model*, as often occurs in the literature. It describes multiphase mixtures evolving under unique velocity and pressure for all phases, a scenario that

is realistic in many practical applications, e.g. condensed phase mixtures, solid explosives, shock propagation into solid alloys, and fast depressurizations triggering liquid-vapor transition.

In 1D, the homogeneous portion of the five-equation model is

$$\begin{cases} \partial_t \alpha_1 + u\partial_z \alpha_1 + \alpha_1\alpha_2 \left(\frac{\rho_1 c_1^2 - \rho_2 c_2^2}{\alpha_1\rho_2 c_2^2 + \alpha_2\rho_1 c_1^2} \right) \partial_z u = 0, \\ \partial_t(\alpha_1\rho_1) + \partial_z(\alpha_1\rho_1 u) = 0, \\ \partial_t(\alpha_2\rho_2) + \partial_z(\alpha_2\rho_2 u) = 0, \\ \partial_t(\rho u) + \partial_z(\rho u^2 + p) = 0, \\ \partial_t(\rho E) + \partial_z[(\rho E + p)u] = 0, \end{cases} \tag{2.27}$$

The eigenvalues of the system are

$$\lambda_1 = u - c_{5eq}, \qquad \lambda_{2,3,4} = u, \qquad \lambda_5 = u + c_{5eq}, \tag{2.28}$$

where the speed of sound is such that

$$\frac{1}{\rho^2 c_{5eq}^2} = \frac{Y_1}{\rho_1^2 c_1^2} + \frac{Y_2}{\rho_2^2 c_2^2}, \tag{2.29}$$

Summarizing, the disequilibrium assumptions of this model are:

$$p_1 = p_2 = p, \qquad T_1 \neq T_2, \qquad u_1 = u_2 = u, \qquad g_1 \neq g_2. \tag{2.30}$$

To close system (2.27), a mixture equation of state is required:

$$p = p(\alpha_1, \rho_1, \rho_2, e). \tag{2.31}$$

Kreeft–Koren [146] have proposed an alternative formulation of Kapila's five-equation model in order to circumvent the numerical problems that could arise due to the presence of nonconservative terms in the void fraction evolutionary equation. This formulation reads:

$$\begin{cases} \partial_t(\alpha_1\rho_1) + \partial_z(\alpha_1\rho_1 u) = 0, \\ \partial_t(\alpha_2\rho_2) + \partial_z(\alpha_2\rho_2 u) = 0, \\ \partial_t(\rho u) + \partial_z(\rho u^2 + p) = 0, \\ \partial_t(\rho E) + \partial_z[(\rho E + p)u] = 0, \\ \partial_t(\alpha_1\rho_1 E_1) + \partial_z[\alpha_1(\rho_1 E_1 + p)u] - pu\partial_z\alpha_1 - (\alpha_1 - Y_1)u\partial_z p + p\alpha_1\alpha_2 \frac{k_{s,1} - k_{s,2}}{\alpha_1 k_{s,1} + \alpha_2 k_{s,2}} \partial_z u = 0. \end{cases} \tag{2.32}$$

where $k_{s,k}$ are the isentropic compressibility factors expressed in Eq. (1.9).

This model, in the original formulation of system (2.27), is extensively used for numerical purposes, especially in the compressible two-phase flow domain.

2.3.5 The four-equation model

The four-equation model (vpT in Fig. 2.2) considers a mixture of phases that are in thermo-mechanical equilibrium but in chemical disequilibrium. It has the structure of the single-phase

Euler system augmented by a mass balance equation for one of the two phases. In one-dimensional geometry, the system of equations is

$$\begin{cases} \partial_t(\alpha_1\rho_1) + \partial_z(\alpha_1\rho_1 u) = 0, \\ \partial_t\rho + \partial_z(\rho u) = 0, \\ \partial_t(\rho u) + \partial_z(\rho u^2 + p) = 0, \\ \partial_t(\rho E) + \partial_z[(\rho E + p)u] = 0. \end{cases} \tag{2.33}$$

The eigenvalues of the system are:

$$\lambda_1 = u - c_{4eq}, \qquad \lambda_{2,3} = u, \qquad \lambda_4 = u + c_{4eq}, \tag{2.34}$$

Using the caloric EoS $e = e(p, \rho, Y_k)$, the speed of sound reads

$$c_{4eq}^2 = \frac{\frac{p}{\rho} - \rho\left(\frac{\partial e(p,\rho,Y_k)}{\partial \rho}\right)_{p,Y_k}}{\rho\left(\frac{\partial e(p,\rho,Y_k)}{\partial p}\right)_{\rho,Y_k}}. \tag{2.35}$$

See Section 4.9 for further developments of this formula.

For one-component two-phase flows, it assumes:

$$p_1 = p_2 = p, \qquad T_1 = T_2 = T, \qquad u_1 = u_2 = u, \qquad g_1 \neq g_2. \tag{2.36}$$

The mixture equation of state, needed to close system (2.33), writes

$$p = p(Y_k, \rho, e). \tag{2.37}$$

This model is very simple and has interesting physical and mathematical properties. It can be cast in a full conservative form, then, there is uniqueness of solution also in the presence of discontinuities. Moreover, it is the simplest model capable of simulating the metastability in a two-phase mixture. This leads to an extensive use of it in many fields as cavitations [117], CO2 depressurizations [177], etc. However, according to the author's opinion, this way of taking into account the metastability is not realistic. In particular, it is too simplistic to consider exclusively the chemical disequilibrium because this leads to the weird coexistence of a metastable phase and a stable non-saturated one (in its single-phase domain). To better understand this feature, one can see the isobar on the T-v diagram reported on Fig. 1.5. A steam-water mixture, where phases are at the same pressure and temperature, could be formed by metastable liquid and superheated vapor or subcooled liquid and metastable vapor. This means that for an evaporation process, the metastable liquid will become superheated vapor. Further, the more the liquid is in a metastable state, the more it will be superheated after that the evaporation has occurred. This is unusual. In fact the metastability is a transitory condition before that the saturated condition is reached. Thus, it seems more adherent to the physics to have a metastable phase that, during a phase transition, becomes saturated.

This can be achieved by changing the thermodynamic assumptions of this model. Phases can be considered to be in thermal and chemical disequilibrium, however, one of the two phases is at saturation conditions. In the case of the vapor be the one at saturation:

$$p_l = p_v = p, \qquad T_l \neq T_v = T_{sat}(p), \qquad u_l = u_v = u, \qquad g_l \neq g_v = g_{sat}(p). \tag{2.38}$$

On the mathematical point of view, adding the thermal disequilibrium to (2.36) means that a degree of freedom is added, demanding an extra transport equation or closure relation. However, by forcing the saturation condition for one of the two phases means that the degrees of freedom of that phase will decrease from two to one (a saturated phase has only one d.o.f., see Section 1.1). Therefore, system (2.36) is sufficient and does not need any extra equation.

Which of the phases is saturated depends on the particular industrial application: in case of a liquid depressurization, the liquid is allowed to reach the metastable conditions and the vapor is set to be at saturation conditions, conversely, for a condensation process in a steam turbine, the vapor is allowed to be metastable and the liquid is set at saturation.

This model is called *Homogeneous Equilibrium Model* (HRM) [28, 29, 84] and is the object of Chapter 4. Evidently, due to the modifications to the thermodynamic assumptions, the HRM cannot be considered as being part of the hierarchy reported in of Fig. 2.2.

2.3.6 The homogeneous equilibrium model

The Homogeneous Equilibrium Model (HEM) considers a mixture made of the liquid and vapor phases of one-component in full thermodynamic equilibrium. The HEM system has formally the structure of the single-phase Euler system. In one-dimensional geometry, the HEM equations are:

$$\begin{cases} \partial_t \rho + \partial_z(\rho u) = 0, \\ \partial_t(\rho u) + \partial_z(\rho u^2 + p) = 0, \\ \partial_t(\rho E) + \partial_z[(\rho E + p)u] = 0. \end{cases} \tag{2.39}$$

The eigenvalues of the system in (2.39) are:

$$\lambda_1 = u - c_{HEM}, \qquad \lambda_2 = u, \qquad \lambda_3 = u + c_{HEM}. \tag{2.40}$$

Using a caloric EoS of the form $e = e(\rho, p)$, for the HEM, the speed of sound reads:

$$c^2_{HEM} = \frac{\frac{p}{\rho} - \rho\left(\frac{\partial e}{\partial \rho}\right)_p}{\rho\left(\frac{\partial e}{\partial p}\right)_\rho}. \tag{2.41}$$

See Section 4.8 for further developments of this formula.

The thermodynamic equilibrium assumptions of the HEM are:

$$p_1 = p_2 = p, \qquad T_1 = T_2 = T_{sat}(p), \qquad u_1 = u_2 = u, \qquad g_1 = g_2 = g_{sat}(p). \tag{2.42}$$

With the constraints expressed in Eq. (2.42), the internal energies and the specific volumes of vapor and liquid are those of the saturation curve. That is:

$$e_v = e_g(p_{sat}), \qquad e_l = e_f(p_{sat}), \qquad v_v = v_g(p_{sat}), \qquad v_l = v_f(p_{sat}), \tag{2.43}$$

where subscripts f and g indicate, respectively, the saturated liquid and the saturated vapor.

To close the system, the required EoS is

$$p = p(\rho, e). \tag{2.44}$$

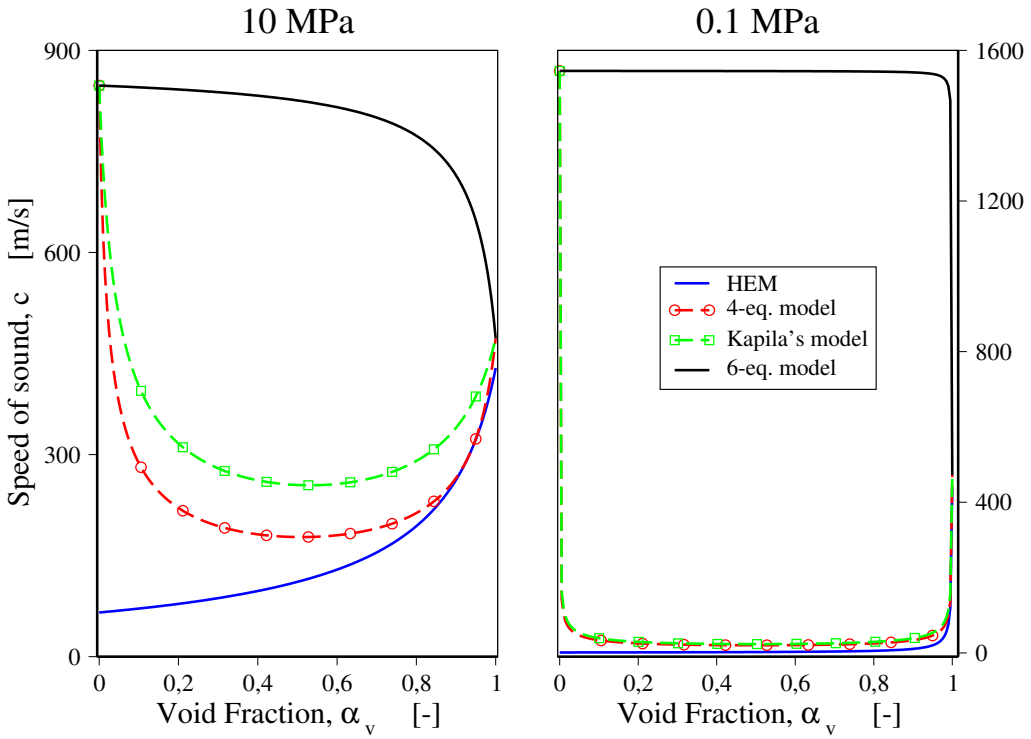

FIGURE 2.3. Celerity of two-phase flow models.

In spite of its simplicity, this model is extensively used for numerous industrial applications. For instance, to simulate heat exchangers (e.g., [211]), for calculating the mass flow rate of critical two-phase flows [237] and even for the analysis of an hypothetical Loss Of Coolant Accident (LOCA) in nuclear power plants [105]. Generally, the HEM is particularly well adapted for the simulation of dispersed bubbly flow [56]. The drawbacks of this model are well known: it cannot reproduce mechanical or thermodynamic non-equilibrium, typical of annular flows and fast depressurizations, respectively. If the deviation from equilibrium is moderate, correction terms can be used (drift flux velocity, subcooled boiling models). However when non-equilibrium effects are more important, additional equations are needed for an accurate prediction of the flow physics.

Notwithstanding, HEM has good mathematical properties which make it suitable for the simulation of wave motions, hence, fast transients.

2.4 Comparison of the speed of sound of two-phase flow models

For a single phase, the speed of sound corresponds to an intrinsic thermodynamic property. The definition of a unique value for the speed of sound of a two-phase fluid does only make sense for certain model assumptions. From a mathematical point of view, for models describing two-phase flows, the expression of the speed of sound stems from the governing systems of equations. Then, it depends on the mixture composition, on the degree of inter-phase equilibrium attained between the phases and on the choice of the EoS.

Figure 2.3 shows the trend of the speed of sound for a steam-water mixture according to the

different homogeneous models described above. An important feature is that increasing the number of admitted disequilibria leads to greater speeds of sound. This is consistent with the well-known sub-characteristic condition [172] that requires that the sound speed associated to a two-phase flow model is reduced whenever an additional equilibrium is assumed [54, 109].

Generally, the two-phase speed of sound is much lower than the phasic speeds on sound. It can even be of few order of magnitudes lower.

As we can see in Fig. 2.3, in the two-phase domain, the speed of sound for all the homogeneous models, except the HEM, is continuous at the single-phase limits, that is, when $\alpha_v \to 0$ and $\alpha_v \to 1$. Whereas, for the HEM, it is discontinuous because one of the main characteristics of the equilibrium EoS is the presence of a "kink" (discontinuity in the derivatives) along the saturation curve. The discontinuities in the speed of sound have been referred to as unphysical by several authors [109, 141, 188, 248]. Generally this is not a numerical issue unless for very specific cases. To understand the mathematical and numerical consequences of this feature, see [181].

Experimentally, it has been noted that its behavior, with respect to the volume fraction, is non-monotonic [118, 140]. The well known Wood's speed of sound [279], which is also the one of the Kapila's 5-equation model, is very close to the experimental data.

We refer to [54, 109] for a discussion on the speed of sound of a hierarchy of relaxed two-phase flow models that includes the models considered here.

Part II

Classical models and accurate equations of state

CHAPTER 3

STEADY-STATE METASTABLE FLOWS: THE FLASHING

Metastability in two-phase flows not only occurs during fast transient phenomena, but also in steady-state flows. There are many examples in industry, especially in the thermal applications. One can mention the natural circulation driven by the nucleation of hot metastable liquid, the Departure from Nucleate Boiling (DNB) phenomena, etc. These are metastable two-phase flows triggered by a thermal flux.

Another cause of metastable two-phase is the retarded nucleation following a pressure decrease, also called *flashing*. More specifically, this occurs when a subcooled liquid is driven into the two-phase domain due to a pressure decrease, but the vaporization does not start at saturation pressure. Due to this delay of vaporization, the liquid becomes metastable.

Flashing typically occurs during the flow between two reservoirs at different pressures. If the flow is choked, that is, the mass flow rate is independent of the condition of the downstream reservoir, it is called *critical*. At the critical section, the velocity of the flows equals the effective local speed of sound of the mixture. As already discussed in Chapter 2, the speed of sound of two-phase flows is not well defined and strongly depends on the disequilibrium assumptions between the phases. For this reason, several critical flow models exist in the literature of multiphase flows.

It is important to comment on two main assumptions of the critical two-phase flow models:

- accounting for the thermal disequilibrium is paramount for flashing,
- the velocity disequilibrium seems to be less important than the thermal one.

In the context of the nuclear industry, the evaluation of the critical mass flow rate is a key feature of the analysis of the Loss of Coolant Accident (LOCA), from both the transient and the stationary point of view. On one hand, a quasi-stationary flow occurs at the breach of the primary system, and many of the emergency systems of the nuclear reactors are designed according to the mass flow rate leaking out of the primary circuit of the reactor. On the other hand, the stationary critical flow is also important for transient applications because many nuclear safety codes (EUROPLEXUS,

RELAP5, CATHARE, WAHA) use it as boundary condition or to account for interfacial terms for the numerical simulation of transient flows.

This chapter gives a benchmark of four critical flow models, with particular attention devoted to the Delayed Equilibrium Model (DEM). It is a rather simple and accurate model that, as we will see in this chapter, is able to predict the critical mass flux and the pressure at the critical section for a wide range of geometrical and thermodynamic conditions of the fluid.

The industrial purpose of this work was to produce a benchmark of the critical flow models in order to improve the critical flow condition of the fast transient dynamics software EUROPLEXUS. This code can use a specific model to simulate the critical flow established at the breach of the primary circuit. From the numerical point of view, a critical flow model is used to evaluate the choked mass flow rate and a coherent pressure at the breach that is set as a *boundary condition* for the compressible flow model.

Prior to this work, in the EUROPLEXUS code the available critical flow models were HEM, Fauske (1962) and Moody (1965). None of them is able to take into account the thermal disequilibrium and the presence of metastable liquid. Given that the Henry-Fauske model (1971) is satisfactory in terms of both critical pressure and mass flux, it has been added to EUROPLEXUS.

Although the initial intent was to integrate the DEM in EUROPLEXUS, it has been finally abandoned because it seems too complicated to add as a critical flow boundary condition since it is not a lumped zero-dimension model but would require a spatial discretization too.

This has been the first research work chronologically done in this PhD thesis. It has served to make clearer the importance of metastability in the investigated phenomena and the secondary importance of the velocity disequilibrium. As a result of this analysis, the subsequent work has been focused on the thermodynamic aspects of the equations of state and on the thermodynamic disequilibrium rather than the mechanical disequilibrium issue.

Benchmark of Delayed Equilibrium Model (DEM) and Classic Two-Phase Critical Flow Models against Experimental Data

International Journal of Multiphase Flow, Vol. 92, 112-130.

M. De Lorenzo[1], Ph. Lafon[1], J.-M. Seynhaeve[2], Y. Bartosiewicz[4].

The safety analysis of Pressurized Water Reactors, in the event of LOCA, strongly depends on the ability to evaluate the discharge rate of coolant inventory through the breach. Due to the huge pressure difference between the primary system and the reactor containment, the mass flow rate is choked at the break. Under such conditions, both mechanical and thermal equilibrium between phases are not ensured.

A general theory to evaluate the two-phase critical mass flow rate is not yet available. However, some models are capable of providing accurate evaluations of either critical mass flux or critical pressure and such a model is the Delayed Equilibrium Model (DEM), which is examined in this article. Here we show how to integrate the DEM system of equations coupling a standard Runge-Kutta method with the Possible-Impossible Flow algorithm to give a simple procedure which does not require sophisticate computational schemes.

The main objective of this work is to compare DEM, Homogeneous Equilibrium Model, Moody (1965) and Henry-Fauske (1971) models to experimental data. The four models were tested and the results from experimental data containing a sample range in excess of 450 conditions compared in determining an appropriate benchmark. Each of the chosen models is representative of a particular category of critical flow models. Furthermore, two-phase critical models provide good estimations depending on the configuration or set of conditions. Consequently, the models have been individually tested incorporating long tubes, short tubes and slits.

This analysis has been carried out for both critical mass flux and critical pressure evaluations.

3.1 Introduction

The Loss Of Coolant Accident (LOCA) is one of the Design Basis Accidents (DBA) of most reactor concepts. The safety analysis of pressurized light water reactors in the event of LOCA strongly depends on the ability to evaluate the discharge rate of coolant inventory through the breach.

The discharging mass flow rate influences the depressurization rate of the primary system and the heat transfer in the core, as a result of the flashing in the core. Establishing an accurate evaluation of the coolant discharge rate at the breach allows one to better design both the Emergency Core Cooling System (ECCS) and the safety systems of the containment.

Due to the huge pressure difference between the primary system and the reactor containment, the mass flow rate is choked at the break, resulting in the mixture velocity of the coolant through the breach equaling the local sound velocity. In such conditions, the flow is referred to as being

[1] IMSIA UMR EDF-CNRS-CEA-ENSTA, Palaiseau, France 91120.
[2] Université Catholique de Louvain (UCL), Louvain la Neuve, Belgium 1348.

critical. Furthermore, the flow is also referred to as being choked when the mass flow rate becomes independent of the downstream flow conditions [242].

The two-phase one-component critical flow plays a paramount role in nuclear safety, but the phenomenon is still pertinent in fossil-fuel power plants, chemical plants and many industrial facilities in which subcooled or two-phase pressurized fluids are used. Another application for two-phase critical flow models is in the pressure-relief valve sizing.

The two-phase critical flow involves the presence of metastable states. Experimental evidences [38, 149, 226] agree that the flashing does not start at saturation pressure, due to the finite vaporization rate of the liquid. During the expansion, part of the metastable liquid becomes saturated, however this mechanism is not clear yet. That is why many models have been developed in the past and why their validation against experimental data is fundamental.

Critical flow of single-phase compressible fluids is well understood and mathematically described. However, notwithstanding improvements made in terms of evaluation of the critical flow, a complete and exhaustive theory for the critical two-phase flow is still not available.

Extensive experimental and theoretical researches have been carried out to clarify this flow phenomenon. Simple ways to calculate the critical mass flow rate are the use of empirical models (as Burnell [40] or Zaloudek [282]) or practical formulas as the ones of Fauske [106], Moody [184], Babitskiy [19] and Henry & Fauske [125]. A review of them is given in Wallis [274] and in D'Auria & Vigni [66].

More complete models are the HRM of Bilicki et al. [29, 84] and the DEM. For the mass transfer between phases, they use an analytical relaxation correlation adjusted with empirical parameters.

Even more complete and elaborated are the so-called *two-fluid* models and the ones describing the nucleation process for the mass and energy transfer between the phases. As Trapp & Ramson [267], Dagan et al. [67] which also derived an empirical correlation for the density of bubble nuclei, or Ardron [9] in which the nucleation model is based on the kinetic theory. We may also mention Elias & Chambre [96, 97], two models based on the bubble transport equation. Boure et al. [37] produced one of the most complete and advanced critical flow models. By using this model, any other consistent model can be obtained. The algorithm used in this article, the Possible-Impossible Flow (PIF) method (cf. Section 3.5.3.2), might be considered as a simplification of the one introduced in [37].

Elias & Lellouche [98] provided a general review of a two-phase critical flow and conducted a systematic evaluation to quantify the discrepancy between theoretical models and experimental data. A more recent review paper is the one of Pinhasi et al. [207] in which all the aspects of the flashing phenomena were discussed focusing on the release of liquid hazardous materials contained in pressurized equipments.

More recently works in this domain are the asymptotic analysis of the EVUT model performed by Valero & Parra [269], the interesting experimental investigation of Fraser & Abdelmessih [111] about the effect of the location of flashing inception, the mechanistic model of Yoon et al. [281], and the work of Kim & Mudawar [142] about choked flow in micro-channel heat sinks.

It is important to bear in mind that most of the theoretical models developed do not take into account the presence of non-condensable gas which reduces considerably the critical mass flow rate

of the mixture. Papers dealing with the infuence of non-condensable gas are Celata et al. [50] and the more recent work of Park et al. [195].

In nuclear safety, codes like RELAP5, CATHARE, WAHA are based on the two-fluid model but as far as the critical flow is concerned, the models used are simple expressions like Henry-Fauske (1971) for RELAP5 code [249], an experimental correlation for the liquid to interface heat flux term in CATHARE code [24], and the HRM correlations [84] in WAHA code [165]. RETRAN code uses fitted forms of Moody (1965) and Henry-Fauske (1971) [180], the fast transient dynamics software EUROPLEXUS [167], for the critical flow conditions adopts the simple formulas provided by HEM, Fauske (1962), Moody (1965) and Henry-Fauske (1971).

In this context, the DEM has been implemented with success in WAHA [18] and in NEPTUNE_CFD [92] codes. In [18, 92] it was shown that the use of DEM in CFD codes allows a very good representation of the experimental data and the results obtained were practically identical to the ones obtained using the primitive steady-state form of the model (see Eq. 3.52). Therefore, the benchmark of the steady-state form of DEM on a wide range of experimental data is the main objective of this paper. Moreover, a comparison with other models will be done, in terms of both critical mass flux and critical pressure. Indeed, in many industrial applications, the pressure evaluation at the location of the breach is essential. However, determining a benchmark for the evaluation of critical pressure is unavailable in literature. Furthermore, many models are only able to accurately calculate the critical mass flux under certain conditions. In order to clarify this evidence, models are assessed utilizing three different configurations: long tubes, short nozzles and slits. Given that a general theory is not yet available, it is important to highlight which models behave better under certain conditions.

The paper is organized as follows. Section 3.2 introduces the main mathematical characteristics of critical flow. In Section 3.3 we introduce the critical flow models used in the paper and their system of equations. The speed of sound of the various models is identified and discussed in Section 3.4. In Section 3.5, practical formulas are derived for the calculation of the critical mass flux. Particular attention is drawn to the description of the Delayed Equilibrium Model: the simplified system of ODE for steady-state applications, its closure laws and the algorithm used to solve it.

Section 3.6 is devoted to the comparison of four different models against experimental data. The four models adopted are:

1. Homogeneous Equilibrium Model, since it does not take into account any non-equilibrium between phases.

2. Moody (1965) model, in which phases are allowed to flow at different velocities.

3. Henry-Fauske (1971) model, given that it is one of the most used non-equilibrium models.

4. Delayed Equilibrium Model, which authors consider to be one of the most physically consistent model, notwithstanding its simplicity.

Finally, Section 3.7 is devoted to the quantitative analysis of the models in terms of mean error and standard deviation with respect to experimental data. This analysis has been carried out for both critical mass flux and critical pressure evaluations.

3.2 Mathematical Characteristics of Critical Flows

The critical flow implies that the mass flow rate is maximum, irrespective of change in the pressure downstream, i.e. for given inlet conditions:

$$\frac{d(GA_z)}{dp} = 0, \tag{3.1}$$

where $G = \rho u$ is the mass flux over a given area A_z, ρ denotes the density and u the fluid velocity. Consider the single-phase flow at steady-state conditions in a uniform cross-section pipe. For an upward one-dimensional flow, the momentum balance equation is

$$\frac{d}{dz}\left(\frac{G^2}{\rho}\right) + \frac{dp}{dz} = -\frac{1}{A_z}\int_{P_z} \tau_w dP_z - \rho g. \tag{3.2}$$

τ_w denotes the wall shear stress, P_z is the perimeter of the channel and g stands for the gravitational constant. The pressure is assumed to be uniform over A_z. According to mass conservation equation, the mass flux G remains constant. Assuming that the flow is governed by a barotropic equation of state such that $\rho = \rho(p)$, the first term of (3.2) can be rewritten as

$$\frac{d}{dz}\left(\frac{G^2}{\rho}\right) = -\frac{G^2}{\rho^2}\frac{d\rho}{dp}\frac{dp}{dz}. \tag{3.3}$$

Here we can recognize the sonic velocity, c, at which pressure disturbances travel in a fluid, i.e.

$$c^2 = \frac{dp}{d\rho}. \tag{3.4}$$

Inserting Eq. (3.3) in (3.2) and solving with respect to pressure gradient, we obtain

$$\frac{dp}{dz} = -\frac{\frac{1}{A_z}\int_{P_z} \tau_w dP_z + \rho g}{1 - \frac{u^2}{c^2}}. \tag{3.5}$$

From this formula we can see that when the fluid velocity approaches the speed of sound,

$$\frac{dp}{dz} \to -\infty. \tag{3.6}$$

This phenomenon is even called the *pressure-knee*.

At steady-state conditions, the governing equations of the two-phase flow constitute a system of non-linear ordinary first order differential equations. Its mathematical form is:

$$\mathbf{A}\frac{d\mathbf{U}}{dz} = \mathbf{b}. \tag{3.7}$$

where $\mathbf{U}$ represents the variable state vector and $\mathbf{b}$ is a source term vector containing body forces, viscous stresses and heat flux. An alternative way to define the critical flow is to require that the matrix of the ODE system be *singular*. Hence, the necessary condition for criticality [37] is

$$det(\mathbf{A}) = 0. \tag{3.8}$$

The conditions expressed in Eq. (3.6) and (3.8) are linked. In fact, the variable state vector $\mathbf{U}$ may contain the pressure p, thus, solving with respect to its derivative we may have: $\frac{dp}{dz} = -\frac{...}{det(\mathbf{A})}$. Hence the necessary condition expressed in (3.8) makes the pressure gradient to diverge.

In the following we will use (3.6) and (3.8) to find the speed of sound of each of the models compared to experimental data, but, before we need to introduce their balance equations.

3.3 Balance Equations of the Models

Critical flow models can be divided according to the kind of non-equilibrium between the two phases. Homogeneous models have got the mechanical constraint that both phases flow at the same velocity. Non-homogeneous models relax this constraint allowing slip between phases. Equilibrium models impose the thermal equilibrium between vapor and liquid phases, whereas, for non-equilibrium models, phases can be at different temperatures. Assuming that phases are in full equilibrium, we obtain the Homogeneous Equilibrium Model.

In the following we give the sets of balance equations that formally define the critical flow models used in the paper. Instead, in Section 3.5, we derive the formulas for the prediction of the critical mass flux.

3.3.1 Balance Equations of the Homogeneous Equilibrium Model

The HEM does not allow any non-equilibrium between phases. Vapor and liquid are at saturation conditions, at same pressure and temperature, flowing at the same velocity. Let us recall the balance equations for a mixture in thermal and mechanical equilibrium between phases (HEM). For one-dimensional flow with variable cross-sectional area, neglecting the effects of body forces, viscous stresses and heat flux, along axis z, it can be written in conservative form as

$$\begin{cases} \partial_t(\rho_m A_z) + \partial_z(\rho_m u_m A_z) = 0, \\ \partial_t(\rho_m u_m A_z) + \partial_z[(\rho_m u_m^2 + p)A_z] = p\ \partial_z A_z, \\ \partial_t(\rho_m E_m A_z) + \partial_z[(\rho_m E_m + p)u_m A_z] = -p\ \partial_t A_z. \end{cases} \tag{3.9}$$

where ρ_m is the mixture density, i.e. $\rho_m = \alpha_v \rho_v + (1-\alpha_v)\rho_l$, indicating with α_v the volume fraction occupied by the vapor phase and subscripts v and l stand for vapor and liquid phases. u_m is the velocity of the mixture, the total energy is $E_m = e_m + \frac{1}{2}u_m^2$ and e_m is the specific internal energy of the mixture.

Assuming that the mixture undergoes an isentropic transformation up to the critical section, a practical formula for predicting the critical mass flow rate can be deduced from system (3.9) (cf. Section 3.5.1).

3.3.2 Balance Equations of Non-Homogeneous Equilibrium Models

This kind of critical flow models supposes phases in thermal equilibrium ($T_l = T_v = T_{sat}(p)$) but relaxes the constraint of mechanical equilibrium ($u_v \neq u_l \neq u_m$). For this purpose, one should need an extra PDE to describe the momentum balance of one of the two phases. However, some critical flow models as Moody [184] or Fauske [106] provide the value of the slip ratio of the two velocities, hence the relative velocity between phases u_r is assigned. In the event that the relative velocity is

known *a priori*, the set of balance equations describing the flow, in conservative form, is [82, 136]

$$\begin{cases} \partial_t(\rho_m A_z) + \partial_z(\rho_m u_m A_z) = 0, \\ \partial_t(\rho_m u_m A_z) + \partial_z\{[\rho_m u_m^2 + p + \rho_m x(1-x)u_r^2]A_z\} = p\ \partial_z A_z, \\ \partial_t(\rho_m E'_m A_z) + \partial_z\{[(\rho_m E'_m + p)u_m + \rho_m(L + (\frac{1}{2} - x)u_r^2 + u_m u_r^2)x(1-x)u_r]A_z\} = -p\ \partial_t A_z. \end{cases} \tag{3.10}$$

The mean velocity u_m is such that $\rho_m u_m = \alpha_v \rho_v u_v + \alpha_l \rho_l u_l$. The relative velocity between phases is $u_r = u_v - u_l$. By introducing the slip ratio $S = u_v/u_l$, the relative velocity is $u_r = \frac{S-1}{1+(S-1)x} u_m$. x denotes the mass fraction of the vapor phase in the mixture and L indicates the latent heat. The mixture total energy is

$$E'_m = e_m + \frac{1}{2}u_m^2 + \frac{1}{2}x(1-x)u_r^2, \tag{3.11}$$

and the mean specific internal energy is such that $\rho_m e_m = \alpha_v \rho_v e_v + \alpha_l \rho_l e_l$.

A closure law for the slip ratio S or the relative velocity u_r is needed to system (3.10). Fauske [106] chose the slip ratio which maximizes the flow momentum:

$$\frac{\partial}{\partial S}[x u_v + (1-x)u_l] = 0. \tag{3.12}$$

Moody [184], the one that maximizes the specific kinetic energy:

$$\frac{\partial}{\partial S}\left[\frac{1}{2}x u_v^2 + \frac{1}{2}(1-x)u_l^2\right] = 0. \tag{3.13}$$

As a result, the slip ratio for Fauske model is $S = (\rho_l/\rho_v)^{1/2}$, whereas, for Moody model is $S = (\rho_l/\rho_v)^{1/3}$.

In the literature, many authors realized that unless for very long tubes, the HEM tends to systematically underestimate the two-phase critical flow. By relaxing the mechanical equilibrium, critical mass flow rate evaluations improve. Given that phases have different densities, it is normal to expect that pressure gradient tends to accelerate the lighter phase, leading to slip ratios larger than unity. By the way, the improvement introduced by considering the slip between the two phases is fictitious. In fact, the slip ratios used in many non-homogeneous models seem to be too high with respect to experimental evidences [270].

Using the method of characteristics, it has been shown that too high slip ratios lead to imaginary characteristics. For instance, Fauske [106], Moody [184] and Moody [186] models have imaginary characteristics for most of the range of interest [258, 268]. Characteristics are real just for slip ratios close to the unity [258]. Hence, a thermal equilibrium model, to be well-posed, must approach the HEM.

Finally, it comes that the underestimation made by the HEM is essentially due to the assumption of thermodynamic equilibrium. This assumption is relaxed in the two following models to be discussed.

3.3.3 Balance Equations of Homogeneous Non-Equilibrium Models

It has been experimentally shown that metastable liquid appears in critical flows. Moby-Dick [226] and Super Moby-Dick [149] tests, held at CEA during the 1970s, are a clear demonstration of the

presence of a metastable phase. The thermal non-equilibrium between phases is due to the finite vaporization rate and it is expected to be more important for short pipes, nozzles, and orifices, where the fluid transit time is very short.

Many models relaxing the thermal equilibrium condition have been formulated in the past. Simple models take into account the metastability by using semi-empirical coefficients. Some of them are a simple empirical formula, for instance: Burnell [40] or Zaloudek [282].

The Henry-Fauske model has been chosen for the comparison because, together with Trapp-Ransom model [267], it is the reference model for RELAP5 code [249]. Formally, Henry-Fauske model could be considered as a Homogeneous Non-Equilibrium Model. For this kind of models, the phases move at the same velocity but a temperature difference exists between phases. In order to allow phases to have a different mean temperature, we need to add a mass balance equation for the vapor phase to the system (3.9)

$$\partial_t(\alpha_v \rho_v A_z) + \partial_z(\alpha_v \rho_v u_m A_z) = \Gamma_v A_z. \tag{3.14}$$

The mass transfer is modeled by means of the source term Γ_v. The latter indicates the intensity of phase transition and tends to introduce a certain delay for the liquid vaporization. Adding Eq. (3.14) to system (3.9) we obtain a 4-equation model formally identical to the one of Bilicki et al. [29].

Imposing the thermodynamic transformation to which the phases undergo, a practical set of equations is obtained from this 4-equation model for the prediction of the critical mass flow rate (cf. Section 3.5.2).

3.3.4 Balance Equations of the Delayed Equilibrium Model

The Delayed Equilibrium Model (DEM) derives from the Lackmé's [158] idea of describing the critical flow as composed of three-phases. The three phases are: saturated liquid and vapor and metastable liquid. This picture of the flow comes from the experimental evidences of Barois [15], in which local temperature measurements oscillate between stagnation temperature T_0 and local saturation temperature $T_{sat}(p)$.

The expansion of the metastable flashing liquid is almost frozen. Due to the high velocities, the transit time is very short, i.e. few milliseconds. Bartosiewicz & Seynhaeve [17] have shown that, between saturated and metastable liquid, the temperature front only penetrates few tens microns. The amount of metastable liquid depletes only due to the increase of the interfacial area given that flow pattern changes.

The basic assumptions of the model are: (i) the mixture is composed by three phases, (ii) two phases are at saturation, then, at thermal equilibrium, the third phase is at a different temperature, (iii) the mixture is at pressure and mechanical equilibrium, (iv) the metastable phase undergoes an isentropic transformation. Table 3.1 helps in understanding how different phases will be indicated from now on, and the assumptions of the model.

Hence, the magnitude y denotes the mass fraction of the stable phase, i.e. saturated liquid and vapor. The subscripts employed to indicate the three phases are: l for saturated liquid phase, v for saturated vapor phase and l,M for metastable liquid phase.

Table 3.1: DEM model

	Saturated vapor	Saturated liquid	Metastable liquid
Volume fraction	α_v	α_l	$\alpha_{l,M}$
Mass fraction	X	$y-X$	$1-y$
Temperature	T_{sat}	T_{sat}	$T_{l,M}$
Pressure	p	p	p
Velocity	u_m	u_m	u_m

Analogously to the Henry-Fauske model, to define the DEM, we can add an extra mass balance equation for one of the three phases to the mixture system of equations reported in (3.9). The mass balance equation for the metastable liquid phase is

$$\partial_t(\alpha_{l,M}\rho_{l,M}A_z)+\partial_z(\alpha_{l,M}\rho_{l,M}u_mA_z)=\Gamma_{l,M}A_z. \tag{3.15}$$

The mass transfer is modeled by means of a source term, $\Gamma_{l,M}$, which describes the rate of disappearance of the metastable phase to increase the quantity of saturated mixture during the flow. Using continuity equation, one obtains

$$\Gamma_{l,M}=-\rho_m\frac{Dy}{Dt}. \tag{3.16}$$

Since it plays a crucial role in the description of the flow, it will be analyzed in Section 3.5.3.1. Given that the DEM is a three-phase model, the specific volume and internal energy for the mixture are

$$v_m=\rho_m^{-1}=Xv_v+(y-X)v_l+(1-y)v_{l,M}, \tag{3.17}$$

$$e_m=Xe_v+(y-X)e_l+(1-y)e_{l,M}. \tag{3.18}$$

It is important to specify that the mass fraction of the saturated vapor (flow quality) can be expressed as

$$X=x_{eq}y, \tag{3.19}$$

where x_{eq} is the thermodynamic quality of the portion of the mixture that is at saturated conditions. As a result, the specific volume of the mixture becomes

$$v_m=y[x_{eq}v_v+(1-x_{eq})v_l]+(1-y)v_{l,M}. \tag{3.20}$$

On the R.H.S. we have grouped in square brackets the portion at equilibrium conditions and the metastable one in the last term.

3.4 Speed of Sound of the Models

As discussed in Section 3.2, we can use three possible ways to identify the critical velocity: i) to impose that the pressure gradient diverges at critical velocity, as in (3.6), ii) to nullify the determinant of **A**, as in (3.8), iii) applying the definition of maximum mass flux given in Eq.(3.1).

In this section we will analyze the critical speed of sound of the models under comparison. Figure 3.1 shows the trend of the speed of sound of the different models for two-phase water. As well-known, the speed of sound of a two-phase mixture is generally much lower than the single-phase speed of sound of each specie. Moreover, the mixture speed of sound is lower at low pressures.

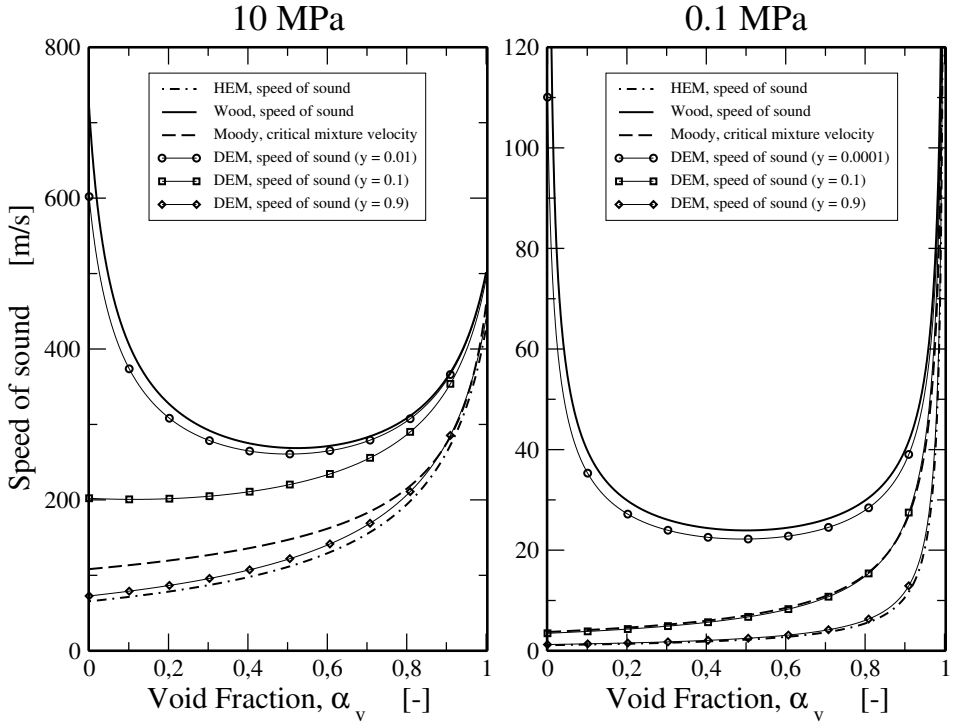

FIGURE 3.1. Speed of sound in vapor-liquid water of the models under comparison. Assuming that the mixture is at mechanical equilibrium, the speed of sound of the HEM is the one accounting for the full thermal equilibrium between the phases, whereas the Wood's one [279] is obtained assuming that the phases are in frozen thermal equilibrium. The speed of sound of DEM, expressed in Eq. (3.42), is extrapolated throughout the whole two-phase domain. Its tends to Wood's one when y is small but tends to the HEM speed of sound when $y \to 1$. For Moody model, the critical mixture velocity, u_m, corresponding to the critical mass flux, G_{cr}, has been plotted.

3.4.1 Speed of Sound of the Homogeneous Equilibrium Model

The HEM is described by the system of equations (3.9), which is written in a conservative form. Recasting this system in an equivalent primitive form, and neglecting time derivatives, we obtain

$$\begin{bmatrix} u_m & \rho_m & 0 \\ 0 & u_m & \rho_m^{-1} \\ 0 & \gamma_{HEM}\, p & u_m \end{bmatrix} \frac{d}{dz} \begin{bmatrix} \rho_m \\ u_m \\ p \end{bmatrix} = \mathbf{b}. \tag{3.21}$$

γ_{HEM} is the dimensionless quantity

$$\gamma_{HEM} = \frac{1}{p \left(\frac{\partial e_m}{\partial p}\right)_{\rho_m}} \left[\frac{p}{\rho_m} - \rho_m \left(\frac{\partial e_m}{\partial \rho_m}\right)_p \right]. \tag{3.22}$$

Note that (3.21) has the same shape of Eq. (3.7). Imposing the determinant to be equal to zero, one obtains

$$det(\mathbf{A}) = u_m \left(u_m^2 - \frac{\gamma_{HEM}\, p}{\rho_m} \right) = 0. \tag{3.23}$$

Unless for the trivial case $u_m = 0$, the determinant is zero when the $u_m = \pm c_{HEM}$. Hence the speed of sound of the HEM, c_{HEM}, is

$$c_{HEM} \triangleq \sqrt{\frac{\gamma_{HEM}\, p}{\rho_m}}. \tag{3.24}$$

Note that the same result can be achieved using the first and the third equation of system (3.21) and making the pressure gradient to diverge. By using thermodynamic relations $de = Tds - pdv$ and $dh = Tds + vdp$, Eq. (3.24) can be rewritten as

$$c_{HEM}^2 = \left(\frac{\partial p}{\partial \rho_m}\right)_s. \tag{3.25}$$

Considering that the mixture is composed by vapor and liquid at saturated conditions, the derivative is

$$\left(\frac{\partial p}{\partial \rho_m}\right)_s = -v_m^2 \left\{\frac{\partial [v_l + x(v_v - v_l)]}{\partial p}\right\}_s^{-1}. \tag{3.26}$$

Finally, a more explicit form is:

$$c_{HEM}^2 = -v_m^2 \left\{\frac{dv_l}{dp} - \left[x\frac{ds_v}{dp} + (1-x)\frac{ds_l}{dp}\right]\frac{v_v - v_l}{s_v - s_l} + x\left(\frac{dv_v}{dp} - \frac{dv_l}{dp}\right)\right\}^{-1}. \tag{3.27}$$

The trend of Eq. (3.27) is depicted in Fig. 3.1 in the entire two-phase domain. It has to be noted that the speed of sound of the HEM has got two discontinuities for $\alpha_v = 0$ and $\alpha_v = 1$. This is due to the presence of a "kink" (discontinuity in the derivatives) of the properties across the saturation curve if the thermal equilibrium is assumed. From Fig. 3.1 we can also see that, according to the HEM, the speed of sound is extremely low for $\alpha_v \approx 0$.

3.4.2 Critical Mass Flux of the Moody Model

In Moody model, two different velocities exist for saturated vapor and liquid. For this reason, it is senseless to define a speed of sound for the mixture. However, we can look for the critical mass flux which makes the pressure gradient to diverge as in Eq. (3.6). The mass flux is defined as:

$$G = \rho_m u_m = \alpha_v \rho_v u_v + \alpha_l \rho_l u_l. \tag{3.28}$$

The mass balance of system (3.10), at steady state, in a uniform cross-section pipe, indicates that $G = cte$. For simplicity, we can also introduce the momentum density (or mixing-cup density), ρ_m^+, i.e. $\frac{1}{\rho_m^+} = \frac{1}{G^2}[\alpha_v \rho_v u_v^2 + (1-\alpha_v)\rho_l u_l^2]$. For an upward vertical flow, the momentum balance of system (3.10) can be rewritten as

$$\frac{d}{dz}\left(\frac{G^2}{\rho_m^+}\right) + \frac{dp}{dz} = -\frac{1}{A_z}\int_{P_z} \tau_w dP_z - \rho_m g. \tag{3.29}$$

Since in Moody model the slip ratio is $S = (\rho_l/\rho_v)^{1/3}$, the momentum density just depends on thermodynamic magnitudes, for instance, $\rho_m^+ = \rho_m^+(p,s)$. If we suppose that the flow is isentropic, using mass and momentum balance equations, the pressure gradient is

$$\frac{dp}{dz} = -\frac{\frac{1}{A_z}\int_{P_z} \tau_w dP_z + \rho_m g}{1 + G^2 \frac{d}{dp}\left(\frac{1}{\rho_m^+}\right)}. \tag{3.30}$$

The vanishing condition of the denominator gives us the critical mass flux:

$$G_{cr}^2 = -\left[\frac{d}{dp}\left(\frac{1}{\rho_m^+}\right)\right]^{-1}. \tag{3.31}$$

In 3.9 the derivative on the R.H.S. of the previous equation is analyzed. Considering that the critical mass flux is $G_{cr} = \rho_{m,cr} u_{m,cr}$, in Fig. 3.1 we plot the trend of the critical mixture average velocity $u_{m,cr}$ in the two-phase domain. The presence of slip between phases makes the critical mass flux to be higher than the HEM one. However this critical mixture average velocity is still very low at low α_v.

3.4.3 Speed of Sound of the Henry-Fauske Model

Considering Henry-Fauske (1971) as a 4-equation model, it is formed by the system of equations (3.9) augmented by the balance equation for the mass of the vapor phase expressed in (3.14). At steady-state, an equivalent primitive form of the system is

$$\begin{bmatrix} u_m & 0 & 0 & 0 \\ 0 & u_m & \rho_m & 0 \\ 0 & 0 & u_m & \rho_m^{-1} \\ 0 & 0 & \gamma_{HF}\, p & u_m \end{bmatrix} \frac{d}{dz} \begin{bmatrix} x \\ \rho_m \\ u_m \\ p \end{bmatrix} = \mathbf{b}. \tag{3.32}$$

γ_{HF} is the dimensionless quantity

$$\gamma_{HF} = \frac{1}{p\left(\frac{\partial e_m}{\partial p}\right)_{\rho_m,x}} \left[\frac{p}{\rho_m} - \rho_m \left(\frac{\partial e_m}{\partial \rho_m}\right)_{p,x}\right]. \tag{3.33}$$

Again, using thermodynamic relations expressed above, one obtains

$$c_{HF}^2 = \left(\frac{\partial p}{\partial \rho_m}\right)_{s,x}. \tag{3.34}$$

This definition is coincident to the speed of sound of the HRM of Bilicki et al. [29]. Now, let us impose the approximations and the hypothesis typical of Henry-Fauske [125] to obtain the proper speed of sound of this model. A more convenient form of (3.34) is given by using fundamental rules for partial derivatives

$$c_{HF}^2 = -v_m^2 \left[\left(\frac{\partial v_m}{\partial p}\right)_{T,x} - \left(\frac{\partial v_m}{\partial s_m}\right)_{p,x}\left(\frac{\partial s_m}{\partial p}\right)_{T,x}\right]^{-1}. \tag{3.35}$$

Considering the liquid as incompressible and supposing that the vapor phase undergoes a polytropic transformation, then $\left(\frac{\partial v_m}{\partial p}\right)_{T,x} \approx -\frac{x_0 v_v}{np}$, where n is the polytropic index. In the phase transition

$$\left(\frac{\partial v_m}{\partial s_m}\right)_p = \frac{v_v - v_l}{s_v - s_l} \approx \frac{v_v - v_{l,0}}{s_{v,0} - s_{l,0}}. \tag{3.36}$$

where $v_{l,0}$, $s_{v,0}$ and $s_{l,0}$ indicate the stagnation phasic properties. The last derivative to be evaluated is

$$\left(\frac{\partial s_m}{\partial p}\right)_{T,x} = x_0 \left(\frac{\partial s_v}{\partial p}\right)_T + (1 - x_0)\left(\frac{\partial s_l}{\partial p}\right)_T. \tag{3.37}$$

Following the original paper of Henry & Fauske [125]:

$$\left(\frac{\partial s_v}{\partial p}\right)_T \approx -\frac{c_{p,v}}{p}\left(\frac{1}{n}-\frac{1}{\gamma_v}\right), \qquad \left(\frac{\partial s_l}{\partial p}\right)_T \approx N\frac{s_{v,0}-s_{l,0}}{s_{v,eq}-s_{l,eq}}\frac{ds_{l,eq}}{dp}, \tag{3.38}$$

where γ_v is the isentropic index for the vapor phase and N is an empirical parameter which takes into account the metastability. It relates the actual change in quality with pressure, to the rate of change occurring under equilibrium conditions: $\frac{dx}{dp} = N\frac{dx_{eq}}{dp}$. Based on experimental observations of Starkman et al. [253], N is estimated as

$$N = \begin{cases} x_{eq}/0.14, & if\ x_{eq} \le 0.14, \\ 1, & if\ x_{eq} > 0.14. \end{cases} \tag{3.39}$$

Finally, inserting these relations in (3.35), the speed of sound of the Henry-Fauske model is

$$c^2_{HF} = v^2_m\left\{\frac{x_0 v_v}{np} + \frac{v_v - v_{l,0}}{s_{v,0}-s_{l,0}}\left[(1-x_0)N\frac{s_{v,0}-s_{l,0}}{s_{v,eq}-s_{l,eq}}\frac{ds_{l,eq}}{dp} - \frac{x_0 c_{p,v}}{p}\left(\frac{1}{n}-\frac{1}{\gamma_v}\right)\right]\right\}^{-1}. \tag{3.40}$$

Here, the speed of sound of this model has been deduced considering that the Henry-Fauske [125] is a 4-equation model but we can recognize that $G_{cr} = \rho_m c_{HF}$ has the same formulation of the one indicated in [125]. Given that this formulation depends on the inlet properties of the mixture, it can not be plotted in Fig. 3.1.

3.4.4 Speed of Sound of the Delayed Equilibrium Model

Formally the system of equations that defines the DEM is similar to (3.32), unless for the first equation that, for the DEM, is referred to the metastable phase. Following the same procedure detailed above in the case of the Henry-Fauske model, one obtains the speed of sound of the DEM:

$$c^2_{DEM} = \left(\frac{\partial p}{\partial \rho_m}\right)_{s,y}. \tag{3.41}$$

Using the definition of mixture specific volume given in (3.20),

$$c^2_{DEM} = -v^2_m\left\{y\frac{d}{dp}\left[x_{eq}v_v + (1-x_{eq})v_l\right]_s + (1-y)\left(\frac{\partial v_{l,M}}{\partial p}\right)_s\right\}^{-1}. \tag{3.42}$$

On the R.H.S., the first term into the curly braces, is similar to the speed of sound of the HEM calculate at the equilibrium quality x_{eq}, i.e. $\frac{d}{dp}\left[x_{eq}v_v + (1-x_{eq})v_l\right]_s = \left(\rho_{m,eq}c_{HEM}\right)^{-2}_{x_{eq}}$, where $\rho^{-1}_{m,eq} = x_{eq}v_v + (1-x_{eq})v_l$. The DEM speed of sound can be rearranged in the same shape of the well-known formula of Wood [279]

$$\frac{1}{\rho^2_m c^2_{DEM}} = \frac{y}{\left(\rho^2_{m,eq}c^2_{HEM}\right)_{x_{eq}}} + \frac{1-y}{\rho^2_{l,M}c^2_{l,M}}. \tag{3.43}$$

From this formula we can see that the DEM exhibits a speed of sound that can span from the one of the HEM (full thermal equilibrium) to the Wood's one (frozen thermal equilibrium). This feature of the model is depicted in Fig. 3.1. In this graph, the DEM speed of sound is plotted by extrapolating Eq. (3.43). In fact the speed of sound of the DEM tends to Wood's one when y is very small, whereas, when $y \to 1$, the speed sound of the DEM is very close to the one of the HEM.

3.5 Calculation of the Critical Mass Flux

In this section we derive more practical sets of equations for the calculation of the critical mass flux and pressure. These will then be used for the benchmark against the experimental data and the comparison of the DEM with the three classical models described up to here.

3.5.1 Calculation of the Critical Mass Flux with Homogeneous Equilibrium Model and Moody Model

Both Eq. (3.24) and (3.31) are local conditions at the critical section, interesting from the physical point of view, but useless for practical purposes since local conditions are unknown. Let us derive a practical equation for predicting the critical mass flux in case of drift between phases. The same formula is also applicable for the HEM if the slip ratio is set to unity.

The evolution from the stagnation condition up to the critical section is assumed to be isentropic. Hence, at any point, including the throat, we have

$$h_0 = x\left(h_v + \frac{1}{2}u_v^2\right) + (1-x)\left(h_l + \frac{1}{2}u_l^2\right). \tag{3.44}$$

The phasic velocities are: $u_v = xG/(\alpha_v \rho_v)$ and $u_l = (1-x)G/[(1-\alpha_v)\rho_l]$. The void fraction is expressed as

$$\alpha_v = \frac{1}{1 + S\frac{1-x}{x}\frac{\rho_v}{\rho_l}}. \tag{3.45}$$

Using the previous equations, the mass flux expressed in (3.28) becomes

$$G = \rho_s \sqrt{2(h_0 - h)}, \tag{3.46}$$

where the slip density is expressed by

$$\rho_s = \left[\frac{x}{\rho_v} + \frac{(1-x)S}{\rho_l}\right]^{-1}\left[x + \frac{(1-x)}{S^2}\right]^{-1/2}. \tag{3.47}$$

To calculate x, we can use the assumption of the isentropic expansion, i.e. $x = (s_0 - s_l)/(s_v - s_l)$. Setting the slip ratio to $S = (\rho_l/\rho_v)^{1/3}$, we recover the practical formula proposed by Moody [184] to calculate the critical mass flux. For $S = 1$ we get an analogous formula for the HEM.

Equation (3.46) and (3.47) depend only on pressure and stagnation conditions. For determining the critical mass flow rate G_{cr}, for HEM and Moody (1965), Eq. (3.46) can be iteratively solved by using the conditions:

$$\left(\frac{\partial G}{\partial p}\right)_{throat} = 0, \qquad \left(\frac{\partial^2 G}{\partial p^2}\right)_{throat} < 0. \tag{3.48}$$

The first condition comes from the impossibility for a pressure perturbation to propagate against the flow direction. The second condition states that the critical mass flow rate achieved is the maximum one. Therefore the calculation of the critical mass flux and pressure reduces to the research of a maximum that has to be done iteratively since fluid properties change with pressure. In order to speed up the calculations, in this article, the Golden Section Search algorithm has been used.

3.5.2 Calculation of the Critical Mass Flux with Henry-Fauske Model

The purpose of Henry & Fauske in [125] was to provide a practical set of equations to calculate the critical mass flux only as a function of stagnation conditions. Despite the simplicity of this model, it allows accounting the non-equilibrium between phases. This way to calculate the critical mass flux is simple and fairly accurate.

The speed of sound of this model is indicated in Eq. (3.40), it follows that the critical max flow rate is $G_{cr} = \rho_m c_{HF}$, which depends on stagnation condition and critical pressure. However the latter is unknown, hence, critical mass flux and pressure equations must be solved together.

Here we include the equation provided by Henry & Fauske in [125] to calculate the pressure at the throat. The pressure ratio between the throat and the stagnation conditions, $\eta = p_t/p_0$, is:

$$\eta = \left[\frac{\frac{1-\alpha_{v,0}}{\alpha_{v,0}}(1-\eta) + \frac{\gamma}{\gamma-1}}{\frac{1}{2\beta\alpha_{v,t}^2} + \frac{\gamma}{\gamma-1}} \right]_{throat}^{\frac{\gamma}{\gamma-1}}. \tag{3.49}$$

where

$$\beta = \left[\frac{1}{n} + \left(1 - \frac{v_{l,0}}{v_{g,t}}\right) \left(\frac{(1-x_0)Np}{x_0\left(s_{v,eq} - s_{l,eq}\right)} \frac{ds_{l,eq}}{dp} \right)_t - \frac{c_{p,v}(1/n - 1/\gamma)}{s_{v,0} - s_{l,0}} \right], \tag{3.50}$$

$$\alpha_{v,0} = \frac{x_0 v_{v,0}}{(1-x_0)v_{l,0} + x_0 v_{v,0}}, \qquad \alpha_{v,t} = \frac{x_0 v_{v,t}}{(1-x_0)v_{l,0} + x_0 v_{v,t}}, \qquad v_{v,t} = v_{v,0}\eta^{-1/\gamma}. \tag{3.51}$$

As discussed above, the metastability is taken into account by an empirical parameter, N, which has been expressed in (3.39). This empirical correlation has been formulated to hold only for dispersed mixtures expected at a nozzle throat. In fact, originally, the Henry-Fauske [125] model was developed for nozzles, orifices and short tubes, in which the assumption of dispersed mixture at the throat is reasonable. Nevertheless, this model has been widely used even for other configurations, like long pipes, with good results.

It tries to account for the effects of the thermal non-equilibrium by means of experimental coefficients. Obviously, the validity of these coefficients is limited to the experimental range for which they have been determined. For example, the range of the Henry-Fauske [125] reported in [114] is $20 \leq p_0 \leq 200\,psia$ for subcooled and saturated inlet conditions, and up to $882\,psia$ for two-phase mixtures. Much lower than the working pressure of Pressurized Water Reactors. However, it is extensively used far away from its experimental ranges with adequate results.

3.5.3 Calculation of the Critical Mass Flux with Delayed Equilibrium Model

The integration of the system of equations formed by (3.9) and (3.15) requires non-negligible computational efforts. One of the aims of this paper is to show that it is possible to obtain very good estimations of critical mass flux and pressure using simple numerical methods.

For steady-state applications, by means of the entropy balance, Feburie et al. [107] gave a very compact form for the DEM. Further simplifications come from Attou & Seynhaeve [11]. Finally, the

DEM can be written as

$$\begin{bmatrix} v_v - v_l & v_l - v_{l,M} & \left(\frac{\partial v_m}{\partial p}\right)_{X,y} & -\frac{v_m}{u_m} \\ 0 & 0 & 1 & \frac{v_m}{u_m} \\ h_v - h_l & h_l - h_{l,M} & \left(\frac{\partial h_m}{\partial p}\right)_{X,y} & u_m \\ 0 & 1 & 0 & 0 \end{bmatrix} \begin{bmatrix} \frac{dX}{dz} \\ \frac{dy}{dz} \\ \frac{dp}{dz} \\ \frac{du_m}{dz} \end{bmatrix} = \begin{bmatrix} \frac{v_m}{A_z}\frac{dA_z}{dz} \\ -\frac{P_z}{A_z}\tau_w - \frac{1}{v_m}gcos\theta \\ \frac{v_m}{u_m}\frac{P_z}{A_z}q' - gcos\theta \\ f(p,y,T_{l,M}) \end{bmatrix}. \tag{3.52}$$

τ_w denotes the wall shear stress, P_z is the perimeter of the channel, θ is the angle between the axis of the channel and the upward vertical direction. q' takes into account the eventual heating/cooling of the channel and is expressed in W/m. System (3.52) is formed by four ordinary first order differential equations. The last equation is

$$\frac{dy}{dz} = f(p,y,T_{l,M}). \tag{3.53}$$

Similarly to $\Gamma_{l,M}$ for the transient flow, $f(p,y,T_{l,M})$ describes the mass transfer for steady-state flows. Namely, it is the formation rate along coordinate z of stable phases, i.e. saturated liquid and vapor, from the liquid metastable phase. Its formulation is discussed in Section 3.5.3.1. The derivatives appearing in the L.H.S. of system (3.52) are

$$\left(\frac{\partial v_m}{\partial p}\right)_{X,y} = X\frac{dv_v}{dp} + (y-X)\frac{dv_l}{dp} - (1-y)\left(\frac{\partial v_{l,M}}{\partial p}\right)_s, \tag{3.54}$$

$$\left(\frac{\partial h_m}{\partial p}\right)_{X,y} = X\frac{dh_v}{dp} + (y-X)\frac{dh_l}{dp} - (1-y)\left(\frac{\partial h_{l,M}}{\partial p}\right)_s. \tag{3.55}$$

The metastable phase is supposed to undergo an isentropic transformation, then

$$\left(\frac{\partial v_{l,M}}{\partial p}\right)_s = -\frac{1}{\rho_{l,M}^2 c_{l,M}^2} \approx 0, \qquad \left(\frac{\partial h_{l,M}}{\partial p}\right)_s = v_{l,M}. \tag{3.56}$$

3.5.3.1 Vaporization during the expansion and closure laws for DEM

The presence of a metastable phase in the model accounts for the vaporization delay experimentally observed [149, 226]. The vaporization delay is governed by the onset pressure of nucleation, p_{onset}, and the evolution of the vaporization index, y. At p_{onset} the probability of nucleation becomes significant, vapor appears and the mixture is accelerated. Lackmé proposed [157]:

$$p_{onset} = k_1 p_{sat}(T_0), \qquad \text{with } k_1 \approx 0.95. \tag{3.57}$$

Generally, experimental facilities use demineralized water, therefore k_1 could be somewhat larger for industrial water applications. Bartosiewicz & Seynhaeve [17] considered $0.95 \leq k_1 \leq 0.98$.

The relation expressed in Eq. (3.57) has the effect to shift the onset of nucleation at a pressure smaller than p_{sat}. In fact, in classical thermodynamics the phase transition occurs at saturation conditions, however, in real systems an isothermal pressure change would very likely carry the

state point into the metastable domain. The deeper the metastability reached, the higher is the probability for the phase change to occur. Here the onset of nucleation is crudely shifted by using a factor k_1, however, this approximation seems to well reproduce the pressure and void fraction evolutions in the long and short pipes (Fig. 3.5, 3.6 and 3.9).

Considering the evolution of the mass fraction of the saturated phase, y, on an infinitesimal interval dz, downstream from the nucleation onset position, Lackmé [159] proposed the relaxation relation

$$dy = k_2(1-y)(p_0-p)^{\frac{1}{4}}dz. \tag{3.58}$$

Thus, the variation of y is proportional to the mass fraction of the metastable liquid $(1-y)$. The term $(p_0-p)^n$ represents the tension that the liquid must tolerate to not vaporize at temperature T_0. The exponent $n=\frac{1}{4}$ comes from the approximated trend of the saturation curve: $p_{sat} \approx (0.01\,T_{sat})^4$.

Using this approach, in long tube configurations, the metastable phase disappears slowly as experimentally observed [149, 226]. Conversely to the approach of Schrock et al. [238], where the metastability disappears almost instantaneously once the metastable limit is reached, similarly to rapid depressurization experiments [94]. Feburie et al. [107] proposed a similar correlation for steam generator cracks and subcooled inlet conditions. Recently, the relaxation law has been written as [17]

$$\frac{dy}{dz} = \left(C_1\frac{P_z}{A_z}+C_2\right)(1-y)\left[\frac{p_{sat}(T_{l,M})-p}{p_{critical}-p_{sat}(T_{l,M})}\right]^{C_3}, \tag{3.59}$$

where $p_{critical} = 220.64\ bar$ for water. Equation (3.59) is the formation rate, along coordinate z of stable phases from liquid metastable phase. The thermodynamic non-equilibrium is function of the local normalized subcooling difference, expressed in terms of pressure difference. Hence, the evolution of the metastable phase is described by both local thermodynamic magnitudes and experimental coefficients, allowing to take into account heterogeneous nucleation at the wall ($C_1\frac{P_z}{A_z}$) and in the bulk (C_2). The experimental coefficients of Eq. (3.59) have been recently adjusted, giving to the model a more general validity. Thus, the coefficients used in this article are the ones in [241]

$$C_1 = 0.008390, \qquad C_2 = 0.633691, \qquad C_3 = 0.228127. \tag{3.60}$$

As long as the nucleation onset pressure has not been reached, the flow is single-phase, hence the wall shear stress, τ_w, is determined by the following formula

$$\tau_l = f\frac{G_l^2}{2\rho_l}, \tag{3.61}$$

where the Fanning friction coefficient f is calculated by the Colebrook's correlation. The wall shear stress in two-phase flow is calculated by using two-phase multipliers

$$\tau_{TP} = \Phi_l^2\tau_l. \tag{3.62}$$

For the two-phase multiplier, the correlation of Lockhart-Martinelli, modified by Richardson (1958), has been adopted

$$\Phi_l^2 = (1-\alpha_v)^{-1.75}. \tag{3.63}$$

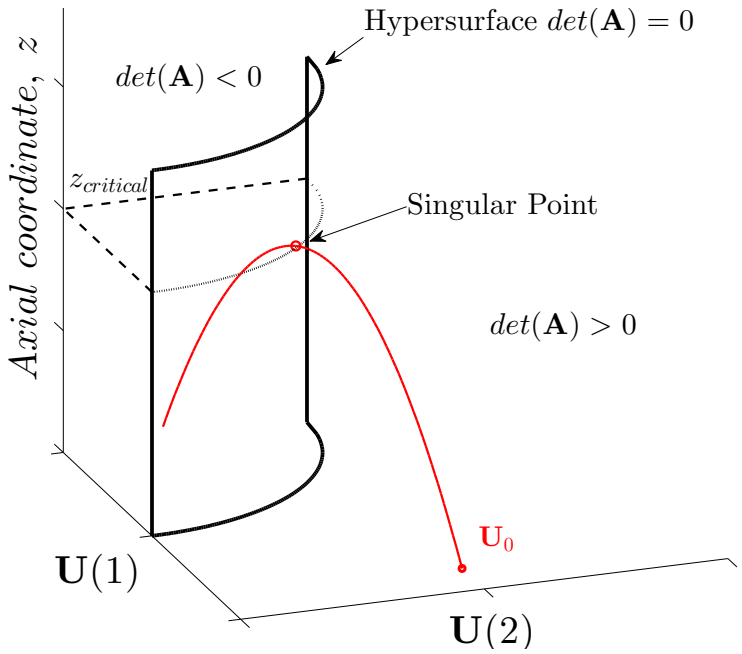

FIGURE 3.2. Schematic example of a critical trajectory in the phase space Ω. The hypersurface, described by $det(\mathbf{A}) = 0$, separates the portion of Ω for which $det(\mathbf{A}) < 0$ by the portion in which $det(\mathbf{A}) > 0$. The singular point represents the intersection between the critical trajectory and the hypersurface at $z = z_{critical}$.

3.5.3.2 Possible-Impossible Flow Algorithm

Let us describe now the numerical method used for solving system (3.52) and its mathematical foundation. The two-phase flow model of Eq. (3.52) constitutes a system of non-linear ordinary first order differential equations as (3.7). The components of $\mathbf{U}$ represent the trajectories in the phase space Ω formed by the n components of $\mathbf{U}$ and the coordinate z. As introduced above in Eq. (3.8), the necessary condition for criticality [37] is $det(\mathbf{A}) = 0$.

In the phase space Ω, the points where $det(\mathbf{A}) = 0$, are either *turning points* or *singular points*. These points form a cylindrical hypersurface in the phase space Ω. The compatibility condition for criticality [37] is

$$det(\mathbf{A}_{(\mathbf{b}),\mathrm{i}}) = 0, \tag{3.64}$$

where $\mathbf{A}_{(\mathbf{b}),\mathrm{i}}$ is the matrix obtained by replacing the i-th column of $\mathbf{A}$ by the source term vector $\mathbf{b}$. It can be demonstrated that if Eq. (3.64) is satisfied for $i = l$, then, $det(\mathbf{A}_{(\mathbf{b}),\mathrm{i}}) = 0 \ \forall i = 1,..,n$ [27].

Points satisfying Eq. (3.8) but not Eq. (3.64) are turning points; points satisfying both together are singular points. Generally, in two-phase flows, singular points are *nondegenerate*, thus, they can be: saddle, nodal or spiral points.

It has to be noted that the necessary critical flow criterion involves only the L.H.S. of Eq. (3.52). Hence, the speed of propagation of a plane wave of small amplitude is insensitive to gravity, tube shape, wall friction and the other terms of $\mathbf{b}$. On the other hand, the compatibility condition involves all the terms of the R.H.S. of Eq. (3.52).

Mathematically, Eq. (3.8) and (3.64), together, represent the *choking criterion*. In the phase space Ω, the points of Eq. (3.8) form a cylindrical hypersurface dividing the subcritical and the supercritical regions (see Fig. 3.2).

To solve Eq. (3.7), therefore system (3.52), the procedure is to start from the point $\mathbf{U}_0$ of the phase space Ω and to integrate along channel axis z until the critical point is detected. Let us explain better this procedure.

As long as $det(\mathbf{A}) \neq 0$, there are no problems in solving system (3.52) with a standard ODE solver. As soon as one of the eigenvalues of matrix $\mathbf{A}$ is equal to zero, hence $det(\mathbf{A}) = 0$, system (3.52) cannot be solved by integration at that particular point.

However, in this article, we want to use the DEM to calculate the critical mass flux and pressure, therefore, the calculation domain arrives up to the critical section. To reach this goal, a standard ODE solver is sufficient since it allows to approach extremely close to a critical point.

From the inlet up to the critical section, the solution of Eq. (3.7), is given by Cramer's rule

$$\frac{dU_i}{dz} = \frac{det(\mathbf{A}_{(\mathbf{B}),\mathrm{i})})}{det(\mathbf{A})} = (\mathbf{A}^{-1}\mathbf{b})_i, \tag{3.65}$$

where $(\mathbf{A}^{-1}\mathbf{b})_i$ is the i-th element of the vector $\mathbf{A}^{-1}\mathbf{b}$.

System (3.52) can be also solved using Eq. (3.65). To be more accurate, the spatial integration of system (3.52) can be done using a standard ODE solver. In this paper, all the calculations have been performed using a six-stage, fifth-order, Runge-Kutta method with a variable space step.

In the case of DEM, the variable vector is $\mathbf{U} = [X,\ y,\ p,\ u_m]^T$. To integrate system (3.52), we need the value of the variable vector $\mathbf{U}_0$ at $z = 0$, i.e. at the inlet of the channel. Usually not all the components of $\mathbf{U}_0$ are known. The inlet pressure, p_0, and the inlet quality of the mixture, X_0, are always known. The fraction of stable phase, y_0, is assumed to be equal to X_0, it means that all the liquid is assumed to be metastable at the inlet of the channel, whether it is saturated or subcooled. However the inlet velocity $u_{m,0}$ is unknown.

To overcome this problem, the system (3.52) is solved coupling the Runge-Kutta method with the Possible-Impossible Flow (PIF) algorithm which provides a good estimation of the inlet velocity.

Physically, the choked flow represents the maximum value of the possible mass fluxes and the minimum value of the impossible mass fluxes. The PIF algorithm incorporates this definition and it might be considered as a simplification of the one introduced in [37] and is similar to the one used by Yoon et al. [281]. The logical scheme of this algorithm is the following:

Step 0: we start from two values of mass flow rate, $\dot{m}_{imp}$ and $\dot{m}_{pos}$. The first is defined to be the impossible mass flow rate (too high) and the latter is a possible flow rate (too low to be the critical one).

Step 1: The inlet velocity is calculated as $u_{m,0} = \frac{\dot{m}_{guess}}{\rho_{m,0} A_{z,0}}$. Where the guessed mass flow rate is: $\dot{m}_{guess} = (\dot{m}_{imp} + \dot{m}_{pos})/2$. All the components of the inlet variable vector $\mathbf{U}_0$ are known now.

Step 2: from the inlet conditions, system (3.52) is integrated using a Runge-Kutta method checking that $det(\mathbf{A})$ does not change its sign (crossing the hypersurface of Fig. 3.2).

Step 3: If $det(\mathbf{A}) \leq 0$ before the end of the pipe, the flow is critical (Impossible Flow). The $\dot{m}_{imp}$ is decreased and we restart from *Step 1*.

Step 4: If $det(\mathbf{A}) > 0$ in all the cells in which the pipe has been discretized, the flow is subcritical (Possible Flow). The $\dot{m}_{pos}$ is increased and we restart from *Step 1*.

The iterative algorithm is stopped when the convergence criterion is satisfied, i.e. $|\dot{m}_{imp} - \dot{m}_{pos}|/\dot{m}_{pos} < \epsilon$, being ϵ the required tolerance. This algorithm is extremely rapid and, as we will see in the following, allows very good estimations of critical mass flux and pressure.

If one wants to solve system (3.52) beyond the critical section, other methods must be used. For instance, the asymptotic steady-state solution of the time-dependent system as done in [227].

3.5.3.3 Computational Mesh

When performing simulations of critical flows, in the computational domain close to the critical section, property gradients can be very large, hence, special attention is required. The discretization must be very fine close to the critical section. Elsewhere, such a fine discretization is not required. Therefore the grid structure can be represented, for instance, by a geometrical sequence as suggested by [144]

$$\Delta z_i = \Delta z_1 \, d^{\,i-1}, \tag{3.66}$$

where d is a constant controlling the grid size; clearly, $d > 0$. Δz_i is the length of the $i-th$ cell of the mesh. By imposing that $\sum_{i=1}^{N} \Delta z_i = L$, we get

$$\Delta z_i = \frac{L(1-d)}{1-d^{N+1}} \, d^{\,i-1}. \tag{3.67}$$

N is the total number of cells in the mesh.

3.6 Comparison against Experimental Data

During the previous decades, many experimental campaigns have been carried out in order to improve the physical understanding of the flashing phenomena. A complete database of the experimental data, until 1986, can be found in [130]. Since then, some other interesting experiments have been performed, for instance [11, 152]. Some of them will be analyzed in this article.

The analysis developed here is the comparison of four critical flow models against experimental data. The chosen four models will be assessed on long tubes, short tubes and small slits. Both subcooled and two-phase inlet conditions will be examined.

HEM, DEM, Moody and Henry-Fauske models have been chosen for this analysis. The aim of this study is to provide a benchmark of these models on different geometrical configurations to figure out which model is more appropriated to be used according to the geometry or the inlet conditions. Further, we want to highlight the completeness of the DEM with respect to other models.

Finally, models will be tested for their capability of predicting critical pressure because of its importance in practical applications, for instance, in safety release valve design.

(a) HEM

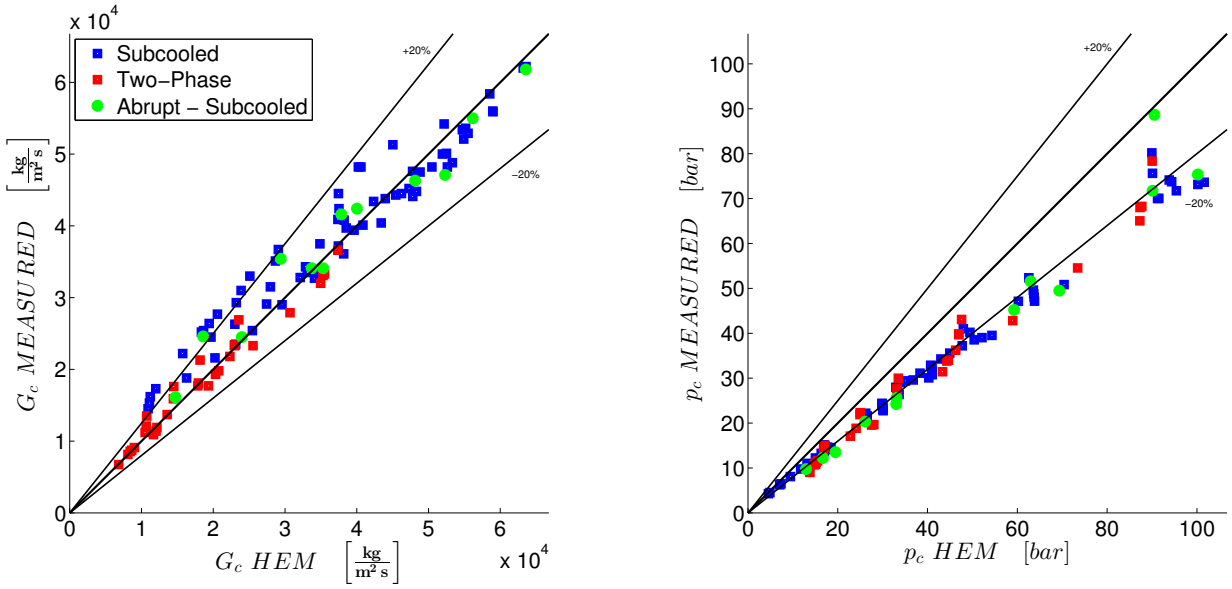

(b) Moody model (1965)

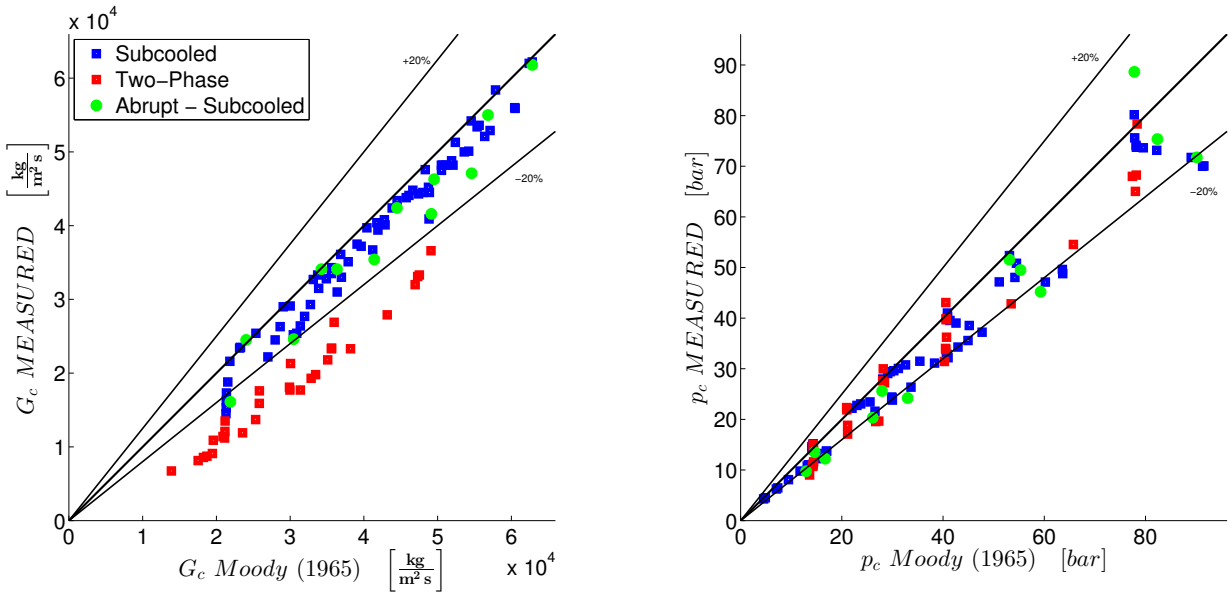

FIGURE 3.3. Benchmarks of HEM and Moody (1965) predictions of critical mass flux, G_c, and critical pressure, p_c, with respect to experimental data of Super Moby Dick, long tubes [149].

Let us recall that the HEM and Moody [184] model are solved to fulfill Eq. (3.48). The research of the maximum mass flux has been done iteratively using the Golden Section Search algorithm. Henry-Fauske [125] is the system formed by the mass flux and the pressure equations in (3.49) to be solved iteratively. For the DEM, the system (3.52) is solved coupling a six-stage, fifth-order, Runge-Kutta method with the Possible-Impossible Flow algorithm as described in Section 3.5.3.2.

(a) Henry-Fauske model (1971)

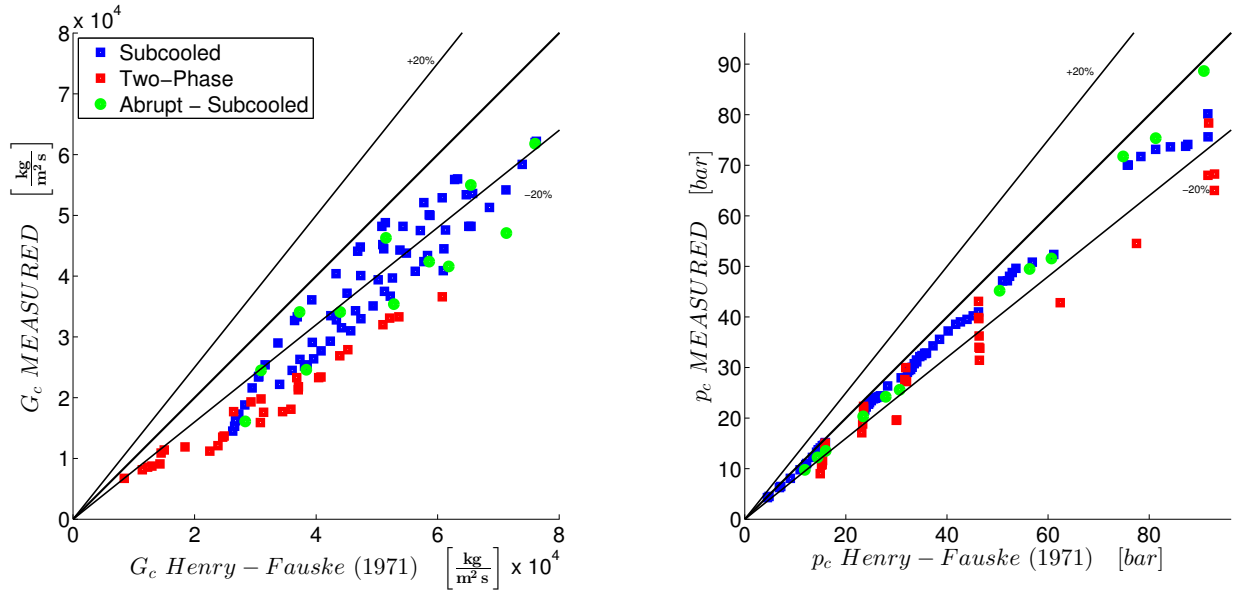

(b) DEM

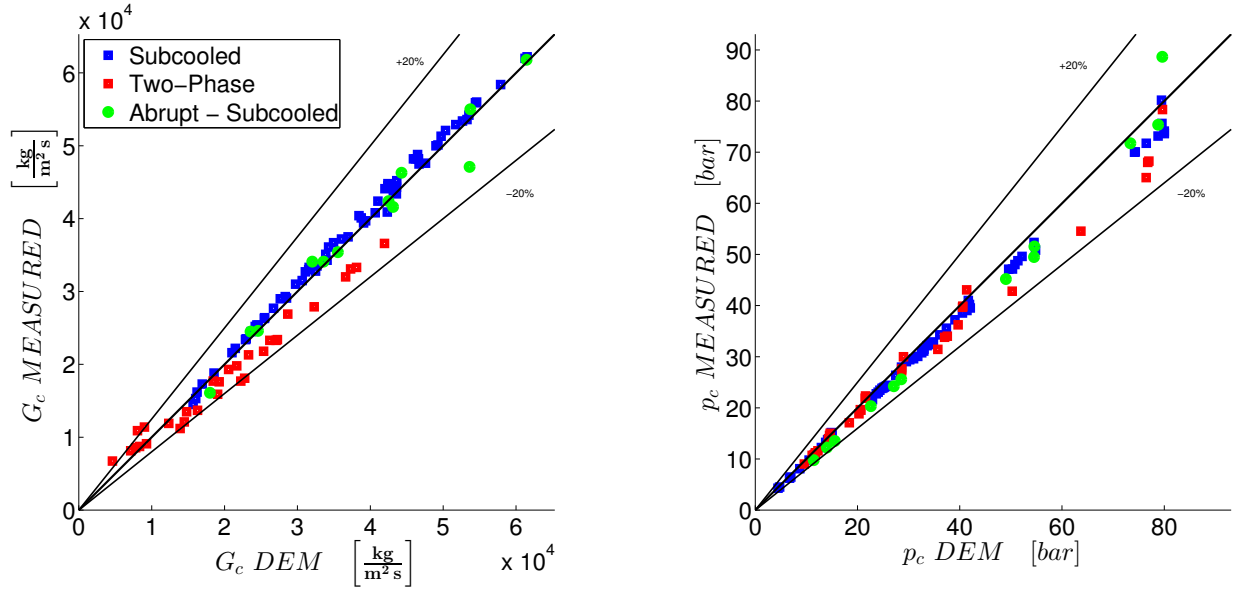

FIGURE 3.4. Benchmarks of Henry-Fauske (1971) and DEM predictions of critical mass flux, G_c, and critical pressure, p_c, with respect to experimental data of Super Moby Dick, long tubes [149].

3.6.1 Critical Two-Phase Flow Through Long Tubes

Long tubes represent the configuration in which most of the models exhibit good results. Certainly, this is the less severe configuration but is quite representative of what happens in particular situations such as a long safety release duct.

About nuclear safety, long tubes with 100% opening at the throat represent the case of Large Break Loss of Coolant Accident (LB-LOCA) when the breach is located at several L/D from the

reactor pressure vessel. If the opening at the throat is reduced, it represents the case of a Small Break LOCA (SB-LOCA).

Among several experiments, we focused the attention on Super Moby Dick (SMD) long configuration tests [38, 149]. The test section of Super Moby Dick facility has been studied and manufactured with extreme care in order to avoid as much as possible 2D and 3D effects. That is quite important for our analysis given that the DEM is a 1D algorithm. Super Moby Dick test section has got three components: a convergent tube, a constant cross-section duct and a conical divergent.

Conical and smooth convergent nozzles have been used and data of both configurations have been used here. The smooth convergent shape is a compromise for getting a strong axial pressure gradient but a small radial gradient and is reported in Fig. 3.5, 3.6. Few tests have been carried out using an abrupt enlargement instead of the conical convergent and are here analyzed. Static pressure measurements have been performed at pressure taps along the tube. Void fraction has been measured by X-rays technique. These local measurements are compared to the profiles predicted by the DEM.

In case of an abrupt enlargement, the location of the critical section corresponds to the throat of the duct, whereas, in the configuration with the divergent, the criticality is generally reached few millimeters downstream from the throat. As discussed in [27], the exact position of the critical section is less defined for divergent nozzles with small opening angle.

Stagnation pressure data of Super Moby Dick long configuration span from 10 to 120 bar. Both subcooled and two-phase inlet conditions are present.

3.6.1.1 Results

Even in long tubes, the fluid transit time is short compared with the vaporization timescale. During the expansion, the thermal non-equilibrium increases since the metastable liquid temperature is almost constant, whereas, the saturated vapor temperature decreases due to the pressure gradient [226]. However, the fraction of metastable liquid decreases.

For two-phase stagnation conditions, higher void fractions are expected in the neighborhood of the critical section, therefore, the mechanical equilibrium could become significant. However, the visual inspection of the flow pattern at the throat, do not justify very high slip ratios as predicted by Moody [184] model.

In terms of critical mass flow rate prediction, the HEM is more accurate than Moody and Henry-Fauske models. On the other hand, using the HEM, the predictions of the critical pressure at the throat are overestimated. The correct prediction of the mass flux coupled to the underestimation of the critical pressure is an evidence of the thermal non-equilibrium effect.

The consequence of the too high slip ratio of the Moody [184] model is clearly visible in Fig. 3.3a. Tests with initially subcooled conditions, achieve a low void fraction at the throat, thus the critical flow rate is well estimated because the thermal non-equilibrium effect is fictitiously accounted by too high mechanical non-equilibrium. Conversely, tests with initially two-phase conditions, have a lower thermal non-equilibrium, hence the mass flow rate is largely overestimated by Moody [184] model, despite the mechanical non-equilibrium is more significant than in subcooled tests.

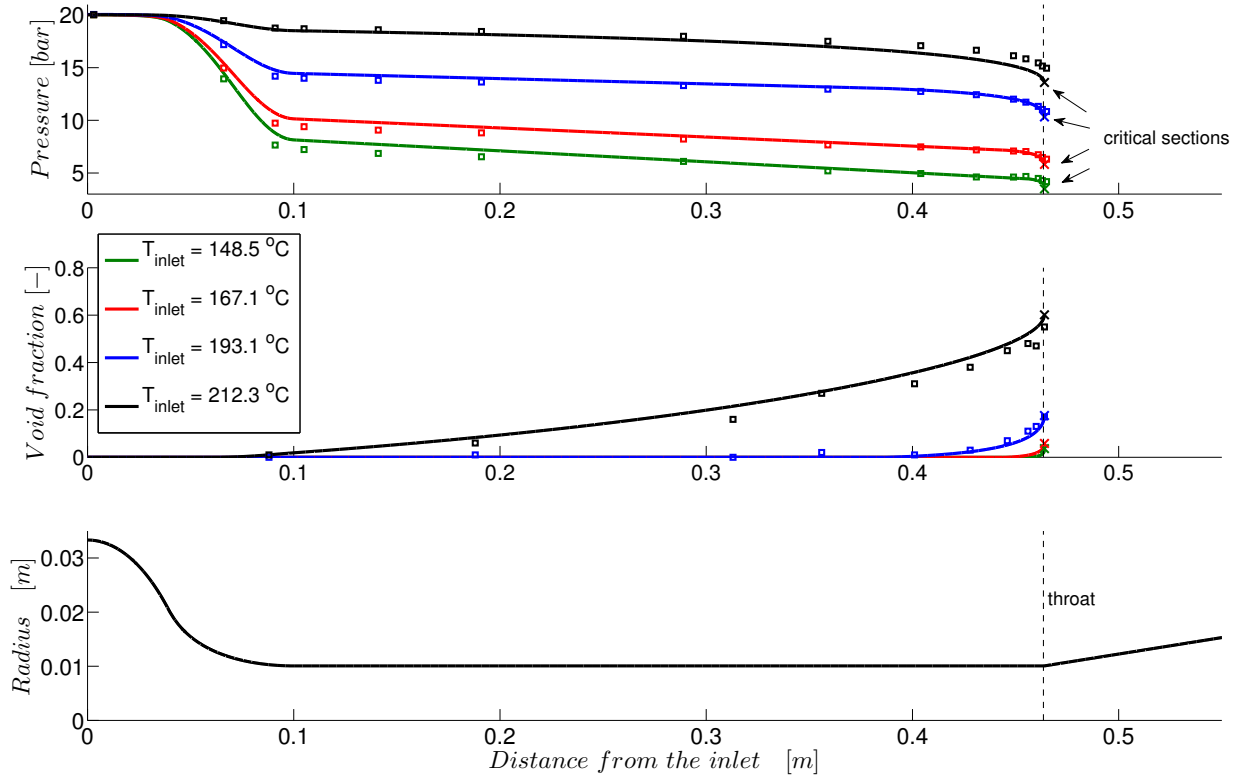

FIGURE 3.5. Pressure and void fraction profiles in SMD test section with stagnation pressure of 20 bar ($T_{sat} = 212.4\,^{o}C$). Solid lines indicate the simulation results of DEM, instead, square markers □ represent the experimental measurements [149]. The locations of the critical section are depicted with the marker ×. In these simulations they have been detected to be around 10^{-3} m downstream from the throat.

Henry-Fauske [125] model tends to overestimate the mass flux since developed for short nozzles and orifices, where friction effect is smaller. The benchmark of the DEM against the experimental data is absolutely positive. Mean errors for both subcooled and two-phase inlet conditions are lower than 6%, however, the standard deviation is higher for two-phase inlet conditions.

About the estimation of the critical pressure, HEM, Moody [184] and Henry-Fauske [125] models exhibit a similar trend for two-phase stagnation conditions. Using these models, the critical pressure is not sensitive to the stagnation flow quality. On Fig. 3.3a and 3.3b, this tendency is shown by vertical red-dot patterns. However, Henry-Fauske [125] model leads to very good estimations of the critical pressure for subcooled water at the inlet.

3.6.1.2 Pressure and Void Fraction Evolutions

The DEM is able to reproduce the pressure and void fraction evolutions in the pipe. Both are assessed against the experimental data in Fig. 3.5 and 3.6.

About the piezometric line in the test section, most of the pressure decrease occurs in the

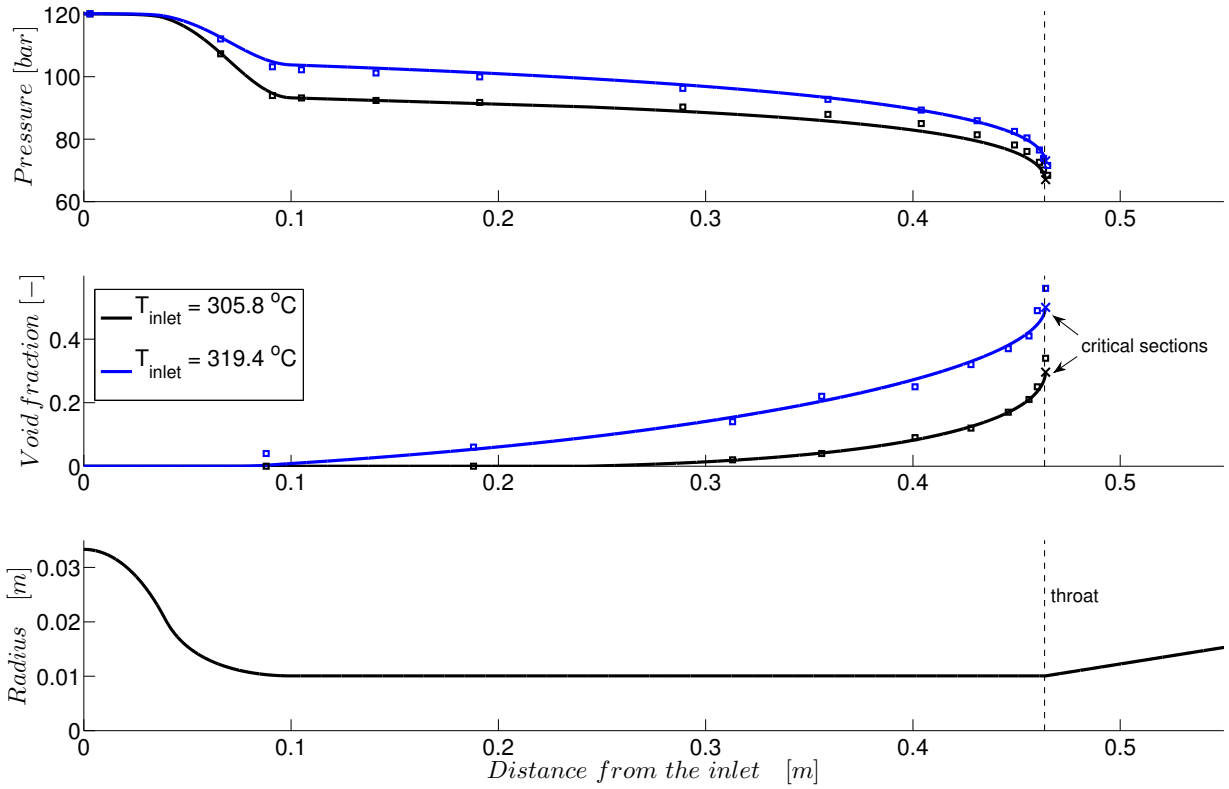

FIGURE 3.6. Pressure and void fraction profiles in SMD test section with stagnation pressure of $120\,bar$ ($T_{sat} = 324.7\,^{o}C$). Solid lines indicate the simulation results of DEM, instead, square markers □ represent the experimental measurements [149]. The locations of the critical section are depicted with the marker ×. In these simulations they have been detected to be around 10^{-3} m downstream from the throat.

convergent section. Friction determines linear pressure losses in the constant cross-section duct. Different slopes represent different Fanning factors (see Eq. (3.61)) due to the increasing Reynolds number for tests with higher degree of subcooling. Once the pressure reaches the value of p_{onset}, pressure losses are increased by the two-phase multiplier. Furthermore, the vaporization makes the fluid to accelerate, therefore, pressure decreases rapidly.

In the simulations reported in Fig. 3.5 and 3.6, the location of the critical section is around 10^{-3} m downstream from the throat. Generally, the more the inlet conditions are subcooled, the lower is the void fraction at the throat. For very high subcooling degrees, the thermal non-equilibrium is rather high, hence, vapor phase appears only in the vicinity of the critical section.

3.6.2 Critical Two-Phase Flow Through Short Nozzles

Short pipes, nozzles and orifices represent configurations in which the non-equilibrium effects are larger. The fluid transit time is very short and the vaporization rate is not sufficiently high to re-establish the equilibrium conditions. Experimental data, with these kind of geometry, are representative of several accidental configurations: breaks in the immediate vicinity of the vessel,

(a) HEM

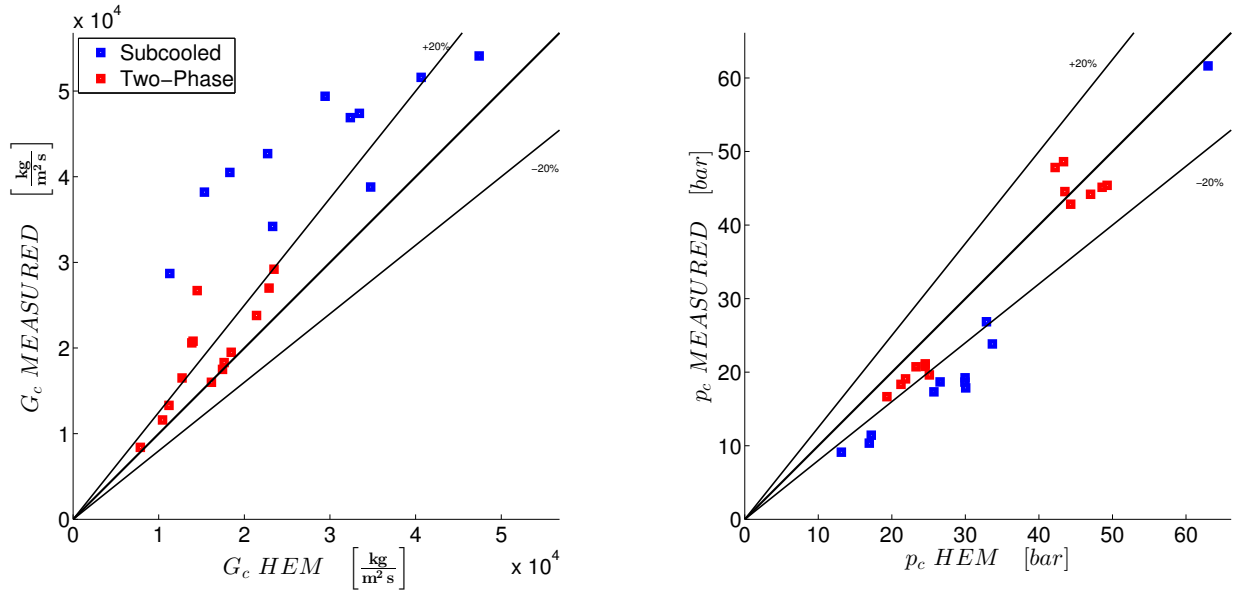

(b) Moody model (1965)

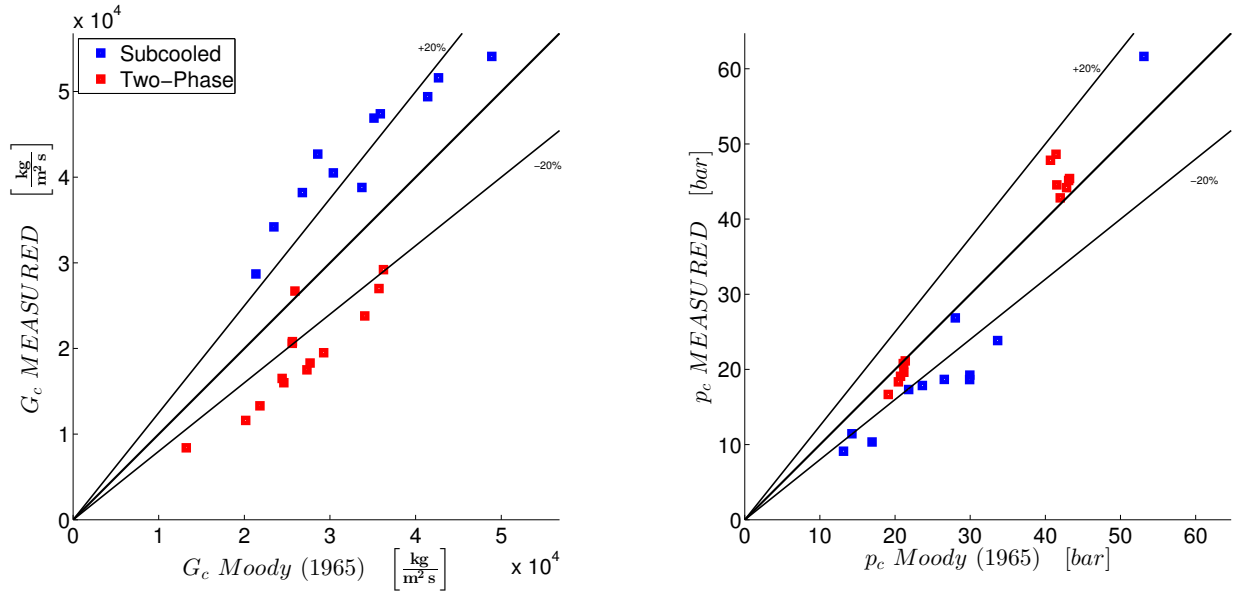

FIGURE 3.7. Benchmarks of HEM and Moody (1965) predictions of critical mass flux, G_c, and critical pressure, p_c, with respect to experimental data of Super Moby Dick, short tubes [150].

breaches of large-diameter pipes, etc.

In literature, much less experimental data are available with respect to long tubes. In this article, the benchmark of the critical flow models has been performed against the Super Moby Dick short configuration data [150]. Similarly to the Super Moby Dick long configuration, 2D and 3D effects have been reduce as much as possible. The test section has got a smooth convergent followed by an abrupt enlargement (see Fig. 3.9). Inlet diameter is 0.087 m, the throat diameter is 0.020 m. Static

(a) Henry-Fauske model (1971)

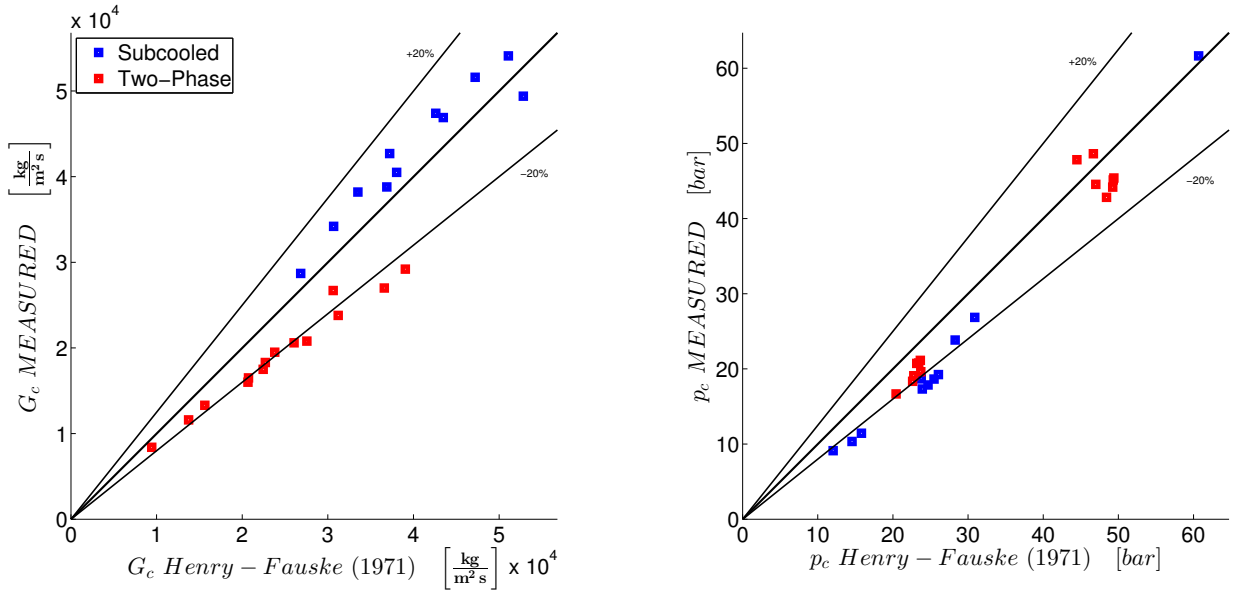

(b) DEM

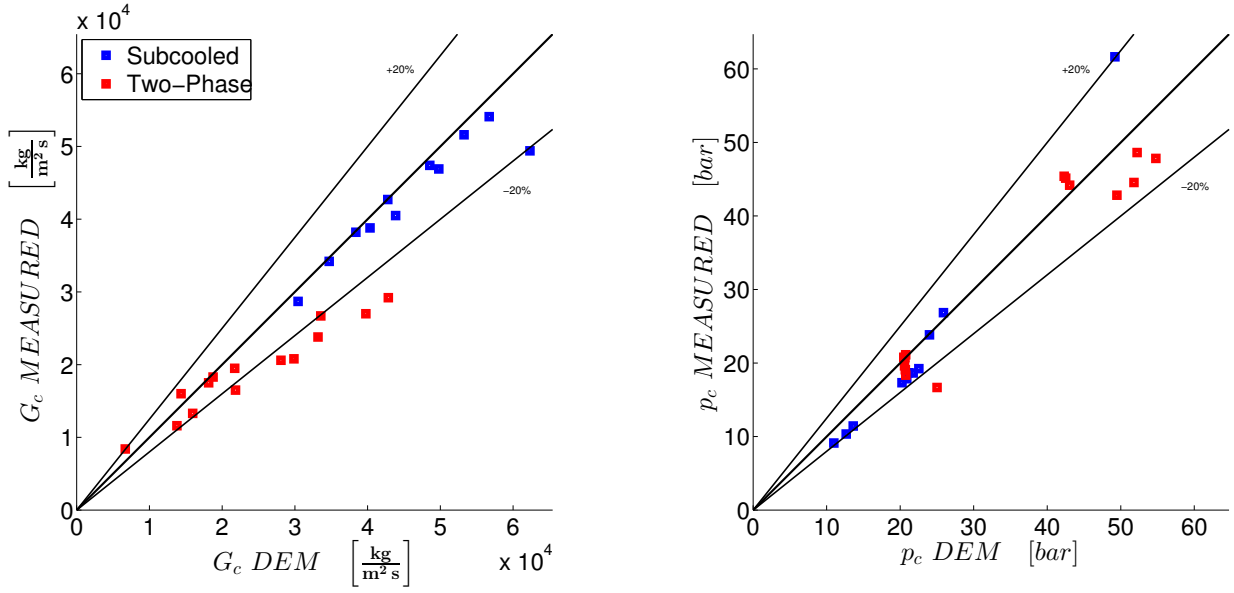

FIGURE 3.8. Benchmarks of Henry-Fauske (1971) and DEM predictions of critical mass flux, G_c, and critical pressure, p_c, with respect to experimental data of Super Moby Dick, short tubes [150].

pressure measurements have been performed at seven pressure taps along the nozzle.

Subcooled tests have been carried out at similar subcooling degrees at $20, 40, 80$ bar and at 234 ^oC for various inlet pressures. Two-phase stagnation tests have been performed at 30 and 64 bar for several inlet flow qualities.

3.6.2.1 Results

Homogeneous critical flow models are less accurate than for the long tube configurations. HEM provides good results only for two-phase stagnation conditions. For subcooled inlet, HEM leads to misleading evaluations of mass fluxes. The mean relative error is -36%, but single relative errors are as high as -60 %. Hence, the experimental mass flux may be more than twice the value predicted by the HEM.

Moody [184] model overestimates the two-phase inlet data but underestimates initially subcooled tests. Reasons are the same as for the long-tube configuration.

As aforementioned, the thermal non-equilibrium effect is predominant on short pipe configurations. In fact, Henry-Fauske [125] and Delayed Equilibrium Model are quite accurate in representing such experimental data (Fig. 3.8a and 3.8b).

3.6.2.2 Pressure Evolutions

The prediction of pressure and void fraction evolutions on short pipes is rather challenging due to the stronger thermal non-equilibrium. However, DEM seems to reproduce correctly the piezometric line in the nozzle. The plot at the top of Fig. 3.9 shows the axial pressure profile of three tests with equal stagnation pressure but different inlet subcooling degrees. The higher the subcooling degree, the stronger is the pressure decrease in the nozzle, because of higher mass fluxes.

Central plot in Fig. 3.9 shows the axial pressure profile of four tests with equal stagnation temperature but different inlet pressure. In short tubes, stagnation temperature seems to be the dominant effect on critical pressure.

3.6.3 Critical Two-Phase Flow Through Slits

Large-Break and Small-Break LOCA represent severe hypothetical accidents of nuclear power plants. In such scenarios, the water of the primary system comes out through the break and flashes. However, the coolant can flow out from the primary system even in non-severe accidental situation. That is the case of critical flow through small slits. In nuclear safety, there is the assumption of leak-before-break, i.e. the presence of detectable leakage threshold [53, 286]. System can continue to operate until such a threshold is reached. Two-phase critical flow models help in predicting the leak rate.

Several experiments are available in literature on this domain. However, very few are representative of industrial situations in which crack diameter is roughly a tenth of millimeter ($D_H \approx 10^{-4}\ m$) [7, 58, 152]. In this article we used the experimental data of John et al. [152]. Here slits are rectangular; one side is 80 mm, the other spans for 0.2 to 0.64 mm. Channel depth is $L = 46\ mm$ long. The inlet conditions of the subcooled liquid water were: pressure p_0 of 40, 60, 80, 100, 120 and $140\,bar$ and subcooling degree ΔT_{sub} of 60, 50, 40, 30, 20, 10 and 2^oC.

For these calculations, channel has been considered of constant cross-section and the wall friction is constant and equal to the experimental value of [152].

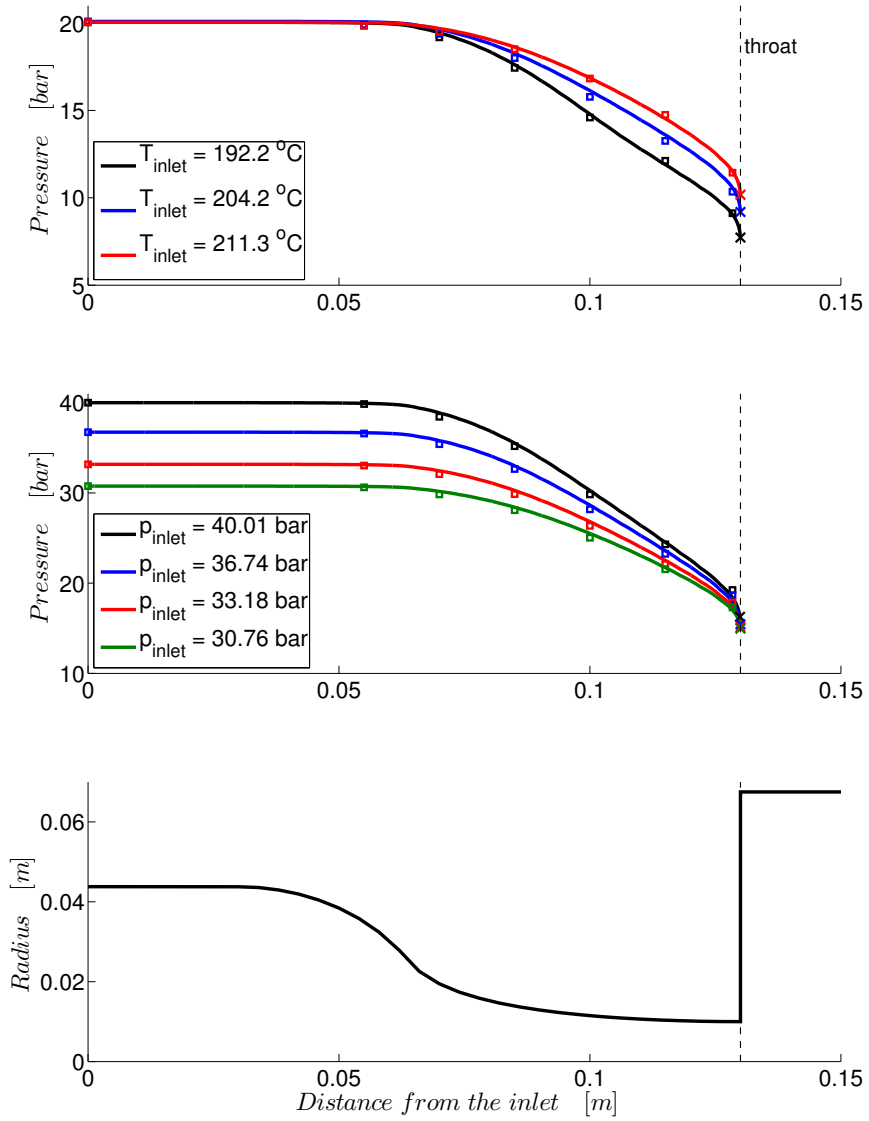

FIGURE 3.9. At the top, there is the pressure profile in SMD short test section for $p_0 = 20\ bar$. In the central plot, the pressure profiles of four tests at $T_0 = 234\ ^oC$ is depicted. At the bottom, we report the geometry of the test section. Solid lines indicate the simulation results of DEM, instead, square markers □ represent the experimental measurements [150]. The locations of the critical section are depicted with the marker × and, practically, coincide with the throat. From the plot on the top the trend is quite clear: the higher the subcooling, the stronger is the pressure decrease in the nozzle. Instead, from the central plot, we can see that the critical pressure, in short nozzles, seems to be not affected by the stagnation pressure. The dominant role is played by the stagnation temperature.

3.6.3.1 Results

These slits are characterized by a large L/D_H ratio, small transit time and large wall roughness. Due to the large L/D_H ratio, as seen above, mechanical and thermal equilibrium can be assumed, leading to evaluate the leak rate using the HEM.

Small transit time and the orifice-like geometry may suggest to use Henry-Fauske model. Figure 3.10 shows that HEM, Moody and Henry-Fauske models would give totally unrealistic critical mass flux. In such a situation, wall friction is the dominant effect, hence, models assuming an isentropic expansion fail.

The delayed equilibrium model, even in this situation, provides very good results. Using the DEM, this particular geometry affects the friction losses but even the nucleation process. In fact, here, heterogeneous nucleation at the wall is the dominant mechanism of vapor formation. This phenomenon is represented by the coefficient C_1 of Eq. (3.59).

Another model that evaluates correctly the critical flow through slits is Pana model [192].

3.7 Benchmark on other Critical Flow Data and Quantitative Analysis

Generally, two-phase critical flow models provides good estimations of the mass flux just within a certain range of inlet conditions or for a particular geometry. In the previous sections, models have been tested on three different geometries into a wide range of thermodynamic conditions at stagnation. However, several models, when assessed against data of two similar experimental facilities, exhibit two different trends [274]. In order to check the behaviors of the four chosen models, the benchmark has been carried out on more than 450 experimental data of different test rigs.

The experimental data used for the assessment come from: Sozzi & Sutherland (1975), Ardron & Ackerman (1978), Boivin (1979), Seynhaeve (1980), BNL (1981), Environmental ('90s) and STEP. Data are both subcooled and two-phase at the inlet. Tube lengths and pipe diameters are widely variable.

To analyze the results, two statistical indicators are used, mean relative error:

$$\mu = \frac{1}{N}\sum_{i=1}^{N}\frac{G_{meas,i} - G_{calc,i}}{G_{meas,i}} \tag{3.68}$$

and standard deviation:

$$\sigma = \sqrt{\frac{1}{N-1}\sum_{i=1}^{N}\left(\frac{G_{meas,i} - G_{calc,i}}{G_{meas,i}} - \mu\right)^2}. \tag{3.69}$$

Similar indicators can be defined for the assessment of the critical pressure predictions. The mean error of each model with respect to the experimental data are summarized in Tab. 3.2 and 3.3, respectively, for the prediction of critical mass flux and pressure. A negative mean error means that the model globally underestimates the mass flux or the pressure at the throat for a particular set of data. The standard deviations are presented in Tab. 3.4 and 3.5.

The performance of a model on a set of experimental data must be judged by using both mean error and standard deviation together. Figure 3.11 shows the trend of HEM, DEM, Moody and Henry-Fauske model against the experimental data just mentioned. Globally, DEM is much less dispersive than the other three models. It is more accurate in most of the set of experimental data examined (Tab. 3.2), and its predictions are the less scattered (Tab. 3.4). The DEM has been originally

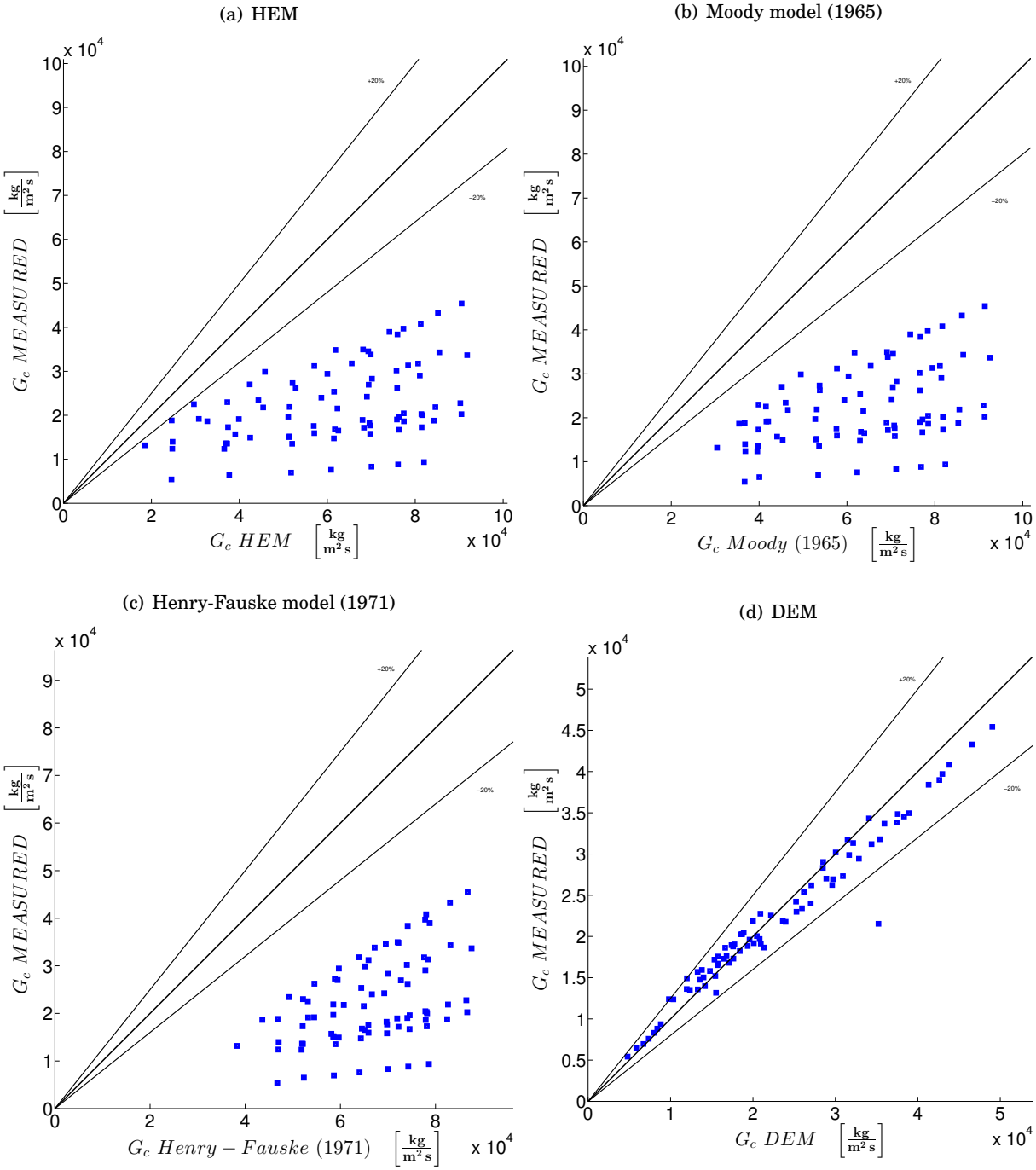

FIGURE 3.10. Benchmarks of HEM, Moody (1965), Henry-Fauske (1971) and DEM predictions of critical mass flux, G_c, with respect to the experimental data of John et al. [152].

developed for subcooled inlet conditions, therefore, it is normal to expect a better agreement in this range. For two-phase stagnation thermodynamic state, HEM predictions fit the data slightly better than DEM, in terms of critical mass flux. However, DEM behaves much better than HEM for critical pressure evaluations.

In case of a two-phase mixture at the inlet, the thermal non-equilibrium during the expansion is lower but still present. Therefore, mixture can be still considered to be composed by three phases. In such a scenario, the rate of disappearance of the metastable phase, could be different than the one of Eq. (3.59), developed for other applications.

Table 3.2: Mean error for critical mass flux predictions

	HEM	**Moody**	**Henry-Fauske**	**DEM**
Two-phase inlet				
SMD long	-0.0064	0.7047	0.6455	0,0603
SMD short	-0.1565	0.4275	0.2511	0,1748
Environmental	-0,1226	2,0749	0,4679	-0,1040
Subcooled inlet				
SMD long	-0.0584	0.0892	0.3162	-0,0186
SMD short	-0.3625	-0.2277	-0.0705	0,0574
John et al. (1988)	2.1699	2.3201	2.5422	0.0096
Environmental	0,0405	0,0335	0,4875	-0,0144
Sozzi&Sutherland (1975)	0,0342	0,1449	0,3679	0,0568
Ardron&Ackerman (1978)	-0,4864	-0,2747	-0,0589	-0,0478
Boivin (1979)	0,0102	0,1973	0,5100	-0,0597
Seynhaeve (1980)	-0,4636	-0,3428	-0,1076	-0,0004
BNL (1981)	-0,2048	-0,2340	0,0014	-0,0105
STEP	-0,2089	-0,3272	-0,1092	0,0169

Table 3.3: Mean error for critical pressure predictions

	HEM	**Moody**	**Henry-Fauske**	**DEM**
Two-phase inlet				
SMD long	0,2757	0,1459	0,2903	0,0615
SMD short	0,0871	-0,0027	0,1140	0,0988
Subcooled inlet				
SMD long	0,2542	0,1445	0,1017	0,0545
SMD short	0,4538	0,3462	0,2896	0,1085

3.8 Conclusions

The physical aspects of the critical two-phase flow have been examined utilizing the Delayed Equilibrium Model and three other well-known models. Particular attention has been paid in discussing the Delayed Equilibrium Model, which describes the flashing flow comprising of three phases.

Homogeneous Equilibrium Model, Moody (1965), Henry-Fauske (1971) and the Delayed Equilibrium Model have been used in this paper. Many models are able to correctly predict the critical mass flux only under certain conditions, however in this article the assessments have been undertaken separately by studying three different configurations: long tubes, short nozzles and slits.

Table 3.4: Standard deviation for critical mass flux predictions

	HEM	**Moody**	**Henry-Fauske**	**DEM**
Two-phase inlet				
SMD long	0,0824	0,2490	0,2040	0,1352
SMD short	0,1377	0,2031	0,0727	0,1894
Environmental	0,0612	0,2098	0,3706	0,0504
Subcooled inlet				
SMD long	0,1167	0,0939	0,1735	0,0333
SMD short	0,1785	0,0770	0,0535	0,0722
John et al. (1988)	1.6462	1.6680	1.7149	0.1126
Environmental	0,1313	0,3663	0,3567	0,0486
Sozzi&Sutherland (1975)	0,3271	0,3598	0,4505	0,0733
Ardron&Ackerman (1978)	0,1145	0,2219	0,2166	0,0843
Boivin (1979)	0,0695	0,1515	0,2290	0,0793
Seynhaeve (1980)	0,0744	0,2147	0,2403	0,0737
BNL (1981)	0,1351	0,1295	0,1165	0,0617
STEP	0,1573	0,1567	0,0544	0,0789

Table 3.5: Standard deviation for critical pressure predictions

	HEM	**Moody**	**Henry-Fauske**	**DEM**
Two-phase inlet				
SMD long	0,1103	0,1552	0,1677	0,0596
SMD short	0,1116	0,0890	0,0896	0,1395
Subcooled inlet				
SMD long	0,0796	0,1211	0,0400	0,0367
SMD short	0,1910	0,2364	0,1317	0,1311

To ascertain the behavior of the particular models, studies have been carried out and the benchmark against more than 450 experimental data analyzed in both a graphical and quantitative representation using mean errors and standard deviations.

The classic models: HEM, Moody (1965) and Henry-Fauske (1971) cannot be considered as global methods for the evaluation of the two-phase critical flow.

HEM exhibits a positive result in evaluating the critical mass flux of long tubes, but predictions of the critical pressure are incorrect. Moody's model is unsuitable under two-phase stagnation conditions, which is unexpected for a non-homogeneous model. Henry-Fauske model overestimates the mass flux in long tubes but provides good results for critical pressure. Given that the model has been developed for nozzles and orifices, the assessment on short tubes is rather positive. Finally, none of the classic models are able to correctly predict the mass flow rate through very narrow slits.

On the other hand, DEM seems to be a more reliable model in all the configurations tested in this article, both in terms of critical pressure and critical mass flux. In fact, apart from a few experiments, the relative error is lower than 20%.

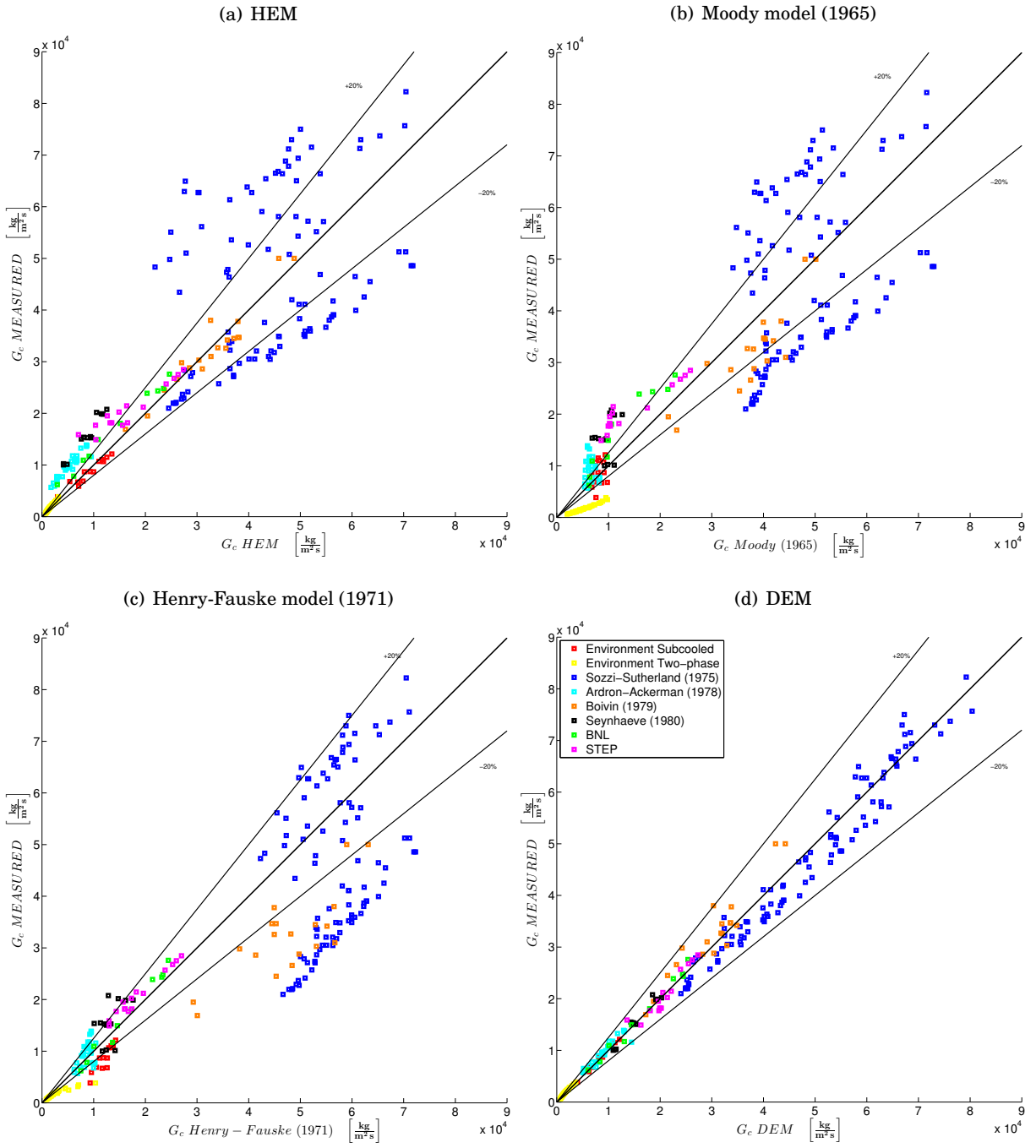

FIGURE 3.11. Benchmarks of HEM, Moody (1965), Henry-Fauske (1971) and DEM predictions of critical mass flux, G_c, with respect to the experimental data.

3.9 Appendix 3.A: Condition of Critical Mass Flux of Moody Model

As discussed in Section 3.4.2, the critical mass flux of Moody [184] corresponds to

$$G_{cr}^2 = -\left[\frac{d}{dp}\left(\frac{1}{\rho_m^+}\right)\right]^{-1}. \tag{3.70}$$

Using the relation given in (3.45), the momentum density is

$$\frac{1}{\rho_m^+} = [xv_v + (1-x)v_l S]\left(x + \frac{1-x}{S}\right) \tag{3.71}$$

Substituting (3.71) in (3.70), and making elementary calculations:

$$\begin{aligned} G_{cr}^{-2} = &-\left\{(v_v - v_l S)\left(x + \frac{1-x}{S}\right) + [xv_v + (1-x)v_l S]\left(1 - \frac{1}{S}\right)\right\}\frac{dx}{dp} \\ &-\left[x\frac{dv_v}{dp} + (1-x)S\frac{dv_l}{dp}\right] \\ &-\left\{(1-x)v_l\left(x + \frac{1-x}{S}\right) - [xv_v + (1-x)v_l S]\frac{1-x}{S^2}\right\}\frac{dS}{dp}. \end{aligned} \tag{3.72}$$

Given that the transformation is isentropic

$$\left(\frac{\partial x}{\partial p}\right)_s = \frac{1}{s_l - s_v}\left[x\frac{ds_v}{dp} + (1-x)\frac{ds_l}{dp}\right]. \tag{3.73}$$

CHAPTER 4

TRANSIENT METASTABLE FLOWS AND STEAM-WATER TABLES

Transient metastable flows often occurs in numerous industrial accidents. Analogously to the stationary metastable flows, the trigger can be of thermal or mechanical kind. For instance, a quick variation of the heat flux, or a sudden change in pressure or velocity may initiate a fast transient in which the wave propagation phenomena are dominant.

Such fast transients can be the *fast depressurizations* caused by the loss of integrity of a pressurized circuit, *waterhammers*, due to the sudden closure/opening of a valve in a circuit or the quick condensation of a vapor pocket in a mixture flows, the rapid *injection of thermal energy* into a fluid, etc. These phenomena are at the root of many industrial accidents, both in nuclear and in conventional industries. They need to be analyzed for their prevention or, at least, the mitigation of their effects.

In the context of nuclear safety, these scenarios represent the very beginning of the Loss of Coolant Accident (LOCA), waterhammers that may take place in the various circuits of a nuclear power plant, energy injection caused by the contact of the coolant with very hot particles of the nuclear fuel when the cladding breaks, etc. A test case of each of these accidental transients is analyzed in this chapter.

In these scenarios, the fluid conditions change rapidly. If the fluid enters into the two-phase domain, a delay of vaporization leads to metastable conditions. In order to correctly simulate these phenomena, the accurate calculation of the fluid properties is crucial, especially when threshold phenomena, such as phase transition, are present. Further, steam-water behavior is already very complex in the stable equilibrium domain but it can be even more complex in the metastable domain where the derivatives of the thermodynamic properties are very large and approach infinity close to the spinodal line. This reasoning led to the adoption of the IAPWS-IF97 EoS for transient simulations, as it was done in the previous chapter for the steady-state calculations. Because the numerical approach is, however, significantly different, a supplementary effort must be undertaken to use the IAPWS-IF97 EoS.

In this chapter, similarly to the previous one, the focus is on the effect of the metastability and the thermodynamic equilibrium recovery process. Contrary to the previous chapter, here the time-dependence is strong, and the calculations have been carried out on the EUROPLEXUS code using an explicit Finite Volume Method. Further, in Chapter 3, the flow was smooth, so the transport equations were manipulated and written in a nonconservative form. This allowed the use of pressure as a state variable; then the fluid properties were calculated in a simple manner. In this chapter, due to the presence of shock waves, the system of transport equations must be written in conservative form. This poses some difficulties in the evaluation of the water properties because the thermodynamic variables that are immediately available from the conservative ones are the density and the internal energy. In this work, we discuss how to calculate the pressure and the other properties when the known fluid variables are the density and the internal energy.

In fact, based on the work of Kunick et al. [133], thermodynamic properties of water have been tabulated on the *e-v* thermodynamic diagram for a fast and accurate interpolation strategy. Some key features of [133] have been adopted in this work, e.g. the method of grid generation for the transformation of the *e-v* thermodynamic diagram into a Cartesian one. However, the method proposed here must not be consider as an evolution of [133] and is not intended to replace this IAPWS Guideline. Rather, it is an author's attempt for the water properties calculation that still suffers of some deficiency with respect to [133]. In particular, in the method proposed here, the interpolating functions are not globally smooth and this may lead to some numerical issues as theoretically explained in [181]. In this sense, some improvements are proposed in the Conclusions of this thesis.

The interpolation strategy just mentioned has been implemented in the EUROPLEXUS code and, more recently, in *Code_Safari*. Concerning the EUROPLEXUS code, prior to this work, a HEM based on an iterative procedure for water calculations was available. This iterative procedure rendered the numerical simulations slow and less robust. After this work, EUROPLEXUS incorporates a HEM that is iterations-free, more robust, and faster (30-70% in terms of CPU time) than the previous one. Moreover, the previous version of the HRM was obsolete and did not provide reliable results. As a further achievement of this work, now EUROPLEXUS also incorporates a reliable HRM coupled to a fast and accurate steam-water tables look-up method.

From this work it is evident that the thermodynamic disequilibrium is the key feature for the correct analysis of fast depressurizations because it greatly affects the amplitude of the rarefaction wave that propagates in the event of a fluid circuit break. For the waterhammers, it is harder to state whether the thermodynamic disequilibrium is important or not, at least for the ones analyzed here. But for an energy injection simulation, the thermodynamic disequilibrium does affect the value of the pressure peak.

Homogeneous Two-Phase Flow Models and Accurate Steam-Water Table Look-up Method for Fast Transient Simulations

International Journal of Multiphase Flow, Vol. 95, 199-219.

M. De Lorenzo[1], Ph. Lafon[1], M. Di Matteo[1,2], M. Pelanti[1], J.-M. Seynhaeve[3], Y. Bartosiewicz[4].

The accurate simulation of fast steam-water transients requires precise algorithms for calculating fluid properties. The system of the governing flow equations must be closed with an Equation of State (EoS) to calculate the pressure as a function of the system conservative variables. For water, accurate analytical EoS for this purpose are not available yet. The aim of this paper is to show an efficient and very accurate algorithm to calculate water properties when the independent variables of the EoS are the density and the specific internal energy. Our algorithm uses a new table look-up method with bicubic interpolation based on the IAPWS-IF97 EoS formulation, and it is able to account for metastable states. The liquid metastability domain is extended until the spinodal curve, here determined and compared with other formulations.

The EoS algorithm is coupled to two classical homogeneous two-phase flow models, namely the Homogeneous Equilibrium Model (HEM) and the Homogeneous Relaxation Model (HRM). HEM and HRM are used to simulate fast depressurization, waterhammer and steam explosion problems. Comparison of the numerical results with available experimental data show the good performance of the proposed algorithms.

4.1 Introduction

Computational Fluid Dynamics simulations require accurate and fast algorithms for calculating fluid properties. In industrial applications, simulations are performed for a wide range of regimes, possibly involving shock wave formation. In such a case, computational algorithms must employ the conservative form of the governing fluid equations. For compressible flow models in conservative form, the appropriate thermodynamic independent variables to be chosen for the pressure law closure are the density ρ (or the specific volume $v = 1/\rho$) and the specific internal energy e.

For liquid and vapor water, accurate Equations of State (EoS), having (ρ, e) as independent variable pair, are not available so far. In the last decade, simple EoS such as the Stiffened Gas (SG) one have been adopted for water and other complex fluids. This SG EoS is based on a linearization around a reference thermodynamic state representing the thermodynamic conditions of the numerical simulation. If the thermodynamic conditions of the simulated flow remain close to the reference state, the use of SG EoS can give fairly good results as shown in [70, 173, 233]. However,

[1] IMSIA UMR EDF-CNRS-CEA-ENSTA, Palaiseau, France 91120.
[2] Politecnico di Torino, Torino, Italy 10129
[3] Université Catholique de Louvain (UCL), Louvain la Neuve, Belgium 1348.

for sufficiently large temperature deviations from the reference linearization value, the SG EoS can provide inaccurate results (see the results in [164]) or even unphysical states [231].

For industrial purposes, especially when nuclear safety is involved, fast high-fidelity CFD simulations are needed. The accuracy of a CFD simulation depends on many features often intercorrelated, however, the precision of the thermodynamic properties calculation is independent from the other numerical aspects, therefore, it should be the first feature to deal with. To obtain a realistic evaluation of the thermodynamic properties, simple EoS are not sufficient and experimental EoS have to be employed. However the direct use of such EoS is time consuming.

Furthermore, CFD codes are frequently used, hence calculations must be performed in an efficient way. For the EoS, the requirement of both accuracy and efficiency can be fulfilled by the tabulation of an accurate EoS at the beginning of the simulation and a look-up table interpolation at each time step, for each cell of the simulation domain.

In one-component two-phase transients, metastable phases often appear, thus, the EoS to be tabulated should be valid also in the metastable domain. For water, an EoS that satisfies all the features discussed so far is the Industrial Formulation release (1997) of the International Association for the Properties of Water and Steam (IAPWS), commonly called IAPWS-IF97 [273]. Indeed it is a simplified form of the most accurate EoS today available, that is the IAPWS-95 [272], but contrarily to this release, the IAPWS-IF97 can be easily extrapolated into the metastable domain.

The aim of this paper is to show an efficient and very accurate algorithm to calculate water properties when the independent variables are the density, ρ and the specific internal energy e. For a given thermodynamic pair (ρ, e), we wish to obtain the corresponding pressure, temperature and speed of sound. The main purpose is to couple this algorithm to two-phase flow models in their conservative form. To reach this goal, thermodynamic properties shall be tabulated on the e-v thermodynamic diagram. The best attempt presented in literature is due to Kunick et al. [133, 147], which is a *Guideline* from the IAPWS and is now implemented in RELAP-7 [22, 221]. Here we present an algorithm based on a bicubic look-up table method for both stable and metastable domains. Moreover, the new algorithm for fluid properties calculation is coupled to two common two-phase flow models, the Homogeneous Equilibrium Model (HEM) [56] and the Homogeneous Relaxation Model (HRM) [28], both within the EUROPLEXUS[4] software. Results of simulations are presented for fast depressurization, waterhammer and energy injection problems. For the fast depressurization test, a novel correlation for the relaxation time to return to equilibrium conditions is also proposed.

The paper is organized as follows. In Section 4.2 we describe the homogeneous two-phase flow models that we consider and the type of EoS that is needed for their closure. Section 4.3 is devoted to the possible strategies to be adopted when an EoS as $p = p(\rho, e)$ is required. In Section 4.4, we detail the EoS today available for water focusing on their capability to deal with metastable fluids. We also discuss the need of an equation for the spinodal line in order to detect, during the simulation, if one of the two phases has attained an unstable state ($(\partial p/\partial v)_T > 0$). Section 4.5 illustrates the construction of the tabulated domain on the e-v thermodynamic diagram, the bilinear mapping of the diagram and the bicubic interpolation technique. This section ends with the comparisons between the interpolated values and the exact solution using the IAPWS-IF97. Results of numerical

simulations performed by EUROPLEXUS with the new look-up table algorithm are presented and discussed in the Section 4.6. Some conclusions are written in Section 4.7.

4.2 Homogeneous two-phase flow models

Different models describing two-phase flows are available in the literature. Here we consider compressible flow models that belong to the class stemming from the Baer–Nunziato model [12]. Models in this class differ primarily in the level of non-equilibrium between the two phases that they are able to take into account.

The most complete model of this type is the seven equation model (Baer–Nunziato 1986), which allows pressure, temperature and velocity non-equilibrium between the phases. The simplest one is the Homogeneous Equilibrium Model (HEM) which assumes pressure, temperature and velocity equilibrium. For a brief but comprehensive discussion about various models for two-phase flows, we refer to [233].

One of the main goals of this article is to illustrate the coupling between two-phase flow models and accurate EoS, both in the equilibrium and metastable domains. For this purpose here the simplest two-phase flow models shall be used. In particular, we will employ the HEM model for the simulation of thermodynamically stable mixtures. In water fast transients and in steady-state flashing mixtures, the liquid phase attains the metastable domain evolving beyond its saturated conditions. To extend our analyses to those cases, the Homogeneous Relaxation Model (HRM) can be employed. This model represents the simplest two-phase flow model able to simulate flows of mixtures containing liquid in metastable conditions.

Both the HEM and HRM can be written in a fully conservative form

$$\partial_t \mathbf{U} + \partial_z \mathbf{F}(\mathbf{U}) = \mathbf{b}, \tag{4.1}$$

where $\mathbf{U}$ is the vector of the conservative variables, $\mathbf{F}$ represents the flux vector and $\mathbf{b}$ accounts for the source terms eventually present. To highlight some thermodynamical features of the models, we also write here these models in their quasi-linear form

$$\partial_t \mathbf{U} + \mathbf{A}(\mathbf{U})\partial_z \mathbf{U} = \mathbf{b}, \tag{4.2}$$

where $\mathbf{A}(\mathbf{U})$ is the Jacobian matrix, defined as

$$\mathbf{A}(\mathbf{U}) = \frac{\partial \mathbf{F}}{\partial \mathbf{U}}. \tag{4.3}$$

In the next two subsections, both the HEM and the HRM are analyzed to underline their mathematical properties. Both are hyperbolic models when appropriate thermodynamical constraints are satisfied. The hyperbolicity is discussed in 4.8 and B, respectively.

[4] EUROPLEXUS code is owned by the Commissariat à l'Energie Atomique et aux Energies Alternatives (CEA) and the Joint Research Centre (JRC) of the European Union.

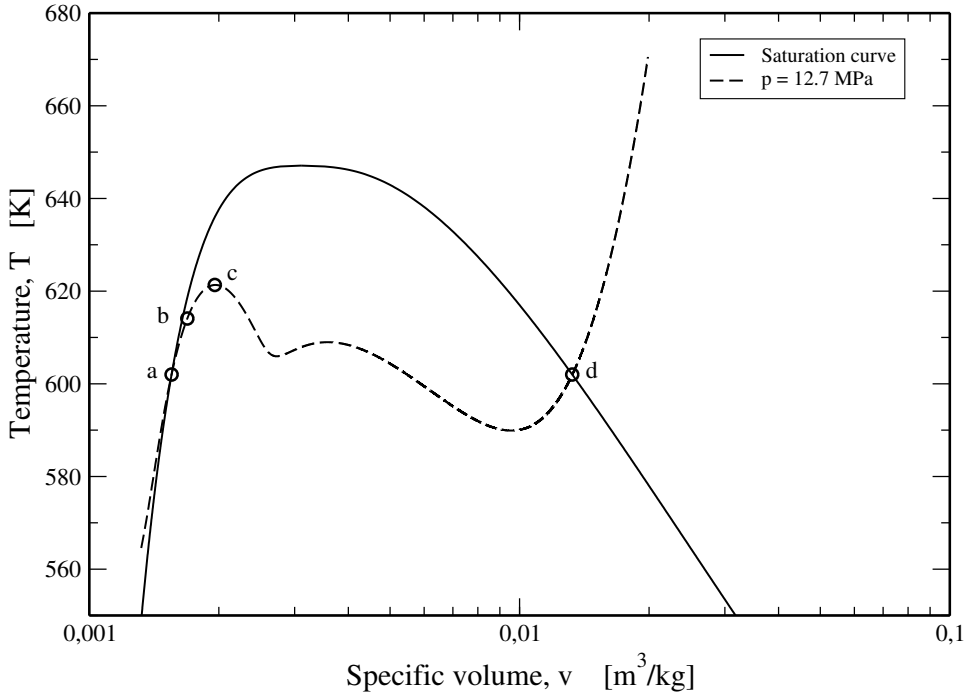

FIGURE 4.1. Isobaric curve on the *T-v* diagram. The plot has been realized using the IAPWS-IF97. The point (a) lies on the liquid saturation curve and represents the thermodynamic state of the liquid phase for the HEM. Point (b) is a metastable state which can represent the state of the liquid phase using HRM. In HRM: $T_l(p) > T_v(p)$. Point (c) is the spinodal limit for the isobaric $p = 12.7 MPa$. In the HRM, the liquid phase cannot overstep this point since the tabulation of the properties is defined until the spinodal line. Therefore, unstable states are not allowed. Point (d) lies on the vapor saturation curve and represents the state of the vapor phase for both HEM and HRM.

4.2.1 Homogeneous Equilibrium Model

The Homogeneous Equilibrium Model (HEM) is a set of partial differential equations that governs the motion of the total mass, the global momentum and the total energy of a mixture in full equilibrium. In spite of its simplicity, this model is extensively used for numerous industrial applications. For instance, to simulate heat exchangers (e.g., [211]), for calculating the mass flow rate of critical two-phase flows [237] and even for the analysis of an hypothetical Loss Of Coolant Accident (LOCA) in nuclear power plants [105]. Generally, the HEM is particularly well adapted for the simulation of dispersed bubbly flow [56]. The drawbacks of this model are well known: it cannot reproduce mechanical or thermodynamic non-equilibrium, typical of annular flows and fast depressurizations, respectively. If the deviation from equilibrium is moderate, correction terms can be used (drift flux velocity, subcooled boiling models). However when non-equilibrium effects are more important, additional equations are needed for an accurate prediction of the flow physics.

Notwithstanding, HEM has good mathematical properties which make it suitable for the simulation of wave motions, hence, fast transients.

We shall consider a mixture made of the liquid and vapor phases of one-component in full thermodynamic equilibrium. The HEM system has formally the structure of the single-phase Euler system. In one-dimensional geometry, the HEM equations are:

$$\begin{cases} \partial_t \rho + \partial_z(\rho u) = 0, \\ \partial_t(\rho u) + \partial_z(\rho u^2 + p) = 0, \\ \partial_t(\rho E) + \partial_z[(\rho E + p)u] = 0. \end{cases} \tag{4.4}$$

The notation is the classical one: ρ is the mixture density, u denotes the velocity of the mixture, p is the pressure, and E is the specific total energy, i.e., $E = e + u^2/2$, where e is the specific internal energy of the mixture.

This is a system of non-linear hyperbolic conservation laws that governs the dynamics of a compressible fluid for which the effects of body forces, viscous stresses and heat flux are neglected. However, for more realistic simulations these phenomena can be taken into account as source terms, i.e. as contributions to the vector **b** of Eq. (4.1).

The thermodynamic equilibrium assumptions of the HEM are:

$$\begin{aligned} p_l &= p_v = p, \\ T_l &= T_v = T_{sat}(p), \\ u_l &= u_v = u, \\ g_l &= g_v = g, \end{aligned} \tag{4.5}$$

where subscripts l and v indicate, respectively, the liquid phase and the vapor one, and where g denotes the Gibbs free enthalpy. The closure laws are:

$$\begin{aligned} e &= x\,e_v(p) + (1-x)\,e_l(p), \\ v &= x\,v_v(p) + (1-x)\,v_l(p), \end{aligned} \tag{4.6}$$

where the specific volume is $v = 1/\rho$ and the quality is $x = \frac{mass\ of\ vapor}{total\ mass}$. With the constraints expressed in Eq. (4.5), the internal energies and the specific volumes of vapor and liquid are those of the saturation curve. That is:

$$e_v = e_g(p_{sat}), \qquad e_l = e_f(p_{sat}), \qquad v_v = v_g(p_{sat}), \qquad v_l = v_f(p_{sat}), \tag{4.7}$$

where subscripts f and g indicate, respectively, the saturated liquid and the saturated vapor. Refer to Fig. 4.1 for a graphic illustration.

In HEM, the flow quality x corresponds to the thermodynamic quality:

$$x = \frac{mass\ of\ vapor}{total\ mass} = \frac{h - h_f}{h_g - h_f}, \tag{4.8}$$

where the enthalpy is $h = e + pv$.

The system of Equations (4.4) is not closed, there are three equations and four unknowns. To close the system, an additional equation must be supplied that links the pressure to the other

thermodynamic variables. Let us consider the *caloric equation of state* with the pair (p, ρ) as independent variables:

$$e = e(p, \rho). \tag{4.9}$$

We are looking for its inverse:

$$p = p(\rho, e). \tag{4.10}$$

As we stressed before for many fluids like water, an accurate EoS expressed in the form of Eq. (4.10) is not available. In the next section we shall discuss various approaches to evaluate the pressure for a given pair of values of specific volume and specific internal energy.

Let us note that a complete description of the thermodynamic conditions of the flow requires an additional relation, the *thermal* equation of state:

$$T = T(p, \rho). \tag{4.11}$$

However, only the caloric EoS is needed to solve the system of equations (4.4). Choosing a thermal EoS does restrict the choice of a caloric EoS but does not determine it.

The behavior of the speed of sound that characterizes the HEM with respect to the vapor volume fraction α_v is depicted in Fig. 4.2. The expression of the speed of sound is reported in 4.8. It has to be noted that the speed of sound of the HEM has two discontinuities for $\alpha_v = 0$ and $\alpha_v = 1$. In fact, one of the main characteristics of the equilibrium equations of state is the presence of a "kink" (discontinuity in the derivatives) along the saturation curve. The discontinuities in the speed of sound have been referred to as unphysical by several authors [109, 141, 188, 248].

4.2.2 Homogeneous Relaxation Model

At the beginning of Section 4.2 we pointed out the existence of a hierarchy of two-phase flow models based on the level of non-equilibrium that they are able to take into account. In certain fast transients of one-component mixtures it is crucial to take into account thermal and chemical non-equilibrium, that is the temperature and Gibbs free enthalpy difference between vapor and liquid. For instance, in depressurizations of subcooled liquids, the pressure evolves very quickly and the liquid becomes metastable due to the finite vaporization rate. Experimental evidences of this phenomenon are reported in [16, 223].

The simplest conservative two-phase flow model that accounts for thermal and chemical non-equilibrium is the Homogeneous Relaxation Model (HRM). The HRM system consists of the mixture Euler equations augmented with a mass equation for one phase with a relaxation source term for the flow quality (see Eq. (4.13)).

An important feature of HRM is the assumption that the vapor phase is always at saturation conditions. Note that this model is different from the 4-equation relaxation model of Flåtten et al. [109], which accounts for chemical non-equilibrium but assumes thermal equilibrium. These different assumptions are reflected in the definition of the relaxation source term and closure relations. Let us also remark that other models such the 5-equation Kapila model [139] or the 6-equation model [200, 234] allow the description of non-equilibrium phenomena, however these models are more difficult to handle numerically due to the presence of non-conservative terms in

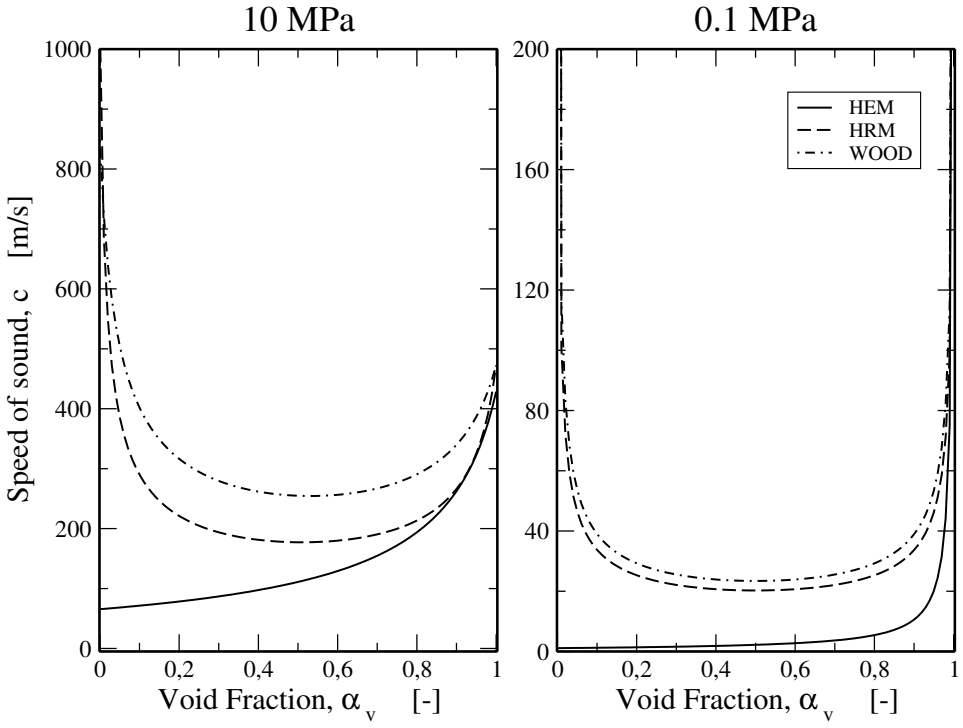

FIGURE 4.2. Mixture speed of sound for water for HEM, HRM and Wood's relation [279]. The plot on the left is at 10 MPa whereas the one on the right is at 0.1 MPa (magnified view). It has to be noted that the speed of sound of the HEM has two discontinuities for $\alpha_v = 0$ and $\alpha_v = 1$, as discussed in 4.8.

the hyperbolic portion. To better enlighten the novel contribution of this article, we preferred here to adopt the simpler HRM, which can describe metastable liquids without the need to address numerical difficulties related to non-conservative products. This is a coherent choice since in the fast transient flow problems here considered the processes related to the metastable states of liquid are crucial. Moreover, using the IAPWS EoS, the description of the properties of the subcooled vapor (metastable with respect to liquid) is complicated since there are no experimental data for its thermodynamic properties [272].

The governing equations of the HRM, in one dimension, are:

$$\begin{cases} \partial_t(\alpha_v \rho_v) + \partial_z(\alpha_v \rho_v u) = \Gamma_{l\to v}, \\ \partial_t \rho + \partial_z(\rho u) = 0, \\ \partial_t(\rho u) + \partial_z(\rho u^2 + p) = 0, \\ \partial_t(\rho E) + \partial_z[(\rho E + p)u] = 0. \end{cases} \tag{4.12}$$

To be able to relax the thermal equilibrium constraint, the mass transfer between the two phases is different with respect to the one of a mixture at saturation conditions. The mass transfer is modeled by means of a source term, $\Gamma_{l\to v}$, which appears on the right hand side in the equation of the mass balance of the vapor phase of Eq. (4.12). This source term tends to relax the current

vapor mass fraction to the equilibrium mass fraction introducing a certain delay for the liquid vaporization:

$$\Gamma_{l\to v} = -\rho \frac{x - x_{eq}}{\Theta}, \tag{4.13}$$

where x_{eq} is the equilibrium quality.

HRM has good mathematical properties for numerical approximation purposes, due to the absence of non-conservative terms. In fact, excluding source terms, this model is under full conservative form. Details about the mathematical properties of the HRM are discussed in [6, 28, 104]. Moreover, HRM also has consistent physical properties in terms of wave propagation. As we can see in Fig. 4.2, in the two-phase domain, the speed of sound for the HRM is continuous and has the same non-monotonic behavior of the well known Wood's speed of sound [279] (which is also the sound speed that characterizes the Kapila 5-equation model). Such a well-known non-monotonic behavior for the mixture sound speed has been experimentally verified by several authors in the literature [118, 140]. Let us note that the curve of the sound speed of the HRM always lays below the curve of the Wood's sound speed, and above the curve of the sound speed of the HEM. This is consistent with the well-known sub-characteristic condition [172] that requires that the sound speed associated to a two-phase flow model is reduced whenever an additional equilibrium is assumed [109]. We observe that the magnitude of the speed of sound of the HRM can be remarkably different with respect to Wood's speed of sound. This difference is smaller at low pressures.

The HRM of Bilicki & Kestin [28, 29, 84] (conversely to [109] and other 4-equation models) for one-component two-phase flows assumes:

$$\begin{aligned} &p_l = p_v = p, \\ &T_l \neq T_v = T_{sat}(p), \\ &u_l = u_v = u. \end{aligned} \tag{4.14}$$

With the relaxations expressed in Eq. (4.14), the internal energies and the specific volumes of vapor are the ones corresponding to the saturation curve. Whereas, for the liquid phase, they are in the metastable region of the superheated liquid, namely, along the isobaric line crossing the vapor saturation curve in (v_g, e_g). Further explanations are reported on Fig. 4.1. Summarizing, we have:

$$e_v = e_g(p), \qquad e_l \neq e_f(p), \qquad v_v = v_g(p), \qquad v_l \neq v_f(p). \tag{4.15}$$

Since in general thermal equilibrium does not hold, the flow quality, x, does not correspond to the thermodynamic quality, i.e.

$$x = \frac{mass\ of\ vapor}{total\ mass} \neq \frac{h - h_f}{h_g - h_f}. \tag{4.16}$$

Another useful relation, obtained from the first two equations of Eq. (4.12), gives the flow quality, or the mass fraction, x:

$$x = \frac{\alpha_v \rho_v}{\rho}. \tag{4.17}$$

This is a relation between the volumetric and mass fractions occupied by the vapor phase.

The closure laws, for Eq. (4.12), are

$$\begin{aligned} e &= x\,e_v(p) + (1-x)\,e_l(p,T_l), \\ v &= x\,v_v(p) + (1-x)\,v_l(p,T_l). \end{aligned} \tag{4.18}$$

Similarly to the HEM, an equation for the pressure is needed. With respect to the HEM, here, the flow quality is a variable needed for the evaluation of the mixture pressure. Then, the pressure law for the HRM has the form:

$$p = p(x,v,e). \tag{4.19}$$

4.3 Steam-water EoS for two-phase models

As seen in the previous section, an EoS to determine the pressure is needed to close the systems of equations (4.4) and (4.12). There are three ways to achieve this goal: to use a simple equation of state, to employ an iterative algorithm adopting an accurate EoS or to use tabulated values.

Generally, simple EoS allow fast properties calculations but they are not accurate and sometimes provide unrealistic results. Hence accurate EoS should be used for reliable simulations, as especially demanded in an industrial context. Iterative algorithms for this type of EoS are time consuming, therefore, these EoS are often used in tabulated forms.

Let us detail further these three options in the next paragraphs.

4.3.1 Use of a simple caloric EoS

The behavior of a single-phase fluid or a mixture could be described by a simple analytical law. Historically, EoS have always been formulated in a thermal form, but for very simple thermal EoS, it is straightforward to obtain a relation as $p = p(\rho, e)$. However, as the complexity of the thermal form increases, it becomes practically unfeasible to get the corresponding $p = p(\rho, e)$. The simplest modelling approach is to assume that a fluid behaves as a *perfect gas*:

$$p = (\gamma - 1)\rho e, \tag{4.20}$$

where $\gamma = c_p/c_v$ is the heat capacity ratio. However this equation is not adapted for stiff fluids such as water.

A very simple generalization of the ideal-gas thermal EoS is the *covolume EoS*, also called Clausius-Noble-Able EoS:

$$p = \frac{(\gamma - 1)\rho e}{1 - b\rho}, \tag{4.21}$$

where b is the covolume and tries to take into account the volume occupied by the molecules themselves.

Historically, one of the most important EoS, in physics, has been the *Van der Waals EoS*:

$$p = \frac{RT}{v - b} - \frac{a}{v^2}. \tag{4.22}$$

The last term accounts for the forces of attraction between molecules. Using a cubic EoS, the hyperbolicity of the Euler system of equations cannot be ensured because of the well-known drawback

of the positive isothermal compressibility, i.e. $(\partial p/\partial v)_T > 0$, in the two-phase domain. Indeed, in the unstable domain enclosed by the spinodal curve, the square of the speed of sound may become negative and wave propagation has no physical sense [181].

In other words, using a cubic EoS, in the metastable domain, the return to equilibrium corresponds to a thermodynamic transformation. However, to preserve the hyperbolicity of the Euler equations, we are interested in a *kinetic process*, as explained in [233], which does not lead to an imaginary speed of sound. To follow a kinetic process, a widely used EoS is the *stiffened gas EoS* (SG-EoS). It is suitable for stiff fluids such as water, since it is the linearization of the Mie-Grüneisen EoS which was initially developed for solids. It reads:

$$p = (\gamma - 1)(e - q)\rho - \gamma P_\infty, \tag{4.23}$$

where γ, P_∞, q are constants to be determined.

The SG-EoS cannot be considered a globally-valid EoS. First of all, it is based on a linearization of fluid properties, therefore, it does not hold in the highly non-linear regions of the thermodynamic diagram as in the neighborhood of the critical point or close to the spinodal curve. Furthermore, the linear nature of this EoS does not allow one to accurately calculate first-order derivatives of thermodynamical properties, such as the speed of sound, c.

Secondly, depending on choices made to determine the constant q, this EoS may not exhibit a spinodal curve. This feature is in disagreement with both theory and experiments [73, 93, 170, 245].

Several authors in the literature have shown that this EoS is appropriate for some test problems, including some industrial test cases [70, 173]. However, since its parameters are defined around a reference state, a sufficiently large temperature change could lead to an erroneous evaluation of the thermodynamic properties (see the results in [164]). For instance, such an EoS is not suitable for the simulation of energy injection transients, whereas, the tabulation method proposed here is valid for any test.

4.3.2 Use of an iterative algorithm for an accurate EoS

A way to accurately evaluate water properties is to use experimental EoS. In the case of water, the large availability of experimental data allowed the formulation of a certain number of equations which have been adopted as International Standards. EoS of this type have been adopted for the present work and they will be discussed more in detail in Section 4.4.

Generally, accurate EoS are expressed as:

$$f = f(\rho, T) \qquad \text{or} \qquad g = g(\rho, T), \tag{4.24}$$

where: $f = u - Ts$ and $g = h - Ts$ are, respectively, the Helmholtz free energy and the Gibbs free enthalpy. Such EoS are very accurate but extremely costly from a computational point of view. For industrial purposes, to reduce the computational time, we have:

$$f = f(p, T) \qquad \text{or} \qquad g = g(p, T). \tag{4.25}$$

These EoS are also called Industrial Formulation EoS. Such accurate EoS are composed by many terms, even few hundreds. Generally, their terms come from a best fit of a huge amount of experimental data, as we shall discuss in Section 4.4. From such a cumbersome EoS, it is not feasible to get an equation in the form: $p = p(\rho, e)$.

However, those EoS can be coupled to the Euler system of equations by using an iterative algorithm. More specifically, the EoS is a non-linear equation to be solved. Details are given in 4.10.

Kunick et al. [133, 147] made a comparison between the iterative inversion of the IAPWS-IF97 and the look-up table interpolation. The iterative procedure is hundreds of times slower than the interpolation.

4.3.3 Look-up table interpolation

In order to have accurate fluid properties evaluations, the time consuming iterative procedure for the EoS could be employed at the beginning of the computation to create a table to be used during the CFD simulation. This method is generally called *look-up table interpolation* of the fluid properties. Even though such a strategy is widely used in many CFD codes [44, 220, 224, 260, 263], most of these codes still use iterative procedures for the pressure calculation because the tabulation of water properties is done with respect to the variable pairs: (p,T), (p,h), (p,s), (p,e) or (T,v).

In order to avoid costly iterative procedures, at least into the single-phase domain, iterative algorithms (see 4.10) could be employed at the beginning of the calculation on a fairly wide number of couples (v,e), so that, during the CFD calculation, pressure, temperature and speed of sound may be evaluated just by interpolation. Therefore, the requirements of both accuracy and efficiency are fulfilled. For such strategy, the best attempt presented in literature belongs to Kunick et al. [133, 147]. In the two-phase domain, the calculation may be still iterative, but the saturation curve can be discretized as a conjunction of splines, easy to handle and at the same time sufficiently accurate and rapid.

A further beneficial feature of the tabulation strategy on the e-v diagram is that we know in advance if a pair (v,e) belongs to the single phase or to the two-phase domain.

In Section 4.5.1 we show an alternative technique to [133, 147], based on bicubic interpolations. Moreover, with the goal of simulating fast transients, the tabulation has to be extended into the metastable domain of water, as has been done in RELAP-7 [22]. Here, this extension is done up to the assumed spinodal curve.

4.4 IAPWS-IF97 and the representation of the liquid spinodal curve

Nowadays the most reliable EoS for water is the IAPWS-95 [272]. It replaced the formulation of Haar et al. [121], which was the adopted international standard since 1984 and still widely used within many codes for Nuclear Safety. The IAPWS-95 is an analytical equation based on a multi-parameter fit of all the experimental data, used for general and scientific purposes. The formulation

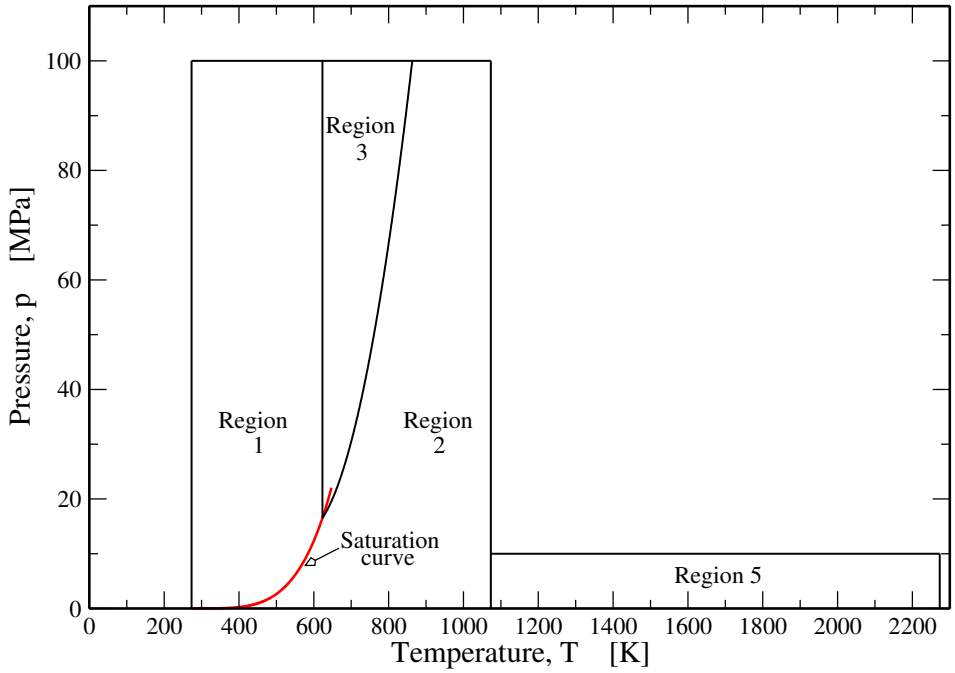

FIGURE 4.3. Region subdivision of the IAPWS-IF97 on the p-T diagram. Region 4 represents the saturation curve.

is a fundamental equation for the specific Helmholtz free energy, f, expressed in dimensionless form. Appropriate combination of derivatives can produce any desired thermodynamic property.

This formulation behaves reasonably also when extrapolated into the metastable domain [272]. However, it is rather difficult to find a formulation indicating the spinodal curve since it exhibits several stiff minima (also called *Marianna Trench*) and stiff maxima (said *Himalaya*) along an isotherm [132].

Because the IAPWS-95 formulation is quite cumbersome and time consuming, IAPWS also maintains a separate formulation recommended for industrial use. It is the IAPWS-IF97 [273], which replaced the IFC-67 [135]. The IAPWS Industrial Formulation 1997 consists of a set of equations for five different regions, each of them is covered by a simple *basic equation* fitting the values resulting from the IAPWS-95.

In this work we have adopted the IAPWS-IF97 for three reasons:

- IAPWS-IF97 is more suitable for the calculation of the spinodal curve, since there are no stiff minima or maxima along isotherms, which instead characterize the IAPWS-95, as discussed above;

- IAPWS-IF97 has an *ad hoc* formulation for the metastable vapor region which involves a low-density gas equation that is considered to be more adequate than IAPWS-95 (see [134]). This choice has been made in view of future work based on the hyperbolic 6-equation model of [200, 234] which would use both metastable liquid and vapor. In the current work, however, metastable vapor states are not considered because HEM and HRM do not need them;

- The discrepancy between the IAPWS-IF97 and the IAPWS-95 is very small [273].

The region subdivision adopted for IAPWS-IF97 is reported in Fig. 4.3.

In addition, IAPWS also provided some *backward equations* to make the calculation of properties faster. However, they are not used in the work presented in this paper, because they are not as accurate as the basic equations.

The entire set of equations originally covered the following range of validity:

$$\begin{aligned} 273.15K \leq T \leq 1073.15K \qquad & p \leq 100MPa, \\ 1073.15K \leq T \leq 2273.15K \qquad & p \leq 10MPa. \end{aligned} \tag{4.26}$$

The subdivision of the entire domain in different regions allows an efficient property computation, even if still too slow for CFD calculations. The IAPWS-IF97 also deals with metastable states, providing reasonable values when extrapolated. Last but not least, the basic equation of Region 3 allows one to easily define a spinodal curve (see Fig. 4.4, 4.6).

All the features discussed here motivated the authors to adopt the IAPWS-IF97 for the tabulation on the *e-v* diagram.

4.4.1 Spinodal and saturation curve for water

From thermodynamics, it is well known that a closed system attains a maximum value of entropy at equilibrium [43]. Hence, the criteria for equilibrium and stability can be expressed as:

$$\begin{aligned} &\delta S = 0 && && \textit{criterion of equilibrium}, \\ &\delta^n S < 0, && \text{for the smallest } n \text{ at which } \delta^n S \neq 0 && \textit{criterion of stability}. \end{aligned} \tag{4.27}$$

Further developments of the last criterion provide two conditions which ensure the stability of a system:

$$\begin{aligned} c_v > 0 \qquad & \textit{criterion of thermal stability}, \\ \left(\frac{\partial p}{\partial v}\right)_T < 0 \qquad & \textit{criterion of mechanical stability}. \end{aligned} \tag{4.28}$$

If both are satisfied, the system is *intrinsically stable*. The criterion of thermal stability is satisfied for all the EoS developed so far, whereas the fulfillment of the mechanical stability criterion is not always ensured. As discussed in Section 4.3.1, cubic EoS satisfy the mechanical stability condition until the so-called spinodal line. The spinodal line separates the unstable domain from the stable/metastable one. In classical thermodynamics phase transition occurs at saturation conditions, on the contrary, in real systems an isothermal pressure change would very likely carry the state point into the metastable domain. The deeper the metastability reached, the higher is the probability for the phase change to occur. The spinodal curve is the limit beyond which phase change has already occurred.

The liquid and vapor spinodal lines connect all the minima of the isotherms (*liquid spinodal*) and all the maxima (*vapor spinodal*) closest to the associated side of the saturation curve within the saturation dome. In these minima and maxima points isotherms have zero slope (see Fig. 4.1, 4.6), hence, spinodal lines mark the location from where the mechanical stability condition is violated.

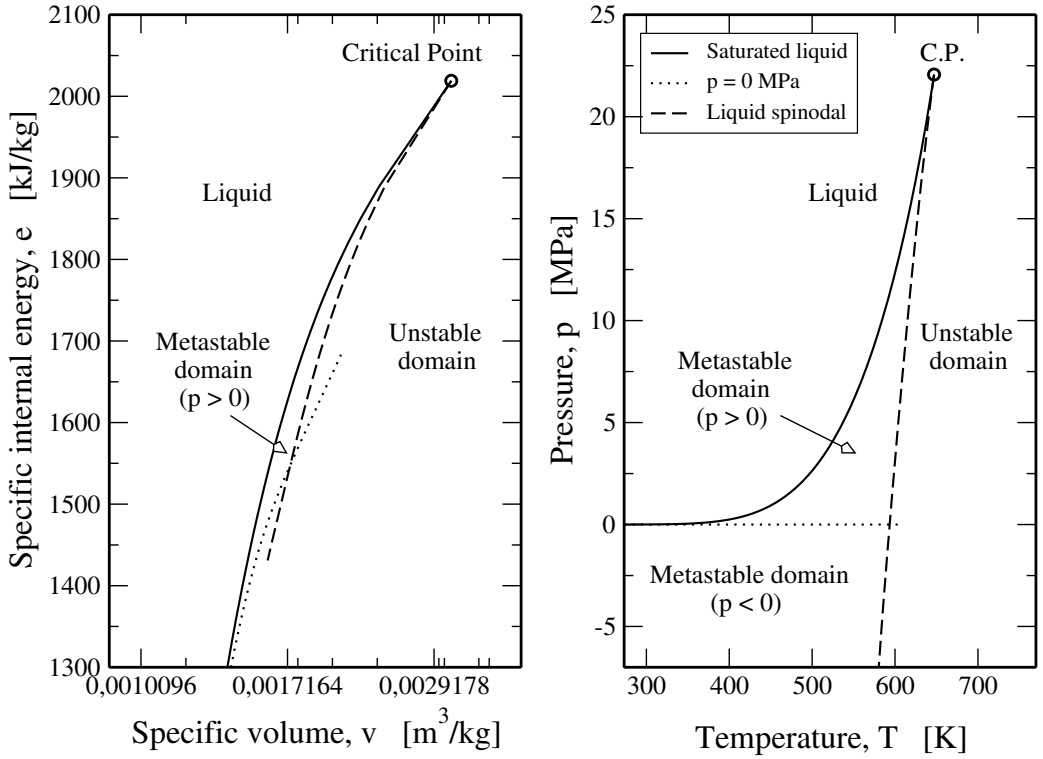

FIGURE 4.4. Metastable domain considered in this work. In both the e-v and p-T thermodynamic planes, the saturated liquid curve, the liquid spinodal and the isobaric of 0 MPa are represented. The unstable domain represents the states where the mechanical stability condition is violated (Eq. (4.28). Below the intersection between the spinodal and the isobaric at $p = 0\ MPa$, the metastable domain refers to negative pressures. Authors decided to restrict the tabulation of the thermodynamic properties just on the metastable states at positive pressure.

In the present work, the spinodal curve has been determined by setting to zero $(\partial p/\partial v)_T$ to detect the limit of the mechanical stability. The resulting spinodal curve agrees with other curves presented in the literature as shown in Fig. 4.5. The curve $(\partial p/\partial v)_T = 0$ has been defined using an optimized Newton-Raphson algorithm [212]. To this end, the basic equation of Region 3 (Fig. 4.3) was used, even slightly below the temperature of $623.15K$ which indicates the boundary between Region 1 and 3. As shown in Fig. 4.6, this choice provides accurate results even when the extrapolation is done below the limit temperature.

Such strategy revealed that the spinodal corresponds to positive values of the pressure until $T \approx 593.50K$. Below this temperature, the limit of mechanical stability corresponds to negative pressures. The constraint of a positive pressure holds for a gas or vapor, but not for a liquid. Negative pressures can be reached by depressurizing a liquid isothermally below its saturation pressure. The possibility for a liquid to be at negative pressure means that it possesses a tensile strength. At equilibrium, water and other liquids do not support an externally applied mechanical tension. They can resist to it in a thermodynamically metastable state, resulting in a negative pressure. The laboratory study of liquids under tension has a long history and the literature abounds with

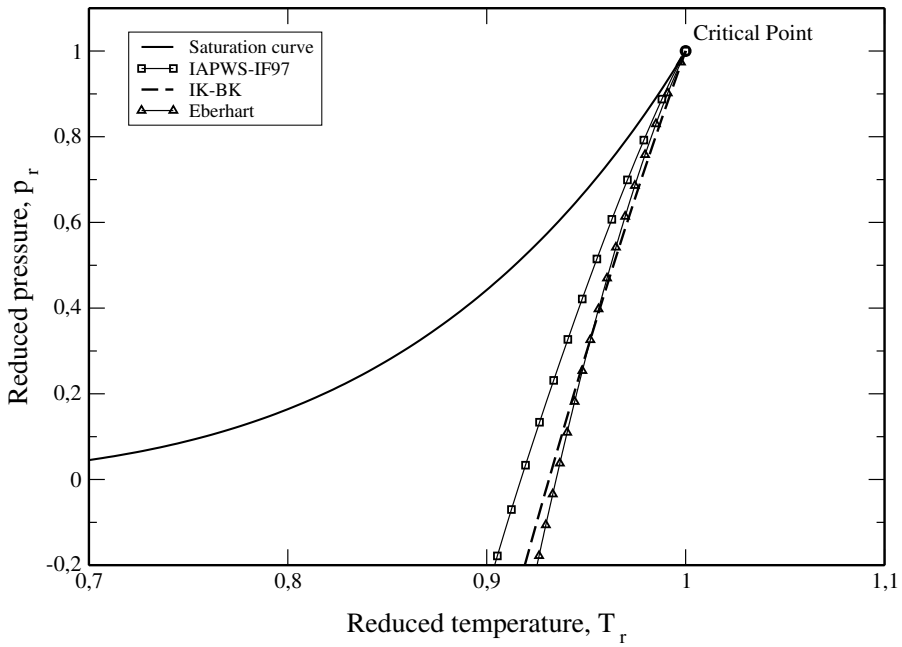

FIGURE 4.5. Trend of spinodal curves on the *p-T* diagram from different formulations. The one determined in this work (labeled as *IAPWS-IF97*) agrees with the other ones proposed in literature [93, 132].

discussions on this subject (e.g. [49, 73, 132, 143, 170, 245, 284]).

However, in this work we limited the tabulation to positive values of the pressure, choosing the isobaric at $p = 0\ MPa$ as border of the metastable domain for temperatures lower than $T \approx 593.50 K$. See Fig. 4.4 for a more effective understanding.

Regarding the saturation curve, the equilibrium criterion is ensured by the equality of Gibbs free enthalpy for the two phases: $g_l = g_v$. Along an isotherm, the Gibbs-Duhem equation between the two saturated states reduces to:

$$g_v - g_l = \int_l^v v dp. \tag{4.29}$$

Then, the saturation curve, $p_{sat}(T)$, can be constructed by requiring the vanishing of Eq. (4.29). The IAPWS-IF97 provides a suitable basic equation that relates saturation pressure and temperature. This simple relation to define the saturation states has been adopted herein.

4.5 Look-up table method for thermodynamic properties evaluation on the *e-v* diagram

Fluid properties calculation during CFD simulations should be as fast as possible, and, at the same time, highly accurate. A look-up table method can meet these requirements through the use of simple interpolation techniques to determine the thermodynamic properties. The Euler equations and mixture model systems for compressible flows such as the ones considered in this paper require a closure law of the form $p = p(\rho, e)$, consequently the best approach is to tabulate the required

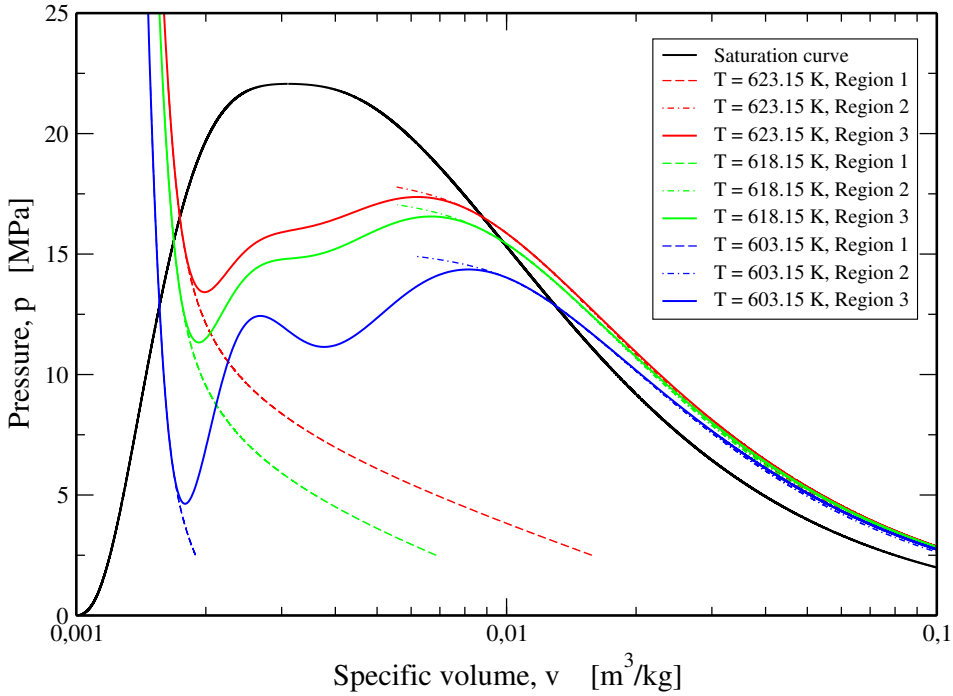

FIGURE 4.6. Isotherms on the p-v diagram calculated at three different temperatures according to three basic equations of state from IAPWS-IF97. The basic equation of region 3 provides accurate results even when extrapolated in metastable region at $T < 623.15\ K$.

properties on a e-v diagram. Such a diagram is quite uncommon in the literature, hence Fig. 4.7 and 4.8 should make the reader more familiar with the behavior of properties in the considered thermodynamic plane.

In this section we present the property evaluation method that has been coupled to the HEM and HRM in the EUROPLEXUS code.

4.5.1 Grid Construction on e-v diagram and bicubic interpolation

The physical domain can be discretized by using a sufficiently high number of nodes. For easiness, the irregular physical domain, e-v, has been transposed in Cartesian transformed domain, Y-X. This feature is depicted in Fig. 4.9.

The physical domain has been mapped as follows. In the liquid and supercritical domain we imposed an equidistant pattern of nodes, hence the distribution is linear, whereas, in the vapor domain the node distribution is logarithmic. Handling such a regular distribution of nodes ensures that, the cell (i, j) containing the point can be immediately found:

$$i = int\left(\frac{Y_0 - Y_{min}}{\Delta Y}\right), \qquad j = int\left(\frac{X_0 - X_{min}}{\Delta X}\right), \tag{4.30}$$

where X and Y are the coordinates on the transformed space. i and j are the indices of the cells along the Y and X directions, respectively. Such a feature is very beneficial in terms of computational

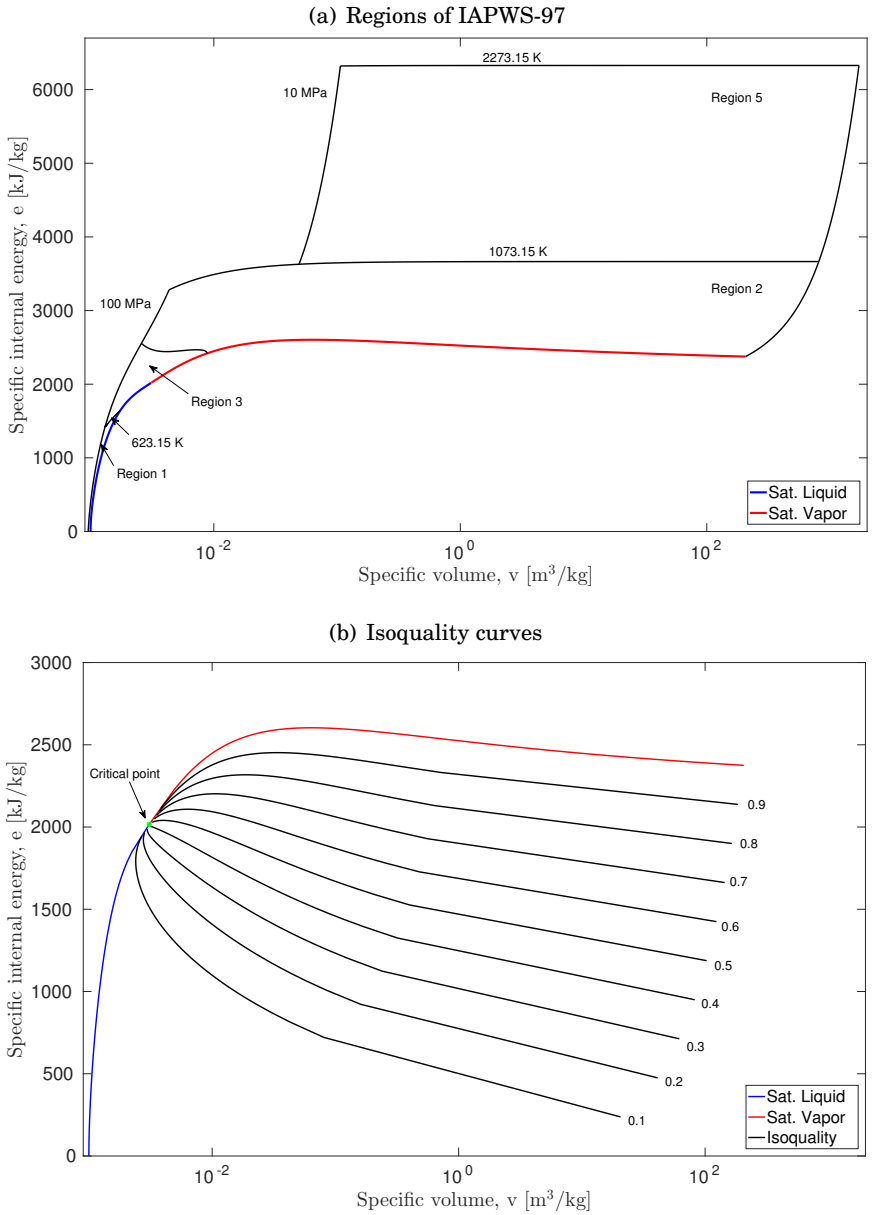

FIGURE 4.7. Thermodynamic diagram *e-v*. (a) reports the region subdivision of the IAPWS-IF97 already illustrated in Fig. 4.3. In (b) we show the trend of the isoquality curves in the two-phase domain. The thermodynamic domain on the *e-v* plane is highly irregular, hence, particular attention is demanded for the node distribution.

time. Then, a *bicubic interpolation* is performed on the Cartesian diagram *Y-X*, using stocked values on the *e-v* diagram.

In [133], the interpolation was a spline based one, hence the coefficients of spline polynomials were determined by providing values of the exact derivatives just at the outer boundary of the grid. Then, constraints were imposed to ensure the continuity of first derivatives throughout the boundaries of the cells of the *e-v* plane.

Differently from [133], here a bicubic interpolation is performed. Thus, the values of the deriva-

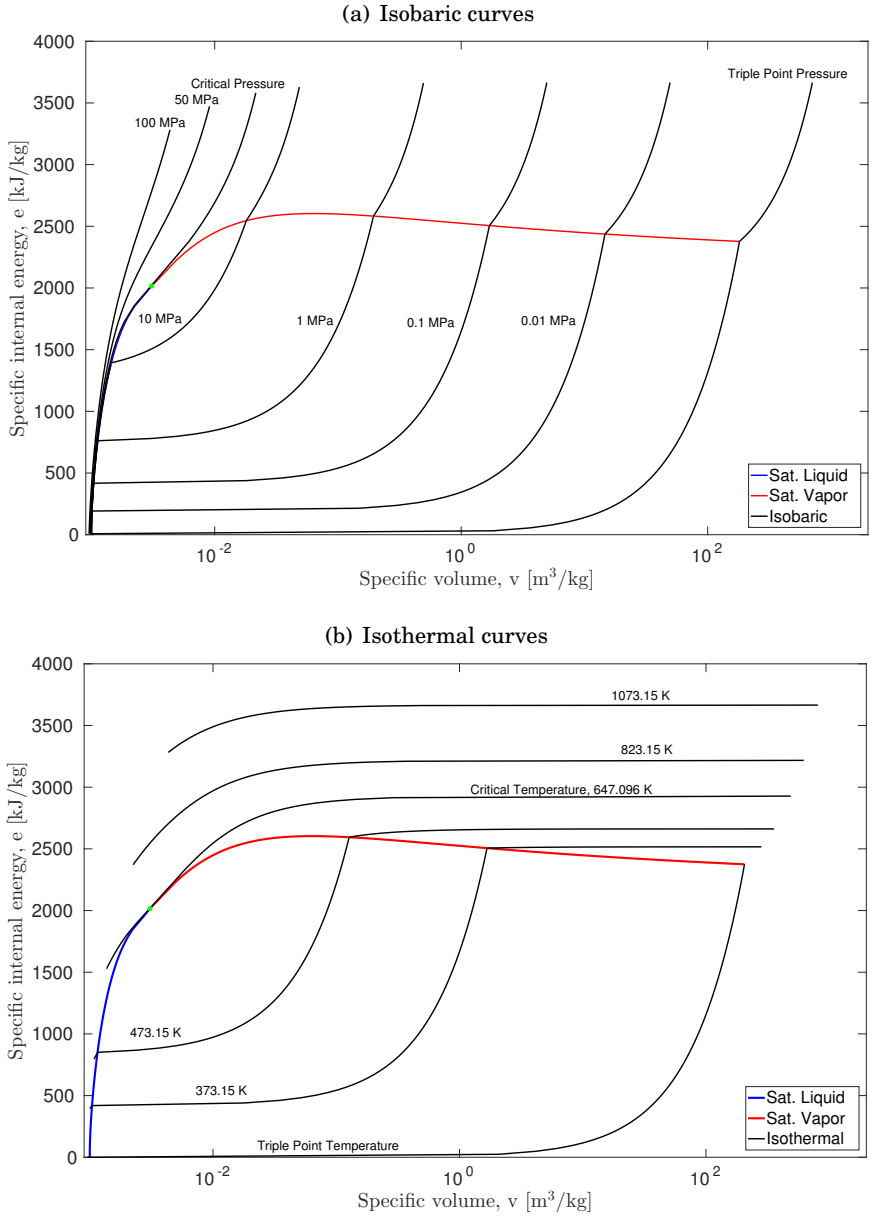

FIGURE 4.8. Thermodynamic diagram e-v. In (a) we can see the isobaric curves in the liquid domain (bottom left corner), two-phase domain and vapor region until $T = 1073.15\ K$. (b) depicts the isothermal curves.

tives are provided in each node of the grid. The bicubic interpolation for the pressure calculation is the object of the following section.

4.5.2 Bicubic interpolation

To perform a bicubic interpolation, the cell must be square. For a given non-uniform quadrilateral on the e-v diagram, its transformation onto a regular cell of an arbitrary Y-X diagram is required. Let us rescale the coordinates Y-X in order to have a square cell of unit length.

The goal is to construct a function such as $(v,e) = \Phi(X,Y)$, where $X \in [0,1]$ and $Y \in [0,1]$, which

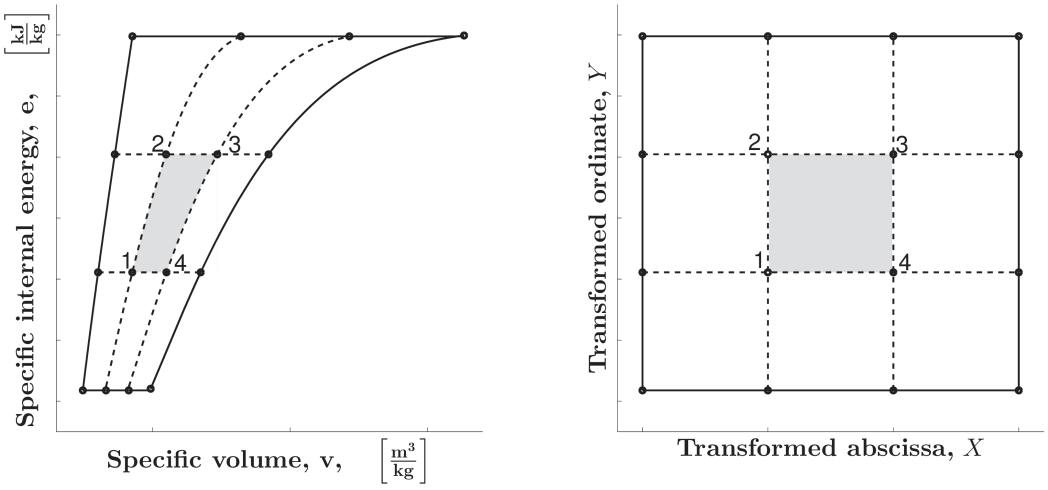

Figure 4.9: Grid of nodes in the physical domain and in the transformed one

describes the entire point space enclosed by the quadrilateral cell. This function, yet to be determined, forms a map that allows us to transform the quadrilateral cell, that is:

$$\Phi : \mathbb{R}^2 \to \mathbb{R}^2 \qquad \text{such that:} \quad \forall (v,e) \in \mathscr{D} \Rightarrow (X,Y) \in \mathscr{D}', \tag{4.31}$$

where $\mathscr{D}$ is the physical domain and $\mathscr{D}'$ the transformed one. The chosen mapping function, fulfilling the requirements of the expression in (4.31), is a *bilinear mapping* [128, 228], that is:

$$v = \alpha_1 + \alpha_2 X + \alpha_3 Y + \alpha_4 XY, \tag{4.32}$$

and

$$e = \beta_1 + \beta_2 X + \beta_3 Y + \beta_4 XY. \tag{4.33}$$

Setting the vertices of the irregular quadrilateral cell on the e-v plane to be the vertices of the unit length square of the transformed space, the α_i, β_i coefficients can be obtained. The indicators i are distributed in the clockwise direction starting from the node in the bottom left corner. The coefficients are calculated solving

$$\begin{bmatrix} 1 & 0 & 0 & 0 \\ 1 & 0 & 1 & 0 \\ 1 & 1 & 1 & 1 \\ 1 & 1 & 0 & 0 \end{bmatrix} \begin{bmatrix} \alpha_1 \\ \alpha_2 \\ \alpha_3 \\ \alpha_4 \end{bmatrix} = \begin{bmatrix} v_1 \\ v_2 \\ v_3 \\ v_4 \end{bmatrix}. \tag{4.34}$$

A similar expression can be written for the relation between e_i and β_i. Finally, in a general framework:

$$\alpha_1 = v_1, \quad \alpha_2 = -v_1 + v_4, \quad \alpha_3 = -v_1 + v_2, \quad \alpha_4 = v_1 - v_2 + v_3 - v_4, \tag{4.35}$$

$$\beta_1 = e_1, \quad \beta_2 = -e_1 + e_4, \quad \beta_3 = -e_1 + e_2, \quad \beta_4 = e_1 - e_2 + e_3 - e_4. \tag{4.36}$$

Given that the grid is formed by horizontal iso-e lines: $\beta_2, \beta_4 = 0$.

During a numerical simulation, the couple (v_0, e_0) must be transformed into the point (X_0, Y_0). That is, the system formed by Eq. (4.32) and (4.33) should be solved. This system is non-linear

but simple enough to be solved analytically. In fact, Y_0 is the solution of the following quadratic equation:

$$aY_0^2 + bY_0 + c = 0, \tag{4.37}$$

for $\beta_2, \beta_4 = 0$, the coefficients are

$$\begin{aligned} a &= \alpha_4\beta_3, \\ b &= \alpha_4(\beta_1 - e_0) + \alpha_2\beta_3, \\ c &= \alpha_2(\beta_1 - e_0). \end{aligned} \tag{4.38}$$

The physical solution is:

$$Y_0 = \frac{-b + \sqrt{b^2 - 4ac}}{2a}. \tag{4.39}$$

Once Y_0 is known, it is straightforward to find X_0 :

$$X_0 = \frac{v_0 - \alpha_1 - \alpha_3 Y_0}{\alpha_2 + \alpha_4 Y_0}. \tag{4.40}$$

Bicubic interpolation needs first and second order cross derivatives to be known into the transformed space. Let us call $F(v,e)$ the function into the physical space and $\tilde{F}(X,Y)$ the corresponding function into the transformed space. In our case, F corresponds to pressure, temperature or speed of sound. Using both first and second order chain rules:

$$\frac{\partial \tilde{F}(X,Y)}{\partial X} = \frac{\partial F}{\partial v}\frac{\partial v}{\partial X} + \frac{\partial F}{\partial e}\frac{\partial e}{\partial X}, \tag{4.41}$$

$$\frac{\partial \tilde{F}(X,Y)}{\partial Y} = \frac{\partial F}{\partial v}\frac{\partial v}{\partial Y} + \frac{\partial F}{\partial e}\frac{\partial e}{\partial Y}, \tag{4.42}$$

$$\frac{\partial^2 \tilde{F}(X,Y)}{\partial X \partial Y} = \frac{\partial F}{\partial v}\frac{\partial^2 v}{\partial X \partial Y} + \frac{\partial F}{\partial e}\frac{\partial^2 e}{\partial X \partial Y} + \frac{\partial^2 F}{\partial v^2}\frac{\partial v}{\partial X}\frac{\partial v}{\partial Y} + \frac{\partial^2 F}{\partial e^2}\frac{\partial e}{\partial X}\frac{\partial e}{\partial Y} + \frac{\partial^2 F}{\partial v \partial e}\left(\frac{\partial v}{\partial X}\frac{\partial e}{\partial Y} + \frac{\partial v}{\partial Y}\frac{\partial e}{\partial X}\right), \tag{4.43}$$

where the first order partial derivatives of the physical coordinates with respect to the transformed ones (i.e. $\frac{\partial v}{\partial X}$, $\frac{\partial e}{\partial X}$, $\frac{\partial v}{\partial Y}$, $\frac{\partial e}{\partial Y}$) are evaluated by using Eq. (4.32) and (4.33). Whereas, first order derivatives of the function F (i.e. $\frac{\partial F}{\partial v}$, $\frac{\partial F}{\partial e}$) have been analytically calculated by using the equations of state provided by IAPWS-IF97. Second order derivatives are approximated by difference quotients of first derivatives instead. More details about derivative calculations are given in 4.11.

The interpolating surface is a polynomial composed of 16 addends, and it describes the function F on the transformed space:

$$\tilde{F}(X,Y) = \sum_{i=0}^{3}\sum_{j=0}^{3} a_{ij} X^i Y^j. \tag{4.44}$$

The 16 coefficients a_{ij} are the elements of the matrix $\mathbf{A}$:

$$\mathbf{A} = \begin{bmatrix} 1 & 0 & 0 & 0 \\ 0 & 0 & 1 & 0 \\ -3 & 3 & -2 & -1 \\ 2 & -2 & 1 & 1 \end{bmatrix} \begin{bmatrix} \tilde{F}_1 & \tilde{F}_2 & \partial_Y \tilde{F}_1 & \partial_Y \tilde{F}_2 \\ \tilde{F}_4 & \tilde{F}_3 & \partial_Y \tilde{F}_4 & \partial_Y \tilde{F}_3 \\ \partial_X \tilde{F}_1 & \partial_X \tilde{F}_2 & \partial_{X,Y} \tilde{F}_1 & \partial_{X,Y} \tilde{F}_2 \\ \partial_X \tilde{F}_4 & \partial_X \tilde{F}_3 & \partial_{X,Y} \tilde{F}_4 & \partial_{X,Y} \tilde{F}_3 \end{bmatrix} \begin{bmatrix} 1 & 0 & -3 & 2 \\ 0 & 0 & 3 & -2 \\ 0 & 1 & -2 & 1 \\ 0 & 0 & -1 & 1 \end{bmatrix}, \tag{4.45}$$

where, for instance, $\partial_X \tilde{F}_1$ indicates the derivative of the function F with respect to the coordinate X at node 1, that is, the node in the bottom left corner.

(a) The whole domain of the IAPWS-97

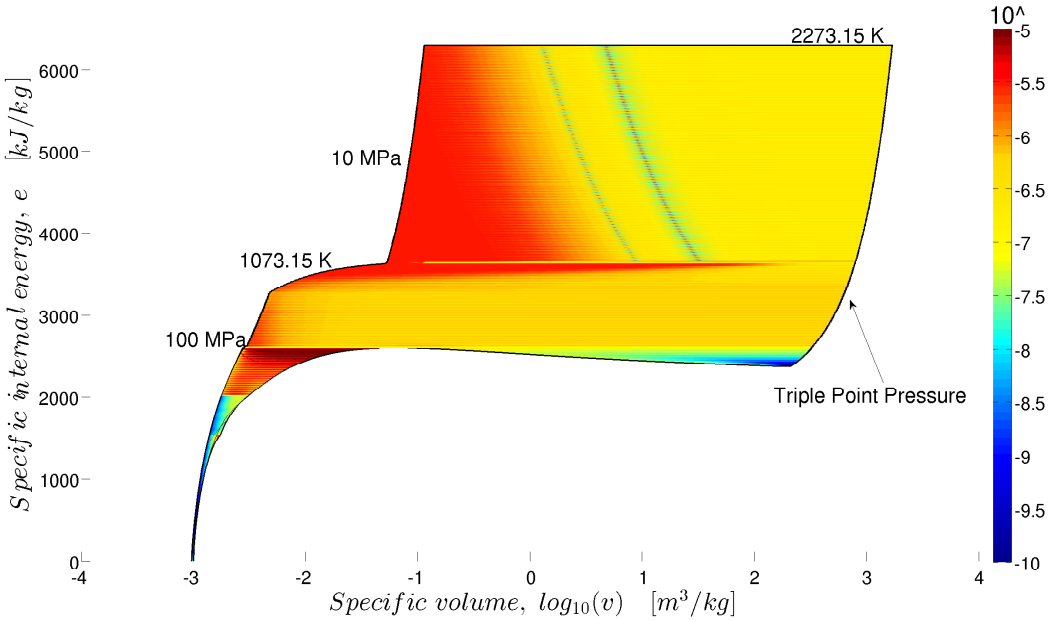

(b) Liquid region

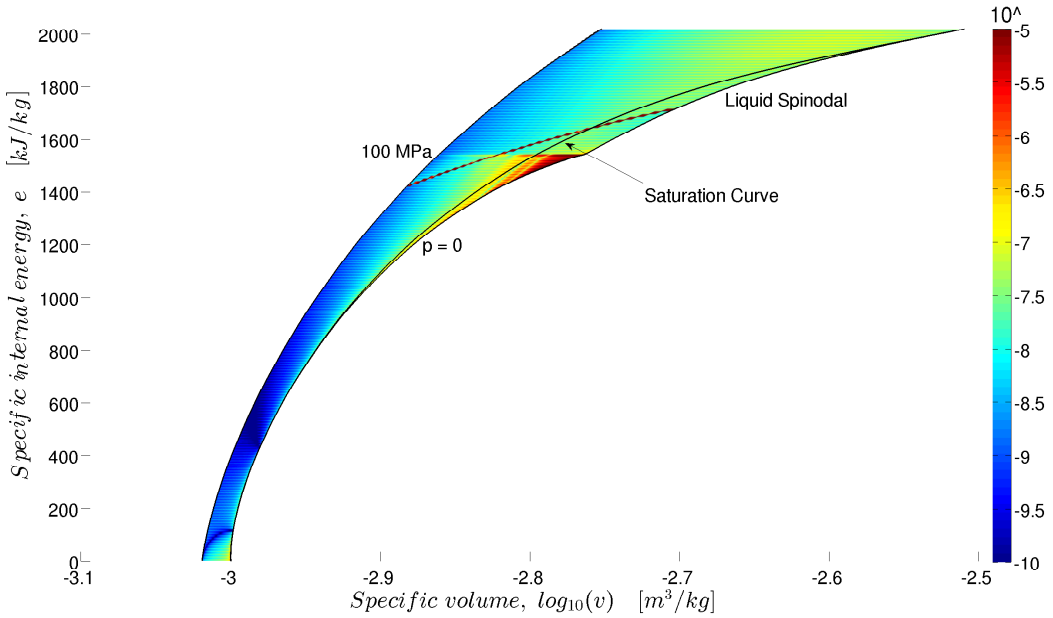

FIGURE 4.10. Distribution of the relative error for pressure between values calculated using the IAPWS-IF97 and the look-up table method here discussed. The error refers to the calculation of $p = p(\rho, e)$ for the Euler system. The first plot reports the error on the whole domain of the IAPWS-IF97 on the *e-v* diagram. The second plot is a magnified view for the liquid region. Here we can observe the trend of the saturation curve, the liquid spinodal and the isobaric of $p = 0\ MPa$. The grid of nodes adopted to map the physical domain consists of 160000 nodes and roughly 3 million points have been tested to produce this plot.

Once the coefficients of the bicubic interpolation are determined, the function is calculated as follows. Let us suppose to be interested in the pressure calculation, thus:

$$p(v,e) = \tilde{p}(X,Y) = [1\ X\ X^2\ X^3]\ \mathbf{A}\ [1\ Y\ Y^2\ Y^3]^T \tag{4.46}$$

where $\mathbf{A}$ is the coefficient matrix of Eq. (4.45).

The function $\tilde{p}(X,Y)$ refers to a Cartesian square grid and, by construction [212], has the following properties: i) the values of the function and the specified derivatives are reproduced exactly at the nodes, and, ii) the function and the specified derivatives change continuously at the edges of the square cells. Furthermore, these smoothness properties do not depend on the accuracy of the specified derivatives [212].

Due to the choice of the bilinear transformation, $p(v,e)$ is still a continuous function across the cell edges in the $e-v$ diagram. However, not all the derivatives are continuous across the edges. Further details about derivatives calculation are given in the next section (cf. 4.5.3).

This procedure for calculating thermodynamic properties has a high level of accuracy. As we can see in Fig. 4.10, the fidelity in the reproduction of the IAPWS-IF97 is very well ensured. Figure 4.10 reports the relative error between the values calculated using the IAPWS-IF97 and the look-up table method here proposed. Pressure is the physical magnitude which has the strongest gradients on the e-v diagram, thus, the most difficult field to be represented. The speed of sound and the temperature have a much smoother trend.

It is worth reminding that the tabulation has been carried out only in the single-phase domain and in the metastable one. Properties calculation into the two-phase domain relies on iterative algorithms which use a spline reconstruction of the saturation curve (4.10).

4.5.3 Derivatives calculation from bicubic splines

For a general function $F(v,e)$, the derivatives are calculated using the chain rule. Let us rewrite Eqs. (4.41) and (4.42) in matrix form:

$$\begin{bmatrix} \frac{\partial \tilde{F}}{\partial X} \\ \frac{\partial \tilde{F}}{\partial Y} \end{bmatrix} = \mathbf{J} \begin{bmatrix} \frac{\partial F}{\partial v} \\ \frac{\partial F}{\partial e} \end{bmatrix}. \tag{4.47}$$

where the Jacobian of the transformation is

$$\mathbf{J} = \begin{bmatrix} \frac{\partial v}{\partial X} & \frac{\partial e}{\partial X} \\ \frac{\partial v}{\partial Y} & \frac{\partial e}{\partial Y} \end{bmatrix}, \tag{4.48}$$

Thus,

$$\begin{bmatrix} \frac{\partial F}{\partial v} \\ \frac{\partial F}{\partial e} \end{bmatrix} = \mathbf{J}^{-1} \begin{bmatrix} \frac{\partial \tilde{F}}{\partial X} \\ \frac{\partial \tilde{F}}{\partial Y} \end{bmatrix}. \tag{4.49}$$

The Jacobian of the transformation must be nonsingular, in order to have an invertible transformation. This requirements ensures that each point within the cell in $e-v$ corresponds to one and only one point in the canonical cell in $Y-X$.

For the bilinear transformation expressed in Eqs. (4.32) and (4.33), with $\beta_2, \beta_4 = 0$, the Jacobian of the transformation is

$$\mathbf{J} = \begin{bmatrix} \alpha_2 + \alpha_4 Y & 0 \\ \alpha_3 + \alpha_4 X & \beta_3 \end{bmatrix}. \tag{4.50}$$

and its inverse is

$$\mathbf{J}^{-1} = \begin{bmatrix} \frac{1}{\alpha_2+\alpha_4 Y} & 0 \\ -\frac{\alpha_3+\alpha_4 X}{\beta_3(\alpha_2+\alpha_4 Y)} & \frac{1}{\beta_3} \end{bmatrix}. \tag{4.51}$$

Given that the interpolating function is the bicubic spline in (4.44), the derivatives in the $Y - X$ domain are

$$\begin{aligned} \frac{\partial \tilde{F}}{\partial X} &= \sum_{i=0}^{3}\sum_{j=0}^{3} a_{ij}\, i X^{i-1} Y^{j}, \\ \frac{\partial \tilde{F}}{\partial Y} &= \sum_{i=0}^{3}\sum_{j=0}^{3} a_{ij}\, j X^{i} Y^{j-1}. \end{aligned} \tag{4.52}$$

Therefore, once the point (X_0, Y_0) is known, the first order partial derivatives can be evaluated by using Eqs. (4.49), (4.51) and (4.52).

Note that first order partial derivatives in the $Y - X$ diagram are continuous at the inter-cell edges, however, this property is not generally verified in the $e - v$ diagram. Analyzing Eq. (4.51), one can observe that continuity is verified only for $\frac{\partial F}{\partial v}$ across the horizontal edges thanks to the regular pattern on nodes along the e-axis. The other derivatives are not continuous but numerical tests have shown that, at the edges, the discrepancy is small.

4.6 Numerical simulations of steam-water transients

The method for properties calculations discussed in the previous sections has been implemented in the EUROPLEXUS fast transient dynamics software, a simulation tool employed for instance in the nuclear safety field.

The numerical method used for this work relies on a Finite Volume discretization for the solution of the PDEs reported in Eq. (4.4), (4.12). The numerical scheme is the HLLC-type method presented and assessed in [70]. As mentioned above, HEM is a homogeneous set of partial differential equations, thus, it does not need additional numerical techniques for its solution.

For the HRM, a fractional step technique is used to solve the system of equations. It means that the numerical method proceeds in two steps. At each time step, first the homogeneous hyperbolic portion of the system with no mass transfer is solved. This step provides the non-equilibrium hydrodynamic field. Then, the mass transfer term is activated where metastable liquid is detected (relaxation step).

The first step represents the convection:

$$\partial_t \mathbf{U} + \partial_z \mathbf{F}(\mathbf{U}) = 0. \tag{4.53}$$

For the HEM the vector of the conservative variable is $\mathbf{U}_{HEM} = (\rho, \rho u, \rho E)^T$, whereas, for the HRM $\mathbf{U}_{HRM} = (\alpha_v \rho_v, \rho, \rho u, \rho E)^T$.

By using the HLLC-type Riemann solver, we compute the approximate solution over the time interval $[t^n, t^n + \Delta t]$ with given initial value $\mathbf{U}^n$. The approximate solution of Eq. (4.53), $\tilde{\mathbf{U}}^n$, will be the initial value for the second step, i.e., the relaxation step. By solving the following ODE:

$$\frac{d\mathbf{U}}{dt} = \mathbf{b}, \tag{4.54}$$

we finally obtain the approximate solution $\mathbf{U}^{n+1}$ corresponding to the time level t^{n+1}.

The source term $\mathbf{b}$ could contain dissipative terms such as wall friction, body forces or injected energy. In the case of the HRM, the vector $\mathbf{b}$ contains the mass transfer term, $\Gamma_{l\to v}$.

4.6.1 Mass transfer for the HRM

The Homogeneous Relaxation Model is handled by adding one more differential equation (i.e. the first equation of system 4.4) to the HEM. This supplementary equation drives the evolution of the quality x. The source term $\Gamma_{l\to v}$ describes how the quality x tends towards its local unconstrained-equilibrium value x_{eq}. In fact the quality is no longer assumed to instantaneously reach the equilibrium value of x_{eq}, hence a relaxation time, $\Theta > 0$, is introduced.

The vapor rate equation is

$$\partial_t(\alpha_v \rho_v) + \partial_z(\alpha_v \rho_v u) = -\rho \frac{x - x_{eq}}{\Theta}. \tag{4.55}$$

By using the continuity equation, this gives

$$\frac{Dx}{Dt} = -\frac{x - x_{eq}}{\Theta}, \tag{4.56}$$

where $D/Dt \equiv \partial_t + u\partial_z$.

As described above, Eq. (4.56) is solved in two steps: convection and relaxation. The convection step over the time interval $[t^n, t^n + \Delta t]$ provides the evolution of the quality from x^n to $\tilde{x}^n$. The relaxation equation becomes

$$\frac{dx}{dt} = -\frac{x - x_{eq}}{\Theta}. \tag{4.57}$$

This equation is integrated over the time interval $[t^n, t^n + \Delta t]$ using as initial value $\tilde{x}^n$. Due to the simple form of Eq. (4.57), the integration is analytical. If $\Theta \neq \Theta(x,t)$:

$$x^{n+1} = x_{eq} - (x_{eq} - \tilde{x}^n)e^{-\frac{\Delta t}{\Theta}}. \tag{4.58}$$

By definition, $x_{eq} > \tilde{x}^n$, therefore $x_{n+1} < x_{eq}$.

Consistently with its construction, the HRM tends to the HEM if $\Theta \to 0^+$, in fact

$$\lim_{\Theta\to 0^+} \left[x_{eq} - (x_{eq} - \tilde{x}^n)e^{-\frac{\Delta t}{\Theta}} \right] = x_{eq}. \tag{4.59}$$

The mass transfer is activated just if metastability is detected. For instance, when a liquid undergoes a depressurization, it becomes metastable. In the case of the HRM, this condition is detected by using the steam-water tables here proposed. A liquid is metastable if the couple (e, v) belongs to the region bounded by the saturation curve and the liquid spinodal. Refer to Fig. 4.4, 4.10b for a graphic illustration. For a two-phase mixture, the metastability is detected when $\tilde{x}^n < x_{eq}$.

4.6.2 Steam-water transients

Now that the numerical strategies have been discussed, we can assess them on three challenging fast transients tests: fast depressurization, waterhammer and steam explosion problems.

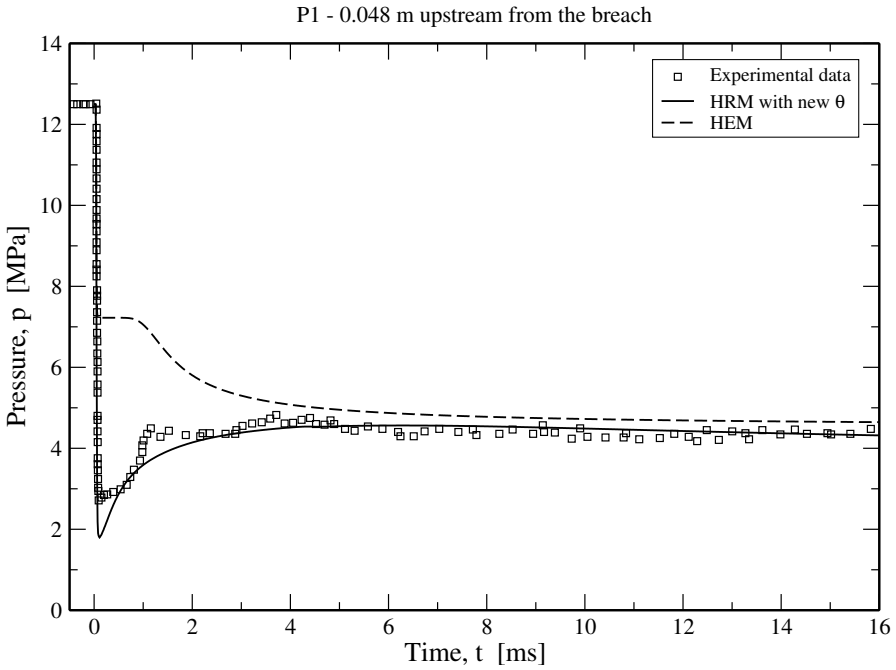

FIGURE 4.11. Pressure evolution in the first $16ms$ of the Bartak's experiment [16] ($12.5MPa$, $563.15K$). Assessment of HEM and HRM using the relaxation time correlation proposed in Eq. (4.62).

4.6.2.1 Depressurization Transients

In the context of nuclear safety, one of the Design Basis Accidents (DBA) is the Loss of Coolant Accident (LOCA), which would occur in the case of a sudden rupture of a primary system pipe. In the '70s-'80s, few experimental facilities have studied the rapid depressurization of vessels or pipes containing water at subcooled conditions [16, 94, 223]. In this section we try to validate the model discussed above against these physically complex and challenging experiments. The benchmark is performed using the experimental data of Bartak [16] and Super Canon test rig [223]. The initial pressure and temperature conditions for the first test are $12.5MPa$ and $563.15K$, and for the second test $15MPa$ and $573.15K$. The corresponding subcooling degrees, i.e. $T_{sat}(p_{in})-T_{in}$, are respectively $38K$ and $42K$.

The arrangement of the Super Canon facility and the measurement devices are shown in Fig. 4.12. Both experiments are triggered by the sudden opening of a rupture disc located at one extremity of the pipe. At that moment, a rarefaction wave originates at the break and moves backward. The very first milliseconds following the rupture are well represented by the Bartak data, whereas, the whole transient is better described by the Super Canon experiments.

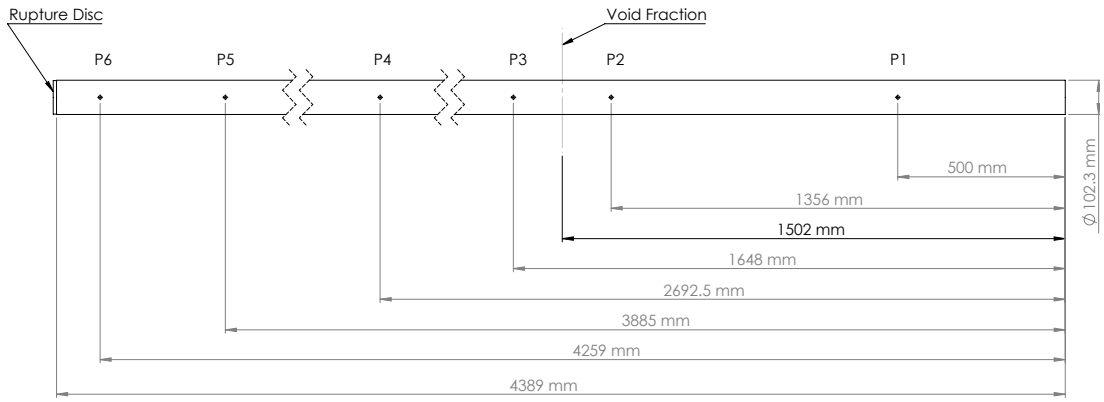

FIGURE 4.12. Schematic of Super Canon experimental facility and location of the measurement devices.

The comparisons of HEM and HRM simulations against the experimental data are reported in Fig. 4.11, 4.13. From the experiments, we know that the measured velocity of the rarefaction wave compares well with the isentropic speed of sound of single-phase water. This feature is well reproduced by both models since the rarefaction wave propagates in the single-phase liquid.

The depressurization is initially abrupt and fast. The pressure reaches values lower than the saturation pressure corresponding to the initial stagnation temperature ($7.4\,MPa$ in Bartak experiment, $8.6\,MPa$ for Super Canon). The difference between the local pressure and the saturation pressure is as high as $5\,MPa$, hence, the liquid water tends to penetrate in depth into the metastable domain. The undershoot is well reproduced by the HRM, whereas, for the HEM, the mixture remains at saturated condition causing the pressure to stay constant for few hundreds milliseconds.

Figure 4.11 shows that the depressurization is stopped by bubble nucleation, which leads to a small but extremely quick increase of pressure. Skripov et al. [246], Alamgir & Lienhard [3] and Bartak [16] agree that bubble nucleation occurs too quickly to be the classical heterogeneous nucleation at the wall cavities. Hence, it could be the *homogeneous nucleation* [43], provoked by the high metastability reached by the liquid. The HRM can reproduce this phenomenon thanks to the exponential rate of return to equilibrium conditions. The mass transfer from liquid to vapor is activated only if metastable conditions are detected.

After the explosion-like nucleation, the pressure remains constant for a while, but at values lower than the saturation one. After $100\,ms$, the wave propagation phenomena are no longer relevant and the pressure decreases due to the emptying of the capacity. In fact, the closed-end system empties at the rate imposed by the two-phase critical flow that sets at break [78].

Finally, the simulation performed with the HRM agrees with most of the features experimentally observed. In this test, the HEM seems to not be sufficient for modeling the acoustic phase of this transient flow due to the impossibility of dealing with metastable liquids.

The HEM was already implemented in EUROPLEXUS, but coupled to an iterative algorithm for the thermodynamic properties calculation. The iterative procedure used steam-water tables developed on the (p,T) diagram. Now, however, the code implements the bicubic look-up table

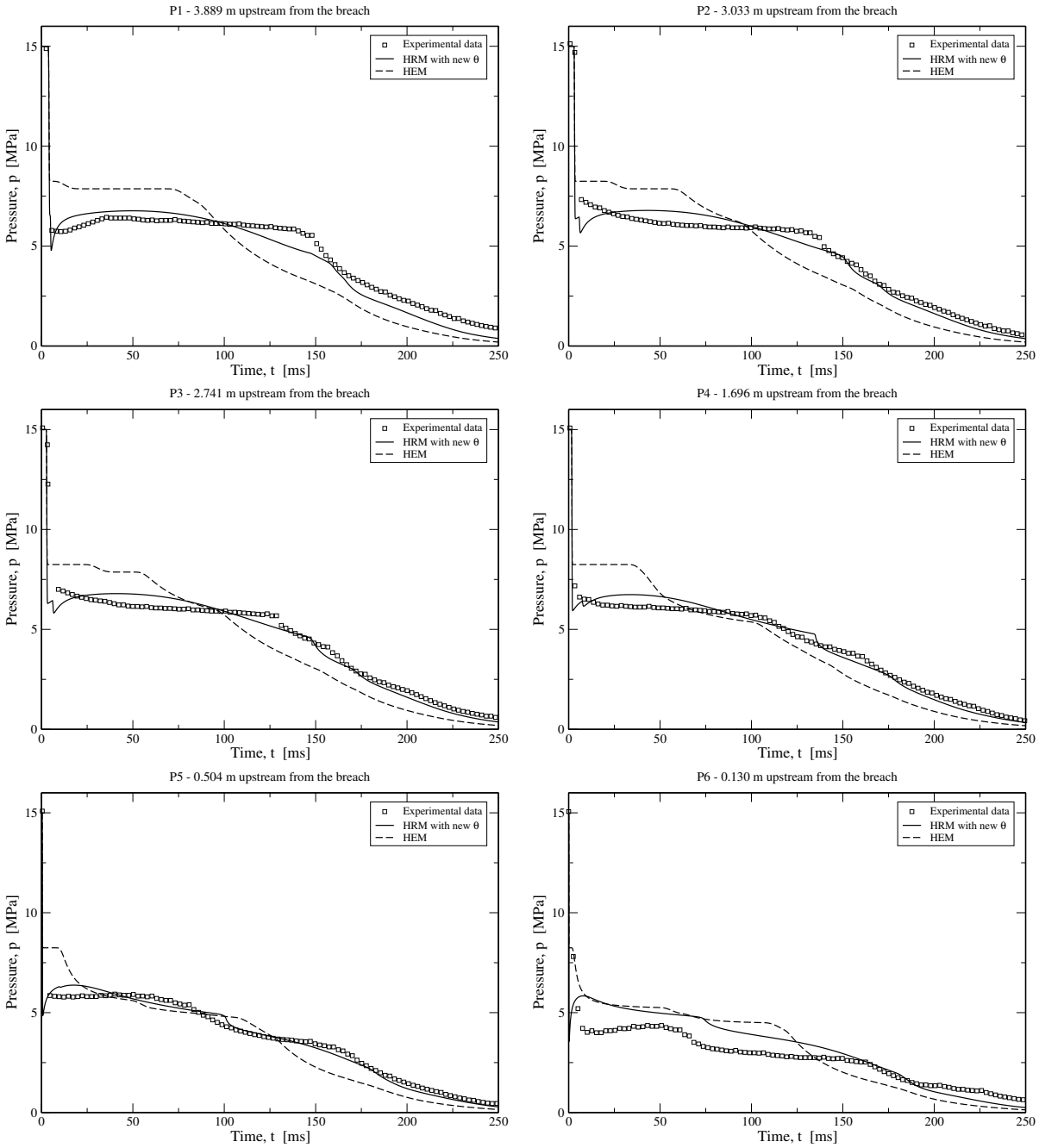

FIGURE 4.13. Assessment of HEM and HRM on a Super Canon experiment. The initial stagnation conditions are 15 MPa and 573.15 K. For this calculation, the 4.389 m long tube has been discretized into a 1000 cells mesh. In the first milliseconds, the difference between local pressure and saturation pressure is as high as 5 MPa. The relaxation time correlation used for this simulation is the one proposed in Eq. (4.62).

algorithm presented in Section 4.5. The direct calculation of properties allows us to save about the 60-65% of the total computational time in the case of a Super Canon experiment. Hence, the calculation lasts 1/3 of the time needed before.

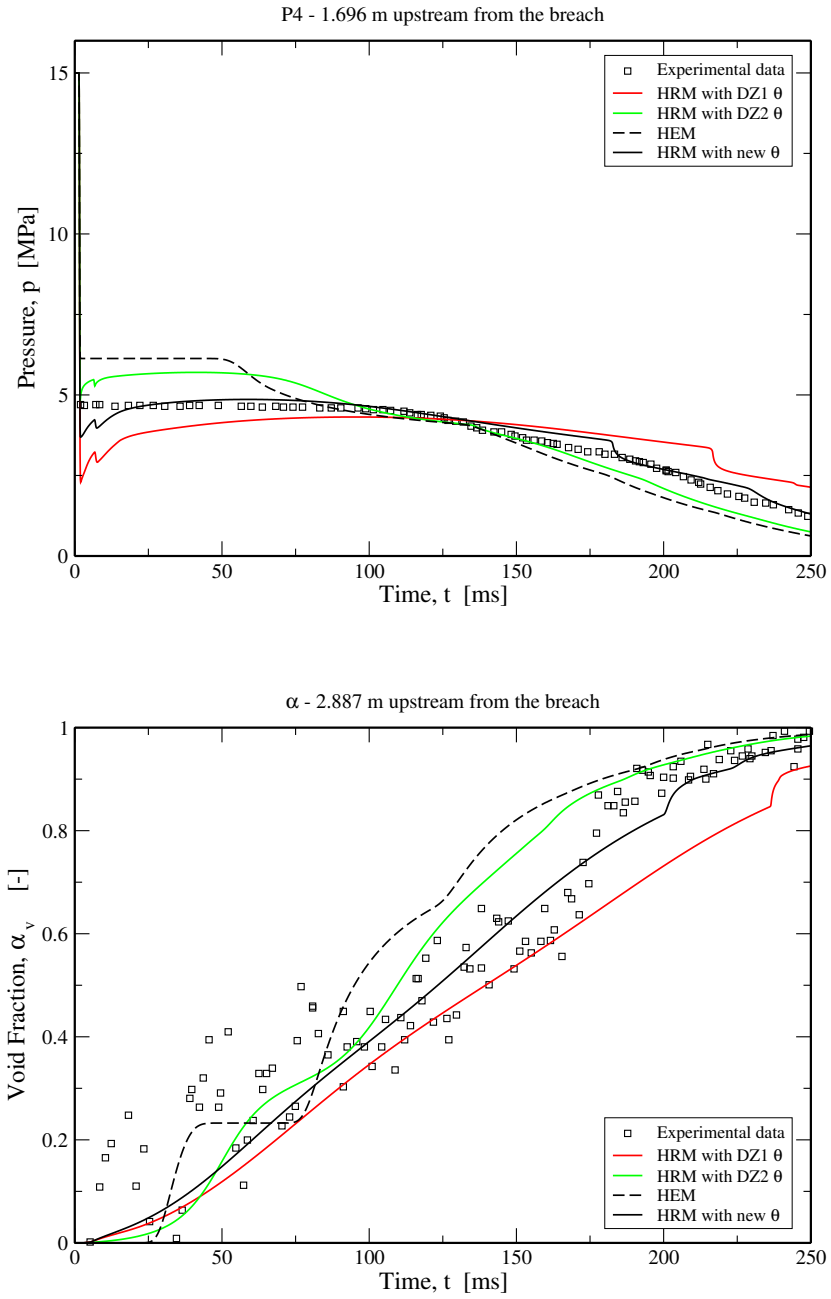

FIGURE 4.14. Comparison between HEM and HRM using different correlations for Θ on pressure and void fraction evolution in the Super Canon experiment with initial data: $15 MPa$, $553.15 K$. In the legend, DZ1 and DZ2 indicate the correlations proposed by Downar-Zapolski et al. [84].

4.6.2.2 Relaxation time correlations

The relaxation time Θ accounts for the delay necessary to reach equilibrium conditions. The relaxation term is of paramount importance in the HRM.

Downar-Zapolski et al. [84] proposed two correlations based on the experimental data of the Moby

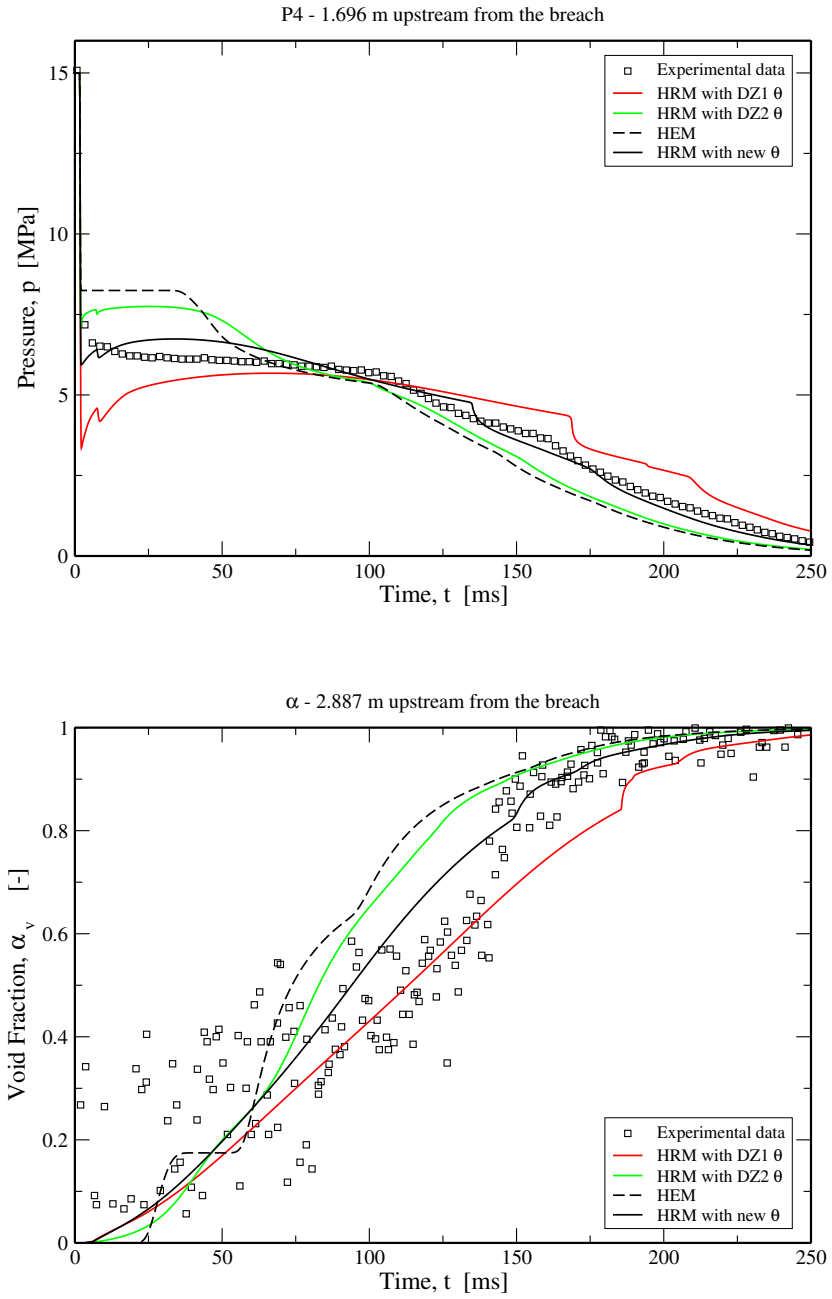

FIGURE 4.15. Comparison between HEM and HRM using different correlations for Θ on pressure and void fraction evolution in the Super Canon experiment with initial data: $15\,MPa$, $573.15\,K$. In the legend, DZ1 and DZ2 indicate the correlations proposed by Downar-Zapolski et al. [84].

Dick [226] facility, which was a test rig for the stationary critical flow in flashing steam-water [78]. The first correlation, here indicated as DZ1, is:

$$\Theta = 6.51 \cdot 10^{-4}\ \alpha_v^{-0.257} \left(\frac{p_{sat} - p}{p_{sat}} \right)^{-2.24}, \tag{4.60}$$

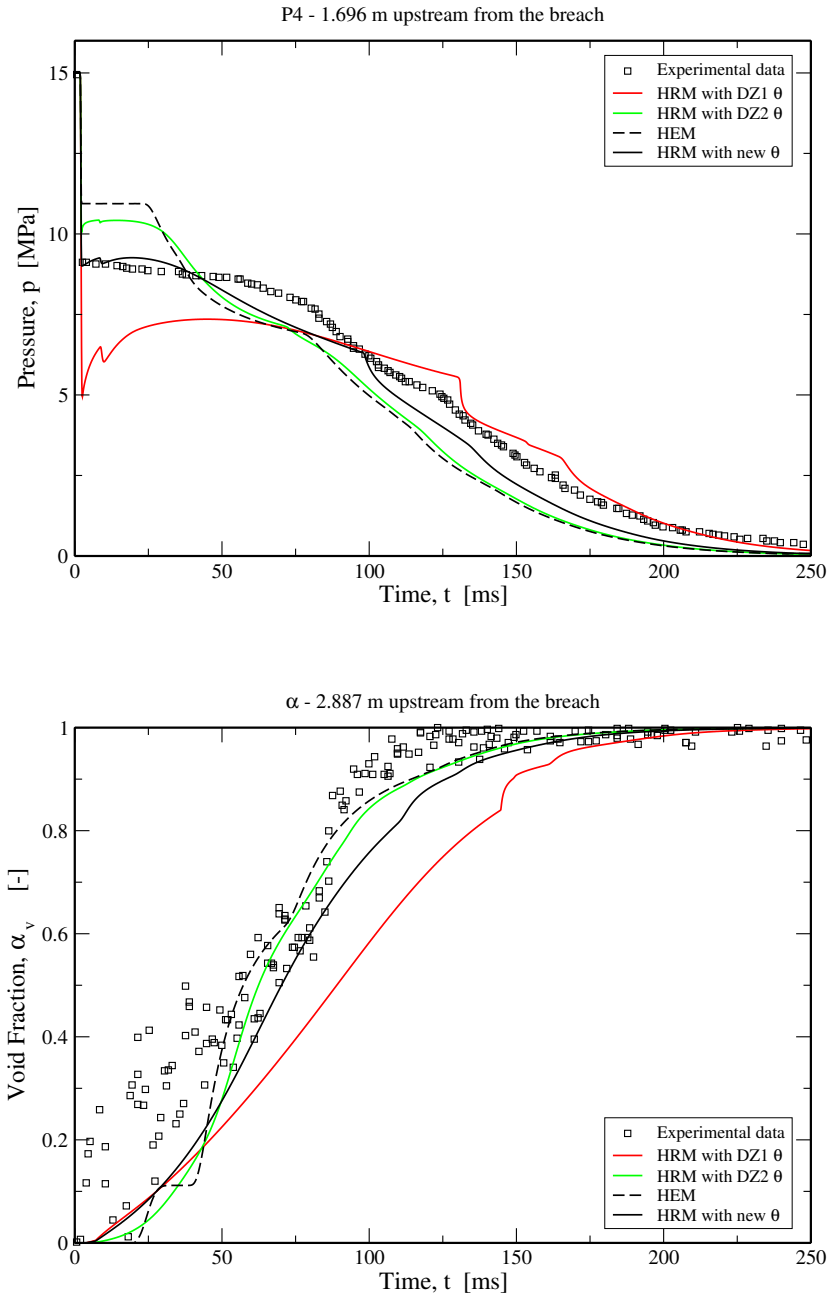

FIGURE 4.16. Comparison between HEM and HRM using different correlations for Θ on pressure and void fraction evolution in the Super Canon experiment with initial data: $15\,MPa$, $593.15\,K$. In the legend, DZ1 and DZ2 indicate the correlations proposed by Downar-Zapolski et al. [84].

the second one, indicated as DZ2, reads:

$$\Theta = 3.84 \cdot 10^{-7}\ \alpha_v^{-0.54} \left(\frac{p_{sat} - p}{p_{crit} - p_{sat}} \right)^{-1.76}, \tag{4.61}$$

where p_{crit} is the pressure of the critical point ($22.064\,MPa$). These correlations express the relax-

ation time Θ in seconds. Gale et al. [112] proved that these correlations well represent the physics of vaporization even in unsteady conditions. However they fail in simulating the Super Canon experiments. Here we propose a correlation that better fits the pressure and void fraction evolution at high pressures:

$$\Theta = 4 \cdot 10^{-5} \ \alpha_v^{-0.25} \left(\frac{p_{sat} - p}{p_{crit} - p_{sat}} \right)^{-1.8} . \tag{4.62}$$

The comparison of the three correlations is reported in Fig. 4.14, 4.15, 4.16. Globally, the correlation here proposed represents better the whole transient of Super Canon experiments. Additionally, it well captures the pressure undershoot following the rarefaction wave (Fig. 4.11). In fluid-structure interaction problems, this feature is crucial because the amplitude of the rarefaction wave is an important factor in calculating the mechanical stress on the structures. For instance, in the event of a full-break LOCA mentioned above, the correct simulation of the rarefaction wave may provide information on the possible damage to the nuclear core.

4.6.3 Waterhammer

Simpson's column-separation-induced waterhammer experiment [244] is a benchmark of many two-phase computer codes because of its simple geometry and the richness of phenomena involved. A pipe is filled by a slow steady state liquid water flow which is interrupted by a sudden closure of the valve at the end of the pipe. The pipe is $36\,m$ long, has constant internal diameter of $0.01905\,m$ and the wall thickness is $0.001588\,m$. The initial thermodynamic state in the pipe in terms of pressure and temperature is $0.3419\,MPa$ and $297.05\,K$, hence, water is single-phase liquid. Two experiments are analyzed here, in the first the liquid initially flows at $0.239\,m/s$, in the second the initial velocity is $0.401\,m/s$. The wave propagation in the tube is triggered by the sudden closure of the valve, waves propagate in the pipe and are reflected at both pipe ends. According to the initial velocity, pressure may decrease enough to attain saturation conditions, thus, generating a vapor pocket at the valve.

For this experimentc, the wave propagation velocity is affected by the elasticity of the pipe. In order to obtain a fair agreement between the simulations and experimental data, the speed of sound is modified according to Allievi's correlation [5]. Here we used the optimal Young's elasticity modulus of the pipe suggested in [112], i.e. $75\,GPa$, however the real one is around $119\,GPa$.

Figure 4.17 shows the assessment of the HEM and the HRM on the experimental data of [244]. The top graph shows the pressure history near the valve for the test with initial velocity equal to $0.239\,m/s$. This value is low enough to not provoke vapor formation. The comparison with experimental data shows very good agreement. Pressure peaks are well described by the simulation except for the time-decreasing amplitude of pressure waves. This feature is not well represented by simulations due to the absence of pressure losses in our numerical method. Of course the HEM and the HRM exactly agree since the fluid is always single-phase liquid.

The bottom graph of Fig. 4.17 shows the pressure history near the valve for the test with initial velocity equal to $0.401\,m/s$. Conversely to the previous test, cavitation occurs and a vapor pocket is created close the valve. Moreover, the disappearance of this pocket generates a new pressure wave, thus a combination of several waves occurs as it is visible at $t \approx 175\,ms$. Again, the lack of dissipative phenomena in our simulations leads to a slight overestimation of pressure peaks. In this

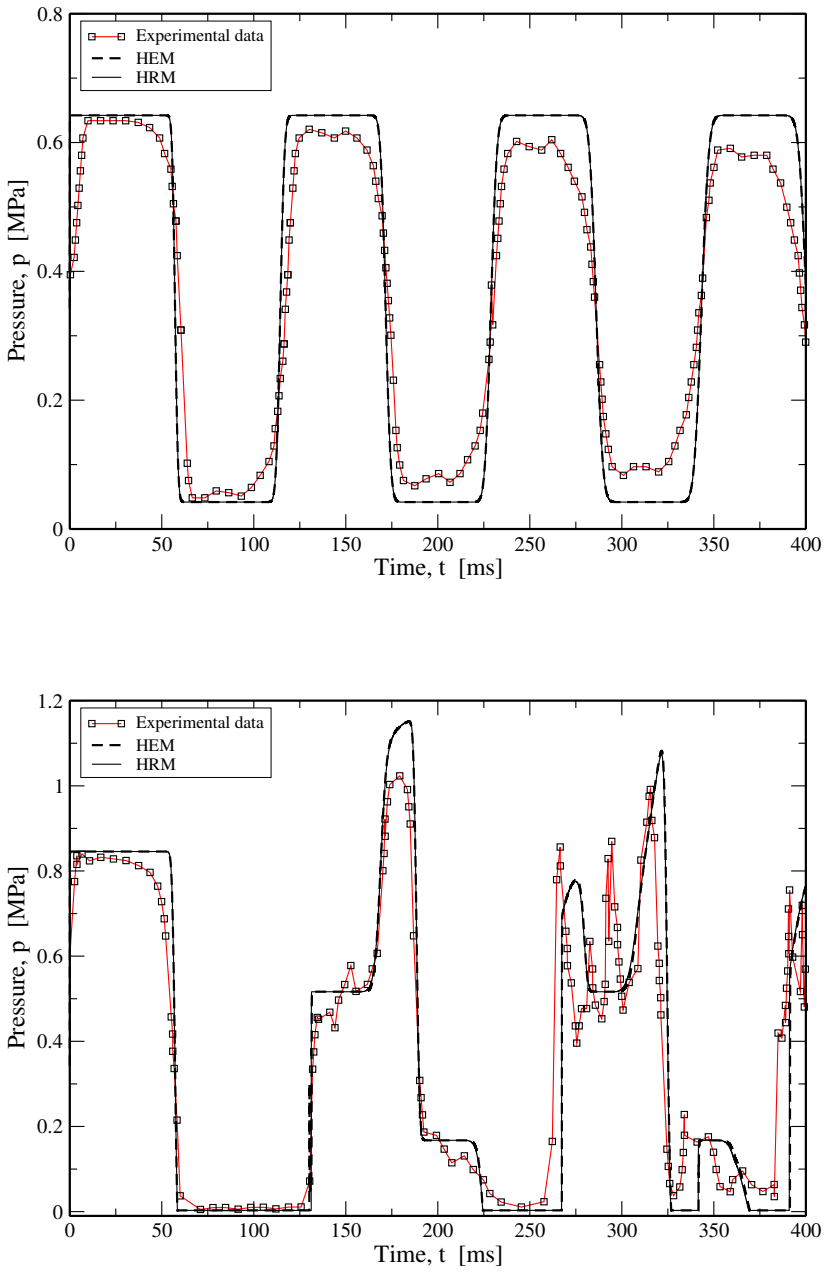

FIGURE 4.17. Pressure history near the valve of Simpson's waterhammer experiment [244]. The top graph shows results for the experiment with initial velocity $0.239\,m/s$, the bottom one for the experiment with initial velocity $0.401\,m/s$. The initial pressure and temperature conditions for both experiments are $0.3419\,MPa$ and $297.05\,K$. For this calculation, the $36\,m$ long tube has been discretized into a 1000 cells mesh.

simulation, the HEM and the HRM are coincident. Few discrepancies between the two models are detected but irrelevant for the global description of the experiment.

Similar considerations about the computational cost as those made in 4.6.2.1 can be made also for

the Simpson's experiment. A comparison between the calculation performed by using the numerical implementation of the HEM previously present in EUROPLEXUS, and the calculation carried out by using the method presented in this work, suggests that the new algorithm that we have developed is less time consuming. The use of an interpolation technique of water properties rather than an iterative one allows us to save the 20-25% of the total computational time that was required before.

4.6.3.1 Steam explosion

A steam explosion is an interaction process between two fluids at very different temperatures. Namely, the temperature of the hot liquid is higher than the saturation temperature of the cold one. Such phenomena are typical of iron foundries due to the interaction between melting metal and coolant water or in petroleum engineering because of the contact of water and liquefied natural gas. In the nuclear industry, steam explosion may occur during a severe reactor accident when the molten fuel comes into contact with the coolant water.

During a steam explosion the energy of the hot liquid is transferred to the coolant in a time scale smaller than the time scale for system pressure relief. Therefore the vaporization leads to the formation of shock waves that might endanger the surrounding structures.

In the context of nuclear safety, Board & Hall [33] recognized that a steam explosion is very similar to a chemical detonation. Similarly to a detonation, the propagation of a shock wave through a pre-mixture of fuel and coolant leads to a quick and fine fragmentation of the fuel, which releases a huge amount of its internal heat. The rapid heating of the coolant produces high pressures which drive the shock forward [23].

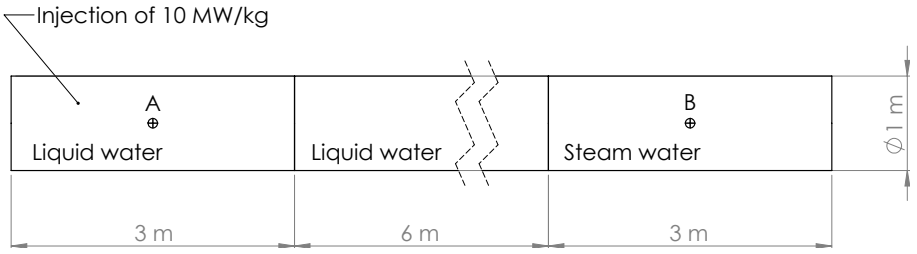

FIGURE 4.18. Schematic of the injection test. The evolution of pressure, velocity, temperature and void fraction at points A and B are illustrated in Fig. 4.19 A and B.

If the steam explosion can be assumed as a chemical detonation [33], a simple numerical modeling might be a quick energy injection. Here we performed a test proposed in [166]. A schematic of the injection test is depicted in Fig. 4.18.

A $12\,m$ long tube is divided into three parts, the leftmost one and the central one contain liquid water, the rightmost part contains vapor. The pressure field is uniform and equal to 3.517 MPa ($T_{sat} = 516\ K$), the liquid is at a temperature of 515.15 K whereas the vapor is at 516.15 K. At $t = 0$, the energy injection starts: $10 MW/kg_{H20}$ are injected in the first portion of the tube for 50 ms. The volume of this portion is roughly 2.36 m^3, containing 1909 kg of liquid water. Hence the injected energy throughout the transient is 0.95 GJ.

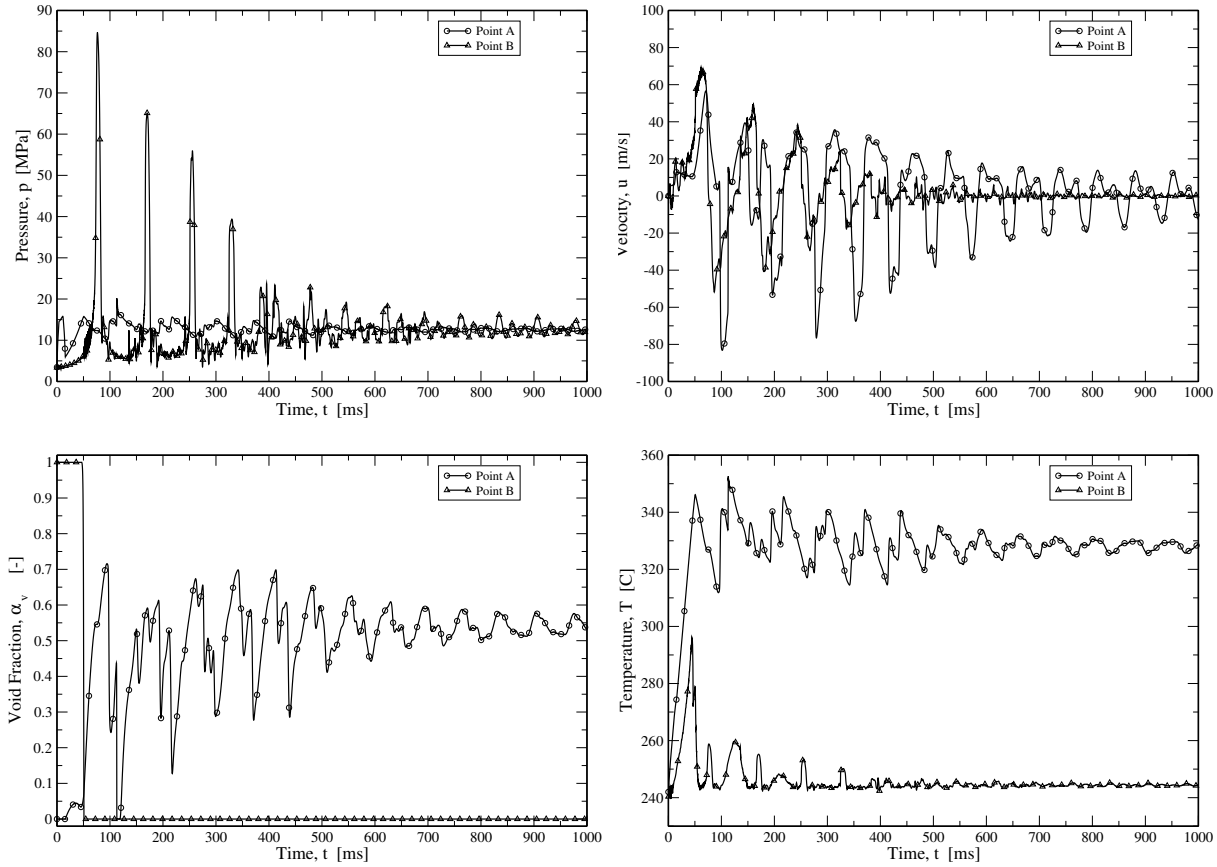

FIGURE 4.19. Temporal evolutions of pressure, velocity, temperature and void fraction at points A and B (Fig. 4.18).

The temporal evolutions at points A and B of pressure, velocity, temperature and void fraction are illustrated in Fig. 4.19. A magnification of the first 55 ms of the transient is reported in Fig. 4.20. The results are obtained by using the homogeneous equilibrium model.

We can see a pressure peak of 16 MPa during the first 15 ms due to the initial confinement of water. As the velocity increases, the pressure decreases rapidly, then increases again smoothly (see Fig. 4.20). Therefore a pressure wave originates and moves rightward. At 80 ms we notice a pressure peak of 85 MPa due to the quick condensation of the vapor at the end of the tube. From now the transient becomes similar to a waterhammer as in Section 4.6.3. Waves propagate in the tube reflecting at the extremities and/or at the location of a sudden change of the acoustic impedance $Z = \rho c$. This occurs, for instance, when the wave is propagating into a liquid and encounters a two-phase mixture.

At the end of the transient, the stagnation pressure is increased and has reached the value of 12 MPa. In fact the pipe can be seen as a closed system without mass and energy transfers with the environment. The energy injection represents the heat exchange with the molten fuel, then, at the end of the transient the injected energy is completely transformed in internal energy.

This kind of transients are really fast and lead to huge pressure peaks. Experimental tests of steam explosion are KROTOS [127](pressure peak of 100 MPa in test K49) or SANDIA [102]. Those

experiments were not reproduced here since the modelling of the heat transfer in such situations is complicated [23] and is not in the objectives of this work. The purpose of this test was to assess the robustness of the numerical method and its capability of dealing with very high pressures and multiple phase changes.

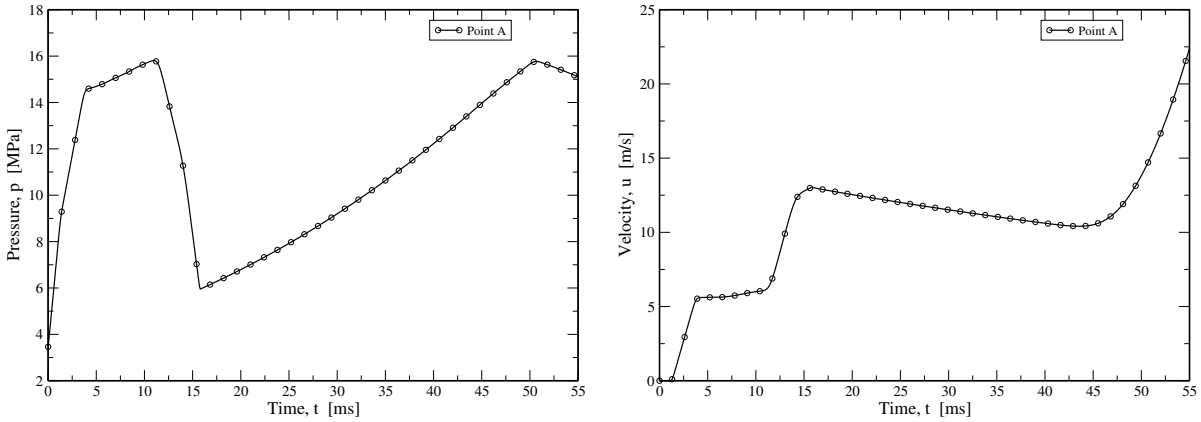

FIGURE 4.20. Magnification of the temporal evolutions of pressure and velocity during the first 55 ms.

4.7 Conclusions

In this article we have proposed an efficient EoS look-up table method for steam-water flow simulations. Our algorithm uses the IAPWS-IF97 EoS formulation and evaluates water properties by interpolation of values tabulated on the e-v thermodynamic diagram. The main features of this algorithm consist in transforming the irregular shaped e-v physical domain into a regular one and in performing a bicubic interpolation in the transformed domain. Such a technique makes the procedure very efficient and at the same time it provides remarkable precision. In particular, in contrast to simple EoS formulations, our method allows an accurate description of regimes where water has a significant non linear behavior, i.e. close to the saturation curve, in the metastable region and close to the critical point.

In fast transients, especially during depressurizations, water becomes metastable. In order to take into account this phenomenon, the tabulation has been performed until the spinodal curve. However the spinodal line has not been clearly experimentally identified yet. Here, it has been determined by extrapolating the basic equation provided by the IAPWS-IF97 EoS.

The steam-water table look up algorithm has been coupled to two simple two-phase flow models, the Homogeneous Equilibrium Model, and the Homogeneous Relaxation Model. Both models are numerically solved by Finite Volume discretizations with a HLLC-type scheme. The methods and algorithms presented in this work have been implemented in EUROPLEXUS, a fast transient dynamics software adopted for instance in the field of nuclear safety.

The performance of the HEM and HRM coupled with the new steam-water table look-up method has been assessed on three challenging fast transients problems: fast depressurization, waterham-

mer and steam explosion tests. For the first two test problems the comparison of numerical results with experimental data show the very good performance of the computational techniques that we have developed. Let us note that for the fast depressurization test, although both the HEM and HRM models prove to be able to describe the main features of the transient flow dynamics, only the HRM can take into account the deep metastability reached in the very first milliseconds of the experiment. For this HRM model, a correlation for the relaxation time to return to equilibrium conditions has been proposed and compared to other correlations found in literature. The correlation proposed here proves to be more accurate for the description of the pressure evolution, which is a very important feature in particular for fluid-structure interaction problems.

Our method has also been assessed for its capability of dealing with very high pressures and multiple phase changes. These are the characteristic features of the considered steam explosion test case.

Finally, let us stress that the algorithm here proposed is very efficient in terms of time consumption. Indeed the global computational time decreased significantly (even of 65% for the Super Canon experiment) through the use of a direct properties calculation rather than an iterative one when the HEM is used.

A further evolution of the present work would be the extension of our technique to the case of metastable states of vapor and its coupling with a more complex two-phase flow model as the hyperbolic 6-equation model presented in Pelanti & Shyue [200].

Acknowledgments

The authors would like to gratefully thank Pascal Galon (CEA) and Frédéric Daude (EDF) for helpful discussions and advices for the implementation of the flow models in EUROPLEXUS.

4.8 Appendix 4.A: HEM - Speed of sound using IAPWS-IF97

The speed of sound in two-phase flows does not correspond to an intrinsic thermodynamic property of the substance, and it depends both on the mixture composition and on the degree of inter-phase equilibrium attained between the phases. For models describing two-phase flows the expression of the speed of sound stems mathematically from the governing systems of equations, and it depends on the choice of the EoS. For the Homogeneous Equilibrium Model the corresponding speed of sound can be obtained by using the definition (formally equal to the one of the single-phase case)

$$c^2_{HEM} = \left(\frac{\partial p}{\partial \rho}\right)_s . \tag{4.63}$$

together with the closure EoS relations for the mixture detailed in Section 2.1. Saurel et al. [233] obtained:

$$\frac{1}{\rho c^2_{HEM}} = \frac{\alpha_v}{\rho_v c_v^2} + \frac{1-\alpha_v}{\rho_l c_l^2} + T\left[\frac{\alpha_v \rho_v}{c_{p,v}}\left(\frac{ds_v}{dp}\right)^2 + \frac{\alpha_l \rho_l}{c_{p,l}}\left(\frac{ds_l}{dp}\right)^2\right] \tag{4.64}$$

Based on the expression above, it is easy to see that the HEM system is hyperbolic with the natural conditions:

$$\rho_k > 0, \qquad T > 0, \qquad c_{p,k} > 0 \tag{4.65}$$

where $k \in \{v, l\}$.

As well known in literature, the HEM has a discontinuous speed of sound (see Fig. 4.2). This feature is exhaustively explained in [109].

The employment of the expression of Eq. (4.64) for CFD simulations is not efficient for the steam-water table look-up method here presented. Let us derive another formulation more convenient and less time-consuming. Following Eq. (4.2), for the HEM, the quasi-linear form reads:

$$\partial_t \begin{bmatrix} \rho \\ u \\ p \end{bmatrix} + \begin{bmatrix} u & \rho & 0 \\ 0 & u & v \\ 0 & \gamma_{HEM}\, p & u \end{bmatrix} \partial_z \begin{bmatrix} \rho \\ u \\ p \end{bmatrix} = \begin{bmatrix} 0 \\ 0 \\ 0 \end{bmatrix}, \tag{4.66}$$

where the dimensionless quantity, γ_{HEM}, is:

$$\gamma_{HEM} = \frac{1}{p\ \partial_p e} \left(\frac{p}{\rho} - \rho\ \partial_\rho e \right). \tag{4.67}$$

The eigenvalues of the system in (4.66) are:

$$\lambda_1 = u - c_{HEM}, \qquad \lambda_2 = u, \qquad \lambda_3 = u + c_{HEM}. \tag{4.68}$$

We define the speed of sound of the HEM, c_{HEM}, as:

$$c_{HEM} \triangleq \sqrt{\frac{\gamma_{HEM}\, p}{\rho}}. \tag{4.69}$$

Using a caloric EoS of the form $e = e(\rho, p)$, for the HEM, the speed of sound reads:

$$c^2_{HEM} = \frac{\frac{p}{\rho} - \rho \left(\frac{\partial e}{\partial \rho} \right)_p}{\rho \left(\frac{\partial e}{\partial p} \right)_\rho} \tag{4.70}$$

where:

$$\begin{aligned} \left(\frac{\partial e}{\partial \rho} \right)_p &= (e_v - e_l) \left(\frac{\partial x}{\partial \rho} \right)_p \\ &= - \frac{(e_v - e_l)}{\rho^2 (v_v - v_l)} \end{aligned} \tag{4.71}$$

and

$$\begin{aligned} \left(\frac{\partial e}{\partial p} \right)_\rho &= \left(\frac{\partial e}{\partial p} \right)_x - \left(\frac{\partial e}{\partial x} \right)_p \left(\frac{\partial \rho}{\partial p} \right)_x \left(\frac{\partial \rho}{\partial x} \right)_p^{-1} \\ &= \left(\frac{\partial e}{\partial p} \right)_x - \frac{e_v - e_l}{v_v - v_l} \left(\frac{\partial v}{\partial p} \right)_x. \end{aligned} \tag{4.72}$$

Finally, c_{HEM} can be determined through the following relation:

$$c^2_{HEM} = \frac{p + \frac{e_v - e_l}{v_v - v_l}}{\rho^2 \left[\left(\frac{\partial e}{\partial p} \right)_x - \frac{e_v - e_l}{v_v - v_l} \left(\frac{\partial v}{\partial p} \right)_x \right]} \tag{4.73}$$

with $\left(\frac{\partial e}{\partial p} \right)_x = \left(x \frac{de_v(p)}{dp} + (1 - x) \frac{de_l(p)}{dp} \right)$, $\left(\frac{\partial v}{\partial p} \right)_x = \left(x \frac{dv_v(p)}{dp} + (1 - x) \frac{dv_l(p)}{dp} \right)$.

In such a form, it is simple to calculate the speed of sound by using a spline reconstruction of the saturation curve as $v_v(p), v_l(p), e_v(p), e_l(p)$. For this work, the spline coefficients have been evaluated using the IAPWS-IF97.

4.9 Appendix 4.B: HRM - Speed of sound using IAPWS-IF97

Similar to the HEM in 4.8, the quasi-linear form of the HRM reads:

$$\partial_t \begin{bmatrix} x \\ \rho \\ u \\ p \end{bmatrix} + \begin{bmatrix} u & 0 & 0 & 0 \\ 0 & u & \rho & 0 \\ 0 & 0 & u & v \\ 0 & 0 & \gamma_{HRM}\, p & u \end{bmatrix} \partial_z \begin{bmatrix} x \\ \rho \\ u \\ p \end{bmatrix} = \begin{bmatrix} 0 \\ 0 \\ 0 \\ 0 \end{bmatrix}, \tag{4.74}$$

where the dimensionless quantity γ_{HRM}, is:

$$\gamma_{HRM} = \frac{1}{p\ \partial_p e}\left(\frac{p}{\rho} - \rho\ \partial_\rho e\right). \tag{4.75}$$

The eigenvalues of the system of equations (4.74) are:

$$\lambda_1 = u - c_{HRM}, \qquad \lambda_{2,3} = u, \qquad \lambda_4 = u + c_{HRM}. \tag{4.76}$$

We define the speed of sound of the HRM, c_{HRM}, as:

$$c_{HRM} \triangleq \sqrt{\frac{\gamma_{HRM}\, p}{\rho}}. \tag{4.77}$$

Again, the System (4.12) is hyperbolic if and only if $\gamma_{HRM} > 0$.

Let us derive a formulation of the speed of sound compatible with IAPWS-IF97. The caloric EoS is $e = e(p,\rho,x)$. Therefore, the speed of sound reads:

$$c^2_{HRM} = \frac{\frac{p}{\rho} - \rho\left(\frac{\partial e(p,\rho,x)}{\partial \rho}\right)_{p,x}}{\rho\left(\frac{\partial e(p,\rho,x)}{\partial p}\right)_{\rho,x}}. \tag{4.78}$$

By using the following thermodynamic relations:

$$de = Tds - pdv, \tag{4.79}$$

$$dh = Tds + vdp, \tag{4.80}$$

equation (4.78) becomes:

$$c^2_{HRM} = \left(\frac{\partial p}{\partial \rho}\right)_{s,x}. \tag{4.81}$$

A more convenient form would be:

$$c^2_{HRM} = -v^2\left[\left(\frac{\partial v}{\partial p}\right)_{T,x} - \left(\frac{\partial v}{\partial T}\right)_{p,x}\left(\frac{\partial s}{\partial p}\right)_{T,x}\left(\frac{\partial s}{\partial T}\right)^{-1}_{p,x}\right]^{-1}. \tag{4.82}$$

The calculation of these derivatives with IAPWS-IF97 is straightforward if we refer to the methodology shown in 4.11. However, we remind that even for the calculation of the speed of sound, the vapor must be set at saturation (see Eq. (4.14)).

4.10 Appendix 4.C: Iterative algorithms for the IAPWS-IF97

Using an Industrial Formulation EoS as the IAPWS-IF97, we can define a residual function, $\mathbf{F} = \mathbf{F}(p,T)$, whose zero gives the thermodynamic variable pair (p,T) we are looking for. The residual function is defined as $\mathbf{F}:\Omega \rightarrow \mathbb{R}^2$, where $\Omega \in \mathbb{R}^2$ is the validity domain of the EoS. For instance, in the single-phase domain, for both the HEM and HRM, we need to solve:

$$\mathbf{F}(p,T) = \begin{pmatrix} e - e_{IAPWS97}(p,T) \\ v - v_{IAPWS97}(p,T) \end{pmatrix}. \tag{4.83}$$

In thermodynamics, according to Gibbs phase rule, the degrees of freedom are 2 in the single-phase region, 1 in the stable two-phase region and 0 for both triple and critical points. Therefore, in the stable two-phase region, the residual function, $\mathbf{F}$, becomes $\mathrm{F}:\mathscr{D} \rightarrow \mathbb{R}$, where $\mathscr{D}$ represents the two-phase domain. In practice, for $\mathrm{F} = \mathrm{F}(p)$, the domain is $\mathscr{D} = [p_{triple}, p_{critic}]$. For $\mathrm{F} = \mathrm{F}(T)$, we have $\mathscr{D} = [T_{triple}, T_{critic}]$.

For instance, considering $\mathrm{F} = \mathrm{F}(p)$, in the stable two-phase domain, the residual function is:

$$\mathrm{F} = e - x\,e_v(p) - (1-x)\,e_l(p) \tag{4.84}$$

where:

$$x = x(p) = \frac{e \; - \; e_l(p)}{e_v(p) - e_l(p)}. \tag{4.85}$$

Equation (4.84) just holds for the stable two-phase domain. Hence, it is not adequate for the HRM. In the metastable two-phase domain, for the HRM, we need to solve:

$$\mathbf{F}(p,T) = \begin{pmatrix} e - x\,e_v(p) - (1-x)\,e_l(p,T) \\ v - x\,v_v(p) - (1-x)\,v_l(p,T) \end{pmatrix}, \tag{4.86}$$

where the flow quality, x, is obtained from Eq. (4.17).

Equations (4.83) and (4.86) are two-dimensional non-linear equations. Solving systems of more than one nonlinear equation is generally hard. To get a globally convergent solver, optimization and backtracking methods are often employed. Various methods of optimization/backtracking exist, authors suggest the ones in [212]. Even though such a procedure allows one to implement very accurate EoS, it is extremely time consuming (hundreds-thousands times longer than a look-up table interpolation [147]).

4.11 Appendix 4.D: Derivatives of IAPWS-IF97 for the Bicubic Interpolation

This paragraph outlines how the needed derivatives for the evaluation of the bicubic interpolation coefficients have been calculated. Therefore it serves as a support tool for a more effective understanding of the procedures presented in 4.5.2.

Let us consider the pressure p as our function F of interest. If the point defined by the couple (v,e) belongs to **Region 1**, **2** or **5** of the IAPWS-IF97 domain, first order derivatives can be evaluated

as:

$$\left(\frac{\partial p}{\partial v}\right)_e = \left(\frac{\partial v}{\partial p}\right)_e^{-1} = \left[\left(\frac{\partial v}{\partial p}\right)_T - \left(\frac{\partial v}{\partial T}\right)_p \left(\frac{\partial e}{\partial p}\right)_T \left(\frac{\partial e}{\partial T}\right)_p^{-1}\right]^{-1}, \tag{4.87}$$

$$\left(\frac{\partial p}{\partial e}\right)_v = \left(\frac{\partial e}{\partial p}\right)_v^{-1} = \left[\left(\frac{\partial e}{\partial p}\right)_T - \left(\frac{\partial e}{\partial T}\right)_p \left(\frac{\partial v}{\partial p}\right)_T \left(\frac{\partial v}{\partial T}\right)_p^{-1}\right]^{-1}, \tag{4.88}$$

where v and e are the coordinates of the thermodynamic plane, while p and T are pressure and temperature that have been determined by setting to zero Eq. (4.83).

In IAPWS-IF97 [273] the basic equations for Region 1, 2 and 5 are expressed in terms of dimensionless specific Gibbs free enthalpy:

$$\frac{g(p,T)}{RT} = \gamma(\pi,\tau), \tag{4.89}$$

where $\pi = p/p^*$ and $\tau = T^*/T$ with given p^* and T^* depending on the region. R represents the specific gas constant of ordinary water. Therefore, it is possible to evaluate the partial derivatives which appear in the square parentheses of Eq. (4.87) and (4.88) as follows:

$$\left(\frac{\partial v}{\partial p}\right)_T = \frac{RT}{p^2}\pi^2\gamma_{\pi\pi}, \tag{4.90}$$

$$\left(\frac{\partial v}{\partial T}\right)_p = \frac{R}{p}\pi\left(\gamma_\pi - \tau\gamma_{\pi\tau}\right), \tag{4.91}$$

$$\left(\frac{\partial e}{\partial p}\right)_T = \frac{RT^*}{p^*}\left(\gamma_{\pi\tau} - \frac{\gamma_\pi}{\tau} - \frac{\pi}{\tau}\gamma_{\pi\pi}\right) = -T\left(\frac{\partial v}{\partial T}\right)_p - p\left(\frac{\partial v}{\partial p}\right)_T, \tag{4.92}$$

$$\left(\frac{\partial e}{\partial T}\right)_p = -R\tau^2\left(\gamma_{\tau\tau} + \frac{\pi}{\tau^2}\gamma_\pi - \frac{\pi}{\tau}\gamma_{\pi\tau}\right), \tag{4.93}$$

with $\gamma_\pi = \left(\partial\gamma/\partial\pi\right)_\tau$, $\gamma_{\pi\pi} = \left(\partial^2\gamma/\partial\pi^2\right)_\tau$ and $\gamma_{\pi\tau} = \partial^2\gamma/(\partial\pi\partial\tau)$.

If the point belongs to **Region 3**:

$$\left(\frac{\partial p}{\partial v}\right)_e = \left(\frac{\partial p}{\partial v}\right)_T - \left(\frac{\partial p}{\partial T}\right)_v \left(\frac{\partial e}{\partial v}\right)_T \left(\frac{\partial e}{\partial T}\right)_v^{-1}, \tag{4.94}$$

$$\left(\frac{\partial p}{\partial e}\right)_v = \left(\frac{\partial p}{\partial T}\right)_v \left(\frac{\partial e}{\partial T}\right)_v^{-1}. \tag{4.95}$$

The basic equation for this region is a fundamental equation for the specific Helmholtz free energy f, expressed in dimensionless form:

$$\frac{f\left(\rho,T\right)}{RT} = \Phi(\delta,\tau), \tag{4.96}$$

where $\delta = \rho/\rho^*$, $\tau = T^*/T$ with ρ^* and T^* equal to the critical values as defined in [273]. Relating the thermodynamic properties to the dimensionless Helmholtz free energy and its derivatives when using Eq. (4.96), it is possible to obtain:

$$\left(\frac{\partial p}{\partial T}\right)_v = -R\delta^2\tau\rho^*\left(\Phi_{\delta\tau} - \frac{\Phi_\delta}{\tau}\right), \tag{4.97}$$

$$\left(\frac{\partial p}{\partial v}\right)_T = -\rho^2\left(\frac{\partial p}{\partial \rho}\right)_T = -\rho^2 RT\left(2\delta\Phi_\delta + \delta^2\Phi_{\delta\delta}\right), \tag{4.98}$$

$$\left(\frac{\partial e}{\partial T}\right)_v = -R\tau^2\Phi_{\tau\tau}, \tag{4.99}$$

$$\left(\frac{\partial e}{\partial v}\right)_T = -\rho^2\left(\frac{\partial e}{\partial \rho}\right)_T = -\rho\delta RT^*\Phi_{\delta\tau}, \tag{4.100}$$

where $\Phi_\delta = (\partial\Phi/\partial\delta)_\tau$, $\Phi_{\delta\delta} = \left(\partial^2\Phi/\partial\delta^2\right)_\tau$, $\Phi_{\tau\tau} = \left(\partial^2\Phi/\partial\tau^2\right)_\delta$ and $\Phi_{\delta\tau} = \partial^2\Phi/(\partial\delta\partial\tau)$.

Then, second order derivatives are approximated as difference quotients of first derivatives:

$$\left(\frac{\partial^2 p}{\partial v^2}\right)_e = \frac{\left(\frac{\partial p}{\partial v}\right)_{v+\delta,e} - \left(\frac{\partial p}{\partial v}\right)_{v-\delta,e}}{2\delta}, \tag{4.101}$$

$$\left(\frac{\partial^2 p}{\partial e^2}\right)_v = \frac{\left(\frac{\partial p}{\partial e}\right)_{e+\delta,v} - \left(\frac{\partial p}{\partial e}\right)_{e-\delta,v}}{2\delta}, \tag{4.102}$$

$$\left(\frac{\partial^2 p}{\partial e\partial v}\right) = \frac{\left(\frac{\partial p}{\partial e}\right)_{v+\delta} - \left(\frac{\partial p}{\partial e}\right)_{v-\delta}}{2\delta}. \tag{4.103}$$

Part III

The single-velocity six-equation two-phase flow model

CHAPTER 5

RIEMANN SOLVERS: A COMPARATIVE STUDY

The numerical simulation of metastable states and the use of steam-water tables are the cornerstones of our approach. Then, we decided to increase the complexity of the two-phase flow model adopting the *single-velocity six-equation model*. It represents a complex two-phase flow model but still with a very simple wave pattern because it is a homogeneous model. This model has two main positive sides with respect to the HRM employed in the previous chapter: (i) the possibility to take into account the eventual metastability of the vapor phase, and (ii) the need of two decoupled equations of state, one per phase. The latter feature ensures a greater robustness and a lower computational cost due to the complete absence of iterative procedures.

Part III is fully devoted to the single-velocity six-equation model and its use for the numerical simulation of fast transients.

In this chapter, we focus on the homogeneous portion of this hyperbolic model. The next chapter provides new modeling and numerical techniques for the source terms of this model, that is, the interphase transfers of mass and energy for the equilibrium recovery. The final chapter uses all the techniques developed in this thesis for the simulation of fast depressurizations.

As concerns its homogeneous portion, the single-velocity six-equation model can not be written in a conservative form. It poses some difficulties for the discretization of the nonconservative terms. Before using this model for the simulation of industrial test cases, a comparative study for the discretization of these terms is appropriate.

We adopt several kinds of discretization to ascertain whether those terms are effectively important or not. From this analysis it was found that, when this model is used to simulate the five-equation Kapila's model, the different discretizations of the nonconservative terms assume a relevant role only in the case of very strong shock waves in the genuinely two-phase mixture. This is not the case of a Loss of Coolant Accident, but it could occur during a waterhammer or a steam explosion.

HLLC-type and path-conservative schemes for a single-velocity six-equation two-phase flow model: a comparative study.

Accepted for publication by Applied Mathematics and Computation.

M. De Lorenzo[1], M. Pelanti[1], Ph. Lafon[1].

The present article deals with the numerical integration of a six-equation single-velocity two-phase flow model with stiff mechanical relaxation. This model can be employed to approximate efficiently the well known single-velocity single-pressure five-equation model of Kapila et al. [Physics of Fluids, 13, 2001]. Work in the literature has shown the efficiency of the six-equation model in simulating complex two-phase flows involving cavitation and evaporation processes. The aim of this work is to present and discuss various numerical schemes for this two-phase model focusing on the integration of the nonconservative terms appearing in the phasic energy equations. In fact, previous work has suggested that the choice of the discretization method for the nonconservative terms often does not play a significant role. Two new methods are proposed: a path-conservative HLLC-type scheme that is based on the Dal Maso–LeFloch–Murat theory, and a generalized HLLC-type scheme that is based on a Suliciu's Riemann solver. The latter scheme has the important property of preserving the positivity of the intermediate states of the conserved quantities. Moreover, we also approximate solutions of the six-equation model by applying two path-conservative schemes recently proposed in the literature, which have been derived from the Osher and HLLEM Riemann solvers. We show comparisons of the different numerical schemes for several test cases, including cavitation problems and shock tubes. An efficiency study for first and second order schemes is also presented. Numerical results show that different methods corresponding to different numerical treatments of the nonconservative terms give analogous results and they are all able to produce accurate approximations of solutions of the Kapila's five-equation model, except, as expected, for shocks in two-phase mixtures with very high pressure ratios.

5.1 Introduction

Multiphase mixtures evolving under unique velocity and pressure for all phases are involved in many practical applications, e.g. condensed phase mixtures, solid explosives, shock propagation into solid alloys, and fast depressurizations triggering liquid-vapor transition. For such problems, the well known two-phase flow model of Kapila et al. [139] is particularly suited. This is a compressible two-phase flow model that belongs to the class stemming from the Baer & Nunziato model [12]. Kapila et al. [139] model involves five partial differential equations: two equations for the phasic masses, one equation for the mixture momentum, one equation for the mixture energy and a nonconservative equation for the volume fraction of one of the phases. In this model the phases evolve at the same velocity with unique pressure but remain in nonequilibrium regarding chemical

[1] IMSIA UMR EDF-CNRS-CEA-ENSTA, Palaiseau, France 91120.

and thermal effects. Therefore this model is suited for simulations involving chemical reactions and phase changes. Allowing pressure nonequilibrium between the phases, we can obtain another reduced model from the full nonequilibrium model in [12], namely a six-equation single-velocity two-phase flow model [139, 200, 234, 283]. When mechanical relaxation terms are incorporated in the model and instantaneous relaxation is assumed, the six-equation model can be used as an alternative way to solving directly the five-equation model of [139].

To simulate multiphase mixtures evolving under unique velocity and pressure, it is also possible to use the 7-equation model of Baer & Nunziato [12] with stiff pressure and velocity relaxation as shown in [74, 283]. However, using the 7-equation model leads to extra equations and much more complicated wave patterns in the Riemann solution structure than is needed in the framework of Godunov-type schemes. This translates to a greater encumbrance of the numerical model. Zein et al. and Ha et al. [120, 283] made a comparison in terms of CPU time between the 6-equation and the 7-equation model and it turned out that the latter can be as much as ten times more expensive.

The 6-equation single-velocity two-phase flow model with stiff pressure relaxation has recently received increasing attention in the literature, see e.g. [55, 120, 200, 202, 234, 283]. An undergoing project of the authors in the context of nuclear reactors safety studies includes the implementation of this model within the EUROPLEXUS[2] code. The aim is to be able to simulate metastable flows that may occur in hypothetical accidents of nuclear power plants. The choice of this model is motivated by several advantageous features both from the physical and numerical solution point of view:

i. capability of dealing with metastable fluids,

ii. effective speed of sound equal to that of Wood [279], thanks to the instantaneous pressure relaxation,

iii. full thermodynamic decoupling between phases' Equations of State (EoS).

iv. simple Riemann solution wave pattern (two acoustic waves and one contact wave like the Euler equations),

iv. greater robustness of numerical approximations with respect to the Kapila's 5-equation model in relation to positivity preservation of the volume fraction.

The third property is undoubtedly a very important feature for the applications we are interested in. In fact, for simulating hypothetical accidents of nuclear power plants, it is of paramount importance to use accurate steam-water properties, in both the stable and metastable thermodynamic domains. Conversely to Kapila's model, the six-equation model needs fully decoupled equations of state for liquid and vapor:

$$p_l = p_l(\rho_l, e_l), \qquad p_v = p_v(\rho_v, e_v), \tag{5.1}$$

where here we have expressed the phasic pressures p_l, p_v of liquid and vapor, respectively, in terms of the phasic densities ρ_l, ρ_v, and of the specific internal energies e_l, e_v. This feature will allow us to

[2]EUROPLEXUS code is owned by the Commissariat à l'Energie Atomique et aux Energies Alternatives (CEA) and the Joint Research Centre (JRC) of the European Union.

easily use the fast and accurate algorithm for water properties calculation proposed by the authors in [79]. Instead, with Kapila's model, iterative algorithms would be necessary in order to guarantee pressure equality, $p_l = p_v = p$. However, for the present paper, only the simple stiffened gas EoS are used. This is in particular advantageous to derive analytical solutions to be used as references.

The six-equation model has nonconservative products appearing in the phasic total energy transport equations, which express interphase total energy transfers. We can recognize two different nonconservative terms in the phasic total energy equations. One refers to the gradient of the volume fraction, which is typical of many two-phase flow models and is inactive across shock waves due to the character of the advection equation of the volume fraction. Another term serves to split the mixture total energy coherently with the assumption of equal velocity and is active across shock waves. The 5-equation model of Kapila et al. [139] also contains nonconservative products. In particular, a nonconservative term depending on the divergence of the velocity appears in the transport equation governing the volume fraction of one of the phases. Due to this term it is difficult to obtain discretizations of the five-equation model that ensure positivity of the volume fraction. This difficulty does not arise in discretizations based on the six-equation model since only a simple homogeneous advection equation for the volume fraction needs to be integrated. On the other hand, the presence of nonconservative terms in the phasic energy equations of the six-equation model poses difficulties in its numerical solution. In the work of Pelanti–Shyue [200, 201] two Riemann solvers were proposed for this two-phase flow model: a Roe-type solver accounting naturally for nonconservative terms through the Roe matrix associated to the quasi-linear form of the model system, and a simple HLLC-type solver that neglects discrete contributions of nonconservative terms in the energy equations. Some comparisons of the solvers suggested that the choice of the discretization of the nonconservative terms does not play a significant role. The aim of the present work is to investigate more in depth the effect of different numerical treatments of the nonconservative terms of the six-equation model. For this model we here present, compare and discuss various finite volume schemes based on different approximate Riemann solvers. Two new methods are proposed: a path-conservative HLLC-type scheme that is based on the Dal Maso, LeFloch, Murat theory [68], and a generalized HLLC-type scheme that is based on a Suliciu's Riemann solver [35]. The latter scheme has the very important property of preserving the positivity of the intermediate states of the conserved quantities. Moreover, we also approximate solutions of the six-equation model by applying two path-conservative schemes recently proposed in the literature, namely the Dumbser-Osher-Toro (DOT) scheme [90] and the HLLEM scheme in [88]. We show comparisons of the different numerical schemes for several test cases, including cavitation problems and shock tubes. All the schemes are compared against the exact solution of the Kapila et al. model when it is available (smooth solutions) or to the Saurel et al. [232] jump conditions when shock waves are involved. An efficiency study for first and second order schemes is also presented. Numerical results show that different methods corresponding to different numerical treatments of the nonconservative terms produce accurate approximations to solutions of the Kapila et al. model, except, as expected, for shocks in two-phase mixtures with very high pressure ratios.

The paper is organized as follows. In Section 5.2 we present the 6-equation single-velocity two-phase flow model with stiff pressure relaxation together with its mathematical characteristics. In

Section 5.3 we discuss the physical meaning of the nonconservative terms in the model and possible numerical approaches for nonconservative systems. Section 5.4 is devoted to the presentation of the numerical methods that we use. Here we present in detail various Riemann solvers for the homogeneous six-equation model and we also briefly recall the pressure relaxation numerical procedure of [200]. Numerical results and comparisons of the different schemes are presented in Section 5.5. Some conclusions and future steps of this work are discussed in Section 5.6.

5.2 The six-equation single-velocity two-phase flow model

The six-equation single-velocity two-phase flow model was initially proposed in Saurel et al. [234] and it was later reformulated by Pelanti & Shyue in [200] to ensure *mixture-energy-consistency* at the discrete level. It is a two-phase, two-pressure system modelling the dynamics of mixture fluids, which can also deal with phase transition when the phases are the liquid and its vapor. To each phase is assigned a density ρ_k, a pressure p_k , a specific internal energy e_k and a volume fraction α_k, where $k = 1,2$. The velocity is assumed to be equal for the two phases. In one spatial dimension the model system reads

$$\begin{cases} \partial_t \alpha_1 + u\partial_z \alpha_1 = \mu(p_1 - p_2), \\ \partial_t(\alpha_1\rho_1) + \partial_z(\alpha_1\rho_1 u) = 0, \\ \partial_t(\alpha_2\rho_2) + \partial_z(\alpha_2\rho_2 u) = 0, \\ \partial_t(\rho u) + \partial_z(\rho u^2 + \alpha_1 p_1 + \alpha_2 p_2) = 0, \\ \partial_t(\alpha_1\rho_1 E_1) + \partial_z[\alpha_1(\rho_1 E_1 + p_1)u] + \Sigma(\mathbf{U}, \partial_z \mathbf{U}) = -\mu p_i(p_1 - p_2), \\ \partial_t(\alpha_2\rho_2 E_2) + \partial_z[\alpha_2(\rho_2 E_2 + p_2)u] - \Sigma(\mathbf{U}, \partial_z \mathbf{U}) = +\mu p_i(p_1 - p_2), \end{cases} \tag{5.2}$$

where: $E_k = e_k + u^2/2$ is the phasic total energy and $\mathscr{E}_k = \rho_k e_k$ is the phasic internal energy. The right hand side describes the pressure relaxation process. Here, $p_i = \frac{Z_2 p_1 + Z_1 p_2}{Z_1 + Z_2}$ indicates the interface pressure, where $Z_k = \rho_k c_k$ is the acoustic impedance of phase k. Since the aim is to approximate solutions of the Kapila's model [139], throughout the paper, the pressure relaxation process is assumed to take place instantaneously: $\mu \to +\infty$. The saturation condition $\alpha_1 + \alpha_2 = 1$ is obviously assumed. The speed of sound associated to the homogeneous portion of system (5.2) is

$$c_{hom} = \sqrt{Y_1 c_1^2 + Y_2 c_2^2}. \tag{5.3}$$

Let us remark however that due to the instantaneous pressure relaxation process the effective speed of sound of system (5.2) is given by the well-known Wood's relation [279]

$$\frac{1}{\rho^2 c_{wood}^2} = \frac{Y_1}{\rho_1^2 c_1^2} + \frac{Y_2}{\rho_2^2 c_2^2}, \tag{5.4}$$

where $Y_k = \alpha_k\rho_k/\rho$ denotes the mass fraction of the specie k and $\rho = \alpha_1\rho_1 + \alpha_2\rho_2$ is the mixture density. Note that the Liu' subcharacteristic condition [172] holds: $c_{wood} \leq c_{hom}$. We refer to [109] for a discussion on the speed of sound of a hierarchy of relaxed two-phase flow models that includes the models considered here. The equation of state used throughout the paper is the stiffened gas EoS

$$p_k = (\gamma_k - 1)(\mathscr{E}_k - \eta_k\rho_k) - \gamma_k\pi_k. \tag{5.5}$$

The nonconservative terms in the phasic total energy equations are

$$\Sigma(\mathbf{U},\partial_z\mathbf{U}) = -u\,[Y_2\partial_z(\alpha_1 p_1) - Y_1\partial_z(\alpha_2 p_2)]. \tag{5.6}$$

These terms are non-zero if $u \neq 0$ and if $Y_1 Y_2 \neq 0$, that is, the fluid is a mixture containing both species moving at non-zero velocity. Together with the equations of state for p_k, this two-phase flow model is a nonlinear hyperbolic system of the form

$$\partial_t\mathbf{U} + \partial_z\mathbf{F}(\mathbf{U}) + \mathbf{B}(\mathbf{U})\partial_z\mathbf{U} = \mathbf{b}, \qquad z \in \mathbb{R}, \quad t \in \mathbb{R}^+, \tag{5.7}$$

where $\mathbf{U} \in \Omega_U \subset \mathbb{R}^6$ is the state vector and Ω_U is the phase-space. The conservative part of the system is contained in the nonlinear flux vector $\mathbf{F} = \mathbf{F}(\mathbf{U})$, and the nonconservative terms are expressed in the nonconservative product $\mathbf{B}(\mathbf{U})\partial_z\mathbf{U}$. Alternatively, the above PDE can be cast in its quasi-linear form

$$\partial_t\mathbf{U} + \mathbf{A}(\mathbf{U})\partial_z\mathbf{U} = \mathbf{b}, \tag{5.8}$$

where the matrix $\mathbf{A}(\mathbf{U}) = \frac{\partial\mathbf{F}}{\partial\mathbf{U}} + \mathbf{B}(\mathbf{U})$ includes both the conservative and the nonconservative terms. The term $\frac{\partial\mathbf{F}}{\partial\mathbf{U}}$ is the Jacobian of the nonlinear flux. The system is hyperbolic since $\mathbf{A}(\mathbf{U})$ has only real eigenvalues and a full set of linearly independent eigenvectors exists. We indicate the matrix of the eigenvalues of with $\Lambda(\mathbf{U}) = \text{diag}(\lambda_1, \lambda_2, ..., \lambda_6)$, where $\lambda_1 \leq \lambda_2, ..., \leq \lambda_6$. The matrices of right and left eigenvectors are $\mathbf{R}(\mathbf{U}) = (\mathbf{r}_1, \mathbf{r}_2, ..., \mathbf{r}_6)$ and $\mathbf{L}(\mathbf{U}) = (\mathbf{l}_1^T, \mathbf{l}_2^T, ..., \mathbf{l}_6^T)$. We assume that left and right eigenvectors be orthonormal: $\mathbf{L}\cdot\mathbf{R} = \mathbf{I}$, i.e. $\mathbf{L} = \mathbf{R}^{-1}$. $\mathbf{A}$ and $\mathbf{B}$ are reported in 5.7, $\mathbf{R}$ in 5.8.

5.3 Nonconservative terms of the six-equation model

The 6-equation single-velocity two-phase flow model introduced in (5.2) presents a nonconservative advection equation of the phasic volume fraction α_1 and nonconservative products in the phasic total energy equations. In this section we analyze the meaning of the latter nonconservative products grouped in $\Sigma(\mathbf{U},\partial_z\mathbf{U})$. First of all, note that the nonconservative products are of opposite sign in the two phasic total energy equations. It means that the mixture total energy $\rho E = \alpha_1\rho_1 E_1 + \alpha_2\rho_2 E_2$ is always conserved independently of $\Sigma(\mathbf{U},\partial_z\mathbf{U})$. This property holds both at the continuous and at the discrete level. A conservative scheme for the conservative portion of the 6-equation system will always guarantee conservation of the mixture total energy, independently of the choice of the numerical discretization of nonconservative terms. This feature is the key to construct a mixture-energy-consistent scheme, and it represents the principal advantage of the total-energy based formulation of [200] versus the internal-energy-based one of [234]. The terms in $\Sigma(\mathbf{U},\partial_z\mathbf{U})$ are, essentially, energy-exchange terms due to forces exerted between phases. We start by the phasic momentum equation

$$\partial_t(\alpha_k\rho_k u) + \partial_z(\alpha_k\rho_k u^2 + \alpha_k p_k) = F. \tag{5.9}$$

As we will see in the following the force denoted by F generates the energy-exchange terms grouped in $\Sigma(\mathbf{U},\partial_z\mathbf{U})$. Being system (5.2) in 1D, here F is a force per unit of volume. Using the continuity equation of phase k, Eq. (5.9) becomes

$$\alpha_k\rho_k\frac{Du}{Dt} + \partial_z(\alpha_k p_k) = F. \tag{5.10}$$

Similarly, the momentum equation of the mixture can be written as

$$\rho \frac{Du}{Dt} + \partial_z(\alpha_1 p_1 + \alpha_2 p_2) = 0. \tag{5.11}$$

Substituting the material derivative $\frac{Du}{Dt}$ of Eq. (5.11) into (5.10), one obtains the expression of the force F:

$$F = Y_2 \partial_z(\alpha_1 p_1) - Y_1 \partial_z(\alpha_2 p_2) \tag{5.12}$$

Obviously, the rate of energy exchange due to the mechanical work is *force* $\cdot$ *velocity*, thus one retrieves Eq. (5.6). To give a physical interpretation of this mechanical work, let us rewrite the force F as

$$F = (Y_2 p_1 + Y_1 p_2)\partial_z \alpha_1 + Y_2 \alpha_1 \partial_z p_1 - Y_1 \alpha_2 \partial_z p_2 \tag{5.13}$$

and suppose that phases have the same pressure $p_1 = p_2 = p$, thus

$$F = p\,\partial_z \alpha_1 + (\alpha_1 - Y_1)\partial_z p. \tag{5.14}$$

Given that the pressure equilibrium has been imposed, we retrieve the same formulation found by Kreeft & Koren [146] for the Kapila's 5-equation model. In fact, the physical interpretation is equivalent. The term $p\,\partial_z \alpha_1$ takes into account the variation of the volume fractions along the geometrical coordinate z. This feature is illustrated in Fig. 5.1 for a stratified flow pattern but holds for a generic flow pattern. Under the assumption of pressure equilibrium, indicating the dashed contours of Fig. 5.1 with S, in differential form, one may write

$$p\,\mathbf{n}\,\mathrm{d}S = \mathrm{d}(\alpha p) - p\,\mathrm{d}\alpha \tag{5.15}$$

where the first term indicates the net pressure force at the two vertical faces located at z and $z + \mathrm{d}z$, and is taken into account in the phasic total energy equations. The second term is the force exerted by the pressure along the interface between z and $z + \mathrm{d}z$. This term is quite typical in the two-phase flow models. It is present in all models treating separately the phasic momentum and/or the phasic energy. Namely, it is encountered in the 7-equation model [12], in the single-velocity 6-equation model, in the widely diffused single-pressure two-fluid 6-equation model [136], and in the reformulation of the Kapila's model made in [146]. Let us note that the nonconservative term in the advection equation for the volume fraction in the six-equation model is associated to a linearly degenerate field, and this term is inactive across shock waves. The volume fractions in this model is invariant across acoustic waves and shocks.

As discussed by Kreeft & Koren [146], the term $(\alpha_1 - Y_1)\partial_z p$ represents a force that ensures the velocity equilibrium between phases. In fact, a pressure gradient would accelerate or decelerate more the lighter phase than the heavier one (Newton's second law of motion), hence this term serves to make a repartition of the mixture total energy that is coherent with the velocity equilibrium. To better explain this feature, let us consider a contact wave with density and volume fractions discontinuities. Left and right velocities must be equal, as well as phasic and mixture pressures, then $u(z,t) = \hat{u}$ and $p_k(z,t) = \hat{p}$, $k = 1,2$, $\forall\, z \in \mathbb{R}$, $\forall\, t \in \mathbb{R}^+$. In this case, system (5.8) can be linearized and written as a system of advection equations:

$$\partial_t \mathbf{U} + \hat{u}\partial_z \mathbf{U} = \mathbf{b}. \tag{5.16}$$

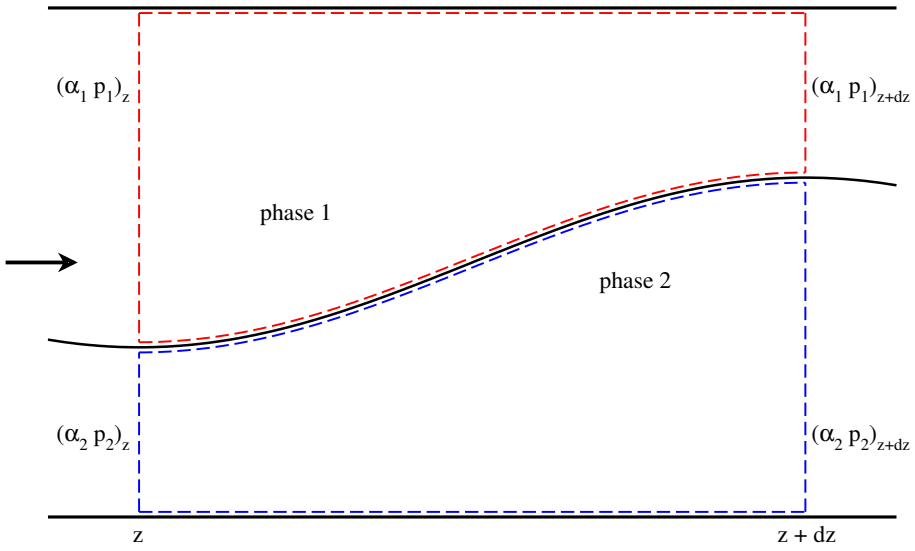

FIGURE 5.1. Sketch of the phasic volume fraction increasing along z. For simplicity, here it has been illustrated as a stratified flow.

This property does not hold if the nonconservative terms of Eq. (5.6) are neglected. Neglecting them, the repartition of the mixture energy would not ensure the velocity equilibrium because the phasic internal energy equations would write

$$\partial_t(\alpha_k\rho_k e_k) + \hat{u}\partial_z(\alpha_k\rho_k e_k) + \hat{p}\hat{u}\partial_z\alpha_k = 0. \tag{5.17}$$

Being (5.17) not an advection equation, it will cause a perturbation of $p_k(z,t)$ across the LD wave, hence, in turn, a perturbation of $u(z,t)$ as just mentioned in [146]. At the discrete level, neglecting them, requires an extra effort to guarantee the pressure and velocity continuity across the LD wave as done in the Riemann solver proposed in [200].

Finally, the choice of the discretization of the nonconservative terms affects the approximation of the repartition of mixture total energy between the two phases. In the following we numerically investigate the effects of different discretizations.

5.3.1 Numerical treatment of the nonconservative terms

The 6-equation single-velocity two-phase flow model is described by a balance system of equations which is not a system of conservation laws. In fact, the matrix of nonconservative terms $\mathbf{B}(\mathbf{U}) \neq 0$ (see 5.8). Due to the nonconservative form of the equations, the standard notion of *weak solution* in the sense of distributions does not apply. More precisely, because of the nonconservative term, $\mathbf{B}(\mathbf{U})\partial_z\mathbf{U}$, and the fact that products of distributions are not defined by the theory of distributions [239], it is not possible to rigorously define the notion of weak solution for system (5.2) and it is not possible to derive Rankine-Hugoniot jump conditions. Moreover, the uniqueness of solutions can not be guaranteed in the presence of discontinuities.

Nonconservative hyperbolic systems arise in a wide range of applications, e.g. in the modeling of two-phase flow [136, 139, 187, 254] but also in the modelling of great deformations of elastoplastic

materials [113, 162]. These systems have proven to be difficult to analyze, nevertheless, their wide range of applications has motivated large efforts both in the theoretical and numerical frameworks. Significant studies have been presented in the literature to address this classical problem, notably the Dal Maso, Le Floch and Murat (DLM) theory [68], and the work by Bianchini & Bressan [26]. The basic idea of the DLM theory is to describe the nonconservative product as

$$[\mathbf{B}(\mathbf{U})\partial_z \mathbf{U}]_\phi = \int_0^1 \mathbf{B}(\phi(\mathbf{U}_\ell, \mathbf{U}_r, s))\frac{\partial \phi}{\partial s} ds, \tag{5.18}$$

when $\mathbf{U}$ has a jump discontinuity from $\mathbf{U}_\ell$ to $\mathbf{U}_r$. Here $\phi(\mathbf{U}_\ell, \mathbf{U}_r, 0) = \mathbf{U}_\ell$ and $\phi(\mathbf{U}_\ell, \mathbf{U}_r, 1) = \mathbf{U}_r$. The DLM theory is a generalization of Volpert's [271] and Toumi's works [266]. Based on the DLM theory, Parés [193] provided a theoretical framework for the design of well-balanced numerical schemes for solving nonconservative hyperbolic systems. Then, several Riemann solvers for nonconservative hyperbolic systems have been designed [47, 88–90, 193, 230, 261]. In this work we will use the Dumbser-Osher-Toro (DOT) scheme [90] and the HLLEM scheme [88]. A new path conservative HLLC scheme is also proposed.

Let us also mention other ways of treating numerically nonconservative terms. First, solvers that are not restricted to systems of conservation laws can incorporate naturally these terms, as in the case of the Roe-type solver of [200] or the new Suliciu-type solver proposed here. In this case we can consider that the resulting schemes define implicitly a path of integration for the nonconservative terms. Another way of dealing with nonconservative terms is to perform a parabolic regularization of the homogeneous nonconservative system using the following *viscous system*: $\partial_t \mathbf{U}^\epsilon + \mathbf{A}(\mathbf{U}^\epsilon)\partial_z \mathbf{U}^\epsilon = \epsilon \partial_{zz} \mathbf{U}^\epsilon$, where the viscosity coefficient $\epsilon \to 0$. Further details are contained in Bianchini & Bressan [26]. Sainsaulieu used a similar approach for two-phase flow calculations [229]. Finally, some authors have employed simple numerical approximations by assuming for instance that nonconservative terms do not vary during each time step. For two-phase flow simulations, such strategy has been extensively adopted to take into account the nonconservative terms for the 5-equation and 7-equation models [231, 234, 283].

5.4 Numerical solution methods

In this section, we discuss the numerical methods used for solving system (5.2). The presence of nonconservative products makes harder the choice of the Riemann solver to be used. The solution is obtained by a succession of operators [256],

$$\mathbf{U}^{n+1} = L_p^{\Delta t} L_{hyp}^{\Delta t} \mathbf{U}^n \tag{5.19}$$

where $L_{hyp}^{\Delta t}$ denotes the hyperbolic operator and $L_p^{\Delta t}$ denotes the integration operator for the pressure relaxation terms. First, we examine the hyperbolic operator, which poses the main difficulties due to the presence of nonconservative terms.

5.4.1 Hyperbolic operator

The application of the hyperbolic operator to $\mathbf{U}^n$ will give an intermediate state $\mathbf{U}^{n+} = L_{hyp}^{\Delta t} \mathbf{U}^n$, which is used in the subsequent step as initial value for the the pressure relaxation. In the so-called

wave propagation form of [168], the second-order numerical scheme for the hyperbolic operator is as follows:

$$\mathbf{U}_i^{n+} = \mathbf{U}_i^n - \frac{\Delta t}{\Delta z}(\mathscr{A}^+\Delta\mathbf{U}_{i-\frac{1}{2}} + \mathscr{A}^-\Delta\mathbf{U}_{i+\frac{1}{2}}) + \frac{\Delta t}{\Delta z}(\mathbf{F}_{i-\frac{1}{2}}^{2nd} - \mathbf{F}_{i+\frac{1}{2}}^{2nd}). \tag{5.20}$$

$\mathscr{A}^\pm\Delta\mathbf{U}_{i+\frac{1}{2}}$ are the so-called fluctuations at the interface $z_{i+\frac{1}{2}}$ between cells i and $i+1$. Namely, $\mathscr{A}^+\Delta\mathbf{U}_{i+\frac{1}{2}}$ is the right-going fluctuation, $\mathscr{A}^-\Delta\mathbf{U}_{i+\frac{1}{2}}$ is the left-going one. The fluctuations can be calculated as:

$$\mathscr{A}^+\Delta\mathbf{U}_{i-\frac{1}{2}} = \sum_{m=1}^{M} s_{i-\frac{1}{2}}^{m+}\mathscr{W}_{i-\frac{1}{2}}^m, \qquad \mathscr{A}^-\Delta\mathbf{U}_{i+\frac{1}{2}} = \sum_{m=1}^{M} s_{i+\frac{1}{2}}^{m-}\mathscr{W}_{i+\frac{1}{2}}^m. \tag{5.21}$$

where $s^+ = \max(s,0)$ and $s^- = \min(s,0)$, and where $\mathscr{W}^m$ and s^m denote the mth wave and associated speed, respectively, of the approximate Riemann solution wave structure. The second-order accuracy of the hyperbolic operator is achieved thanks to the second-order correction fluxes:

$$\mathbf{F}_{i+\frac{1}{2}}^{2nd} = \frac{1}{2}\sum_{m=1}^{M}|s_{i+\frac{1}{2}}^m|\left(1-\frac{\Delta t}{\Delta z}|s_{i+\frac{1}{2}}^m|\right)\mathscr{W}_{i+\frac{1}{2}}^{m,2nd} \tag{5.22}$$

where $\mathscr{W}_{i+\frac{1}{2}}^{m,2nd}$ are a modified version of $\mathscr{W}_{i+\frac{1}{2}}^m$ obtained by applying a limiter function (cf. [168]). In the following, we detail the various Riemann solvers used to calculate the fluctuations.

5.4.1.1 HLLC solver of Pelanti & Shyue without nonconservative terms

Let us recall here the approximate solver proposed in [200] for system (5.2). This solver does not discretize the nonconservative terms $\Sigma(\mathbf{U},\partial_z\mathbf{U})$ in the phasic total energy equations of (5.2) but it is built to guarantee the pressure and velocity continuity across the contact discontinuity. Except for the first equation, which describes the advection of α_1, the system is now in a conservative form. In such a case, the interfacial fluctuations of Eq. (5.20) may be defined as:

$$\mathscr{A}^+\Delta\mathbf{U}_{i-\frac{1}{2}} = \mathbf{F}_i - \mathbf{F}_{i-\frac{1}{2}}^{HLLC}, \qquad \mathscr{A}^-\Delta\mathbf{U}_{i+\frac{1}{2}} = \mathbf{F}_{i+\frac{1}{2}}^{HLLC} - \mathbf{F}_i. \tag{5.23}$$

This solver consists in applying the HLLC method [265] to the conservative portion of the system plus the advection equation for α_1. The resulting solver consists of three waves $\mathscr{W}^i$, $i=1,2,3$, moving at speeds

$$s^1 = S_\ell, \qquad s^2 = S^*, \qquad s^3 = S_r, \tag{5.24}$$

that separate four constant states $\mathbf{U}_\ell$, $\mathbf{U}_\ell^*$, $\mathbf{U}_r^*$ and $\mathbf{U}_r$. Here we indicate with ${}^*\ell$, ${}^*r$ quantities corresponding to the states $\mathbf{U}_\ell^*$ and $\mathbf{U}_r^*$ adjacent (respectively on the left and on the right) to the middle wave propagating at speed S^*. Following Davis [72] we define

$$S_\ell = \min(u_\ell - c_\ell, u_r - c_r), \qquad S_r = \max(u_\ell + c_\ell, u_r + c_r). \tag{5.25}$$

The speed S^* is then determined as in [264]:

$$S^* = u^* = \frac{p_r - p_\ell + \rho_\ell u_\ell(S_\ell - u_\ell) - \rho_r u_r(S_r - u_r)}{\rho_\ell(S_\ell - u_\ell) - \rho_r(S_r - u_r)}. \tag{5.26}$$

The left and right sound speeds c_ℓ and c_r correspond to the sound speed of the homogeneous six-equation model c_{hom} in (5.3). Note that although nonconservative terms are neglected in this simple

HLLC solver in the definition of the waves for the phasic total energies, the speed of sound used in the definition of the speeds of the waves is the one of the model that does include nonconservative terms. The middle states $\mathbf{U}_\ell^*$, $\mathbf{U}_r^*$ have been defined in [200] so as to satisfy the following Rankine–Hugoniot conditions, based on the conservative portion of the system:

$$\begin{aligned} F^{(\zeta)}(\mathbf{U}_r) - F^{(\zeta)}(\mathbf{U}_r^*) &= S_r(\mathbf{U}_r^{(\zeta)} - \mathbf{U}_r^{*(\zeta)}), \\ F^{(\zeta)}(\mathbf{U}_\ell^*) - F^{(\zeta)}(\mathbf{U}_\ell) &= S_\ell(\mathbf{U}_\ell^{*(\zeta)} - \mathbf{U}_\ell^{(\zeta)}), \\ F^{(\zeta)}(\mathbf{U}_r^*) - F^{(\zeta)}(\mathbf{U}_\ell^*) &= S^*(\mathbf{U}_r^{*(\zeta)} - \mathbf{U}_\ell^{*(\zeta)}), \end{aligned} \tag{5.27}$$

$\zeta = 2, \ldots, 6$. Then, the middle states are obtained as

$$\mathbf{U}_\iota^* = \begin{bmatrix} \alpha_{1,\iota} \\ (\alpha_1\rho_1)_\iota \frac{S_\iota - u_\iota}{S_\iota - S^*} \\ (\alpha_2\rho_2)_\iota \frac{S_\iota - u_\iota}{S_\iota - S^*} \\ \rho_\iota \frac{S_\iota - u_\iota}{S_\iota - S^*} S^* \\ (\alpha_1\rho_1)_\iota \frac{S_\iota - u_\iota}{S_\iota - S^*} \left(E_{1,\iota} + (S^* - u_\iota)\left(S^* + \frac{p_{1,\iota}}{\rho_{1,\iota}(S_\iota - u_\iota)} \right) \right) \\ (\alpha_2\rho_2)_\iota \frac{S_\iota - u_\iota}{S_\iota - S^*} \left(E_{2,\iota} + (S^* - u_\iota)\left(S^* + \frac{p_{2,\iota}}{\rho_{2,\iota}(S_\iota - u_\iota)} \right) \right) \end{bmatrix}, \tag{5.28}$$

$\iota = \ell, r$. The waves for this simple HLLC-type solver are

$$\mathscr{W}^1 = \mathbf{U}_\ell^* - \mathbf{U}_\ell, \quad \mathscr{W}^2 = \mathbf{U}_r^* - \mathbf{U}_\ell^*, \quad \mathscr{W}^3 = \mathbf{U}_r - \mathbf{U}_r^*. \tag{5.29}$$

5.4.1.2 Suliciu-type relaxation Riemann solver

We present in this section a new Suliciu-type Riemann solver for the 6-equation two-phase model by extending the Suliciu's relaxation Riemann solver presented in [35] for the Euler equations. Similar to the case of the Euler equations, this solver will prove to be equivalent to a HLLC solver for the discretization of the conservative equations and of the the volume fraction equation of the two-phase system. We will show indeed that this solver defines a class of HLLC-type methods that differ for the definition of some constant parameters, which affect the discretization of the non-conservative terms. A particular choice of these parameters gives a Riemann solver exactly equivalent to the one described in Section 5.4.1.1 that neglects nonconservative terms.

The Suliciu's solver [35] belongs to the class of relaxation Riemann solvers [169], which are based on the idea of approximating the solution of the original system by the solution of an extended system called relaxation system. The latter is assumed to relax to the original system, whose variables define the Maxwellian equilibrium. We refer to [35, 151, 169] for details, and we just present the structure of the relaxation system associated to (5.2). Following [35] we approximate the solution of a Riemann problem for the original six-equation model by the solution of an augmented system that has the property of having characteristic fields all linearly degenerate. Let us introduce two auxiliary relaxation variables Π_k, $k = 1,2$, which are meant to relax toward the partial pressures, thus at equilibrium: $\Pi_k = \alpha_k p_k, \quad k = 1,2$. The phasic pressures are governed by

$$\partial_t p_k + u\partial_z p_k + \rho_k c_k^2 \partial_z u = 0, \tag{5.30}$$

and the partial pressures by

$$\partial_t(\alpha_k p_k) + u\partial_z(\alpha_k p_k) + Y_k c_k^2 \rho \partial_z u = 0. \tag{5.31}$$

This suggests the form of the equations for new variables Π_k, which are independent variables of the relaxation system. We introduce the constant parameters C_k, $k = 1,2$, and we replace in the above equations (5.31) the terms $Y_k c_k^2 \rho^2$ by C_k^2, $k = 1,2$, and $(\alpha_k p_k)$ by Π_k. In order to be able to specify different constant C_k for the left and right wave structure of the Riemann problem solution, we also introduce advection equations for C_k. The Suliciu's relaxation system associated to (5.2) is

$$\partial_t \alpha_1 + u\partial_z \alpha_1 = 0, \tag{5.32a}$$
$$\partial_t(\alpha_1\rho_1) + \partial_z(\alpha_1\rho_1 u) = 0, \tag{5.32b}$$
$$\partial_t(\alpha_2\rho_2) + \partial_z(\alpha_2\rho_2 u) = 0, \tag{5.32c}$$
$$\partial_t(\rho u) + \partial_z(\rho u^2 + \Pi_1 + \Pi_2) = 0, \tag{5.32d}$$
$$\partial_t(\alpha_1\rho_1 E_1) + \partial_z(\alpha_1\rho_1 E_1 u + \Pi_1 u) + u(Y_1\partial_z\Pi_2 - Y_2\partial_z\Pi_1) = 0, \tag{5.32e}$$
$$\partial_t(\alpha_2\rho_1 E_2) + \partial_z(\alpha_2\rho_1 E_2 u + \Pi_2 u) - u(Y_1\partial_z\Pi_2 - Y_2\partial_z\Pi_1) = 0, \tag{5.32f}$$
$$\partial_z\Pi_1 + u\partial_z\Pi_1 + C_1^2/\rho\ \partial_z u = 0, \tag{5.32g}$$
$$\partial_z\Pi_2 + u\partial_z\Pi_2 + C_2^2/\rho\ \partial_z u = 0, \tag{5.32h}$$
$$\partial_z C_1 + u\partial_z C_1 = 0, \tag{5.32i}$$
$$\partial_z C_2 + u\partial_z C_2 = 0. \tag{5.32j}$$

The eigenvalues of system (5.32) are:

$$\tilde{\lambda}_{1,10} = u \mp \tilde{c}_\mathrm{m}, \quad \tilde{c}_\mathrm{m} = \frac{C_\mathrm{m}}{\rho}, \quad C_\mathrm{m} = \sqrt{C_1^2 + C_2^2}, \quad \tilde{\lambda}_2 = \ldots \tilde{\lambda}_9 = u. \tag{5.33}$$

All the characteristic fields are linearly degenerate, hence we can easily find the exact solution of the relaxation system through the Riemann invariants.

Riemann invariants Across the contact discontinuity associated to the eigenvalue u:

$$u = \text{const.}, \quad \Pi_\mathrm{m} = \text{const.}, \tag{5.34}$$

where we have defined $\Pi_\mathrm{m} = \Pi_1 + \Pi_2$. Across fields associated to the eigenvalues $u \mp \tilde{c}_\mathrm{m}$:

$$\alpha_k, Y_k = \text{const.}, \quad k = 1,2, \tag{5.35a}$$
$$\frac{1}{\rho} + \frac{\Pi_k}{C_k^2} = \text{const.}, \quad k = 1,2, \tag{5.35b}$$
$$u \mp \tilde{c}_\mathrm{m} = \text{const.}, \tag{5.35c}$$
$$C_2^2\Pi_1 - C_1^2\Pi_2 = \text{const.}, \tag{5.35d}$$
$$Y_k e_k - \frac{\Pi_k^2}{2C_k^2} = \text{const.}, \quad k = 1,2, \tag{5.35e}$$
$$C_k = \text{const.}, \quad k = 1,2. \tag{5.35f}$$

By using (5.35b) and (5.35c) we also deduce:

$$\Pi_k \pm \frac{C_k^2}{C_{\rm m}} u = \text{const.}, \quad k = 1,2, \tag{5.36}$$

and by using (5.35d) and (5.35b):

$$\frac{1}{\rho} + \frac{\Pi_{\rm m}}{C_{\rm m}^2} = \text{const.}. \tag{5.37}$$

Then, by using (5.36), we infer:

$$\Pi_{\rm m} \pm C_{\rm m} u = \text{const.}. \tag{5.38}$$

Let us note first that $(\Pi_k)_{\ell,r} = (\alpha_k p_k)_{\ell,r}$, and $(\Pi_{\rm m})_{\ell,r} = (p_{\rm m})_{\ell,r}$, where $p_{\rm m} = \alpha_1 p_1 + \alpha_2 p_2$. The relations (5.34) and (5.38) determine the quantities $u_\ell^* = u_r^* = u^*$ and $(\Pi_{\rm m})_\ell^* = (\Pi_{\rm m})_r^* = \Pi_{\rm m}^*$:

$$u^* = \frac{\rho_\ell \tilde{c}_{{\rm m}\ell} u_\ell + \rho_r \tilde{c}_{{\rm m}r} u_r + p_{{\rm m}\ell} - p_{{\rm m}r}}{\rho_\ell \tilde{c}_{{\rm m}\ell} + \rho_r \tilde{c}_{{\rm m}r}}, \quad \Pi_{\rm m}^* = \frac{\rho_\ell \tilde{c}_{{\rm m}\ell} p_{{\rm m}\ell} + \rho_r \tilde{c}_{{\rm m}r} p_{{\rm m}r} - \tilde{c}_{{\rm m}\ell}\tilde{c}_{{\rm m}r}(u_r - u_\ell)}{\rho_\ell \tilde{c}_{{\rm m}\ell} + \rho_r \tilde{c}_{{\rm m}r}}. \tag{5.39}$$

The expression (5.37) determines $\rho_{\ell,r}^*$:

$$\rho_{\ell,r}^* = \left(\frac{1}{\rho_{\ell,r}} + \frac{c_{r,\ell}(u_r - u_\ell) \mp (p_{{\rm m}r} - p_{{\rm m}\ell})}{c_{\ell,r}(c_\ell + c_r)} \right)^{-1}, \tag{5.40}$$

and through (5.35a) we can determine $(\rho_k)_{\ell,r}^* = (Y_k \rho / \alpha_k)_{\ell,r}^*$. Then we can find through (5.36):

$$(\Pi_k)_{\ell,r}^* = (\Pi_k)_{\ell,r} + \frac{(C_k)_{\ell,r}^2}{(C_{\rm m}^2)_{\ell,r}} (\Pi_{\rm m}^* - p_{{\rm m}\ell,r}), \quad k = 1,2. \tag{5.41}$$

Finally (5.35e) determines the specific phasic internal energies $(e_k)_{\ell,r}^*$. Then the intermediate states for the partial phasic energies per unit volume can be expressed as:

$$(\alpha_k \rho_k e_k)_{\ell,r}^* = (\alpha_k \rho_k)_{\ell,r}^* (e_k)_{\ell,r} + \rho_{\ell,r}^* \left(\frac{(C_k^2)_{\ell,r}}{2((C_{\rm m}^2)_{\ell,r})^2} (\Pi_{\rm m}^* - p_{\ell,r})^2 + \frac{(\Pi_k)_{\ell,r}}{(C_{\rm m}^2)_{\ell,r}} (\Pi_{\rm m}^* - p_{\ell,r}) \right), \tag{5.42}$$

and the corresponding total energies are:

$$(\alpha_k \rho_k E_k)_{\ell,r}^* = (\alpha_k \rho_k e_k)_{\ell,r}^* + (\alpha_k \rho_k)_{\ell,r}^* \frac{u^{*2}}{2}, \tag{5.43}$$

where we recall the notation $E_k = e_k + \frac{u^2}{2}$. Let us also note also that by using (5.35d) and (5.35e) we obtain for the mixture specific internal energy $e = Y_1 e_1 + Y_2 e_2$ the invariant:

$$e - \frac{\Pi_{\rm m}^2}{2C_{\rm m}^2} = \text{const.}. \tag{5.44}$$

We observe that the expressions of the invariants (5.34), (5.37), (5.38) and (5.44) are identical to those of the Suliciu's solver for the Euler equations with now $\Pi_{\rm m}$ and $C_{\rm m}$ playing the role of the relaxation variable associated to the pressure p and the constant $C = \rho c$ of the single-phase case, respectively. Therefore the solution for the intermediate states $(\cdot)_{\ell,r}^*$ of the mixture quantities of the two-phase solver has the same form of the solution for the intermediate states of the standard single-phase Suliciu's solver (see formulas in Bouchut's book [35]). It follows that the intermediate states for α_k and the conserved quantities (partial densities, mixture momentum, mixture total

energy) are identical to those of the HLLC solver of Section 5.4.1.1, and also to those of the path-conservative HLLC solver of Section 5.4.1.5, as long as $S_\ell = u_\ell - \tilde{c}_{\mathrm{m}\ell}$ and $S_r = u_r + \tilde{c}_{\mathrm{m}r}$. Note that the intermediate states for the conserved quantities depend merely on the sum $C_{\mathrm{m}}^2 = C_1^2 + C_2^2$, and only the intermediate states for the phasic energies depend on the individual parameters C_1 and C_2. The choice of C_1 and C_2 for a given definition of C_{m} defines the partition of the phasic energies within the mixture, based on the invariant (5.35d). This is related to the fact that the choice of C_1 and C_2 determines implicitly a specific choice of the integration path used for the approximation of the nonconservative terms in the energy equations.

Choice of parameters The parameters C_k need to be chosen so that Liu's subcharacteristic condition [172] holds:

$$\tilde{c}_{\mathrm{m}} = \frac{\sqrt{C_1^2 + C_2^2}}{\rho} \geq c_{\mathrm{m}}, \tag{5.45}$$

where $c_{\mathrm{m}} = c_{hom}$ in (5.3). Hence the simplest natural definition for the parameters of the local right and left states would be $(C_k^2)_{\ell,r} = (Y_k c_k^2 \rho^2)_{\ell,r}$, which implies $(\tilde{c}_{\mathrm{m}})_{\ell,r} = (c_{\mathrm{m}})_{\ell,r}$. This would be also the less dissipative choice. However, this definition is not suited when shocks are involved in the solution structure. The idea here is to consider well known robust definitions of the wave speeds used for the HLLC solver (described in Section 5.4.1.1) to define first $\tilde{c}_{\mathrm{m}}$ and then C_k. Here in particular we consider the definition of the wave speeds for the Suliciu's (HLLC) single-phase solver of Bouchut [35]. This definition allows one to ensure preservation of positivity of the intermediate states of the conserved quantities. To this aim we define:

$$(\tilde{c}_{\mathrm{m}})_{\ell,r} = (c_{\mathrm{m}})_{\ell,r} + X_{\ell,r}, \tag{5.46a}$$

where

$$\text{if } p_r - p_\ell \geq 0, \quad \left\{ \begin{array}{l} X_\ell = \xi \left(\frac{p_r - p_\ell}{\rho_r c_{\mathrm{m}r}} + u_\ell - u_r \right)_+ \\ X_r = \xi \left(\frac{p_\ell - p_r}{\rho_\ell \tilde{c}_{\mathrm{m}\ell}} + u_\ell - u_r \right)_+ \end{array} \right. , \text{ if } p_r - p_\ell \leq 0, \quad \left\{ \begin{array}{l} X_r = \xi \left(\frac{p_\ell - p_r}{\rho_\ell c_{\mathrm{m}\ell}} + u_\ell - u_r \right)_+ \\ X_\ell = \xi \left(\frac{p_r - p_\ell}{\rho_r \tilde{c}_{\mathrm{m}r}} + u_\ell - u_r \right)_+ \end{array} \right. . \tag{5.46b}$$

For positivity the constant $\xi \geq 1$ must satisfy [35]:

$$\frac{\partial}{\partial \rho} \left(\rho \sqrt{\frac{\partial p_{\mathrm{m}}(\rho, s_1, s_2, \alpha_1, Y_1)}{\partial \rho}} \right) \leq \xi \sqrt{\frac{\partial p_{\mathrm{m}}(\rho, s_1, s_2, \alpha_1, Y_1)}{\partial \rho}}. \tag{5.46c}$$

Assuming a stiffened gas equation of state for each phase, we can satisfy the condition above by defining:

$$\xi = \frac{\max(\gamma_1, \gamma_2) + 1}{2}. \tag{5.46d}$$

Then we observe:

$$\tilde{c}_{\mathrm{m}}^2 = Y_1 c_1^2 + Y_2 c_2^2 + X^2 + 2X c_{\mathrm{m}} = Y_1(c_1^2 + X^2 + 2X c_{\mathrm{m}}) + Y_2(c_2^2 + X^2 + 2X c_{\mathrm{m}}). \tag{5.47}$$

Hence we propose the following definition:

$$(C_k^2)_{\ell,r} = (Y_k)_{\ell,r}((c_k^2)_{\ell,r} + X_{\ell,r}^2 + 2X_{\ell,r}(c_{\mathrm{m}})_{\ell,r})\rho_{\ell,r}^2. \tag{5.48}$$

Note that with this choice C_k vanishes when Y_k vanishes, that is a natural requirement. Based on the analogy of the two-phase case with the single-phase case in [35] we infer that this choice (5.48) of the parameters guarantees positivity of the intermediate states for the mixture density, the partial densities, and of the mixture energy of this Suliciu-type solver. Let us recall that α_k, as well as Y_k, is governed by an advection equation, hence positivity is preserved for the intermediate states of these variables. Since as we have noted above only the intermediate states of the phasic energies depend on the individual parameters C_k, if negative phasic energies are found for the intermediate states (see (5.35e)), we can always redefine $(C_k)_{\ell,r}$ in order to preserve positivity, still keeping the same values $(C_{\rm m})_{\ell,r}$. Finally, let us remark that if we define

$$(C_k^2)_{\ell,r} = (Y_k C_{\rm m}^2)_{\ell,r} \tag{5.49}$$

then the resulting Suliciu's solver is completely equivalent to the HLLC solver described in Section 5.4.1.1, which neglects the discretization of the nonconservative terms in the phasic energy equations of system (5.2). This observation gives some insight on the underlying approximation in this case: the evolution of the phasic pressures is governed by a fraction of the mixture speed of sound corresponding to the mass fraction, rather than by the phasic sound speeds, and in this situation there is no phasic energy transfer related to nonconservative terms. We then can estimate the difference of the wave components for the phasic energies for the case of the new Suliciu/HLLC-type solver based on (5.48) and the previous HLLC-type solver based on (5.49):

$$((\alpha_k\rho_k E_k)^*_{\ell,r})_{\rm Suliciu} = ((\alpha_k\rho_k E_k)^*_{\ell,r})_{\rm HLLC} + \Delta(\alpha_k\rho_k E_k)^*_{\ell,r}, \tag{5.50}$$

with

$$\Delta(\alpha_k\rho_k E_k)^*_{\ell,r} = \frac{\rho^*_{\ell,r}}{2(C_{\rm m}^2)_{\ell,r}}(\Pi^* - p_{{\rm m}\ell,r})^2\left(\frac{(C_k^2)_{\ell,r}}{(C_{\rm m}^2)_{\ell,r}} - (Y_k)_{\ell,r}\right). \tag{5.51}$$

Note that we can write

$$\Delta(\alpha_k\rho_k E_k)^*_{\ell,r} = (-1)^{k-1}\frac{\rho^*_{\ell,r}}{2(C_{\rm m}^2)_{\ell,r}}(\Pi^* - p_{{\rm m}\ell,r})^2\frac{(Y_2C_1^2 - Y_1C_2^2)_{\ell,r}}{(C_{\rm m}^2)_{\ell,r}}. \tag{5.52}$$

Moreover we can observe that if we use the definition (5.48) the contributions of $X_{\ell,r}$ cancel out in the above term $(Y_2C_1^2 - Y_1C_2^2)_{\ell,r}$, which results to be equal to $(Y_2Y_1(c_1^2 - c_2^2))_{\ell,r}$. Let us note for completeness of the presentation that the Davis' definition of the speeds of the HLLC solver described in Section 5.4.1.1 corresponds to the definition:

$$\tilde{c}_{{\rm m}\ell} = \max(c_{{\rm m}\ell}, (c_{{\rm m}r} + u_\ell - u_r)), \quad \tilde{c}_{{\rm m}r} = \max(c_{{\rm m}r}, (c_{{\rm m}\ell} + u_\ell - u_r)), \tag{5.53}$$

and we can for instance employ the following definitions for the constants C_k:

$$(C_k^2)_{\ell,r} = (Y_k\tilde{c}_k^2\rho)^2_{\ell,r}, \quad k = 1,2, \tag{5.54a}$$

where

$$(\tilde{c}_k)^2_{\ell,r} = \begin{cases} (c_k)^2_{\ell,r} & \text{if} \quad (c_{\rm m})_{\ell,r} \geq (c_{\rm m})_{r,\ell} + u_\ell - u_r, \\ (c_k)^2_{r,\ell} + 2(u_\ell - u_r)(c_{\rm m})_{r,\ell} + (u_\ell - u_r)^2 & \text{otherwise.} \end{cases} \tag{5.54b}$$

In summary, the presented Suliciu-type solver defines a class of HLLC-type solvers for the six-equation two-phase system that includes the solver that was presented by Pelanti & Shyue in [200]. Positivity preservation for this class of solvers can be ensured by the choice of the wave speeds in (5.46).

5.4.1.3 Path-conservative Dumbser-Osher-Toro solver

In the context of numerical schemes for hyperbolic systems with nonconservative terms, Parés [193] introduced the path-conservative schemes based on the theory in [68]. Within this formalism, the first order path-conservative scheme corresponds to the one of Eq. (5.20) without second-order corrections. Coherently with [68], the *compatibility condition* for nonconservative systems is:

$$\mathscr{A}^{+}\Delta\mathbf{U}_{i+\frac{1}{2}}+\mathscr{A}^{-}\Delta\mathbf{U}_{i+\frac{1}{2}}=\int_{0}^{1}\mathbf{A}(\phi(\mathbf{U}_{i},\mathbf{U}_{i+1},s))\frac{\partial\phi}{\partial s}ds. \tag{5.55}$$

The fundamental issue with these numerical schemes is that, in the presence of discontinuities, the numerical solution may not converge to the specified entropic weak solution [1, 45, 126]. Dumbser & Toro [90] applied this formalism to the Osher Riemann solver (RS) to extend this solver to nonconservative hyperbolic systems. We decided to adopt here this RS to integrate system (5.2). This choice is motivated by the nice features that characterize the Osher RS. In fact, it does not need an entropy fix (in contrast with Roe-type path-conservative schemes [193, 266]) and it does not lead to excessive numerical diffusion since it attributes a different numerical viscosity to each characteristic field. The interfacial fluctuations according to the path-conservative Dumbser-Osher-Toro (DOT) scheme are

$$\mathscr{A}^{\pm}\Delta\mathbf{U}_{i+\frac{1}{2}}=\frac{1}{2}\int_{0}^{1}\left(\mathbf{A}(\phi(\mathbf{U}_{i},\mathbf{U}_{i+1},s))\pm\left|\mathbf{A}(\phi(\mathbf{U}_{i},\mathbf{U}_{i+1},s))\right|\right)\frac{\partial\phi}{\partial s}ds, \tag{5.56}$$

where $|\mathbf{A}|=\mathbf{R}|\Lambda|\mathbf{R}^{-1}$ and $|\Lambda(\mathbf{U})|=\mathrm{diag}(|\lambda_1|,...,|\lambda_6|)$. This is a general definition which depends on the family of path ϕ, which is a characteristic of the nonconservative system. Similarly, the Rankine–Hugoniot condition in the framework of the DLM theory depends on the family of path ϕ if the system is nonconservative [68, 162, 193]. By a mathematical point of view, the choice of the family of paths is important as it determines the speed of propagation of discontinuities, nevertheless, it has been observed that in certain situations this choice does not significantly alter the numerical results [222]. In the following, we observe the same feature as in [222] for the path-conservative HLLC scheme proposed below. Sometimes, the choice of the path is based on a physical background [163, 219], but, very often, a simple *segment path*

$$\phi(\mathbf{U}_{i},\mathbf{U}_{i+1},s)=\mathbf{U}_{i}+s(\mathbf{U}_{i+1}-\mathbf{U}_{i}) \tag{5.57}$$

is chosen. For a segment path, the fluctuations of the DOT path-conservative scheme become

$$\mathscr{A}^{\pm}\Delta\mathbf{U}_{i+\frac{1}{2}}=\frac{1}{2}\left(\int_{0}^{1}\left(\mathbf{A}(\phi(\mathbf{U}_{i},\mathbf{U}_{i+1},s))\pm\left|\mathbf{A}(\phi(\mathbf{U}_{i},\mathbf{U}_{i+1},s))\right|\right)ds\right)(\mathbf{U}_{i+1}-\mathbf{U}_{i}). \tag{5.58}$$

The numerical evaluation of this path integral can be done via any numerical quadrature rule. For this work, similarly to [90], we adopted a Gauss-Legendre rule. Finally, the interfacial fluctuations are calculated as:

$$\mathscr{A}^{\pm}\Delta\mathbf{U}_{i+\frac{1}{2}}=\frac{1}{2}\left(\sum_{j=1}^{G}\left(\omega_{j}\mathbf{A}(\phi(\mathbf{U}_{i},\mathbf{U}_{i+1},s_{j}))\pm\left|\mathbf{A}(\phi(\mathbf{U}_{i},\mathbf{U}_{i+1},s_{j}))\right|\right)\right)(\mathbf{U}_{i+1}-\mathbf{U}_{i}). \tag{5.59}$$

All the calculations presented in this paper are obtained using a three-point Gauss-Legendre rule. Nevertheless, several numerical experiments have been carried out to ascertain that no differences

would be detected using a more accurate quadrature algorithm (fifteen-point Gauss-Legendre rule). Finally, formula (5.59) provides a compact form to calculate interfacial fluctuations since only the matrices $\mathbf{A}$, $|\Lambda|$, $\mathbf{R}$, and $\mathbf{R}^{-1}$ are needed (see 5.7 and 5.8). However, this is very costly from a computational point of view. The need to take into account the nonconservative terms leads to evaluate the matrix eigenstructure several times at each interface at each time step, which implies an important computational cost.

5.4.1.4 Path-conservative HLLEM solver

Dumbser & Balsara [88] have recently proposed a nonconservative formulation of the well-known HLL Riemann solver. Using the classical similarity variable $\xi = z/t$, the approximate solution is

$$\mathbf{U}(\xi) = \begin{cases} \mathbf{U}_\ell, & \text{if } \xi \le S_\ell, \\ \mathbf{U}^* + \varphi \mathbf{R}^*(\bar{\mathbf{U}}) 2\delta^*(\bar{\mathbf{U}}) \mathbf{L}^*(\bar{\mathbf{U}}) \frac{\mathbf{U}_r - \mathbf{U}_\ell}{S_r - S_\ell} \left(\xi - \frac{1}{2}(S_r + S_\ell) \right), & \text{if } S_\ell < \xi < S_r, \\ \mathbf{U}_r, & \text{if } \xi \ge S_r. \end{cases} \tag{5.60}$$

The inner state is represented by a linear approximation containing a flattener $\varphi \in [0,1]$. We take $\bar{\mathbf{U}} = \mathbf{U}_r - \mathbf{U}_\ell$ as intermediate state. The matrix δ^* is the generalization of the scalar coefficient δ introduced by Einfeldt [95]. The expression of the interfacial fluctuations is

$$\left(\mathscr{A}^\pm \Delta \mathbf{U}_{i+\frac{1}{2}} \right)^{hllem} = \left(\mathscr{A}^\pm \Delta \mathbf{U}_{i+\frac{1}{2}} \right)^{hll} \pm \varphi \frac{S_r S_\ell}{S_r - S_\ell} \mathbf{R}^*(\bar{\mathbf{U}}) \delta^*(\bar{\mathbf{U}}) \mathbf{L}^*(\bar{\mathbf{U}}) (\mathbf{U}_{i+1} - \mathbf{U}_i). \tag{5.61}$$

Here $\left(\mathscr{A}^\pm \Delta \mathbf{U}_{i+\frac{1}{2}} \right)^{hll}$ are the interfacial fluctuations in the case that the inner state is constant ($\varphi = 0$ in Eq. (5.60)) as in the original HLL solver. These fluctuations are

$$\begin{aligned} \left(\mathscr{A}^- \Delta \mathbf{U}_{i+\frac{1}{2}} \right)^{hll} &= -\frac{S_\ell}{S_r - S_\ell} \left(\mathbf{F}_{i+1} - \mathbf{F}_i + \tilde{\mathbf{B}}(\mathbf{U}_i, \mathbf{U}^*)(\mathbf{U}^* - \mathbf{U}_i) + \tilde{\mathbf{B}}(\mathbf{U}^*, \mathbf{U}_{i+1})(\mathbf{U}_{i+1} - \mathbf{U}^*) \right) \\ &\quad + \frac{S_r S_\ell}{S_r - S_\ell} (\mathbf{U}_{i+1} - \mathbf{U}_i), \\ \left(\mathscr{A}^+ \Delta \mathbf{U}_{i+\frac{1}{2}} \right)^{hll} &= +\frac{S_r}{S_r - S_\ell} \left(\mathbf{F}_{i+1} - \mathbf{F}_i + \tilde{\mathbf{B}}(\mathbf{U}_i, \mathbf{U}^*)(\mathbf{U}^* - \mathbf{U}_i) + \tilde{\mathbf{B}}(\mathbf{U}^*, \mathbf{U}_{i+1})(\mathbf{U}_{i+1} - \mathbf{U}^*) \right) \\ &\quad - \frac{S_r S_\ell}{S_r - S_\ell} (\mathbf{U}_{i+1} - \mathbf{U}_i). \end{aligned} \tag{5.62}$$

The term $\tilde{\mathbf{B}}(\mathbf{U}_i, \mathbf{U}^*)$ is the straight path-integration of the nonconservative terms according to DLM-theory

$$\tilde{\mathbf{B}}(\mathbf{U}_i, \mathbf{U}^*) = \int_0^1 \tilde{\mathbf{B}}(\phi(\mathbf{U}_i, \mathbf{U}^*, s))\, ds. \tag{5.63}$$

This Riemann solver does not need an entropy fix and uses only part of the eigenstructure of the hyperbolic system (conversely to the DOT-RS). Notwithstanding, calculations are rather costly.

5.4.1.5 Path-conservative HLLC solver

The path-conservative Riemann solvers discussed above use entirely or partially the eigenstructure of the system. Here we design a new simple and efficient path-conservative HLLC solver that does not need to calculate it. This will result to be much more efficient in terms of computational cost.

Moreover, both the DOT and the HLLEM path-conservative solvers adopt the approximation that a linear path connects the left and the right states in the phase space across a discontinuity. The path-conservative HLLC solver here proposed extends the integration of the nonconservative terms to the more general family of the *polynomial paths*:

$$\phi(s) = \mathbf{U}^- + s^m(\mathbf{U}^+ - \mathbf{U}^-), \tag{5.64}$$

where $m \in \mathbb{N}$. Let us recall that according to the DLM theory [68], across a discontinuity:

$$\lambda\{\mathbf{U}\}_\phi = \int_0^1 \mathbf{A}(\phi(\mathbf{U}^-, \mathbf{U}^+, s))\frac{\partial \phi}{\partial s} ds, \tag{5.65}$$

here and in the following, $\{a\} = (a^+ - a^-)$, where a^+ is the value on the right of a discontinuity, a^- the value on the left. λ is the signal velocity. Equivalently:

$$\lambda\{\mathbf{U}\}_\phi = \{\mathbf{F}(\mathbf{U})\} + \int_0^1 \mathbf{B}(\phi(\mathbf{U}^-, \mathbf{U}^+, s))\frac{\partial \phi}{\partial s} ds, \tag{5.66}$$

Mass and momentum conservation equations are in conservative form then $\lambda\{\mathbf{U}(j)\} = \{\mathbf{F}(\mathbf{U}(j))\}$, $j = 2,3,4$. For the components $\mathbf{U}(j)$, $j = 2,3,4$, the jump conditions do not depend on the choice of the path ϕ. Let us analyze the jump conditions of the phasic-total-energy equations in which nonconservative products are present. Since across a shock wave the volume fractions α_k does not vary, the jump conditions of $\alpha_k \rho_k E_k$ is

$$\lambda\{\alpha_k \rho_k E_k\}_\phi = \{\alpha_k(\rho_k E_k + p_k)u\} + (-1)^{k+1} \int_0^1 -u\left(Y_2 \alpha_1 \frac{\partial}{\partial s}(p_1)_\phi - Y_1 \alpha_2 \frac{\partial}{\partial s}(p_2)_\phi\right) ds, \tag{5.67}$$

In order to write the pressure gradient in terms of conservative variables, the EoS is needed. The stiffened gas EoS of Eq. (5.5) expressed in terms of $\mathbf{U}$ components is

$$p_k = (\gamma_k - 1)\left(\frac{\alpha_k \rho_k E_k}{\alpha_k} - \frac{1}{2}\frac{\alpha_k \rho_k}{\alpha_k}\frac{(\rho u)^2}{\rho^2} - \eta_k \frac{\alpha_k \rho_k}{\alpha_k}\right) - \gamma_k \pi_k, \tag{5.68}$$

After some algebraic manipulations, we find that the phasic pressure gradient is

$$\frac{\alpha_k}{\kappa_k}\partial_z p_k = \left[\left(Y_k - \frac{1}{2}\right)u^2 - \eta_k\right]\partial_z(\alpha_k \rho_k) + Y_k u^2 \partial_z(\alpha_j \rho_j) - Y_k u \partial_z(\rho u) + \partial_z(\alpha_k \rho_k E_k). \tag{5.69}$$

Using Eq. (5.69), the nonconservative terms are

$$\begin{aligned}\Sigma = {} & Y_2\left[\left(Y_1\kappa_2 - \kappa_1\left(Y_1 - \frac{1}{2}\right)\right)u^3 + \kappa_1\eta_1 u\right]\ \partial_z(\alpha_1\rho_1) + Y_1Y_2(\kappa_1 - \kappa_2)u^2\ \partial_z(\rho u) \\ & - Y_1\left[\left(Y_2\kappa_1 - \kappa_2\left(Y_2 - \frac{1}{2}\right)\right)u^3 + \kappa_2\eta_2 u\right]\ \partial_z(\alpha_2\rho_2) - Y_2\kappa_1 u\ \partial_z(\alpha_1\rho_1E_1) + Y_1\kappa_2 u\ \partial_z(\alpha_2\rho_2E_2).\end{aligned} \tag{5.70}$$

We can now integrate the nonconservative terms using the DLM theory:

$$\begin{aligned}\int_0^1 \Sigma\, ds = {} & Y_2\left[Y_1\kappa_2 - \kappa_1\left(Y_1 - \frac{1}{2}\right)\right]\int_0^1 u^3\frac{\partial}{\partial s}(\alpha_1\rho_1)_\phi ds + Y_2\kappa_1\eta_1\int_0^1 u\frac{\partial}{\partial s}(\alpha_1\rho_1)_\phi ds \\ & - Y_1\left[Y_2\kappa_1 - \kappa_2\left(Y_2 - \frac{1}{2}\right)\right]\int_0^1 u^3\frac{\partial}{\partial s}(\alpha_2\rho_2)_\phi ds - Y_1\kappa_2\eta_2\int_0^1 u\frac{\partial}{\partial s}(\alpha_2\rho_2)_\phi ds \\ & + Y_1Y_2(\kappa_1 - \kappa_2)\int_0^1 u^2\frac{\partial}{\partial s}(\rho u)_\phi ds - Y_2\kappa_1\int_0^1 u\frac{\partial}{\partial s}(\alpha_1\rho_1E_1)_\phi ds + Y_1\kappa_2\int_0^1 u\frac{\partial}{\partial s}(\alpha_2\rho_2E_2)_\phi ds.\end{aligned} \tag{5.71}$$

Due to the choice of the integration path made in Eq. (5.64), the derivative of the jth element of the conservative variable vector is $\frac{\partial}{\partial s}(U_j)_\phi = (U_j^+ - U_j^-)\, m\, s^{m-1}$, then

$$\int_0^1 \Sigma\, ds = \tilde{\Sigma}_{2,3,4} - Y_2\kappa_1\{\alpha_1\rho_1E_1\}m\int_0^1 us^{m-1}ds + Y_1\kappa_2\{\alpha_2\rho_2E_2\}m\int_0^1 us^{m-1}ds, \tag{5.72}$$

where $\tilde{\Sigma}_{2,3,4}$ accounts for the path integration of components $\mathbf{U}(j),\ j = 2,3,4$ and is

$$\begin{aligned}\tilde{\Sigma}_{2,3,4} = &\left[Y_2\left(Y_1\kappa_2 - \kappa_1\left(Y_1 - \frac{1}{2}\right)\right)\{\alpha_1\rho_1\} - Y_1\left(Y_2\kappa_1 - \kappa_2\left(Y_2 - \frac{1}{2}\right)\right)\{\alpha_2\rho_2\}\right] m\int_0^1 u^3 s^{n-1}ds \\ &+ Y_1Y_2(\kappa_1 - \kappa_2)\{\rho u\}m\int_0^1 u^2 s^{n-1}ds + \left[Y_2\kappa_1\eta_1\{\alpha_1\rho_1\} - Y_1\kappa_2\eta_2\{\alpha_2\rho_2\}\right] m\int_0^1 us^{n-1}ds\end{aligned} \tag{5.73}$$

We recall that $\{a\} = (a^+ - a^-)$, where a^+ is the value on the right of a discontinuity, a^- the value on the left. From Eqs. (5.72), (5.73), one can see that the integration of the velocity across the interface assumes a relevant role for the integration of the nonconservative terms of system (5.2). As we already mentioned, the path-conservative HLLC scheme here proposed aims to integrate the nonconservative terms using the conservative variables of the state vector $\mathbf{U}$. Hence, the integral of the velocity that we now indicate as $\tilde{u}$ is:

$$\tilde{u} = m\int_0^1 us^{m-1}ds = m\int_0^1 \frac{(\rho u)^- + s^m[(\rho u)^+ - (\rho u)^-]}{\rho^- + s^m(\rho^+ - \rho^-)}s^{m-1}ds. \tag{5.74}$$

It can be numerically evaluated using, for instance, a Gauss-Legendre quadrature rule. We adopted a similar strategy for the integration of u^2 and u^3 present in Eq. (5.71). Finally, the jump condition across a shock becomes

$$\lambda\{\alpha_k\rho_kE_k\}_\phi = \{\alpha_k(\rho_kE_k + p_k)u\} + (-1)^{k+1}\tilde{\Sigma}_{2,3,4} + (-1)^k\left(Y_2\kappa_1\{\alpha_1\rho_1E_1\} - Y_1\kappa_2\{\alpha_2\rho_2E_2\}\right)\tilde{u}. \tag{5.75}$$

Across the contact discontinuity, we have the following invariants: $u_\ell^* = u_r^* = u^*$, $p_{m,\ell}^* = p_{m,r}^* = p_m^*$, where $p_m = \alpha_1p_1 + \alpha_2p_2$. Using the invariance of p_m across the contact discontinuity, the jump of the phasic total energy equations is:

$$\lambda\{\alpha_k\rho_kE_k\}_\phi = \{\alpha_k(\rho_kE_k + p_k)u\} + (-1)^k u^*\int_0^1 \alpha_1\frac{\partial}{\partial s}(p_1)_\phi ds + (-1)^k u\int_0^1 p_1\frac{\partial}{\partial s}(\alpha_1)_\phi ds. \tag{5.76}$$

After some calculations, across a contact discontinuity

$$\lambda\{\alpha_k\rho_kE_k\}_\phi = \{\alpha_k(\rho_kE_k + p_k)u\} + (-1)^k u^*\left(\alpha_{1,r}p_{1,r}^* - \alpha_{1,\ell}p_{1,\ell}^*\right). \tag{5.77}$$

The first 4 components of the middle state vectors $\mathbf{U}_\ell^*$ and $\mathbf{U}_r^*$ are equal to the ones in Eq. (5.28). In order to design a new path-conservative HLLC-type scheme, we need to determine $\rho_{1,\ell}^*E_{1,\ell}^*$, $\rho_{2,\ell}^*E_{2,\ell}^*$, $\rho_{1,r}^*E_{1,r}^*$ and $\rho_{2,r}^*E_{2,r}^*$. Let us write the jump relations of $\alpha_1\rho_1E_1$ across the left-going shock of the HLLC wave pattern:

$$S_\ell(\rho_{1,\ell}^*E_{1,\ell}^* - \rho_{1,\ell}E_{1,\ell}) = [(\rho_{1,\ell}^*E_{1,\ell}^* + p_{1,\ell}^*)u^* - (\rho_{1,\ell}E_{1,\ell} + p_{1,\ell})u_\ell] + \frac{1}{\alpha_{1,\ell}}\int_0^1 \Sigma(\mathbf{U}_\ell, \mathbf{U}_\ell^*, s)ds. \tag{5.78}$$

The previous jump condition, completed by Eq. (5.75) and the stiffened gas EoS, provides the left-intermediate phasic total energies. Generalizing this procedure for the right-intermediate states,

one obtains the intermediate total energies of phase $k=1$, where $\iota=\ell,r$:

$$\begin{aligned}\rho^*_{1,\iota}E^*_{1,\iota} = \Big[&\rho_{1,\iota}E_{1,\iota}(S_\iota-u_\iota+Y_2\kappa_1\tilde{u})+(\rho^*_{2,\iota}E^*_{2,\iota}-\rho_{2,\iota}E_{2,\iota})(Y_1\kappa_2\tilde{u}\frac{\alpha_{2,\iota}}{\alpha_{1,\iota}})\\ &-\left(\Pi_1+\kappa_1\rho^*_{1,\iota}(\frac{1}{2}u^{*2}+\eta_1)\right)u^*-p_{1,\iota}u_\iota-\tilde{\Sigma}_{2,3,4}/\alpha_{1,\iota}\Big]/\left[S_\iota-(1+\kappa_1)u^*+Y_2\kappa_1\tilde{u}\right].\end{aligned} \tag{5.79}$$

Similarly, for $\rho^*_{2,\iota}E^*_{2,\iota}$, forming an algebraic linear system with 2 unknowns and 2 equations that can be easily solved by substitution.

Proposition 5.1. *The path-conservative HLLC-type scheme designed for the 6-equation two-phase flow model (5.2) satisfies the consistency condition:*

$$\sum_{j=0}^{m-1}\lambda_{j+1}(\mathbf{U}_r-\mathbf{U}_\ell)=F(\mathbf{U}_r)-F(\mathbf{U}_\ell)+\int_0^1\mathbf{B}(\phi(\mathbf{U}_\ell,\mathbf{U}_r,s))\frac{\partial\phi}{\partial s}ds. \tag{5.80}$$

For instance, for the equation of total energy of phase 1, the consistency condition is:

$$\begin{aligned}S_\ell(\alpha_{1,\ell}\rho^*_{1,\ell}E^*_{1,\ell}-\alpha_{1,\ell}\rho_{1,\ell}E_{1,\ell})+S^*(\alpha_{1,r}\rho^*_{1,r}E^*_{1,r}-\alpha_{1,\ell}\rho^*_{1,\ell}E^*_{1,\ell})+S_r(\alpha_{1,r}\rho_{1,r}E_{1,r}-\alpha_{1,r}\rho^*_{1,r}E^*_{1,r})=\\ \alpha_{1,r}(\rho_{1,r}E_{1,r}+p_{1,r})u_r-\alpha_{1,\ell}(\rho_{1,\ell}E_{1,\ell}+p_{1,\ell})u_\ell+\widetilde{\Sigma}_{\ell,r},\end{aligned} \tag{5.81}$$

where $\widetilde{\Sigma}_{\ell,r}=\widetilde{\Sigma}_{\ell,\ell*}+\widetilde{\Sigma}_{\ell*,r*}+\widetilde{\Sigma}_{r*,r}$ is the integral of the nonconservative terms across the three waves. Proposition 5.1 can by verified by substituting (5.75) and (5.77) in Eq. (5.81).

5.4.2 Pressure relaxation operator

In the previous sections we discussed and developed solution procedures for the hyperbolic portion of the system, without accounting for relaxation source terms. Relaxation terms are of paramount importance since they describe the physical process occurring at the interface between the species. Thanks to the pressure relaxation operator, solutions to the 6-equation model approximate solutions of the pressure equilibrium Kapila et al. [139] model. Note also that this relaxation step leads to an effective speed of sound that corresponds to the the Wood's one [279] defined in (5.4), which also characterizes the pressure-equilibrium 5-equation model.

First, let us recall that the complete solution of the six-equation two-phase flow model is obtained by the succession of operators

$$\mathbf{U}^{n+1}=L_p^{\Delta t}L_{hyp}^{\Delta t}\mathbf{U}^n. \tag{5.82}$$

The hyperbolic operator described in the previous sections provides the intermediate solution $\mathbf{U}^{n+}=L_{hyp}^{\Delta t}\mathbf{U}^n$, which will now be used as initial condition for the pressure relaxation operator $L_p^{\Delta t}$. This operator is defined by the solution of the following system of ordinary differential equations:

$$\begin{aligned}\partial_t\alpha_1&=\mu(p_1-p_2),\\ \partial_t\left(\alpha_1\rho_1\right)&=0,\\ \partial_t\left(\alpha_2\rho_2\right)&=0,\\ \partial_t\left(\rho u\right)&=0,\\ \partial_t\left(\alpha_1\rho_1E_1\right)&=-\mu p_i(p_1-p_2),\\ \partial_t\left(\alpha_2\rho_2E_2\right)&=\mu p_i(p_1-p_2).\end{aligned} \tag{5.83}$$

During this pressure relaxation process, the two phases having initially different pressures relax toward an equilibrium state with pressure $\tilde{p}$. This is a volume transfer process where the phasic volume fractions also tend toward an equilibrium value corresponding to the equilibrium pressure $\tilde{p}$. Let us observe that the mixture density ρ, the partial densities $\alpha_k\rho_k$, the velocity u and the mixture energies E and e are invariant. On the other hand, the phasic densities ρ_k, the phasic total energies E_k and the phasic internal energies e_k vary during this process, as well as the phasic pressures and volume fractions. By employing suitable approximations of the interface pressure appearing in the phasic energy equations in (5.83), we can formulate a system of algebraic equations for the relaxed equilibrium state attained for $\mu \to \infty$. These equilibrium conditions are directly employed in the numerical procedure used to impose instantaneous mechanical relaxation. For the stiffened gas EOS these algebraic conditions are particularly simple since they reduce to the solution of a quadratic equation for the relaxed equilibrium pressure. Note that with this algorithm to handle infinite-rate pressure relaxation we do not actually discretize the ODE system (5.83) above, hence the parameter μ does not need to be defined. We refer to [200] for further details.

5.5 Test problems

We present here a selection of two-phase test problems in 1D geometry. The first two test problems deal with rarefaction waves, hence the simulation results can be compared to the exact solution of the Kapila et al. [139] model. The last two test problems also contain shock waves. If a discontinuity is located in a single-phase fluid, locally the flow is described by the Euler model, hence the jump conditions are the classic Rankine-Hugoniot ones, and an exact solution is available. If a discontinuity is located in a multiphase mixture, due to presence of nonconservative products in the Kapila et al. [139] model, an exact solution is not available since jump relations can not be analytically derived. For this test, simulation results will be compared to an 'exact' solver containing prescribed jump conditions. The latter are the ones derived in [232] in the case of weak strength shocks. In fact, if the shock is sufficiently weak, a smooth profile can be observed. The smoothness of this profile is due to a dispersion process, characteristic for multiphase mixtures [232]. These jump conditions present several interesting physical-mathematical features: (i) are in agreement with the single phase limit, (ii) are symmetric for all phases, (iii) conserve the mixture total energy, (iv) guarantee the volume fraction positivity, (v) for weak shocks, the Hugoniot curves are tangent to the isentropes, (vi) have been validated against many experimental tests.

Some authors have encoded them directly into the Riemann solver, for instance this has been done in the hybrid Glimm-Roe solver of [2], or as an artificial heat source to coherently do the mixture energy repartition [204], or correcting the thermodynamic path in the shock layer by forcing each point to belong to the mixture Hugoniot curve [205]. The latter has been also used in [235, 236]. In the Riemann solvers that we presented in the previous sections we did not encode any physical jump relation. However we will use the jump conditions of [232] to make a comparison between the various solvers and their different ways to discretize the nonconservative terms.

The simulations carried out in this section are only at the first order because we aim to compare the different Riemann solvers avoiding the influence of second order corrections on the integration

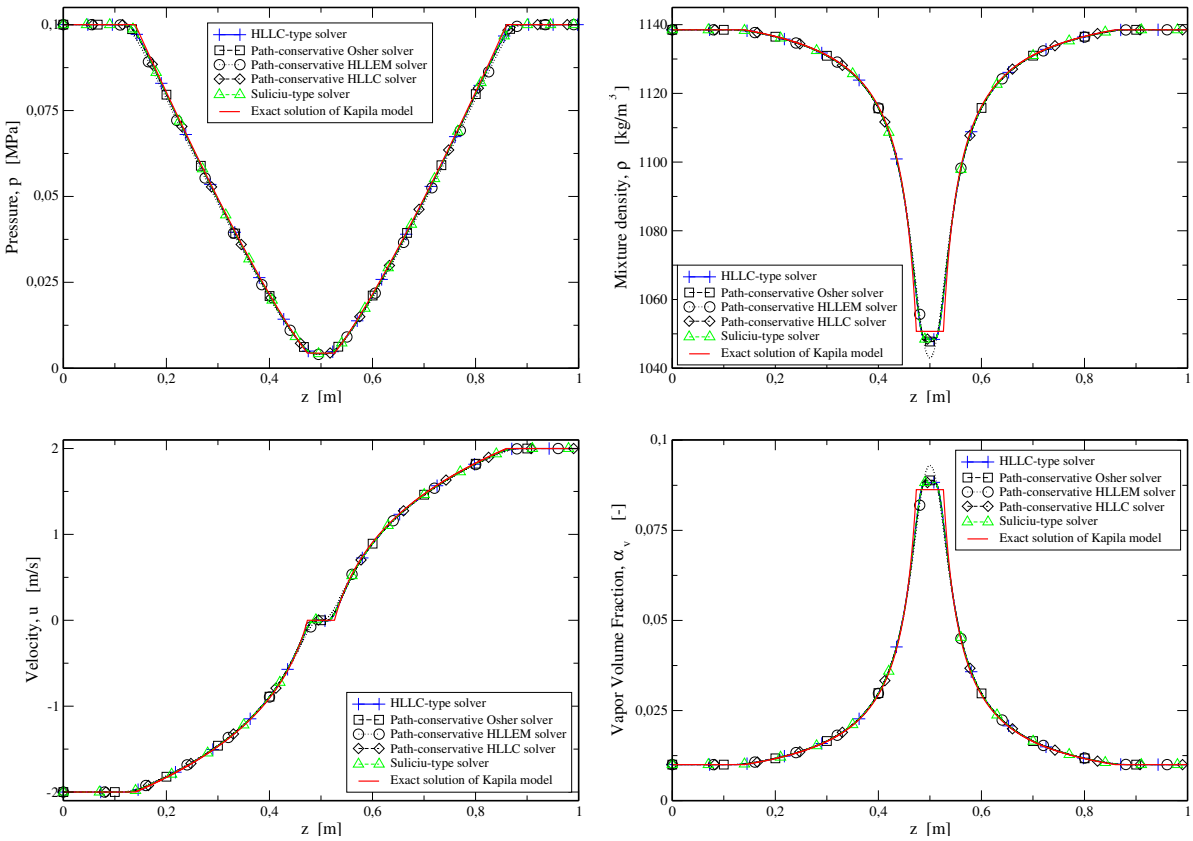

FIGURE 5.2. Numerical results for the water cavitation test with $|u| = 2\,m/s$, $t_{output} = 3.2\ ms$, $2 \cdot 10^4$ cells.

of nonconservative terms. However second-order solvers are used for the efficiency comparison. All the numerical results have been obtained with a $CFL = 0.5$ and with a very high number ($2 \cdot 10^4$) of cells in order to avoid any influence of the numerical diffusion on the results and to have mesh independence. The simulations have been performed by using the basic Fortran libraries of the CLAWPACK software [168].

5.5.1 Water cavitation tube problem

We first consider a one-dimensional cavitation tube problem proposed in [233]. A mixture of liquid-vapor water fills a tube of unit length. The initial conditions are

$$\begin{cases} \rho_v = 0.63\,kg/m^3,\ \rho_l = 1150\,kg/m^3,\ u = -2\,m/s,\ p = 10^5 Pa,\ \alpha_v = 10^{-2}, & for\ 0\,m \le z \le 0.5\,m, \\ \rho_v = 0.63\,kg/m^3,\ \rho_l = 1150\,kg/m^3,\ u = +2\,m/s,\ p = 10^5 Pa,\ \alpha_v = 10^{-2}, & for\ 0.5\,m \le z \le 1\,m. \end{cases} \tag{5.84}$$

The vapor is uniformly distributed throughout the tube. A velocity discontinuity is set at $z = 0.5\,m$ at initial time $t = 0$. On the left of the discontinuity the velocity is $u = -2\,m/s$, on the right, $u = 2\,m/s$. This Riemann problem generates two rarefaction waves and a trivial contact discontinuity wave of zero speed, provoking a low-density flow in the center of the tube. The parameters for the Stiffened

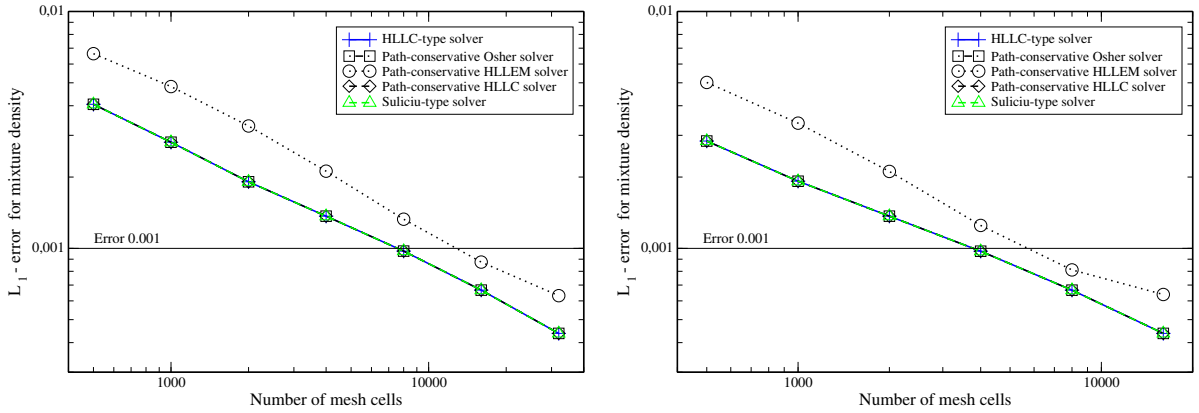

FIGURE 5.3. Mesh convergence study on the water cavitation test with initial velocity $|u| = 2\,m/s$. On the left, we show the first order trend and on the right the second order trend obtained with *minmod* limiter.

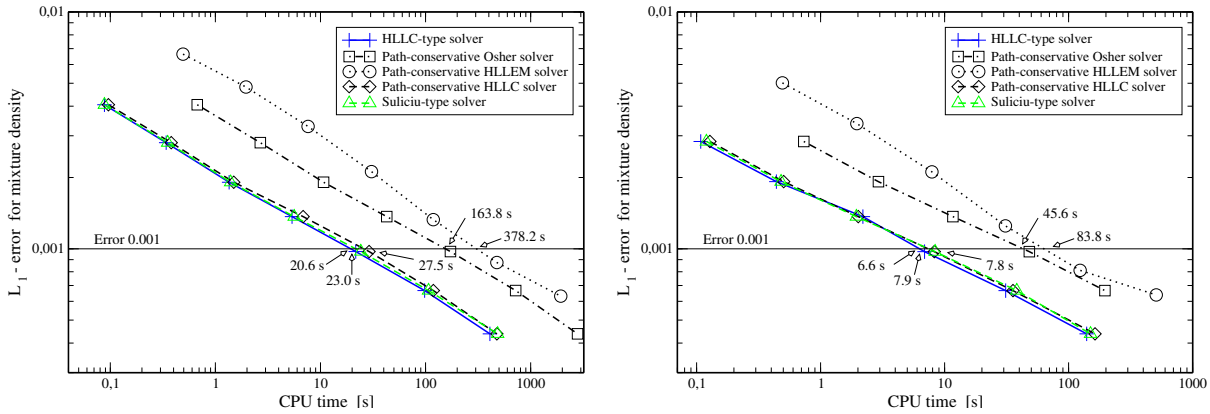

FIGURE 5.4. Efficiency study on the water cavitation test with initial velocity $|u| = 2\,m/s$. On the left, we show the first order trend and on the right the second order trend obtained with *minmod* limiter.

Gas EoS are $\gamma_1 = 4.4$, $\pi_1 = 6 \times 10^8\ Pa$, $\eta = 0\ J/kg$, $\gamma_2 = 1.4$, $\pi_2 = 0\ Pa$ and $\eta = 0\ J/kg$.

The simulation results are compared to the exact solutions of Kapila's model in Fig. 5.2. By using any of the five RS introduced in the previous sections, numerical solutions of the six-equation model with stiff mechanical relaxation accurately reproduce the exact results of the 5-equation model. In particular, the results are practically indistinguishable for all the solvers, except for the HLLEM-RS that introduces a small smearing around the contact discontinuity wave, which is visible in the vapor volume fraction plot of Fig. 5.2. This feature is expected and is due to the fact that the HLLEM-RS is not *complete* since it uses only two waves to approximate a three-wave model such as system (5.2). Instead, all the other Riemann solvers used in this work use as many waves as the system (5.2).

In order to compare the precision of the various RS and the computational time required to achieve a given precision, a mesh convergence and an efficiency studies have been carried out at both first and second order (see Fig. 5.3 and 5.4). The second order results are obtained using the

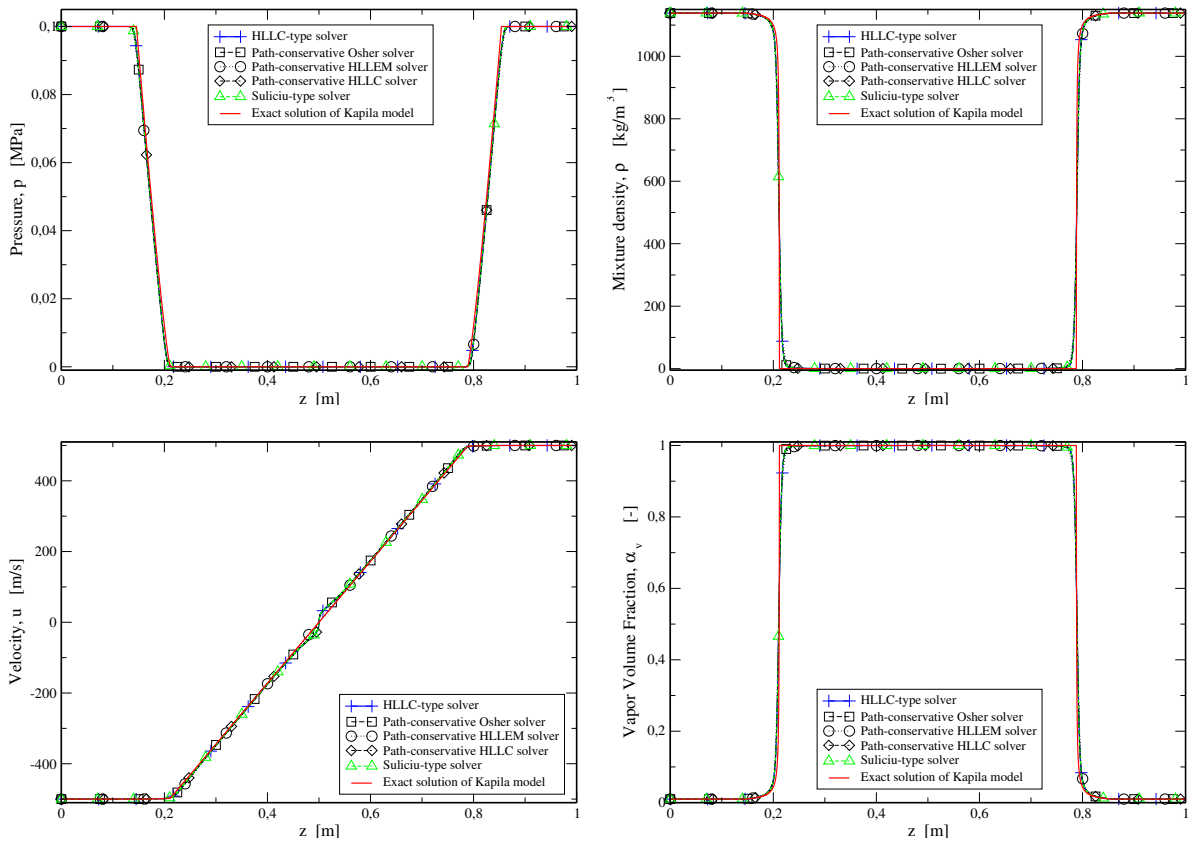

FIGURE 5.5. Numerical results for the water cavitation test with $|u| = 500\,m/s$, $t_{output} = 0.58\ ms$, $2 \cdot 10^4$ cells..

higher-order correction fluxes of Eq. (5.22), employing the *minmod* limiter. The HLLEM-RS is much more diffusive and costly than the other solvers since it is not a complete solver as stated above. The Osher solver is as diffusive as the other three solvers, however, it is much more costly because it needs to calculate the eigenstructure of the system at each interface for each time step. The other three RS have a similar trend in terms of numerical diffusivity an computational cost.

Figure 5.5 shows the water cavitation problem when the initial velocity is set as $|u| = 500\,m/s$ at both sides of the discontinuity located at $z = 0.5\,m$. In this case, the two rarefaction waves generated are stronger and create a very low density region in the center of the tube. From both cavitation tests we can also see that the discretization of the nonconservative terms does not play a key role. In fact, the HLLC solver of Pelanti & Shuye does not take them into account and, nevertheless, the results coincide with the ones of path-conservative and Suliciu's schemes.

5.5.2 Dodecane liquid-vapor shock tube problem: shock in pure vapor

We now present a shock tube problem to assess the behavior of the five RS when a shock propagates in one of the two phases. Here the tube is filled of nearly pure liquid dodecane on the left and of nearly pure vapor on the right. A pressure discontinuity is set at $z = 0.75\,m$ at initial time $t = 0$. The

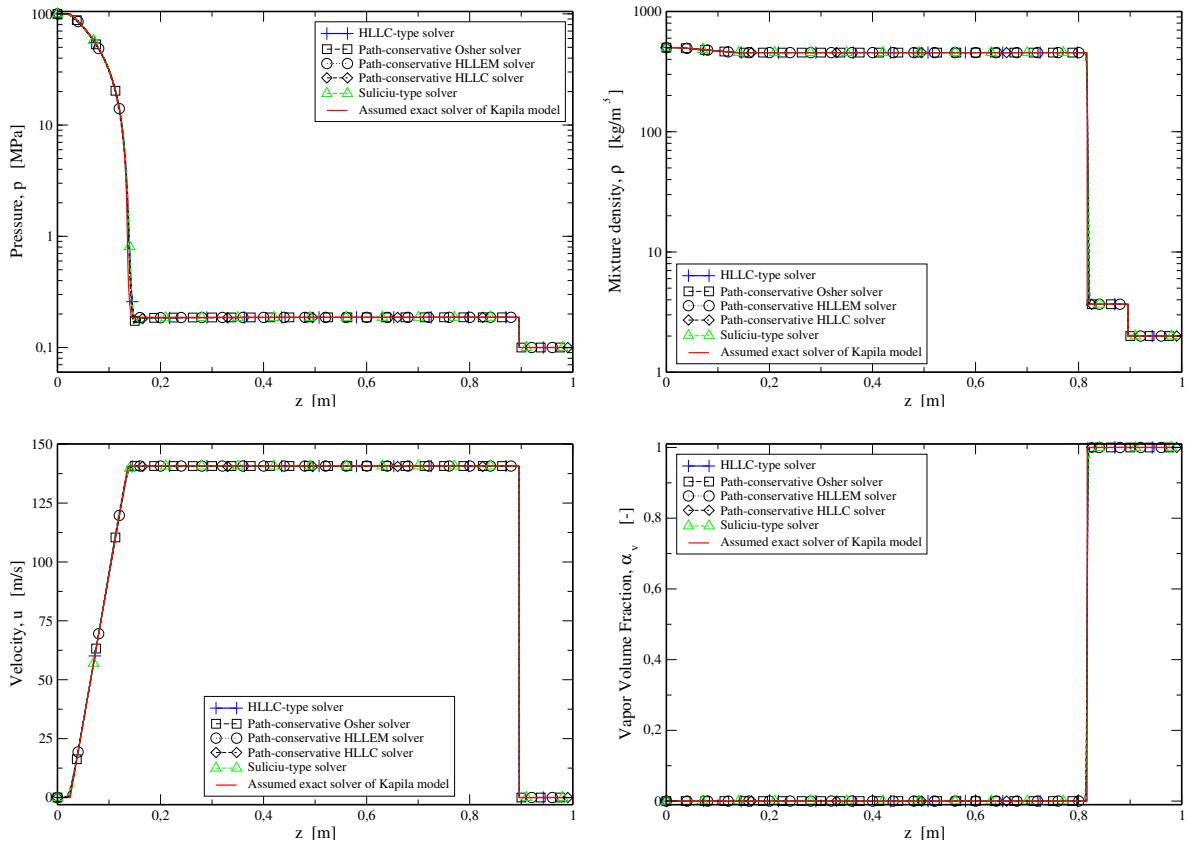

FIGURE 5.6. Numerical results for the dodecane liquid-vapor shock tube problem in Sec. 5.5.2, $t_{output} = 0.473\ ms$.

initial conditions are

$$\begin{cases} \rho_v = 2 kg/m^3,\ \rho_l = 500 kg/m^3,\ u = 0 m/s,\ p = 10^8 Pa,\ \alpha_v = 10^{-8} & for\ 0 m \le z \le 0.75 m \\ \rho_v = 2 kg/m^3,\ \rho_l = 500 kg/m^3,\ u = 0 m/s,\ p = 10^5 Pa,\ \alpha_v = 1 - 10^{-8} & for\ 0.75 m \le z \le 1 m \end{cases} \tag{5.85}$$

The parameters for the Stiffened Gas EoS are $\gamma_1 = 2.35$, $\pi_1 = 4 \times 10^8\ Pa$, $\eta = 0\ J/kg$, $\gamma_2 = 1.025$, $\pi_2 = 0\ Pa$ and $\eta = 0\ J/kg$. A discontinuity of 1000 bar exists at the initial time. This Riemann problem generates a left-going rarefaction wave, a right-going shock and an in-between contact discontinuity that separates liquid and vapor dodecane. As for the previous test, the simulations performed with the five RS exhibit indistinguishable results, which completely match the exact results of the 5-equation model (see Fig. 5.6).

5.5.3 Dodecane liquid-vapor shock tube problem: shock in the mixture

Let us modify the previous test in order to have a shock wave occurring in the two-phase mixture. The initial conditions are the ones in (5.85) except that on the left $\alpha_v = 0.3$ and on the right $\alpha_v = 0.7$. Now the shock tube is filled of a two-phase mixture on both sides of the discontinuity. The results are plotted in Fig. 5.7. The left-going rarefaction wave has a much smaller amplitude with respect to

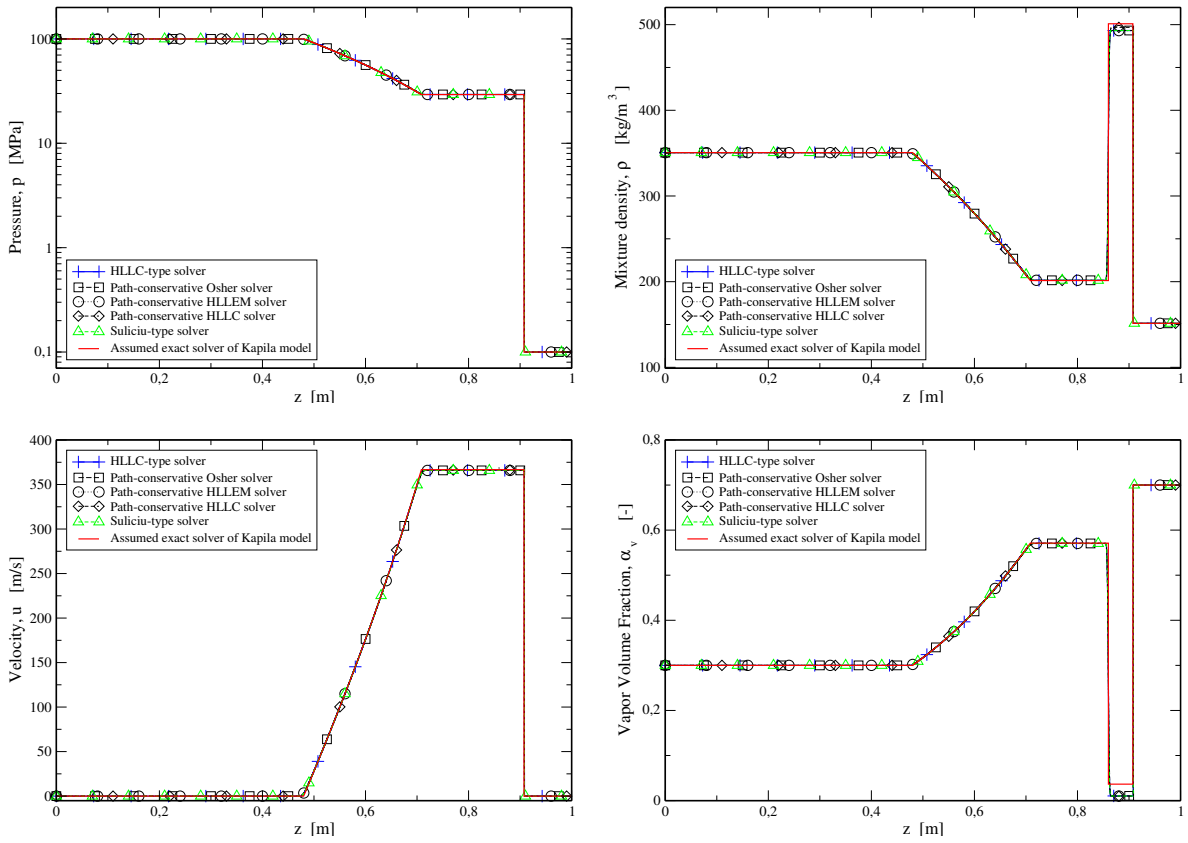

FIGURE 5.7. Numerical results for the dodecane liquid-vapor shock tube problem in Sec. 5.5.3, $t_{output} = 0.35\ ms$.

the previous test and the strength of the shock wave depends on the RS adopted. This dependency is visible in Fig. 5.7 on the plot of the most sensitive variables, the volume fractions and the mixture density. In particular, the path-conservative Osher and HLLEM schemes, the proposed Suliciu scheme and the HLLC solver of [200] converge to the same solution, whereas, the proposed path-conservative HLLC scheme converges to a different solution. Moreover, none of the RS here adopted matches the Kapila's model jump conditions of [232]. Let us also mention nevertheless that since we are dealing here with a very strong shock wave, the adequacy of the jump conditions of Saurel et al. [232] is questionable, since they are derived for weak strength shocks. Note that if a conservative variable is not correctly calculated across a shock, the shock velocity is wrong. Looking at the vapor volume fraction plot of Fig. 5.7, we can see that the shock velocity calculated by all solvers is larger than the one of the assumed exact solver.

We now generalize this test and the left pressure is now a parameter. In this way the strength of the initial discontinuity can be varied and we can see in Fig. 5.8 its effect. Namely, when the shock is weak or mild, all solvers coincides and the prediction of the shock speed coincides as well. However, if the shock is particularly strong (initial pressure ratio larger than 200), different discretization of the nonconservative terms can lead to different results and shock speed evaluations. For this parametric study we have introduced another way to discretize the nonconservative product, i.e. a

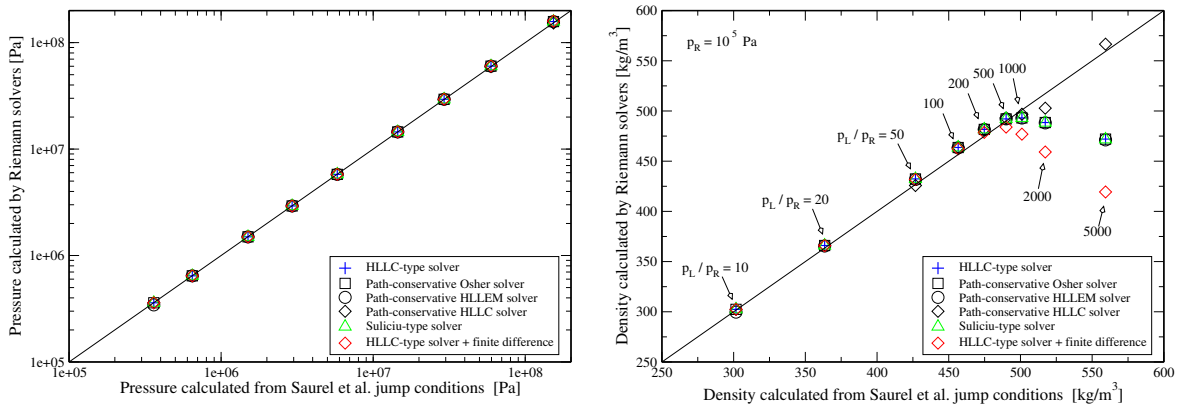

FIGURE 5.8. Benchmark test for the approximate Riemann solvers against the Saurel et al. [232] shock relations. The test case is the one presented in Section 5.5.3, but here the left pressure is a parameter. Increasing the pressure ratio at the initial discontinuity location, approximate Riemann solvers converge to different weak solutions (see plot on the right). When the Riemann problem strength becomes high, shock speeds are clearly different.

simple finite difference approximation. This technique is frequently adopted in the literature but it is the one that exhibits the highest discrepancy with respect to Saurel et al. [232] shock relations. It is worth mentioning that four schemes are totally coincident: the HLLC of [200] that neglects the nonconservative terms, the Suliciu's scheme, the Osher and the HLLEM path-conservative schemes. Another interesting feature is that the pressure calculated by the various solver, at least in this test, is always coincident to the one given by the Saurel et al. [232] shock relations. In fact the pressure seems not so much sensitive to the phasic total energy repartition.

As mentioned above, if one wants to obtain a post-shock state coherent to the one described by the Saurel et al. [232] shock relations, several methods exist [2, 204, 205, 235, 236]. In Fig. 5.9 we show the numerical results of a Glimm solver, coupled to the Saurel et al. [232] shock relations, that is able to reproduce the post-shock state of [232]. For generating random numbers, both the intrinsic Fortran 90 function and the van der Corput sequence have been used. The latter guarantees less noisy results [57]. From Fig. 5.9 we can see that the plateaux are correctly calculated, however they are translated with respect to the assumed exact solution. The distance between the numerical result and the prescribed exact one reduces with the increasing quality of the randomness sequence [57] and increasing the mesh cells.

Finally, in Fig. 5.10 we show the effect of the pressure relaxation operator on the results obtained by some of the considered Riemann solvers, by plotting results obtained with and without activation of the instantaneous mechanical relaxation process. First, we notice that in regions where the solution is smooth (rarefaction waves) there are no significant differences in the results of the various solvers. Relevant discrepancies are noticed around shocks, if no pressure relaxation is activated. Nevertheless, as it was already suggested in [200] (with no numerical demonstration), the pressure relaxation process tends to reduce the differences in the results between the various solvers.

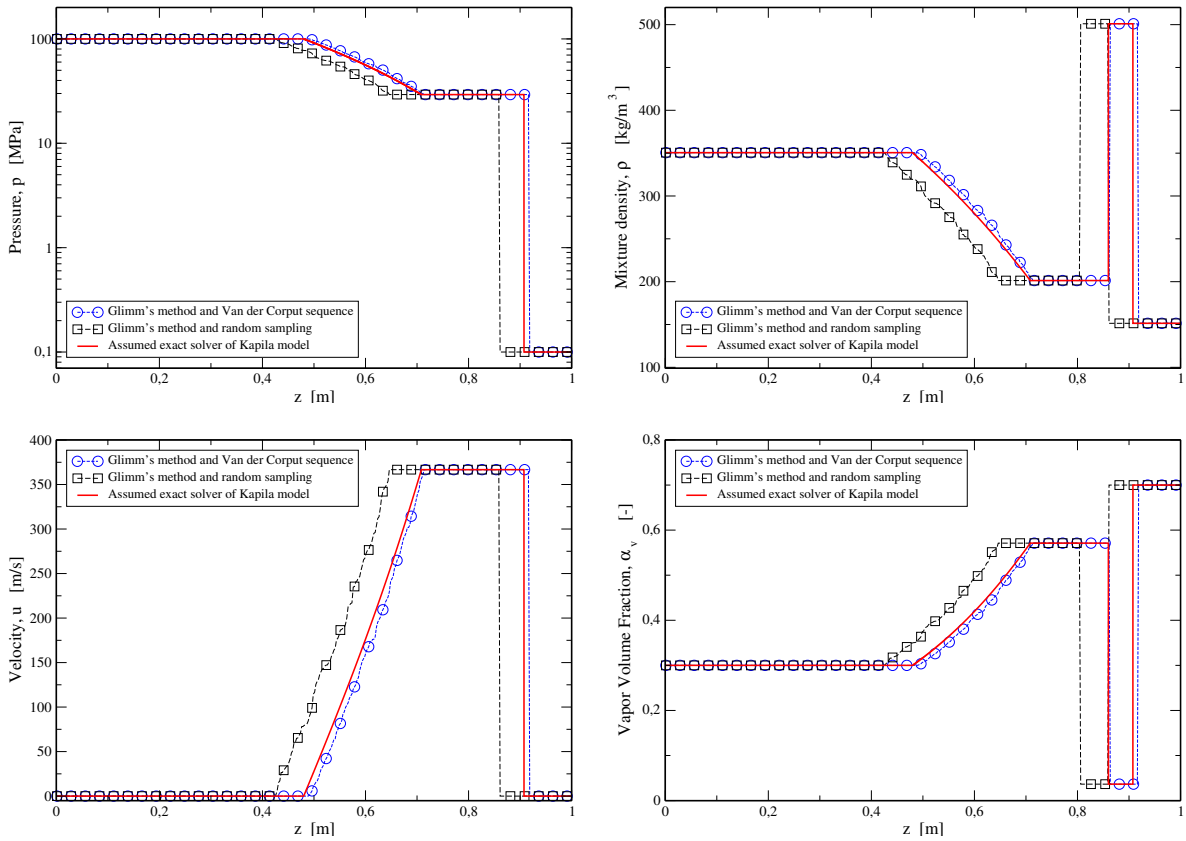

FIGURE 5.9. Numerical results for the dodecane liquid-vapor shock tube problem in Sec. 5.5.3 with Glimm's method. $CFL = 0.45$, $t_{output} = 0.35\ ms$, 500 cells.

In fact, when pressure relaxation is not activated, the mixture energy repartition between the phases is dictated solely by the Riemann solver, and noticeable differences can be expected for different treatments on non-conservative products. Instead, when instantaneous mechanical relaxation is forced to the solution of the 6-equation model, the resulting energy repartition is constrained by phasic pressure equality. This constraint entails a reduced degree of freedom and a significant reduction in the differences between various solvers.

5.6 Conclusions

In this work we have discussed various ways to numerically integrate the single-velocity 6-equation two-phase flow model of [200, 234], focusing in particular on different discretization methods for the nonconservative terms appearing in the phasic energy equations of the model system. In [200], a simple HLLC-type solver was employed, which does not account for these nonconservative terms. Two new Riemann solvers have been designed to build numerical methods for the approximation of system (5.2): a path-conservative HLLC solver and a Suliciu-type solver. The new Suliciu-type solver represents a generalization of the HLLC-type solver of [200], and it is shown to be equivalent to the solver in [200] for a particular definition of the solver's parameters. One important property of this

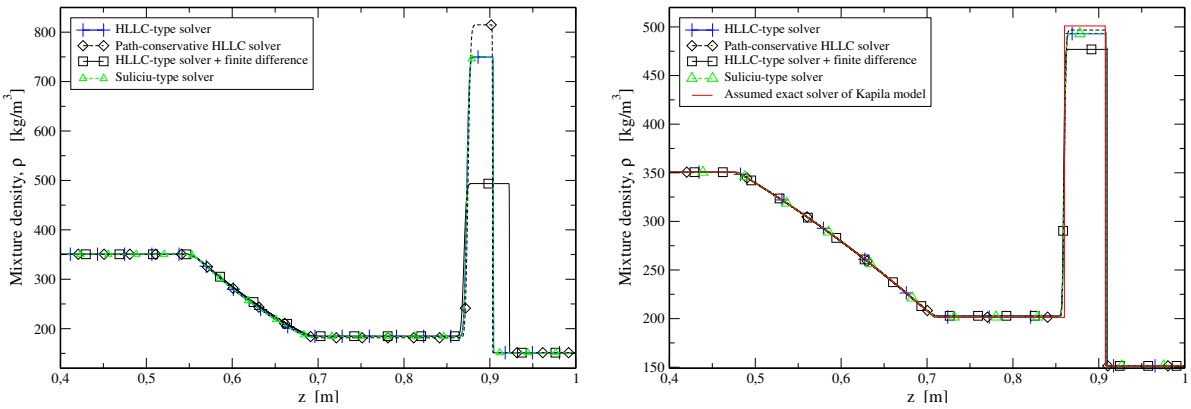

FIGURE 5.10. Numerical results for the dodecane liquid-vapor shock tube problem. On the left, the two phases evolve with different pressures (no mechanical relaxation). On the right, instantaneous mechanical relaxation is activated at each time step. The pressure relaxation procedure reduces the differences in the results obtained by the various solvers, decreasing also the discrepancies in the shock velocity.

new solver is that it preserves positivity of densities, energies and volume fractions, when a suitable definition of the solver's wave speeds is used. Then, we have adopted two path-conservative schemes presented in the literature, namely the schemes based on the DOT and the HLLEM Riemann Solvers.

The new path-conservative HLLC and Suliciu-type solvers allow us to take into account the nonconservative products with no relevant increase of the computational cost, whereas the DOT-RS and the HLLEM-RS are shown to be extremely expensive (see Fig. 5.4). For smooth solution test cases such as the cavitation tube tests the numerical results of the considered solvers, which all account for nonconservative terms, do not differ from the results obtained with the simple HLLC-type Riemann solver proposed in [200] that neglects those terms. Furthermore, in these problems all the solvers are able to reproduce the exact solution of the five-equation model corresponding to the limit of the considered six-equation model with instantaneous pressure relaxation. The various Riemann solvers' results also allow us to match exact solutions of the 5-equation model when simulating problems involving shocks in nearly pure phases. In this case, the nonconservative terms are not active across the shock wave.

When simulating shocks in genuine two-phase mixture regions various Riemann solvers produce different results. Discrepancies in the results between the various solvers and between the solvers and the 'assumed exact' solution of the five-equation model based on the jump relations of [232] appear to be small for weak and mild shocks. Differences however become significant for shocks characterized by strong pressure ratios. The incapability of recovering the correct shock speed is a well-known drawback of nonconservative two-phase flow models. Path-conservative schemes are not able to overcome this difficulty, even with a careful physically motivated choice of the integration path [1]. In the literature one of the most effective approach to circumvent this problem for two-phase flows is due to Abgrall & Kumar, who encoded the Saurel et al. [232] shock relations into a hybrid Glimm-Roe solver [2]. One disadvantage of this technique is that Glimm's method uses an exact

Riemann solver, so that it might be very difficult to extend this approach to treat arbitrary equations of states, which is an important goal of our current and future studies. Other methods to impose the prescribed jump conditions of [232] are reported in [204, 205].

In conclusion, despite inaccuracies for very strong shocks in multiphase mixtures, the finite volume schemes based on Riemann solvers that we have presented for the six-equation model with stiff pressure relaxation can provide accurate approximation of solution of the five-equation Kapila's equilibrium model for many flow problems, and the choice of the discretization of the nonconservative terms in the phasic energy equations often has no relevant role. Among the solvers, the new Suliciu-type solver has the advantage of retaining the simplicity of the HLLC-type solver of [200] and guaranteeing positivity preservation. In the future, we are are interested in extending the solution methods that we presented for the six-equation model to physically realistic EoS for steam and water, as the ones already implemented and discussed in [79] for other classical two-phase flow models. Ultimately, our aim is to develop computational tools to simulate fast transient flows and flashing flows [78] relevant for nuclear safety studies.

5.7 Appendix 5.A: Matrices of the 6-equation single-velocity two-phase flow model

We report here the matrices that characterize the one-dimensional (homogeneous) 6-equation model, which has the quasi-linear form $\partial_t \mathbf{U} + \mathbf{A}(\mathbf{U})\partial_z \mathbf{U} = 0$. We have:

$$\mathbf{A}(\mathbf{U}) = \begin{bmatrix} u & 0 & 0 & 0 & 0 & 0 \\ 0 & uY_2 & -uY_1 & Y_1 & 0 & 0 \\ 0 & -uY_2 & uY_1 & Y_2 & 0 & 0 \\ -\varpi_1+\varpi_2 & A_{42} & A_{43} & 2u-u(\kappa_1 Y_1+\kappa_2 Y_2) & \kappa_1 & \kappa_2 \\ (-\varpi_1+\varpi_2)uY_1 & A_{52} & A_{53} & Y_1H_1-u^2Y_1(\kappa_1 Y_1+\kappa_2 Y_2) & u+\kappa_1 uY_1 & uY_1\kappa_2 \\ (-\varpi_1+\varpi_2)uY_2 & A_{62} & A_{63} & Y_2H_2-u^2Y_2(\kappa_1 Y_1+\kappa_2 Y_2) & uY_2\kappa_1 & u+\kappa_2 uY_2 \end{bmatrix}, \tag{5.86}$$

where $\varpi_k = \rho_k c_k^2 - p_k(1+\kappa_k)$ with $\kappa_k = \frac{\partial p_k(\mathscr{E}_k,\rho_k)}{\partial \mathscr{E}_k}$, $k = 1,2$ (for the SG EOS $\varpi_k = \gamma_k \pi_k$), and

$$A_{42} = -u^2 + \chi_1 - \kappa_1 \frac{u^2}{2} + u^2(\kappa_1 Y_1 + \kappa_2 Y_2), \qquad A_{43} = -u^2 + \chi_2 - \kappa_2 \frac{u^2}{2} + u^2(\kappa_1 Y_1 + \kappa_2 Y_2),$$
$$A_{52} = -Y_1 H_1 u + uY_1\left(\chi_1 - \kappa_1 \frac{u^2}{2}\right) + u^3 Y_1(\kappa_1 Y_1 + \kappa_2 Y_2),$$
$$A_{53} = -Y_1 H_1 u + uY_1\left(\chi_2 - \kappa_2 \frac{u^2}{2}\right) + u^3 Y_1(\kappa_1 Y_1 + \kappa_2 Y_2),$$
$$A_{62} = -Y_2 H_2 u + uY_2\left(\chi_1 - \kappa_1 \frac{u^2}{2}\right) + u^3 Y_2(\kappa_1 Y_1 + \kappa_2 Y_2),$$
$$A_{63} = -Y_2 H_2 u + uY_2\left(\chi_2 - \kappa_2 \frac{u^2}{2}\right) + u^3 Y_2(\kappa_1 Y_1 + \kappa_2 Y_2).$$

Such a matrix can be considered as the composition of a conservative and a nonconservative contribution: $\mathbf{A}(\mathbf{U}) = \frac{\partial \mathbf{F}}{\partial \mathbf{U}} + \mathbf{B}(\mathbf{U})$. The matrix containing the nonconservative terms is:

$$\mathbf{B}(\mathbf{U}) = \begin{bmatrix} u & 0 & 0 & 0 & 0 & 0 \\ 0 & 0 & 0 & 0 & 0 & 0 \\ 0 & 0 & 0 & 0 & 0 & 0 \\ 0 & 0 & 0 & 0 & 0 & 0 \\ u(Y_2\varpi_1 + Y_1\varpi_2) & B_{5,2} & B_{5,3} & u^2 Y_1 Y_2(\kappa_1 - \kappa_2) & -uY_2\kappa_1 & uY_1\kappa_2 \\ -u(Y_2\varpi_1 + Y_1\varpi_2) & -B_{5,2} & -B_{5,3} & -u^2 Y_1 Y_2(\kappa_1 - \kappa_2) & +uY_2\kappa_1 & -uY_1\kappa_2 \end{bmatrix}, \tag{5.87}$$

where

$$B_{5,2} = -uY_2\chi_1 + u^3 Y_2\left[-\kappa_1\left(Y_1 - \frac{1}{2}\right) + Y_1\kappa_2\right], \quad B_{5,3} = +uY_1\chi_2 - u^3 Y_1\left[-\kappa_2\left(Y_2 - \frac{1}{2}\right) + Y_2\kappa_1\right].$$

5.8 Appendix 5.B: Model System Eigenstructure

The eigenvalues of the matrix $\mathbf{A}(\mathbf{U})$ are

$$\lambda_1 = u - c, \quad \lambda_2 = \lambda_3 = \lambda_4 = \lambda_5 = u, \quad \lambda_6 = u + c, \tag{5.88}$$

where u is the velocity in the z direction, and c the mixture sound speed in (5.3). The matrix $\mathbf{R}(\mathbf{U}) = (\mathbf{r}_1, \mathbf{r}_2, ..., \mathbf{r}_6)$ of the corresponding right eigenvectors $\mathbf{r}_k$, $k = 1, \ldots, 6$, can be taken as:

$$\mathbf{R}(\mathbf{U}) = \begin{bmatrix} 0 & 0 & 0 & 0 & 1 & 0 \\ Y_1 & 0 & 0 & 1 & 0 & Y_1 \\ Y_2 & 0 & 1 & 0 & 0 & Y_2 \\ u - c & 0 & u & u & 0 & u + c \\ Y_1(H_1 - uc) & -\frac{\kappa_2}{\kappa_1} & \frac{\kappa_2}{\kappa_1}H_2 - \frac{c_2^2}{\kappa_1} & H_1 - \frac{c_1^2}{\kappa_1} & \frac{\varpi_1 - \varpi_2}{\kappa_1} & Y_1(H_1 + uc) \\ Y_2(H_2 - uc) & 1 & 0 & 0 & 0 & Y_2(H_2 + uc) \end{bmatrix}, \tag{5.89}$$

where we have denoted with $H_k = h_k + \frac{u^2}{2}$ the specific total enthalpy of phase k.

CHAPTER 6

EoS-INDEPENDENT RELAXATION PROCEDURES

The single-velocity six-equation model is able to take into account the full thermodynamic disequilibrium between phases. Liquid and vapor may be at different pressure, temperature and chemical potential. This disequilibrium leads to the presence of metastable phases. However, as explained in Chapter 1, the lifetime of a metastable phase is limited since a stable phase is always going to appear sooner or later [73]. In fact, phases exchange energy and mass at their separation interface reducing the thermodynamic disequilibrium and tending towards the saturated equilibrium conditions.

This chapter is devoted to the description of these interphase transfers for the equilibrium recovery. Mathematically, they consist of source terms for the single-velocity six-equation model. They are decomposed in three source terms, each accounting a different physical phenomenon. One represents the energy and volume repartitions that make phases to tend towards the same pressure. Another one models the sensible heat transfer triggered by the temperature disequilibrium. The last one, models the mass and latent heat transfers due to the chemical disequilibrium.

The final goal of Part III of this thesis is to develop a single-velocity six-equation model, fully coupled to the steam-water tables, for the accurate simulation of metastable water flows. In order to couple such a model with a tabulated equation of state, the numerical procedures that implement the interphase transfers must be equation of state independent. Further, to accurately take into account the presence of metastable phases, the interphase transfers can not be instantaneous.

In this chapter we show how to construct *non-instantaneous EoS-independent numerical procedures* for the modeling of interphase transfers between metastable phases. These developments represent the main scientific contribution of this Ph.D. thesis.

Here the attention is drawn on the construction and on the verification of these novel numerical procedures. In the next chapter, this methodology will be validated against the experimental data of fast depressurizations.

A hyperbolic phase-transition model with non-instantaneous EoS-independent relaxation procedures

Submitted to Journal of Computational Physics.

M. De Lorenzo[1], Ph. Lafon[1], M. Pelanti[1].

This article deals with the thermodynamic equilibrium recovery mechanisms in two-phase flows and their numerical modeling. The two phases, initially at different pressures, temperatures and chemical potentials, are supposed to be driven towards equilibrium conditions by three relaxation processes. First, a mechanical process applies to relax phasic pressures, then a thermal process, to allow the sensible heat transfer between the phases at different temperatures, and, lastly, a chemical process that is responsible for the mass transfer.

The two-phase flow model is composed of six partial differential equations with source terms that allows the description of mixtures at full thermodynamic disequilibrium. Its homogeneous portion is hyperbolic and it is solved by a second-order accurate finite volume scheme that uses a HLLC-type approximate Riemann solver. The source terms modeling the relaxation processes are separately integrated as three systems of ordinary differential equations.

The main contributions of this paper are: the capability of describing the possibly non-instantaneous time delay of equilibrium recover in a novel way, the equation of state independence of the numerical scheme, and the possibility to take into account the morphology of the flow pattern by using the interfacial area between phases.

6.1 Introduction

The modeling of two-phase flows has seen greatly improvement in the last two decades. At the same time, new numerical methods have been proposed enhancing capabilities and robustness in the integration of two-phase flow models.

Many authors in the literature have developed numerical schemes that are suited only for analytical and too simplistic Equations of State (EoS). One of the main goals of this paper is to tackle this deficiency, providing numerical schemes that are EoS-independent. The only constraints demanded of the EoS are the ones dictated by the thermodynamics.

This work is motivated by the existence of fluids that have very complex behaviors, e.g. water. Such fluids are described with complex EoS or others based on the best-fitting of experimental data [251, 272, 273] and can not be accurately described by analytical EoS. Moreover, when dealing with phase-transition phenomena, fluids are often in metastable conditions, wherein the fluid behavior is even more complex with properties varying rapidly in the thermodynamic state space. Hence only detailed EoS can represent these behaviors.

In two-phase flows there are many more degrees of freedom and unknowns than in single-phase flow. Some of them depend on the morphology of how phases are distributed, that is, the flow pattern.

[1] IMSIA UMR EDF-CNRS-CEA-ENSTA, Palaiseau, France 91120.

Several phenomena are flow pattern dependent, e.g. the critical mass flow rate and the critical heat flux. Here we are not going to examine in depth the morphology of the phase distribution, however, we try to insert in our model one of the most important parameters, i.e. the interfacial area.

The two-phase flow model here considered is the one in [139, 200, 234] and is a reduced model of the Baer & Nunziato 7-equation model [12]. It allows a full thermodynamic disequilibrium between phases since they are at different pressure, temperature and chemical potential. Hence two separate EoS are required, one describing the behavior of each phase. This reduced model comes from the assumption that phases move at the same velocity.

The two-phase model is composed of six Partial Differential Equations (PDE) with source terms. Its homogeneous portion is hyperbolic and is solved by the HLLC-type Riemann solver proposed in [200] and is second order accurate since second order corrections are applied. The source terms are responsible of the relaxation processes. Being the phases at different pressure, temperature and chemical potential, we call relaxation processes such procedures that tend to establish the thermodynamic equilibrium.

In fact phases are supposed to undergo three consecutive relaxations: i) a mechanical process, in order to relax phasic pressures towards an equilibrium pressure, ii) a thermal process, to allow the sensible heat transfer between the phases at different temperatures, iii) a chemical process that models the mass transfer phenomena.

These relaxations do not take place instantaneously in nature. Among them, the pressure relaxation process is the fastest one, however the others can not always be considered as instantaneous. In some transient phenomena as fast depressurizations, the delay of vaporization and the appearance of metastable phases are key features to well represent the properties evolution (see [79]). Nonetheless, even some steady-state phenomena as the flashing are strongly influenced by the delay of vaporization. Therefore it seems much more appropriate to consider these relaxations as non-instantaneous.

Each of these relaxations forms a system of Ordinary Differential Equations (ODE) that can be numerical integrated with an ODE solver. Here we have used explicit Runge-Kutta algorithms of high order of accuracy.

The work here presented is part of an undergoing authors' project, in the context of nuclear reactors safety studies, at the end of which this model will be implemented within the fast transient dynamics software EUROPLEXUS[2]. The objective is to simulate metastable flows that may occur in hypothetical accidents of nuclear power plants.

The plan of the paper is the following. In Section 6.2 we present the homogeneous part of the six-equation single-velocity two-phase flow model together with its mathematical characteristics. In Section 6.3 we introduce the thermodynamical parameters that will be used throughout the paper. Here we report as well some physical constraints to which those parameters undergo.

Section 6.4 is the main part of the paper and is devoted to the physical and mathematical modeling of the relaxation processes. Their irreversibility is discussed in Section 6.11 and their

[2]EUROPLEXUS code is owned by the Commissariat à l'Energie Atomique et aux Energies Alternatives (CEA) and the Joint Research Centre (JRC) of the European Union.

well-posedness is analyzed in Section 6.12. Other system of ODEs for the quasi-instantaneous thermo-chemical relaxation processes are provided in Section 6.10.

The numerical methods for the hyperbolic operator and the relaxation procedures are described in Section 6.5. 1D and 2D representative test cases are reported, respectively, in Sections 6.7 and 6.8. In some tests we adopt the stiffened gas EoS to be able to compare the present relaxation procedures and the instantaneous procedures of [200]. Some other test for water are performed by adopting the IAPWS-IF97, a very accurate EoS based of experimental data. The conclusions and the future steps of our work are discussed in Section 6.9.

6.2 Six-equation single-velocity two-phase flow model

The six-equation single-velocity two-phase flow model initially appeared in [139] as a transition model to obtain the pressure-equilibrium five-equation model from the seven-equation model of Baer & Nunziato [12]. Later Saurel et al. [234] proposed it as a surrogate of the celebrated Kapila five-equation model to avoid some numerical difficulties of the latter [234]. It was then reformulated by Pelanti & Shyue in [200] to ensure *mixture-energy-consistency* at the discrete level. The six-equation model is a two-phase, two-pressure system modeling the dynamics of mixture fluids that can also deal with phase transition when the phases are the liquid and its vapor.

To each phase is assigned a density ρ_k, a pressure p_k, a specific internal energy e_k and a volume fraction α_k, where $k = 1,2$. The velocity is assumed to be equal for the two phases. The governing equations consist of mass and energy balance laws for each phase, the momentum balance for the mixture, plus an advection equation for one of the two phases. The homogeneous portion of the system model reads

$$\begin{cases} \partial_t \alpha_1 + \mathbf{u}\cdot\nabla\alpha_1 = 0, \\ \partial_t(\alpha_1\rho_1) + \nabla\cdot(\alpha_1\rho_1\mathbf{u}) = 0, \\ \partial_t(\alpha_2\rho_2) + \nabla\cdot(\alpha_2\rho_2\mathbf{u}) = 0, \\ \partial_t(\rho\mathbf{u}) + \nabla\cdot(\rho\mathbf{u}\otimes\mathbf{u} + \alpha_1 p_1 + \alpha_2 p_2) = 0, \\ \partial_t(\alpha_1\rho_1 E_1) + \nabla\cdot[\alpha_1(\rho_1 E_1 + p_1)\mathbf{u}] + \Sigma(\mathbf{U},\nabla\mathbf{U}) = 0, \\ \partial_t(\alpha_2\rho_2 E_2) + \nabla\cdot[\alpha_2(\rho_2 E_2 + p_2)\mathbf{u}] - \Sigma(\mathbf{U},\nabla\mathbf{U}) = 0, \end{cases} \tag{6.1}$$

where: $E_k = e_k + \frac{1}{2}\mathbf{u}\cdot\mathbf{u}$ are the specific total energies and $\rho = \alpha_1\rho_1 + \alpha_2\rho_2$ is the mixture density. Two other useful quantities are: the phasic mass fraction $Y_k = \alpha_k\rho_k/\rho$ and the phasic partial density $m_k = \alpha_k\rho_k$.

The nonconservative terms that appear in the phasic total energy equations are

$$\Sigma(\mathbf{U},\nabla\mathbf{U}) = -\mathbf{u}\cdot[Y_2\nabla(\alpha_1 p_1) - Y_1\nabla(\alpha_2 p_2)]. \tag{6.2}$$

These terms are non-zero if $|\mathbf{u}| \neq 0$ and if $Y_1 Y_2 \neq 0$, that is, if the fluid is a mixture containing both species moving at non-zero velocity.

The mixture saturation condition is assumed

$$\alpha_1 + \alpha_2 = 1. \tag{6.3}$$

The above system of partial differential equations is hyperbolic and its eigenvalues associated to the direction $\mathbf{n} \in \mathbb{R}^d$, $|\mathbf{n}| = 1$, are

$$\lambda_1 = \mathbf{u}\cdot\mathbf{n} - c_{hom}, \quad \lambda_{2,\dots,4+d} = \mathbf{u}\cdot\mathbf{n}, \quad \lambda_{5+d} = \mathbf{u}\cdot\mathbf{n} + c_{hom}, \tag{6.4}$$

where d indicates the spatial dimension, and the speed of sound of the associated homogeneous model is

$$c_{hom} = \sqrt{Y_1 c_1^2 + Y_2 c_2^2}. \tag{6.5}$$

The quantities c_k are the phasic isentropic speeds of sound and will be defined in the next section. In Fig. 6.1 the frozen speed of sound of this model is compared to the ones of other two-phase flow models. However, those sound speeds do not take into account the effect of the source terms. Thanks to the relaxation processes, the effective speed of sound of system (6.1) will be lower than the one depicted in Fig. 6.1. This feature is guaranteed by the sub-characteristic condition [172] that requires that the sound speed associated to a two-phase flow model is reduced whenever an additional equilibrium is assumed (see [109] for a discussion of the speed of sound in relaxed two-phase flow models).

In order to close the system, two equations of state (EoS) are needed, one for each phase. They are of the form of the *incomplete EoS* [63] (see Section 6.3):

$$p_k = p_k(\rho_k, e_k) \tag{6.6}$$

and are considered to be of class C^2.

6.3 Equations of state and thermodynamic quantities

An equation of state is a thermodynamic equation relating state variables and describes the physical behavior of the matter. We can distinguish *complete* equations of state and *incomplete* ones [63, 181]. The complete EoS, expressed in natural variables, are

$$e(s,v), \quad f(T,v), \quad g(T,p), \quad h(s,p) \tag{6.7}$$

and do not need other relations to describe the thermodynamic behavior of the matter. The other physical quantities are the combination of the partial derivatives of the complete EoS. On the contrary, incomplete EoS do need additional relations. For instance, Eq. (6.6) has no information about temperature. Moreover, an incomplete EoS can not determine a corresponding complete EoS as shown in [181].

An incomplete EoS would be sufficient if the thermo-chemical relaxations were not involved. However, modelling phase transition phenomena requires a complete EoS; therefore, we assume that each phase behaves according to a complete EoS, and that the corresponding phasic incomplete

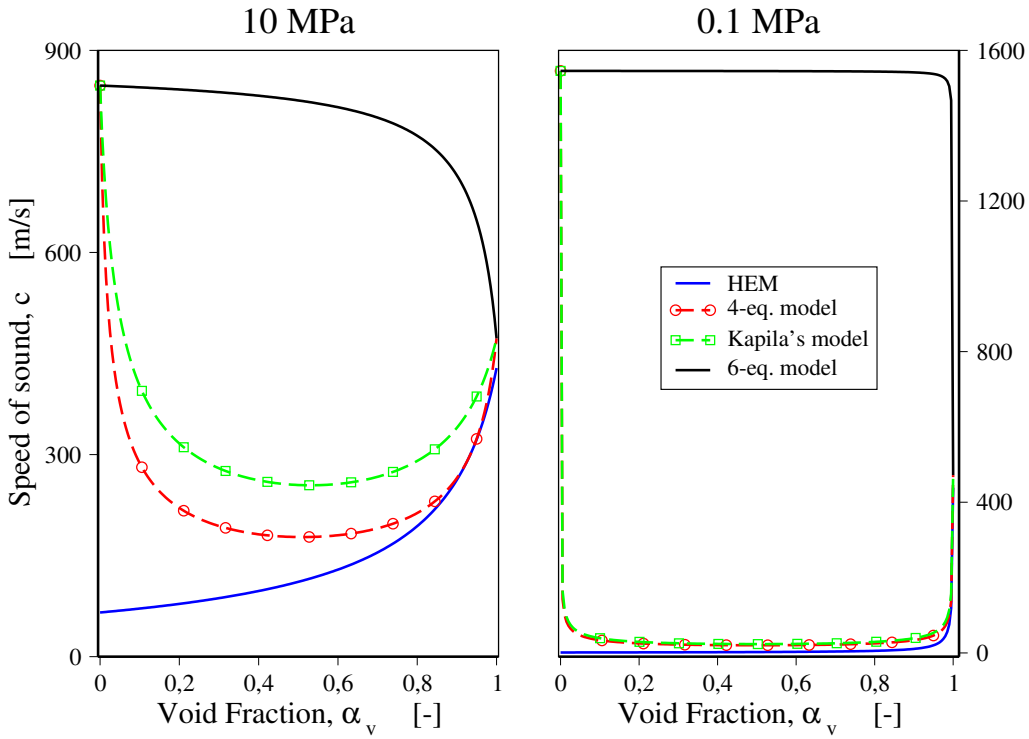

FIGURE 6.1. Sound speed of two-phase flow models. The frozen speed of sound reported in Eq. (6.5) is here depicted in black.

EoS $p_k(\rho_k, e_k)$ are known. When an explicit EoS as (6.6) is not available, iterative algorithms will be used.

Given that the paper deals with EoS-independent algorithms, we use in the following thermodynamic properties to express the partial derivatives of thermodynamic variables. Here we give the definitions of the direct measurable quantities. The phasic specific heats at constant volume and pressure are

$$C_{v,k} = \left(\frac{\partial e_k}{\partial T_k}\right)_{\rho_k} = T_k \left(\frac{\partial s_k}{\partial T_k}\right)_{\rho_k}, \qquad C_{p,k} = \left(\frac{\partial h_k}{\partial T_k}\right)_{p_k} = T_k \left(\frac{\partial s_k}{\partial T_k}\right)_{p_k}. \tag{6.8}$$

The phasic isothermal and isentropic compressibility factors are

$$K_{T,k} = \frac{1}{\rho_k}\left(\frac{\partial \rho_k}{\partial p_k}\right)_{T_k}, \qquad K_{s,k} = \frac{1}{\rho_k}\left(\frac{\partial \rho_k}{\partial p_k}\right)_{s_k}. \tag{6.9}$$

The phasic coefficients of thermal expansion are

$$\beta_k = -\rho_k \left(\frac{\partial \rho_k}{\partial T_k}\right)_{p_k}. \tag{6.10}$$

These quantities may be related by two identities

$$\frac{K_{s,k}}{K_{T,k}} = 1 - \frac{\beta_k^2 T_k}{\rho_k C_{p,k} K_{T,k}} = \frac{C_{v,k}}{C_{p,k}}. \tag{6.11}$$

In addition to the measurable phasic quantities, two dimensionless parameters will be also used in the following. The adiabatic exponent γ_k and the Grüneisen coefficient Γ_k:

$$\gamma_k = \frac{1}{\rho_k p_k}\left(\frac{\partial^2 e_k}{\partial v_k^2}\right)_{s_k} = \frac{1}{p_k K_{s,k}}, \qquad \Gamma_k = \frac{1}{\rho_k}\left(\frac{\partial p_k}{\partial e_k}\right)_{\rho_k} = \frac{\beta_k}{C_{v,k} K_{T,k}}. \tag{6.12}$$

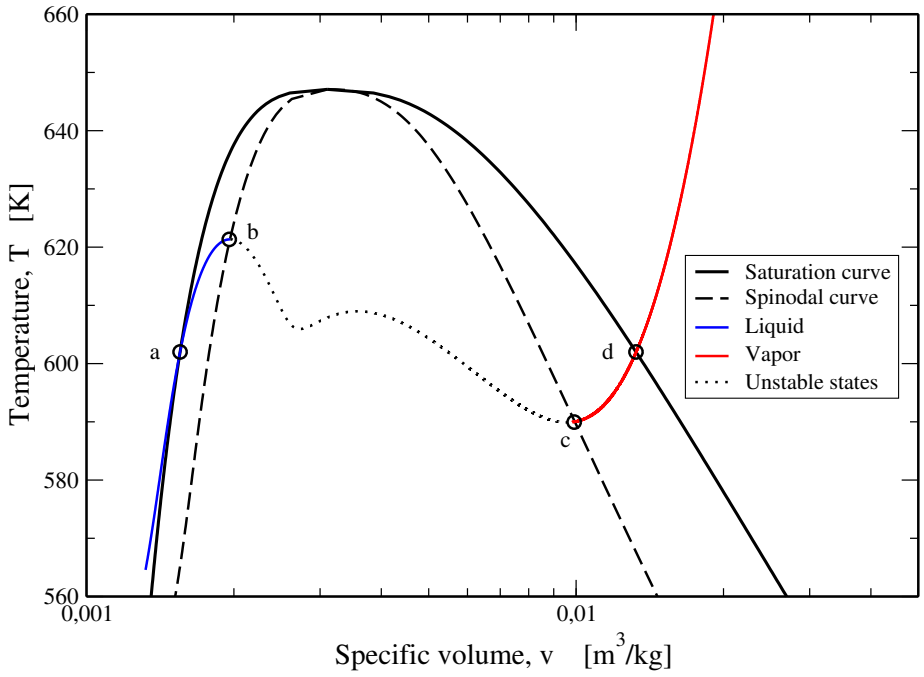

FIGURE 6.2. T-v diagram of water. The plot has been realized using the IAPWS-IF97. Here we can see the saturation curve, the spinodal curve ($(\partial p_k/\partial v_k)_{T_k} = 0$) and an isobaric curve (i.e. $p = 12.7 MPa$). The latter has been divided in three portions: the blue one represents the liquid states, the red one denotes the vapor states and the black dotted curve refers to the unstable states that connect the previous ones. Going rightwards along the isobaric curve, up to point (a) water is liquid in a stable state, from (a) to (b) water is a metastable liquid, from (b) to (c) the fluid is in unstable conditions, from (c) to (d) water is in metastable vapor conditions and, starting from point (d), the vapor is stable.

The values of the quantities introduced in this section have some constraints dictated by thermodynamic stability. It is well known that a closed system attains a maximum value of entropy at equilibrium [43]. Hence, the criteria for equilibrium and stability can be expressed, respectively, as:

$$\delta S_k = 0, \qquad \delta^n S_k < 0 \ \text{ for the smallest } n \text{ at which } \delta^n S_k \neq 0. \tag{6.13}$$

Further developments of the last criterion provide two conditions which ensure the thermodynamic stability of a system:

$$C_{v,k} > 0, \qquad \left(\frac{\partial p_k}{\partial v_k}\right)_{T_k} < 0. \tag{6.14}$$

The first is called *criterion of thermal stability*, the latter *criterion of mechanical stability*. If both are satisfied, the system is said to be *intrinsically stable*. Thermodynamic stability also provides other constraints:

$$C_{p,k} \geq C_{v,k} \geq 0, \qquad K_{T,k} \geq K_{s,k} \geq 0, \qquad \gamma_k \geq 0. \tag{6.15}$$

This means that the phasic isentropic speeds of sound are

$$c_k = \sqrt{\frac{1}{\rho_k K_{s,k}}} > 0. \tag{6.16}$$

A deeper analysis of real fluids behavior [181] suggests also that, except for very special case [25],

$$\gamma_k \geq 1, \qquad \beta_k \geq 0, \qquad \Gamma_k \geq 0. \tag{6.17}$$

The criterion of thermal stability is generally satisfied by the EoS, however the respect of the mechanical stability is not always ensured. Many EoS satisfy the mechanical stability until the so-called *spinodal line*, the line that separates the unstable domain from the stable/metastable one (see Fig. 6.2).

Cubic EoS as van der Waals' EoS, as well as some experimental EoS, exhibit the spinodal line. An example is given in Fig. 6.2 where we plot the saturation, the spinodal curves and an isobar for water according to the IAPWS-IF97 EoS. This figure also shows how we will treat the phasic EoS. The IAPWS-IF97 is a complete EoS for liquid and vapor water, hence, when we calculate $p_l = p_l(\rho_l, e_l)$, the couple (ρ_l, e_l) must lie in the liquid domain, that is, up to the liquid spinodal curve. Similarly, the couple (ρ_v, e_v) must always lie in the vapor domain, that is, up to the vapor spinodal curve. None of the phases can ever lie in the unstable domain given that it would be unphysical but also because it leads to non-real speed of sounds, hence, ill-posed hyperbolic systems. In this way we can treat stable and metastable phases without violating the thermodynamic conditions provided in Eqs. (6.14), (6.15), (6.16).

In equilibrium thermodynamics the phase transition occurs at saturation conditions. On the contrary, in real systems, it very often occurs when fluids are in the metastable domain. Especially in the context of fast transients, to well describe the physical phenomena, phases must be able to lie in the metastable regions. For this reason, in this paper the mass transfer occurs when one of the phases is metastable. The mass transfer from a metastable phase to the other takes place as a kinetic process, thus the spinodal curve is the limit beyond which phase change has already happened.

Other constraints are

$$\rho_k > 0, \quad e_k > 0, \quad T_k > 0, \tag{6.18}$$

where the latter comes from the third law of thermodynamics.

6.4 Physical modeling of the relaxation processes

The relaxation procedures discussed in this section aim to be EoS-independent and to describe the time-dependent process towards the equilibrium state.

In the literature, most of the works deal with instantaneous relaxation procedures to be used for very simple EoS such as the perfect gas or the stiffened gas EoS. In this section we show how to construct the dynamical systems of Ordinary Differential Equations (ODEs) that describe the physics involved in the successive relaxation processes. First the pressure equilibrium step, then the temperature relaxation one and, finally, the mass transfer procedure.

The systems of ODEs are initially cast in the form:

$$\mathbf{A}(t, \mathbf{y})\mathbf{y}' = \mathbf{B}(t, \mathbf{y}), \qquad \mathbf{A} \in \mathbb{R}^{q \times q}, \quad \mathbf{y}, \mathbf{B} \in \mathbb{R}^q. \tag{6.19}$$

The matrix $\mathbf{A}(t,\mathbf{y})$ will depend on the intrinsic relations between the independent variables, that is, the components of $\mathbf{y}$. It describes the dependency between the time derivatives of the independent variables and does not depend on the modeling choices that will be made about the mass transfer or the pressure relaxation rate. Conversely, $\mathbf{B}(t,\mathbf{y})$ depends only on the modeling choices.

To solve this nonlinear ODE system, it is useful to rewrite it in the canonical form

$$\mathbf{y}' = \mathbf{F}(t,\mathbf{y}), \tag{6.20}$$

where $\mathbf{F}(t,\mathbf{y}) = \mathbf{A}(t,\mathbf{y})^{-1}\mathbf{B}(t,\mathbf{y})$. In order for $\mathbf{A}$ to be invertible, its rows must be linearly independent, that is, the number of equation of the system must equal its degrees of freedom.

In thermodynamics, each phase has two degrees of freedom (except for triple and critical points and the saturation curve), further, the mixture density and internal energy do not vary because of the mass and energy conservation. This means that a system composed by two phases has three degrees of freedom. For instance, two of them define the state of phase 1 and the third one describes the amount of phase 1 in the mixture.

In the pressure and temperature relaxation procedures, since no mass transfer takes place, the amount of one phase in the mixture remains unchanged, hence, the degrees of freedom reduce to two. Referring to Eq. (6.19), formally, we can state that for the three relaxation procedures:

$$q_{pres.}, q_{temp.} = 2, \qquad q_{chemical} = 3. \tag{6.21}$$

The vector of independent variables for the pressure and temperature relaxations will be: $\mathbf{y} = [\rho_1, e_1]^T$ so that it will be quite easy to calculate the phasic pressures as $p_k = p(\rho_k, e_k)$, that is the same form of EoS required for the convective step (see Eq. (6.6)). Instead, for the chemical relaxation step, the independent variables are: $\mathbf{y} = [m_1, \rho_1, e_1]^T$.

During the relaxation step, the mixture density ρ and internal energy e do not change since each mesh cell can be considered as a closed thermodynamic system. Thus it is possible to express the magnitudes of phase 2 as dependent parameters of the magnitudes of phase 1 and of the mixture, that is

$$\alpha_2 = 1 - \frac{m_1}{\rho_1}, \qquad \rho_2 = \rho_1 \frac{\rho - m_1}{\rho_1 - m_1}, \qquad e_2 = \frac{\rho e - m_1 e_1}{\rho - m_1}. \tag{6.22}$$

These definitions come, respectively, from the mixture saturation condition (6.3) and the mixture mass and energy invariance during the mass relaxation procedure.

In the following we describe the relaxation procedures starting from the fastest one, the pressure relaxation, then we discuss the thermal and chemical relaxations that may provoke a significant energy transfer between the phases.

Before proceeding, let us clarify some physical considerations that stand behind our modeling choices. The heat exchange, in nature, occurs in two ways: *sensible heat* (conduction, convection and radiation) and *latent heat*. Hence the power per unit volume exchanged between the phases, for instance from phase 1 to phase 2, can be split as

$$q^V_{1\to 2} = q^V_{1\to 2,sens.} + q^V_{1\to 2,latent}. \tag{6.23}$$

The first provokes a temperature change of both phases, leading them towards an equilibrium temperature. The second is the energy released or absorbed during a mass transfer. An important

physical constraint is

$$q^V_{1\to 2,sens.} \times q^V_{1\to 2,latent} \geq 0. \tag{6.24}$$

Which means that if the sensible heat transfer occurs from phase 1 to phase 2, that is $T_1 > T_2$, the latent heat must be transfered in the same direction, that is $g_1 > g_2$.

For the thermo-chemical modeling, in the literature, we can find two different approaches. The first is to consider that the heat exchanged is mainly the latent one, neglecting the sensible heat transfer. As a result the mass and energy transfers are intimately correlated. Of this kind, we may mention [24, 225, 252]. The second is to separate, into two different relaxation procedures, the two phenomena. This is usually done forcing an instantaneous thermal equilibrium, then, during the chemical relaxation procedure, the phase evolve at the same temperature. For instance, the works of [64, 200, 233, 283] are of this kind.

When considering non-instantaneous relaxation processes, at the end of the thermal relaxation step, the phasic temperatures may still be different, therefore the mass transfer can take place between phases in thermal disequilibrium. We think that our procedure is physically consistent and is a more general approach than the two kinds of modeling mentioned above. In fact, on the one hand, sensible heat transfer occurs, hence it needs to be included as source term of system (6.1), however, it does not take place instantaneously. This physical process is taken into account in Section 6.4.2, and is called in the following as *temperature relaxation process*. On the other hand, it is adherent to the physics to consider that when phase transfer occurs, a temperature disequilibrium exists between the phases. This process is described in Section 6.4.3, and is called in the following as *mass transfer* or *chemical relaxation process*.

6.4.1 Pressure relaxation

At the end of the convection step, vapor and liquid evolve at different pressures. At the interface, the two phases exert a force that is proportional to the interface pressure, hence, a positive resultant force is applied to the lower pressure phase by the higher pressure phase. This force makes the system to tend towards the pressure equilibrium condition. However, as far as the equilibrium condition is not achieved, the phase at higher pressure makes a positive work since it expands its volume. A work exchange between the phases means that the phasic internal energies change.

This procedure is devoted to the modeling of this process in order to quantify the phasic internal energies changes, and as a result, the void fraction change. To this end, we consider each mesh cell as an isolated thermodynamic system (no-exchange of mass and energy with the outside world), composed by two subsystems that can be considered as closed thermodynamic systems (no-exchange of mass between them). Evidently, these subsystems delimit the liquid and the vapor. The first law of thermodynamics for closed systems can be written for each phase. For phase 1:

$$\Phi_{th,2\to 1} - W_{1\to 2} = \frac{d}{dt}(\rho_1 e_1 V_1). \tag{6.25}$$

Here we use the typical convention of positive heat when it is provided from the outside world to the system, and positive work when it is done by the system to the outside.

The heat transfer will be taken into account in the next relaxation process, hence: $\Phi_{th,2\to1} = 0$. Considering that $V_k = \alpha_k V$, the first law reads:

$$-p_{int} V \frac{d\alpha_1}{dt} = \frac{d}{dt}(\rho_1 e_1 V_1). \tag{6.26}$$

As concerns the void fraction time derivative, using basic rules of calculus, it can be rewritten as

$$\frac{d\alpha_1}{dt} = \frac{1}{\rho_1}\left[\frac{dm_1}{dt} - \alpha_1 \frac{d\rho_1}{dt}\right]. \tag{6.27}$$

During this relaxation, no mass transfer occurs, therefore m_1 stays constant. Using this information and Eq. (6.27), the first principle for the phase 1 is:

$$\frac{de_1}{dt} = \frac{p_{int}}{\rho_1^2}\frac{d\rho_1}{dt}. \tag{6.28}$$

An analogous relation can be found for phase 2.

Now we need to provide a relation for the modeling of the temporal rate of change of one of the variables. A reasonable choice, already employed in the literature, is to consider that the volume fractions vary proportionally to the pressure difference between the phases, that is

$$\frac{d\alpha_1}{dt} \propto (p_1 - p_2). \tag{6.29}$$

In fact, the pressure difference is the main driver of this relaxation process, hence, it is a realistic hypothesis. As stated before, we prefer to adopt ρ_1 and e_1 as independent variables because we want to be able to calculate the phasic pressures as $p_k = p(\rho_k, e_k)$. Eqs. (6.27) and (6.29) define the rate of change of ρ_1, instead, (6.28) defines the one of e_1. For such a case, system (6.19) takes the form:

$$\begin{bmatrix} 1 & 0 \\ -\frac{p_{int}}{\rho_1^2} & 1 \end{bmatrix} \frac{d}{dt} \begin{bmatrix} \rho_1 \\ e_1 \end{bmatrix} = \begin{bmatrix} -\frac{\rho_1}{\alpha_1}\frac{p_1 - p_2}{\Theta^p} \\ 0 \end{bmatrix}, \tag{6.30}$$

where $\Theta^p > 0$ is the characteristic time of the pressure relaxation process and is, generally, rather small. If we cast system (6.30) in the canonical form (see Eq. (6.20)), it reads

$$\begin{cases} \frac{d\rho_1}{dt} = -\frac{\rho_1}{\alpha_1}\frac{p_1 - p_2}{\Theta^p}, \\ \frac{de_1}{dt} = -\frac{p_{int}}{m_1}\frac{p_1 - p_2}{\Theta^p}. \end{cases} \tag{6.31}$$

Given that the pressure relaxation process is rather fast, another modeling choice can be made, alternatively to Eq. (6.29). We propose this new method because it guarantees better computational features, that is, the possibility to employ a semi-analitycal numerical procedure. We suppose that the pressure disequilibrium follows an exponential decrease in time:

$$\frac{d(p_1 - p_2)}{dt} = -\frac{p_1 - p_2}{\Theta^p}. \tag{6.32}$$

The analytical solution of (6.32), for $\Theta^p \neq \Theta^p(t, p_k)$, is

$$(p_1 - p_2)(t) = (p_1 - p_2)_{t=0}\, e^{-t/\Theta^p}. \tag{6.33}$$

that is always positive. This choice allows us to construct numerical schemes that are more physically consistent avoiding that the pressure disequilibrium may change its sign (for $\Theta^p > 0$).

Let us construct a dynamical system as (6.30), built having in (6.32) its driver towards the equilibrium. Using the caloric EoS: $e_k = e_k(p_k, \rho_k)$, the time derivative of the specific internal energy is

$$\frac{de_k}{dt} = \left(\frac{\partial e_k}{\partial p_k}\right)_{\rho_k} \frac{dp_k}{dt} + \left(\frac{\partial e_k}{\partial \rho_k}\right)_{p_k} \frac{d\rho_k}{dt}. \tag{6.34}$$

Solving for $\frac{dp_k}{dt}$:

$$\frac{dp_k}{dt} = \rho_k \Gamma_k \left[\frac{de_k}{dt} - \left(\frac{\partial e_k}{\partial \rho_k}\right)_{p_k} \frac{d\rho_k}{dt}\right], \tag{6.35}$$

As derived in Eq. (6.28), $\frac{de_k}{dt} = \frac{p_{int}}{\rho_k^2}\frac{d\rho_k}{dt}$, hence

$$\frac{dp_k}{dt} = \rho_k \Gamma_k \left[\frac{p_{int}}{\rho_k^2} - \left(\frac{\partial e_k}{\partial \rho_k}\right)_{p_k}\right] \frac{d\rho_k}{dt}. \tag{6.36}$$

In order to obtain a relation for the time-evolution of ρ_1, we need to express a dependency relation between $\frac{d\rho_1}{dt}$ and $\frac{d\rho_2}{dt}$. To this end, one should use the constraint of the mass conservation for the mixture. Considering that $\rho = \alpha_1\rho_1 + \alpha_2\rho_2$ and that $\frac{d\rho}{dt} = 0$, one obtains

$$\frac{d\rho_2}{dt} = -\frac{\rho_1 - \rho_2}{\alpha_2\rho_1}\frac{dm_1}{dt} - \frac{\alpha_1\rho_2}{\alpha_2\rho_1}\frac{d\rho_1}{dt}, \tag{6.37}$$

however, for the pressure relaxation step, m_1 stays constant. Plugging (6.36) and (6.37) into (6.32), and rearranging, one obtains:

$$a\frac{d\rho_1}{dt} = -\frac{p_1 - p_2}{\Theta^p}. \tag{6.38}$$

where

$$a = \rho_1\Gamma_1\left[\frac{p_{int}}{\rho_1^2} - \left(\frac{\partial e_1}{\partial \rho_1}\right)_{p_1}\right] + \rho_2\Gamma_2\frac{\alpha_1\rho_2}{\alpha_2\rho_1}\left[\frac{p_{int}}{\rho_2^2} - \left(\frac{\partial e_2}{\partial \rho_2}\right)_{p_2}\right]. \tag{6.39}$$

a is a bounded function for $\alpha_2 > 0$ however its sign may depend on the choice of p_{int}.

We can rewrite the ODE system as:

$$\begin{bmatrix} a & 0 \\ -\frac{p_{int}}{\rho_1^2} & 1 \end{bmatrix} \frac{d}{dt}\begin{bmatrix} \rho_1 \\ e_1 \end{bmatrix} = \begin{bmatrix} -\frac{p_1 - p_2}{\Theta^p} \\ 0 \end{bmatrix}, \tag{6.40}$$

that, in the canonical form becomes

$$\begin{cases} \frac{d\rho_1}{dt} = -\frac{1}{a}\frac{p_1 - p_2}{\Theta^p}, \\ \frac{de_1}{dt} = -\frac{p_{int}}{a\rho_1^2}\frac{p_1 - p_2}{\Theta^p}. \end{cases} \tag{6.41}$$

This ODE system is the one that will be employed in our numerical scheme. For a sufficiently small Θ^p, at the end of the pressure relaxation process, the two phasic pressures would be very close each other. For instance, for $\Theta^p = \Delta t^{conv}/9$, the final pressure disequilibrium is around the 0.01% of the initial one. As a result, after the pressure relaxation procedure, phases may be considered roughly in pressure equilibrium for $\Theta^p < \Delta t^{conv}/9$.

For the analysis of the irreversibility of the pressure relaxation see 6.11.1.

6.4.2 Temperature relaxation

At the end of the pressure relaxation step, the phases are roughly at same pressure but at a different temperature. During this step, the phasic temperatures tend towards an equilibrium temperature for the mixture. Similarly to the approach of the previous section, the mesh cell is considered as an isolated thermodynamic system composed of two closed subsystems that identify each of the two phases.

For phase 1, the first law is again the one reported in Eq. (6.25). However the heat flux is not anymore zero, but equal to

$$\Phi_{th,2\to1} = hA_{int}(T_2 - T_1). \tag{6.42}$$

Here we consider that the sensible heat is mainly due to convection. h is the heat transfer coefficient expressed in $W/m^2 \cdot K$ and A_{int} is the interface area expressed in m^2 and flow pattern dependent. This dependency is taken into account just at the beginning of the temperature relaxation step and then A_{int} is not supposed to vary during the process.

The first principle for phase k is

$$\frac{de_k}{dt} = \frac{hA_{int}}{m_k V}(T_j - T_k) + \frac{p_{int}}{\rho_k^2}\frac{d\rho_k}{dt}. \tag{6.43}$$

Since the pressure equilibrium is almost achieved at the end of the previous relaxation step, we impose the dynamical pressure equilibrium

$$\frac{dp_1}{dt} = \frac{dp_2}{dt}. \tag{6.44}$$

It does not mean that we impose $p_1(t) = p_2(t) = p(t)$, rather that the pressure difference between phases does not change during the heat transfer process. Using Eq. (6.35), this condition becomes

$$\rho_1\Gamma_1\left\{\frac{hA_{int}}{m_1V}(T_2 - T_1) + \left[\frac{p_{int}}{\rho_1^2} - \left(\frac{\partial e_1}{\partial \rho_1}\right)_{p_1}\right]\frac{d\rho_1}{dt}\right\} = \rho_2\Gamma_2\left\{\frac{hA_{int}}{m_2V}(T_1 - T_2) + \left[\frac{p_{int}}{\rho_2^2} - \left(\frac{\partial e_2}{\partial \rho_2}\right)_{p_2}\right]\frac{d\rho_2}{dt}\right\}. \tag{6.45}$$

Phasic densities can be correlated by (6.37) and this, finally, provides the temporal evolution equation of ρ_1:

$$a\frac{d\rho_1}{dt} = -\frac{hA_{int}}{V}(T_2 - T_1)\left(\frac{\Gamma_1}{\alpha_1} + \frac{\Gamma_2}{\alpha_2}\right). \tag{6.46}$$

where a is the one defined in (**??**). For such a case, we can write the ODE system:

$$\begin{bmatrix} a & 0 \\ -\frac{p_{int}}{\rho_1^2} & 1 \end{bmatrix}\frac{d}{dt}\begin{bmatrix}\rho_1 \\ e_1\end{bmatrix} = \begin{bmatrix} -\frac{hA_{int}}{V}(T_2 - T_1)\left(\frac{\Gamma_1}{\alpha_1} + \frac{\Gamma_2}{\alpha_2}\right) \\ \frac{hA_{int}}{m_1V}(T_2 - T_1)\end{bmatrix}, \tag{6.47}$$

which, in the canonical form becomes

$$\begin{cases} \frac{d\rho_1}{dt} = -\frac{hA_{int}}{V}(T_2 - T_1)\frac{1}{a}\left(\frac{\Gamma_1}{\alpha_1} + \frac{\Gamma_2}{\alpha_2}\right), \\ \frac{de_1}{dt} = -\frac{hA_{int}}{V}(T_2 - T_1)\left[\frac{p_{int}}{a\rho_1^2}\left(\frac{\Gamma_1}{\alpha_1} + \frac{\Gamma_2}{\alpha_2}\right) - \frac{1}{m_1}\right]. \end{cases} \tag{6.48}$$

hA_{int}/V is assigned or calculated at the beginning of this relaxation procedure and is assumed to not change during this process. In order to close the system, we need to provide the phasic EoS $p_k = p_k(\rho_k, e_k)$, $T_k = T_k(\rho_k, e_k)$ (or alternatively, $T_k = T_k(\rho_k, p_k)$) and the values of c_k and Γ_k.

We can see that system (6.48) does not need any characteristic time for this process since it is intrinsically defined, somehow, by hA_{int}/V and the other thermodynamic properties.

For the analysis of the irreversibility of the temperature relaxation see 6.11.2.

In the case of a quasi-instantaneous temperature relaxation with a general EoS, instead of arbitrarily increasing the morphological term hA_{int}/V, one can employ the semi-analytic procedure proposed in 6.10.1. It will give rise to a much more robust numerical scheme.

6.4.3 Mass transfer

This procedure allows the mass transfer for both condensation and evaporation events. In the following, we assume that the mass transfer occurs from phase 1, the *giver*, to phase 2, the *taker*. This means that, in terms of chemical potentials, $g_1 > g_2$. In an evaporation process, phase 1 is the liquid and phase 2 is the vapor, for a condensation process, it is the opposite.

An important assumption is to neglect the exchange of specific kinetic and potential energies since phases move at the same velocity at the same vertical level, therefore, a portion of mass, when passing from phase 1 to phase 2, does not change its specific kinetic energy. If the same mass transfer technique is adopted for the 7-equation model [12], or for any other model with velocity disequilibrium, this exchange should be taken into account.

The heat transfer has been already taken into account in the previous relaxation process, thus $\Phi_{th,2\to1} = 0$. The mass conservation law for the open system defined by the phase 1 is

$$\frac{dM_1}{dt} = V\frac{dm_1}{dt} = -G_{1\to2}A_{int}. \tag{6.49}$$

The mass conservation law for the open system of phase 2 is

$$\frac{dM_2}{dt} = V\frac{dm_2}{dt} = +G_{1\to2}A_{int}. \tag{6.50}$$

Obviously, due to the global mass conservation of the closed system represented by phase 1 and 2 together:

$$\frac{dm_1}{dt} = -\frac{dm_2}{dt}. \tag{6.51}$$

The mixture energy conservation provides a relation between the specific energies time derivatives :

$$\frac{de_2}{dt} = -\frac{e_1 - e_2}{m_2}\frac{dm_1}{dt} - \frac{m_1}{m_2}\frac{de_1}{dt}. \tag{6.52}$$

Similarly to what done in Section 6.4.2, in the following we impose the pressure equilibrium by forcing condition (6.44). Thanks to Eqs. (6.37) and (6.52) we can express the dependency relation between $\frac{d\rho_1}{dt}$, $\frac{d\rho_2}{dt}$, and $\frac{de_1}{dt}$, $\frac{de_2}{dt}$, Eq. (6.44) is equivalent to

$$i_p\frac{dm_1}{dt} + j_p\frac{d\rho_1}{dt} + k_p\frac{de_1}{dt} = 0, \tag{6.53}$$

where

$$\begin{aligned} i_p &= \rho_2\Gamma_2\frac{e_1 - e_2}{m_2} + \left(\frac{\partial p_2}{\partial \rho_2}\right)_{e_2}\frac{\rho_1 - \rho_2}{\alpha_2\rho_1}, \\ j_p &= \left(\frac{\partial p_1}{\partial \rho_1}\right)_{e_1} + \left(\frac{\partial p_2}{\partial \rho_2}\right)_{e_2}\frac{\alpha_1\rho_2}{\alpha_2\rho_1}, \\ k_p &= \rho_1\Gamma_1 + \rho_2\Gamma_2\frac{m_1}{m_2}. \end{aligned} \tag{6.54}$$

Since the mass transfer process occurs after the temperature relaxation step, the temperature difference between the phases stays constant, which means:

$$\frac{dT_1}{dt} = \frac{dT_2}{dt}. \tag{6.55}$$

By considering $e_k = e_k(T_k, \rho_k)$, its time derivative is:

$$\frac{de_k}{dt} = C_{v,k}\frac{dT_k}{dt} + \left(\frac{\partial e_k}{\partial \rho_k}\right)_{T_k}\frac{d\rho_k}{dt}. \tag{6.56}$$

Solving for $\frac{dT_k}{dt}$:

$$\frac{dT_k}{dt} = \frac{1}{C_{v,k}}\left[\frac{de_k}{dt} - \left(\frac{\partial e_k}{\partial \rho_k}\right)_{T_k}\frac{d\rho_k}{dt}\right]. \tag{6.57}$$

Imposing that the temperature difference stays constant, one obtains

$$i_T\frac{dm_1}{dt} + j_T\frac{d\rho_1}{dt} + k_T\frac{de_1}{dt} = 0, \tag{6.58}$$

where

$$\begin{aligned} i_T &= \frac{1}{C_{v,2}}\frac{e_1 - e_2}{m_2} + \left(\frac{\partial T_2}{\partial \rho_2}\right)_{e_2}\frac{\rho_1 - \rho_2}{\alpha_2\rho_1}, \\ j_T &= \left(\frac{\partial T_1}{\partial \rho_1}\right)_{e_1} + \left(\frac{\partial T_2}{\partial \rho_2}\right)_{e_2}\frac{\alpha_1\rho_2}{\alpha_2\rho_1}, \\ k_T &= \frac{1}{C_{v,1}} + \frac{1}{C_{v,2}}\frac{m_1}{m_2}. \end{aligned} \tag{6.59}$$

For a general closure law for the mass transfer, system (6.19) takes the form:

$$\begin{bmatrix} 1 & 0 & 0 \\ i_p & j_p & k_p \\ i_T & j_T & k_T \end{bmatrix}\frac{d}{dt}\begin{bmatrix} m_1 \\ \rho_1 \\ e_1 \end{bmatrix} = \begin{bmatrix} -G_{1\to 2}\frac{A_{int}}{V} \\ 0 \\ 0 \end{bmatrix} \tag{6.60}$$

where matrix $\mathbf{A}_m(\mathbf{y})$ gives the dependency of the independent variables: m_1, ρ_1, e_1 for any closure law for the mass transfer. Conversely, the right hand side depends exclusively from this closure law.

The inverse matrix is:

$$\mathbf{A}_m^{-1} = \begin{bmatrix} 1 & 0 & 0 \\ \frac{i_p k_T - k_p i_T}{k_p j_T - j_p k_T} & \frac{-k_T}{k_p j_T - j_p k_T} & \frac{k_p}{k_p j_T - j_p k_T} \\ \frac{j_p i_T - i_p j_T}{k_p j_T - j_p k_T} & \frac{j_T}{k_p j_T - j_p k_T} & \frac{-j_p}{k_p j_T - j_p k_T} \end{bmatrix}, \tag{6.61}$$

hence, the canonical form for the ODE system is

$$\begin{cases} \frac{dm_1}{dt} = -G_{1\to 2}\frac{A_{int}}{V}, \\ \frac{d\rho_1}{dt} = -G_{1\to 2}\frac{A_{int}}{V}\frac{i_p k_T - k_p i_T}{k_p j_T - j_p k_T}, \\ \frac{de_1}{dt} = -G_{1\to 2}\frac{A_{int}}{V}\frac{j_p i_T - i_p j_T}{k_p j_T - j_p k_T}. \end{cases} \tag{6.62}$$

This system describes the temporal evolution of ρ_1 and e_1 that complies with: (i) the mixture mass conservation, (ii) the mixture energy conservation, (iii) the pressure equilibrium, and, (iv) the

phasic temperature difference invariance, for a given mass transfer term that defines the temporal evolution of m_1. Thus, to close the system, a closure law for the mass transfer term $G_{1\to 2}A_{int}$ is needed.

In the context of the non-equilibrium two-phase flow, various closure laws have been formulated to describe the mass transfer process. For instance nucleation models (see [208, 214]), statistical mechanics theory (see [275–277]), or simpler relaxation models. However, an important physical feature to be respected is that: the deeper the metastability reached, the higher is the probability for the phase change to occur. For instance it can be taken into account by considering the mass transfer rate to be somewhat proportional to the chemical disequilibrium:

$$\frac{dm_1}{dt} = -\frac{g_1 - g_2}{\Theta^g}\frac{A_{int}}{V}, \qquad \Theta^g > 0, \tag{6.63}$$

where the parameter Θ^g is the characteristic relaxation time towards the chemical equilibrium of the mixture. Another way is to use the mass relaxation law of Bilicki and co-workers [28, 29, 84]:

$$\frac{dm_1}{dt} = -\frac{m_1 - m_{1,eq}}{\Theta^g}, \qquad \Theta^g > 0 \tag{6.64}$$

that is, the partial masses (or, equivalently, the mass fractions) relax exponentially towards the equilibrium condition defined by $m_{1,eq}$. In [28, 29, 84] the authors provided also some closure laws for Θ^g however they are intended just for flashing flows.

For the analysis of the irreversibility of the mass transfer process see 6.11.3.

In the case of a quasi-instantaneous Gibbs free enthalpy relaxation with a general EoS, the semi-analytic procedure proposed in 6.10.2 guarantees a greater numerical robustness than (6.62).

6.5 Numerical solution methods

Considering the contribution of the relaxation sources, the six-equation model becomes a system of six PDEs with source terms:

$$\begin{cases} \partial_t \alpha_1 + \mathbf{u}\cdot\nabla\alpha_1 = \frac{\alpha_1}{a\rho_1\Theta^p}(p_1 - p_2) + \frac{\alpha_1}{a\rho_1}\frac{hA_{int}}{V}(T_1 - T_2) - \frac{1}{\rho_1}\left(1 - \alpha_1\frac{i_p k_T - k_p i_T}{k_p j_T - j_p k_T}\right)G_{1\to 2}\frac{A_{int}}{V}, \\ \partial_t(\alpha_1\rho_1) + \nabla(\alpha_1\rho_1\mathbf{u}) = -G_{1\to 2}\frac{A_{int}}{V}, \\ \partial_t(\alpha_2\rho_2) + \nabla(\alpha_2\rho_2\mathbf{u}) = +G_{1\to 2}\frac{A_{int}}{V}, \\ \partial_t(\rho\mathbf{u}) + \nabla(\rho\mathbf{u}\otimes\mathbf{u} + \alpha_1 p_1 + \alpha_2 p_2) = 0, \\ \partial_t(\alpha_1\rho_1 E_1) + \nabla[\alpha_1(\rho_1 E_1 + p_1)\mathbf{u}] + \Sigma = -\frac{\alpha_1 p_{int}}{a\rho_1\Theta^p}(p_1 - p_2) + b_T\frac{hA_{int}}{V}(T_1 - T_2) - b_g G_{1\to 2}\frac{A_{int}}{V} \\ \partial_t(\alpha_2\rho_2 E_2) + \nabla[\alpha_2(\rho_2 E_2 + p_2)\mathbf{u}] - \Sigma = +\frac{\alpha_1 p_{int}}{a\rho_1\Theta^p}(p_1 - p_2) - b_T\frac{hA_{int}}{V}(T_1 - T_2) + b_g G_{1\to 2}\frac{A_{int}}{V} \end{cases} \tag{6.65}$$

where $b_T = \alpha_1\rho_1\left[\frac{p_{int}}{a\rho_1^2}\left(\frac{\Gamma_1}{\alpha_1} + \frac{\Gamma_2}{\alpha_2}\right) - \frac{1}{\alpha_1\rho_1}\right]$ and $b_g = \alpha_1\rho_1\frac{j_p i_T - i_p j_T}{k_p j_T - j_p k_T}$.

In this section, we discuss the numerical methods used for solving system (6.65). The solution is obtained by a succession of operators [256] of first order,

$$\mathbf{U}_i^{n+1} = L_{source}^{\Delta t}\, L_{hyp}^{\Delta t}\, \mathbf{U}_i^n \tag{6.66}$$

or second order

$$\mathbf{U}_i^{n+1} = L_{source}^{\Delta t/2} L_{hyp}^{\Delta t} L_{source}^{\Delta t/2} \mathbf{U}_i^n, \tag{6.67}$$

where L_{hyp} and L_{source} denote, respectively, the hyperbolic and the source operator. The latter is composed by three operators: L_p, L_T, L_g that are, respectively, the operators for pressure, temperature and chemical potential relaxation procedures. Considering for simplicity the first order operator splitting, at the end of the hyperbolic operator the state vector is $\mathbf{U}^{n+} = L_{hyp}^{\Delta t}\mathbf{U}^n$, that is used as initial value for the pressure relaxation operator at the end of which the state variable is $\mathbf{U}^{n+,p} = L_p^{\Delta t}\mathbf{U}^{n+}$. This is used as initial value for the temperature relaxation and the result will be $\mathbf{U}^{n+,pT} = L_T^{\Delta t}\mathbf{U}^{n+,p}$, which, in turn, is the initial value for the mass transfer procedure, giving, finally: $\mathbf{U}^{n+,pTg} = L_g^{\Delta t}\mathbf{U}^{n+,pT}$.

6.5.1 Hyperbolic operator

The application of the hyperbolic operator to $\mathbf{U}^n$ will give an intermediate state

$$\mathbf{U}^{n+} = L_{hyp}^{\Delta t}\mathbf{U}^n, \tag{6.68}$$

which is used in the subsequent step as initial value for the integration of the pressure relaxation terms. For simplicity we describe the solver for the 1D system. In the so-called *wave propagation form* of [168], the second-order numerical scheme for the hyperbolic operator has the following form:

$$\mathbf{U}_i^{n+} = \mathbf{U}_i^n - \frac{\Delta t}{\Delta z}(\mathscr{A}^+\Delta\mathbf{U}_{i-\frac{1}{2}} + \mathscr{A}^-\Delta\mathbf{U}_{i+\frac{1}{2}}) + \frac{\Delta t}{\Delta z}(\mathbf{F}_{i-\frac{1}{2}}^{2nd} - \mathbf{F}_{i+\frac{1}{2}}^{2nd}). \tag{6.69}$$

Here $\mathscr{A}^{\pm}\Delta\mathbf{U}_{i+\frac{1}{2}}$ are the so-called fluctuations at the interface $z_{i+\frac{1}{2}}$ between cells i and $i+1$. Namely, $\mathscr{A}^+\Delta\mathbf{U}_{i+\frac{1}{2}}$ is the right-going fluctuation, $\mathscr{A}^-\Delta\mathbf{U}_{i+\frac{1}{2}}$ is the left-going one. Following [168], the fluctuations can be calculated in terms of the wave solution structure of local Riemann problems at interfaces $z_{i+\frac{1}{2}}$ as:

$$\mathscr{A}^+\Delta\mathbf{U}_{i-\frac{1}{2}} = \sum_{m=1}^{M} s_{i-\frac{1}{2}}^{m+}\mathscr{W}_{i-\frac{1}{2}}^m, \qquad \mathscr{A}^-\Delta\mathbf{U}_{i+\frac{1}{2}} = \sum_{m=1}^{M} s_{i+\frac{1}{2}}^{m-}\mathscr{W}_{i+\frac{1}{2}}^m. \tag{6.70}$$

where $s^+ = \max(s,0)$ and $s^- = \min(s,0)$, and where $\mathscr{W}^m$ and s^m , $m = 1,\ldots,M$, indicate the waves and speeds, respectively, representing the Riemann solution structure for initial data pairs $(\mathbf{U}_i, \mathbf{U}_{i+1})$. An approximate Riemann solver is needed to compute these quantities. Here we will consider Riemann solvers composed of $M = 3$ waves. This well represents the wave pattern of system (6.1), which is composed of three waves as the single-phase Euler equations.

The second-order accuracy of the hyperbolic operator is achieved thanks to the second-order correction fluxes:

$$\mathbf{F}_{i+\frac{1}{2}}^{2nd} = \frac{1}{2}\sum_{m=1}^{M} |s_{i+\frac{1}{2}}^m| \left(1 - \frac{\Delta t}{\Delta z}|s_{i+\frac{1}{2}}^m|\right)\mathscr{W}_{i+\frac{1}{2}}^{m,2nd} \tag{6.71}$$

where $\mathscr{W}_{i+\frac{1}{2}}^{m,2nd}$ are a modified version of $\mathscr{W}_{i+\frac{1}{2}}^m$ obtained by applying a limiter function (cf. [168]).

To calculate the fluctuations we have adopted the approximate solver proposed in [200] for system (6.1). This solver does not discretize the nonconservative terms $\Sigma(\mathbf{U}, \partial_z\mathbf{U})$ in the phasic total energy equations. This choice has been analyzed and discussed in [80], where we conclude that,

except for very strong shocks in the two-phase mixture, these nonconservative terms do not affect the numerical results when the pressure relaxation operator is activated.

Except for the first equation, which describes the advection of α_1, the system is now in a conservative form. In such a case, the interfacial fluctuations of Eq. (6.69) may be defined as:

$$\mathscr{A}^+\Delta\mathbf{U}_{i-\frac{1}{2}} = \mathbf{F}_i - \mathbf{F}^{HLLC}_{i-\frac{1}{2}}, \qquad \mathscr{A}^-\Delta\mathbf{U}_{i+\frac{1}{2}} = \mathbf{F}^{HLLC}_{i+\frac{1}{2}} - \mathbf{F}_i. \tag{6.72}$$

The terms $\mathbf{F}^{HLLC}_{i\pm\frac{1}{2}}$ have been defined applying the idea of the HLLC solver of Toro et al. [265] and consists in applying the standard HLLC method to the conservative portion of the system plus the advection equation for α_1. The resulting solver consists of three waves $\mathscr{W}^i$, $i = 1,2,3$, moving at speeds

$$s^1 = S_\ell, \qquad s^2 = S^*, \qquad s^3 = S_r, \tag{6.73}$$

that separate four constant states $\mathbf{U}_\ell$, $\mathbf{U}^*_\ell$, $\mathbf{U}^*_r$ and $\mathbf{U}_r$. Here we indicate with subscripts ${}^*\ell$, ${}^*r$ quantities corresponding to the states $\mathbf{U}^*_\ell$ and $\mathbf{U}^*_r$ adjacent (respectively on the left and on the right) to the middle wave propagating at speed S^*. Following Davis [72] we define

$$S_\ell = \min(u_\ell - c_\ell, u_r - c_r), \qquad S_r = \max(u_\ell + c_\ell, u_r + c_r). \tag{6.74}$$

The speed S^* is then determined as in [264]:

$$S^* = u^* = \frac{p_r - p_\ell + \rho_\ell u_\ell(S_\ell - u_\ell) - \rho_r u_r(S_r - u_r)}{\rho_\ell(S_\ell - u_\ell) - \rho_r(S_r - u_r)}. \tag{6.75}$$

The left and right sound speeds c_ℓ and c_r correspond to the sound speed of the homogeneous six-equation model c_{hom} in (6.5). Note that although nonconservative terms are neglected in this simple HLLC solver in the definition of the waves for the phasic total energies, the speed of sound used in the definition of the speeds of the waves is the one of the model that does include nonconservative terms. The middle states $\mathbf{U}^*_\ell$, $\mathbf{U}^*_r$ have been defined in [200] so as to satisfy the following Rankine–Hugoniot conditions, based on the conservative portion of the system:

$$\begin{aligned} F^{(\zeta)}(\mathbf{U}_r) - F^{(\zeta)}(\mathbf{U}^*_r) &= S_r(\mathbf{U}^{(\zeta)}_r - \mathbf{U}^{*(\zeta)}_r), \\ F^{(\zeta)}(\mathbf{U}^*_\ell) - F^{(\zeta)}(\mathbf{U}_\ell) &= S_\ell(\mathbf{U}^{*(\zeta)}_\ell - \mathbf{U}^{(\zeta)}_\ell), \\ F^{(\zeta)}(\mathbf{U}^*_r) - F^{(\zeta)}(\mathbf{U}^*_\ell) &= S^*(\mathbf{U}^{*(\zeta)}_r - \mathbf{U}^{*(\zeta)}_\ell), \end{aligned} \tag{6.76}$$

$\zeta = 2,\dots,6$. Then, the middle states are obtained as

$$\mathbf{U}_{*\iota} = \begin{bmatrix} \alpha_{1,\iota} \\ (\alpha_1\rho_1)_\iota \frac{S_\iota - u_\iota}{S_\iota - S^*} \\ (\alpha_2\rho_2)_\iota \frac{S_\iota - u_\iota}{S_\iota - S^*} \\ \rho_\iota \frac{S_\iota - u_\iota}{S_\iota - S^*} S^* \\ (\alpha_1\rho_1)_\iota \frac{S_\iota - u_\iota}{S_\iota - S^*} \left(E_{1,\iota} + (S^* - u_\iota)\left(S^* + \frac{p_{1,\iota}}{\rho_{1,\iota}(S_\iota - u_\iota)} \right) \right) \\ (\alpha_2\rho_2)_\iota \frac{S_\iota - u_\iota}{S_\iota - S^*} \left(E_{2,\iota} + (S^* - u_\iota)\left(S^* + \frac{p_{2,\iota}}{\rho_{2,\iota}(S_\iota - u_\iota)} \right) \right) \end{bmatrix}, \tag{6.77}$$

$\iota = \ell, r$. The waves for this simple HLLC-type solver are

$$\mathscr{W}^1 = \mathbf{U}^*_\ell - \mathbf{U}_\ell, \quad \mathscr{W}^2 = \mathbf{U}^*_r - \mathbf{U}^*_\ell, \quad \mathscr{W}^3 = \mathbf{U}_r - \mathbf{U}^*_r. \tag{6.78}$$

6.5.2 Relaxation operators

The relaxation operators are essentially represented by the three systems of ODEs reported in Eqs. (6.41), (6.48), (6.62). They can be solved by both implicit and explicit ODE solvers. Generally speaking, the implicit ODE solvers are more robust due to their larger *A-stable* domain however their are much more expensive than the explicit schemes since a nonlinear system must be solved at each time step. Especially when dealing with time consuming EoS, the computational cost of this kind of ODE solvers could be too high. Further due to the so-called Dahlquist barrier, the *A-stability* is lost for an implicit scheme with accuracy order higher than 2 (unless using coupled methods).

For this work, ODE solvers with this order of accuracy have proven to not be adequate. For instance, we have tested implicit low-accuracy ODE solvers (*backward Euler* and *Crank-Nicolson* solvers) for the temperature relaxation, and we observed that the pressure equilibrium between the phases is often violated. This means that the heat exchange does not occur anymore at the mechanical equilibrium as imposed by Eq. (6.44). Analogously, using implicit low-accuracy ODE solvers for the mass transfer procedure, the thermal and the mechanical equilibrium are often violated as well. These provoked the appearance of some oscillations in our 1-D shock-tube tests.

For the calculations made in this article we mainly used high order explicit Runge-Kutta (RK) methods with adaptive stepsize. The order of accuracy of the RK algorithms tested spanned from 3 to 8. However the most used one was the so-called RK45, i.e. the algorithm proposed by Fehlberg [108], that is, a method of forth order with an error estimator of fifth order for the calculation of the variable time step. The drawback of this explicit method is the loss of stability for stiff problems. The stiffness of our ODE systems depends on the values of some parameters: Θ^p for the pressure relaxation, hA_{int}/V for the temperature relaxation and Θ^g for the mass transfer process. For very low values of Θ^p, Θ^g and for very high values of hA_{int}/V, the ODE systems may become stiff.

The pressure relaxation procedure is often stiff since we aim to approximate unique-pressure flows. This may cause unphysical behaviors as the phasic pressures intersections.

On the other hand, as we have already mentioned, using time consuming EoS, it would be too expensive to employ implicit methods for stiff ODEs. Hence we needed to assume that the pressure disequilibrium follows an exponential decrease in time as shown in (6.32). The latter has an analytical solution, reported in (6.33), that can be used for computational purposes designing a semi-analytical algorithm. The canonical form of the pressure relaxation ODE system can be rewritten as

$$\begin{cases} \frac{d\rho_1}{dt} = -\frac{1}{a\Theta^p}(p_1 - p_2)_{hyp}\ e^{-t/\Theta^p}, \\ \frac{de_1}{dt} = -\frac{p_{int}}{a\rho_1^2\Theta^p}(p_1 - p_2)_{hyp}\ e^{-t/\Theta^p}. \end{cases} \tag{6.79}$$

Here $(p_1 - p_2)_{hyp}$ is the pressure disequilibrium at the end of the hyperbolic step. This choice has been very beneficial allowing to construct a very robust pressure relaxation scheme, preventing the intersection of phasic pressures.

Similarly, if one is interested in quasi-instantaneous thermal and chemical relaxations, but wants to continue using an explicit ODE solver, we suggest to use the semi-analytic procedures proposed in 6.10.1 and 6.10.2.

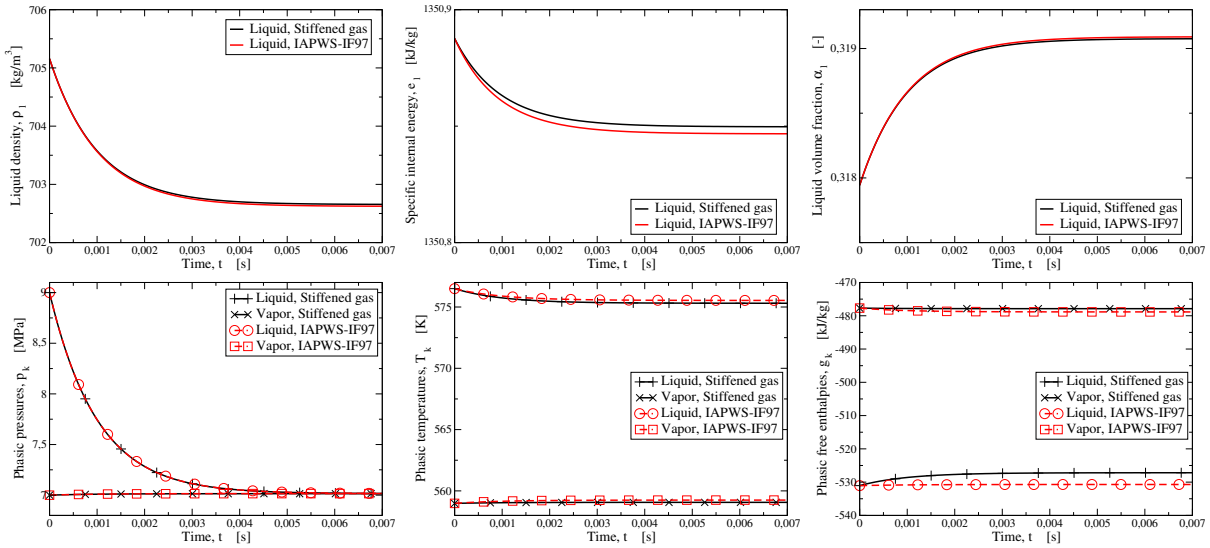

FIGURE 6.3. Time evolution of properties during the pressure relaxation step. On the left, ρ_l, e_l, α_l, on the right phasic pressures, temperatures and free enthalpies. The initial conditions are: liquid water at 9 MPa and the vapor water at 7 MPa, both close to their respective saturation temperatures. Both the stiffened gas and the IAPWS-IF97 EoS are considered and their trends are qualitatively similar. For this case $\Theta^p = 10^{-3}\,s$.

6.6 Equilibrium recovery test

The relaxation procedures proposed in this paper aim to drive the liquid-vapor mixture from a disequilibrium state towards the equilibrium state (with an arbitrary rapidity). The disequilibrium state is the one provided by the hyperbolic operator, then, the relaxations are applied cell by cell. In this section we verify that the proposed procedures are able to recover the correct equilibrium state. Moreover, we compare results for an accurate EoS and a very simple one, showing the advantage of working with costly but accurate EoS.

Let us take a disequilibrium mixture of liquid and vapor water, at rest. The liquid is at $p_l = 9\ MPa$ and $T_l = T_{sat}(p_l) - 1K \approx 575.50K$, thus, in subcooled conditions. The vapor is at $p_v = 7\ MPa$ and $T_v = T_{sat}(p_v) + 1K \approx 559.98K$, hence in superheated conditions. The mixture is composed by 10% in mass of vapor. If the mixture had been in a full thermodynamic equilibrium, then: $p_l = p_v = p_{eq} \approx 8.29\ MPa$, $T_l = T_v = T_{sat}(p_{eq}) \approx 570.69K$, $g_l = g_v = g_{sat}(p_{eq}) \approx -513.32kJ/kg$ and the vapor quantity would be 12.4%.

Now, starting from this disequilibrium state, we want to recover the equilibrium one solving in succession the three systems of ODEs reported in Eqs. (6.41), (6.48), (6.62). Here we have chosen as mass transfer driver the chemical potential disequilibrium as reported in Eq. (6.63).

The results of the three relaxations processes are presented in Fig. 6.3, 6.4, 6.5. In the first, phasic pressures converge to an equilibrium value that is rather close to the initial vapor pressure. This is obvious given that a small increase of the volume occupied by the liquid makes its pressure to reduce dramatically. In fact the liquid has a much more stiff behavior than the vapor. The pressure disequilibrium decays exponentially as imposed by (6.32). During this transient the thermal and

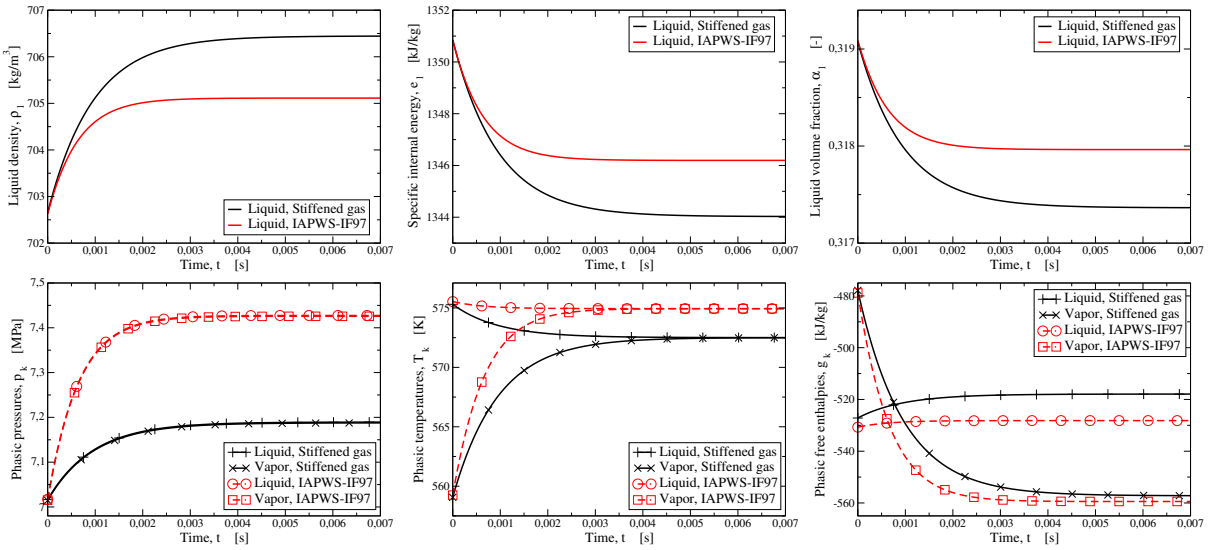

FIGURE 6.4. Time evolution of properties during the temperature relaxation step. On the left, ρ_l, e_l, α_l, on the right phasic pressures, temperatures and free enthalpies. The initial conditions correspond to the final conditions of the previous case (see Fig. 6.3). For this case we consider $hA_{int}/V = 10^8\, W/(m^3\, K)$, which is not a realistic value, however it has been chosen to show that phasic temperatures converge, while the phasic pressure maintain their small discrepancy.

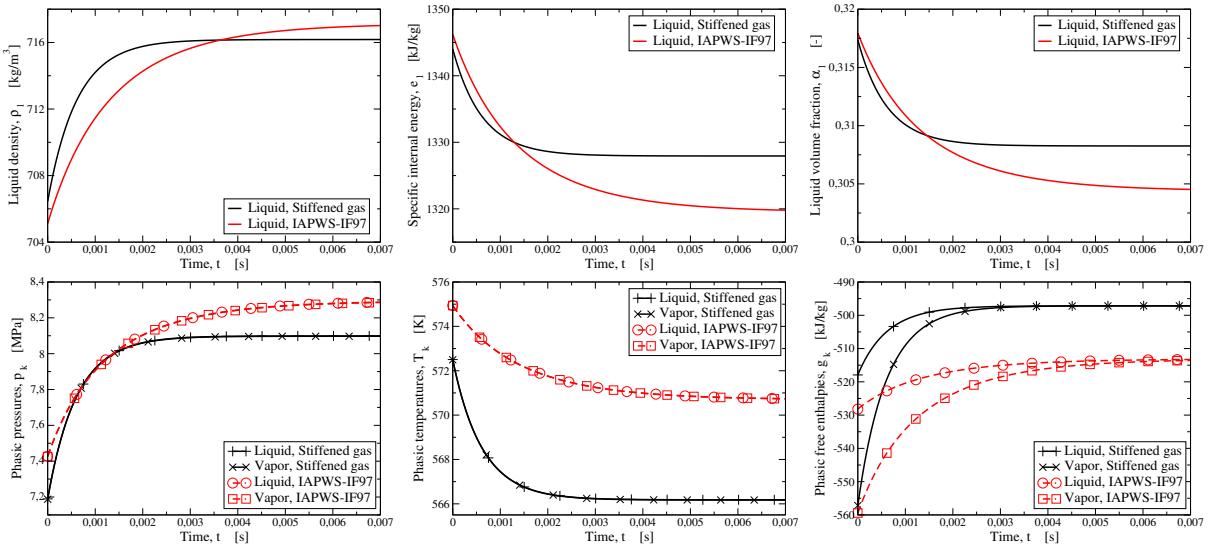

FIGURE 6.5. Time evolution of properties during the chemical relaxation step. On the left, ρ_l, e_l, α_l, on the right phasic pressures, temperatures and free enthalpies. The initial conditions correspond to the final conditions of the previous case (see Fig. 6.4). For this case we consider $A_{int}/V = 1\ m^{-1}$ and $\Theta^g = 7\, m^4/(kg\ s)$.

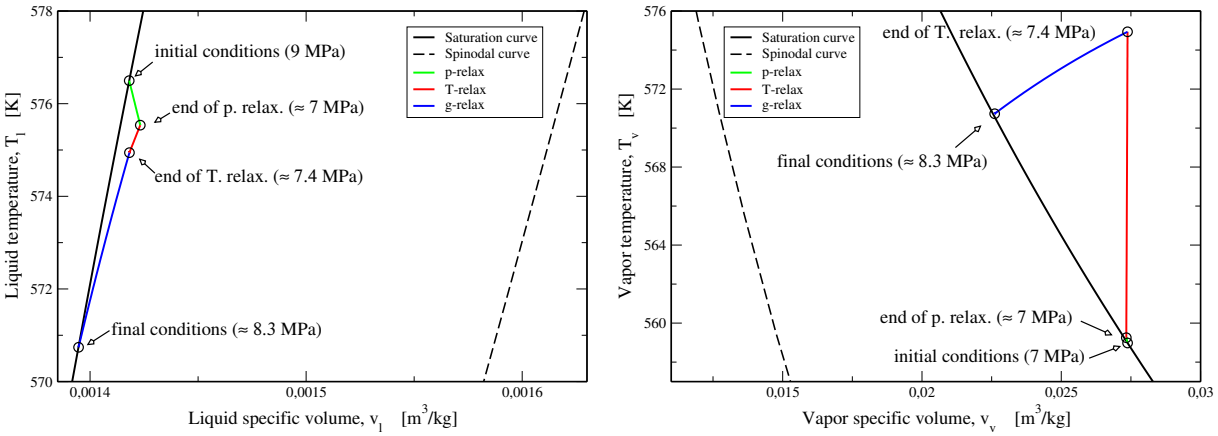

FIGURE 6.6. Evolution on the $T-v$ of liquid (on the left) and vapor (on the right), described by the IAPWS-IF97, for the equilibrium recovery test (cf. Section 6.6).

chemical disequilibrium stay almost unchanged. It is remarkable how the stiffened gas EoS is able to well represent the water behavior. However, this was expected due to the fact that in the phase space, the SG-EoS and IAPWS-IF97 had similar trends (see Fig. 6.14). The parameter for the stiffened gas EoS have been calculated as in [129].

Then the mixture undergoes a sensible heat transfer process to equilibrate their phasic temperatures. For this case we consider $hA_{int}/V = 10^8\, W/(m^3\, K)$, which is not a realistic value, but it has been chosen to make phases to converge towards an equilibrium temperature. During this process, the pressure difference stays constant as enforced in Eq. (6.44). Let us notice that notwithstanding with the effort to calculate reliable SG coefficients, the two EoS converge to a different equilibrium state: the discrepancy is roughly of $2\,bar$ and $2K$. The reasons are essentially two: the SG coefficients are constant, but even more important, the behavior in the phase space is different (see Fig. 6.15) given the different trends of the EoS derivatives. Note that the phasic free enthalpies intersect during this relaxation process and this is not an unphysical behavior. In fact, being almost at the same pressure and temperature, phases may have very similar phasic free enthalpies. Unphysical would be that the liquid phase has a higher temperature but a lower free enthalpy than the vapor, violating the condition in (6.24). Another unphysical phenomenon would be the intersection of the phasic free enthalpies during the mass transfer process that would violate the second law of thermodynamics.

Finally, the mixture at pressure and temperature equilibrium undergoes a mass transfer process that will establish the chemical equilibrium. This process is driven by Eq. (6.63) and takes place with mechanical and thermal equilibrium as guaranteed by Eqs. (6.44) and (6.55). Due to the different behavior of the thermodynamic derivatives, the dynamical behavior of the two considered EoS is also affected. First, this is visible by the fact that the same value of the characteristic time Θ^g produces different time evolutions. Namely, the SG-EoS is much faster than the IAPWS-IF97 in recovering the full equilibrium. Secondly, the two EoS converge to different equilibrium states (the discrepancy is around $2\,bar$ and $4K$).

At the end, the IAPWS-IF97 has reached the correct equilibrium condition whereas the SG-EoS

has not. The paths followed by the phases described by the IAPSW-IF97 onto the $T-v$ diagram are reported in Fig. 6.6.

6.7 1-D numerical tests

We now present some numerical tests of Riemann problems in 1D geometry. The relaxation procedures developed above and reported in Eqs. (6.41), (6.48), (6.62) are now coupled to the hyperbolic operator described in Section 6.5.1 for two-phase flow calculations.

This section presents first some numerical tests involving fluids governed by the stiffened gas EoS to show the consistency of our relaxation techniques with the instantaneous relaxation procedures developed in [200]. Moreover, due to the simplicity of this EoS, for some tests we are able to make a comparison with an exact solution. Then we tackle the challenging task of dealing with a complex EoS: the already mentioned IAPWS-IF97. Some comparisons are done between the present model and the classical homogeneous equilibrium model (HEM). The latter has also been integrated in CLAWPACK and its EoS is handled by the look-up table technique presented in [79].

Unless specified, all the numerical results have been obtained with $CFL = 0.8$ on 1000 cell meshes.

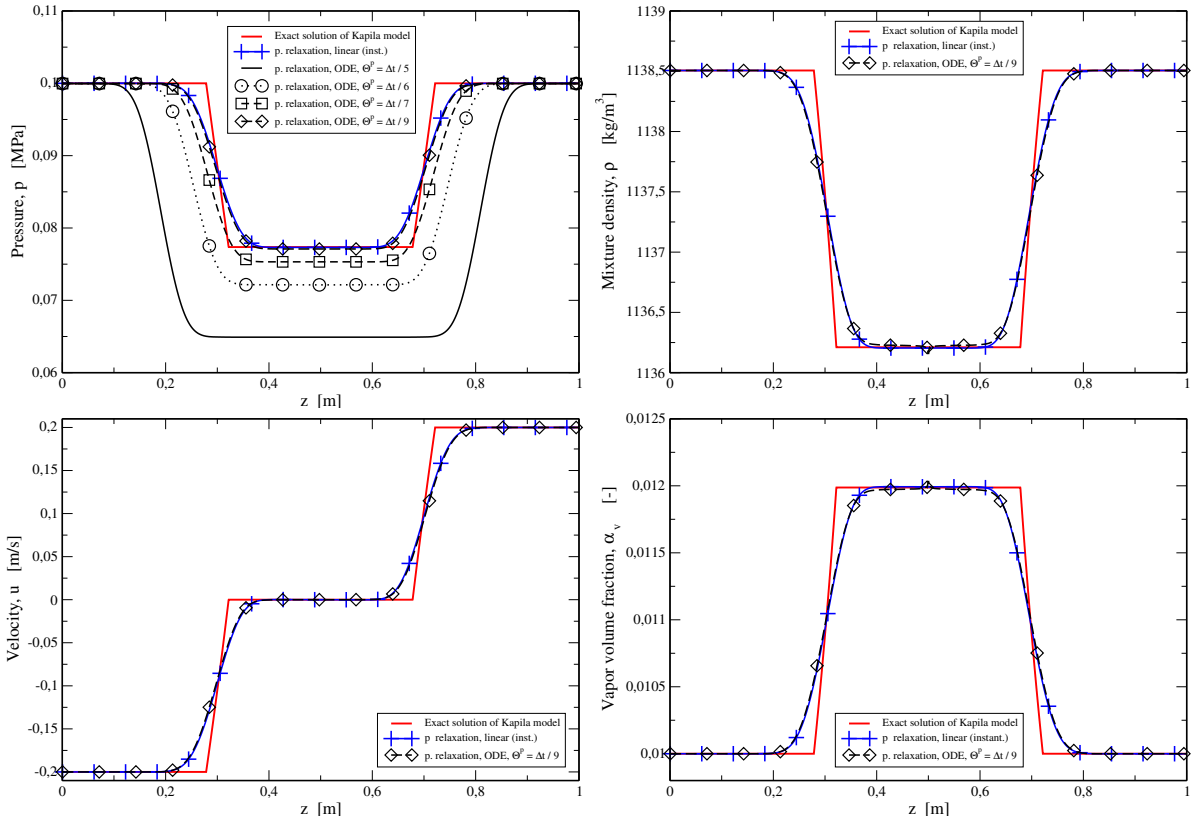

FIGURE 6.7. Numerical results for the water cavitation test with initial velocity $|u| = 0.2\,m/s$. Initial parameters are reported in Eq. (6.80), $t_{output} = 0.2\ ms$. Calculations made with 1000 cells, second order HLLC-type scheme for the hyperbolic operator and RK45 as ODE solver.

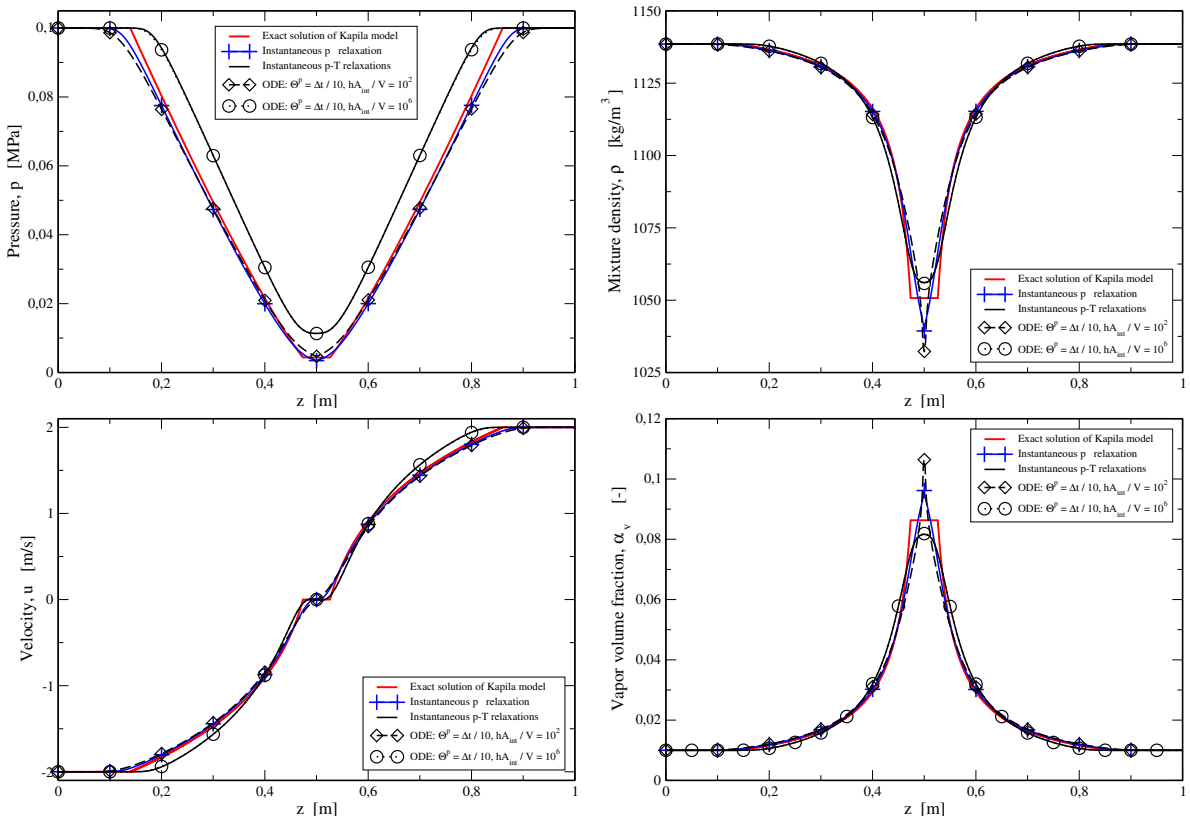

FIGURE 6.8. Numerical results for the water cavitation test with initial velocity $|u| = 2\,m/s$. Initial parameters are reported in Eq. (6.80), $t_{output} = 0.32\ ms$. Calculations made with 5000 cells, second order solver for the hyperbolic operator and RK45 as ODE solver.

6.7.1 Water cavitation problem with the stiffened gas EoS

A velocity discontinuity is initially set at the middle of a pipe of 1 m length, the velocity value being $-|u|$ on the left side and $+|u|$ on the right side. The fluid is a mixture of vapor and liquid water at the same thermodynamic conditions in the entire pipe. Due do the initial velocity discontinuity, two rarefaction waves generate moving leftwards and rightwards. They are symmetric given that the absolute value of the initial velocity is equal on the two sides of the pipe. A trivial contact discontinuity wave of zero speed appears as well in the center of the pipe.

Here we test two different strengths of the initial velocity discontinuity: a mild one with $|u| = 0.2\,m/s$ and a stronger one with $|u| = 2\,m/s$. The initial conditions are the same for both tests and are:

$$\begin{cases} \rho_v = 0.63\,kg/m^3,\ \rho_l = 1150\,kg/m^3,\ p = 10^5 Pa,\ \alpha_v = 10^{-2}, & for\ 0\,m \le z \le 0.5\,m, \\ \rho_v = 0.63\,kg/m^3,\ \rho_l = 1150\,kg/m^3,\ p = 10^5 Pa,\ \alpha_v = 10^{-2}, & for\ 0.5\,m \le z \le 1\,m. \end{cases} \tag{6.80}$$

For both tests, the fluid is described by the stiffened gas EoS. However, two different set of EoS parameters are used. For the first test, they are reported in Tab. 6.1. For the second test, they are reported in Tab. 6.2.

TABLE 6.1. Parameters for the Stiffened Gas EoS for liquid and vapor water (first test in Sec. 6.7.1) [234].

Phase	γ	$\pi\ [Pa]$	$\eta\ [J/kg]$
liquid	4.4	6×10^8	0
vapor	1.4	0	0

TABLE 6.2. Parameters for the Stiffened Gas EoS for liquid and vapor water (second test in Sec. 6.7.1) [200].

Phase	γ	$\pi\ [Pa]$	$\eta\ [J/kg]$	$c_v\ [J/(kgK)]$
liquid	2.35	10^9	-1167×10^3	1816
vapor	1.43	0	$+2030\times10^3$	1040

For the first test, the simulation results are reported in Fig. 6.7. They are compared to the exact solutions of Kapila's model and to the instantaneous relaxation procedures of [200]. In the pressure plot we can see that as the characteristic time of the pressure relaxation decreases, the pressure profile tends to the exact one of the Kapila's model and to the one provided by the instantaneous pressure relaxation technique of [200]. Further, the strength and the speed of the rarefaction waves decrease for smaller Θ^p.

For the second test, the simulation results are reported in Fig. 6.8. Here we analyze the impact of the temperature relaxation which follows a quasi-instantaneous pressure relaxation ($\Theta^p = \Delta t/10$). The parameter that controls the rapidity of the temperature relaxation process is hA_{int}/V. When it is small, the temperature relaxation is slow, hence the numerical results are close to the one of the Kapila's model. When it is large, the temperature relaxation is fast and we are able to reproduce the numerical results obtained by the instantaneous pressure and temperature relaxation procedures of [200]. In fact for $hA_{int}/V = 10^6\,W/(m^3\,K)$ the results are practically indistinguishable with the ones of [200].

6.7.2 Water cavitation test with the IAPWS-IF97 EoS

A 1 m length tube is filled by saturated water and steam at thermochemical equilibrium. The vapor phase occupies a small part (1%) of the tube volume. The initial conditions are

$$\begin{cases} p = 10\ MPa,\ T_k = T_{sat}(p),\ u = -5\,m/s,\ \alpha_v = 10^{-2}, & for\ 0\,m \le z \le 0.5\,m, \\ p = 10\ MPa,\ T_k = T_{sat}(p),\ u = +5\,m/s,\ \alpha_v = 10^{-2}, & for\ 0.5\,m \le z \le 1\,m. \end{cases} \tag{6.81}$$

At time $t = 0$ a velocity discontinuity of $|u| = 5\,m/s$ is set at the center of the tube and generates two rarefaction waves. In Fig. 6.9 we show the effect of the different relaxation procedures. Here the pressure and the temperature relaxations are quasi-instantaneous, i.e. we used $\Theta^p = \Delta t/10$ and $hA_{int}/V = 10^{11}\,W/(m^3\,K)$. The mass transfer is driven by the phasic Gibbs free enthalpy difference as already mentioned in Eq. (6.63). As made visible by the plot of the phasic temperatures, both temperatures decreases and an important thermal disequilibrium exists between the liquid and the vapor. The liquid is metastable because its local pressure is lower than the saturation pressure corresponding to its local temperature. The temperatures are then equilibrated by the

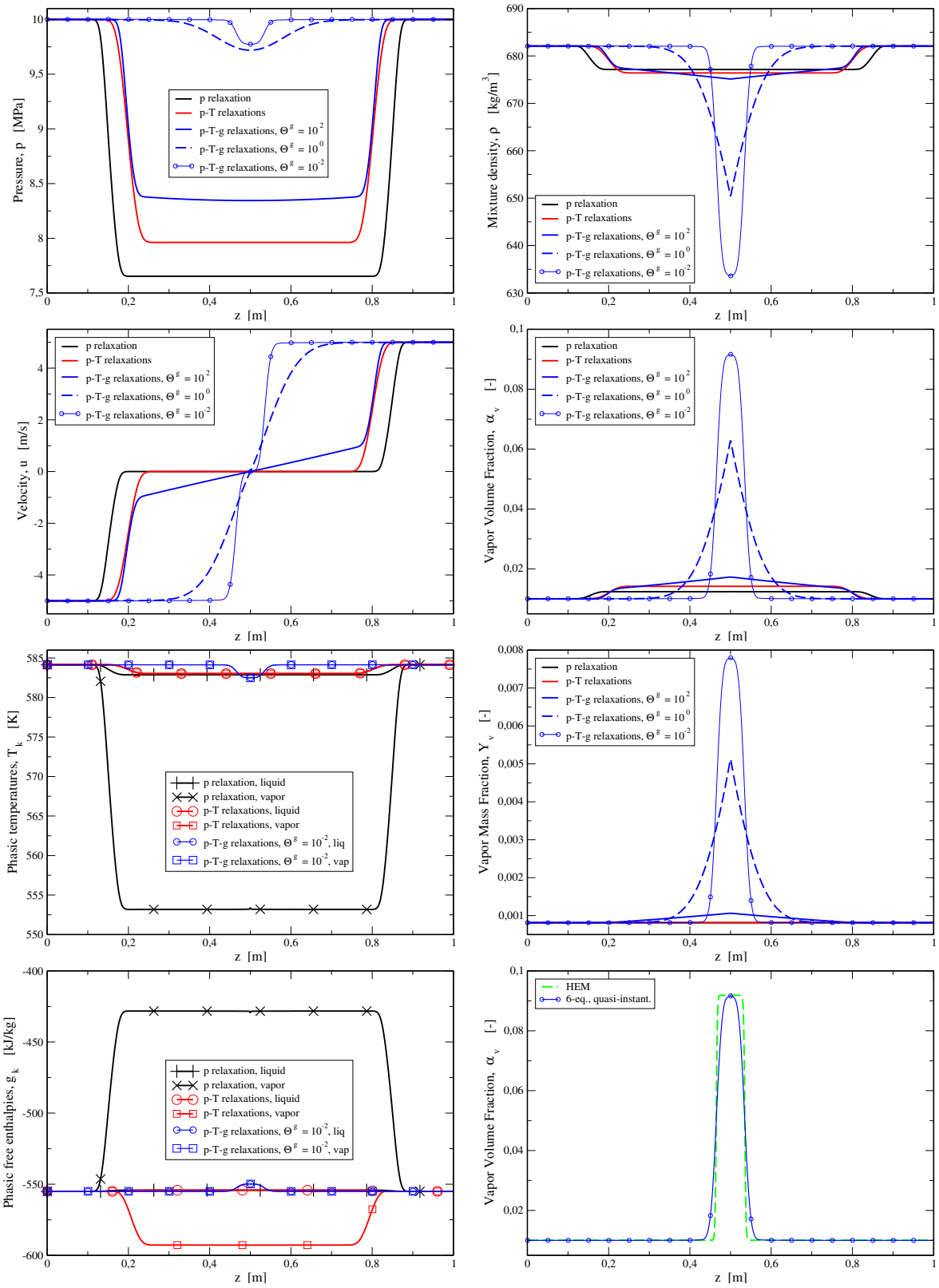

FIGURE 6.9. $t_{output} = 0.5\ ms$, 1000 cells, second order solver for the hyperbolic operator and Runge-Kutta 4-5 as ODE solver.

temperature relaxation procedure. However, a chemical disequilibrium exists between the phases and the liquid has a higher Gibbs free enthalpy. Finally, the mass transfer procedure tends to reduce the chemical disequilibrium increasing the quantity of vapor and the phasic Gibbs free enthalpies are indistinguishable. From the vapor mass fraction plot we can see that the quantity of vapor at the center of the tube is ten times larger than the initial amount.

As in the previous case, the strength and the speed of the waves vary according to the heat and mass transfer occurring between the two phases. In particular, when a quasi-instantaneous pressure relaxation is performed, the 6-equation model tends to the Kapila's model therefore the speed of sound of the model will be the one of Wood [279]. When a quasi-instantaneous temperature relaxation is performed, our code behaves like a 4-equation model in which the only disequilibrium between phases is the chemical one. Hence the speed of sound is even lower than the Wood's one (see Fig. 6.1). Finally, applying the mass transfer with different characteristic times Θ^g, the behavior changes deeply. For a fast mass transfer, our code behaves as a HEM with a very low celerity [79].

As concerning the wave pattern, unless for the case in which the mass transfer is fast, it is quite different to the typical one of a cavitation tube. For instance the two *plateaux* between the tails of the rarefaction waves and the contact discontinuity do not exist anymore. They are restored when the model tends to the HEM, i.e. for a very low Θ^g. For values lower than $\Theta^g = 10^{-2}$, the results do not change anymore.

About the incidence of the source terms on the wave pattern and the possible lost of the constant states one may refer to [21].

In Fig. 6.9 we present also a comparison between the 6eq. model with very fast relaxation procedures and the classic HEM for the most sensible magnitude, i.e. the void fraction. The wave amplitudes are the same, however, for the same mesh, CFL number and limiter, the HEM is much less diffusive than the 6eq. model.

6.7.3 Evaporation-condensation shock tube test with the IAPWS-IF97 EoS

The tube is filled by saturated water and steam at thermochemical equilibrium. The initial conditions are

$$\begin{cases} p = 10\ MPa,\ T_k = T_{sat}(p),\ u = 0\,m/s,\ \alpha_v = 0.4, & for\ 0\,m \le z \le 0.5\,m, \\ p = \ 9\ MPa,\ T_k = T_{sat}(p),\ u = 0\,m/s,\ \alpha_v = 0.6, & for\ 0.5\,m \le z \le 1\,m. \end{cases} \tag{6.82}$$

At time $t = 0$ a pressure discontinuity of 1 MPa is set at the center of the tube. This Riemann problem generates a left-going rarefaction wave and right-going contact discontinuity and shock. In Fig. 6.10 we show the effect of the different relaxation procedures. The pressure and temperature relaxations are quasi-instantaneous, i.e. we used $\Theta^p = \Delta t/10$ and $hA_{int}/V = 10^{11}\,W/(m^3\ K)$. The mass transfer is driven by the phasic Gibbs free enthalpy difference.

In the two *plateaux* adjacent the contact discontinuity, phases assume different temperatures and the thermodynamic disequilibrium is of opposite kind. At the tail of the rarefaction wave, the liquid is hotter than the vapor, meanwhile, in the post-shock plateau the vapor is hotter than the liquid. Then the temperature relaxation procedure takes place and the phases reach the thermal equilibrium, but, the chemical disequilibrium persists. At the tail of the rarefaction wave the liquid

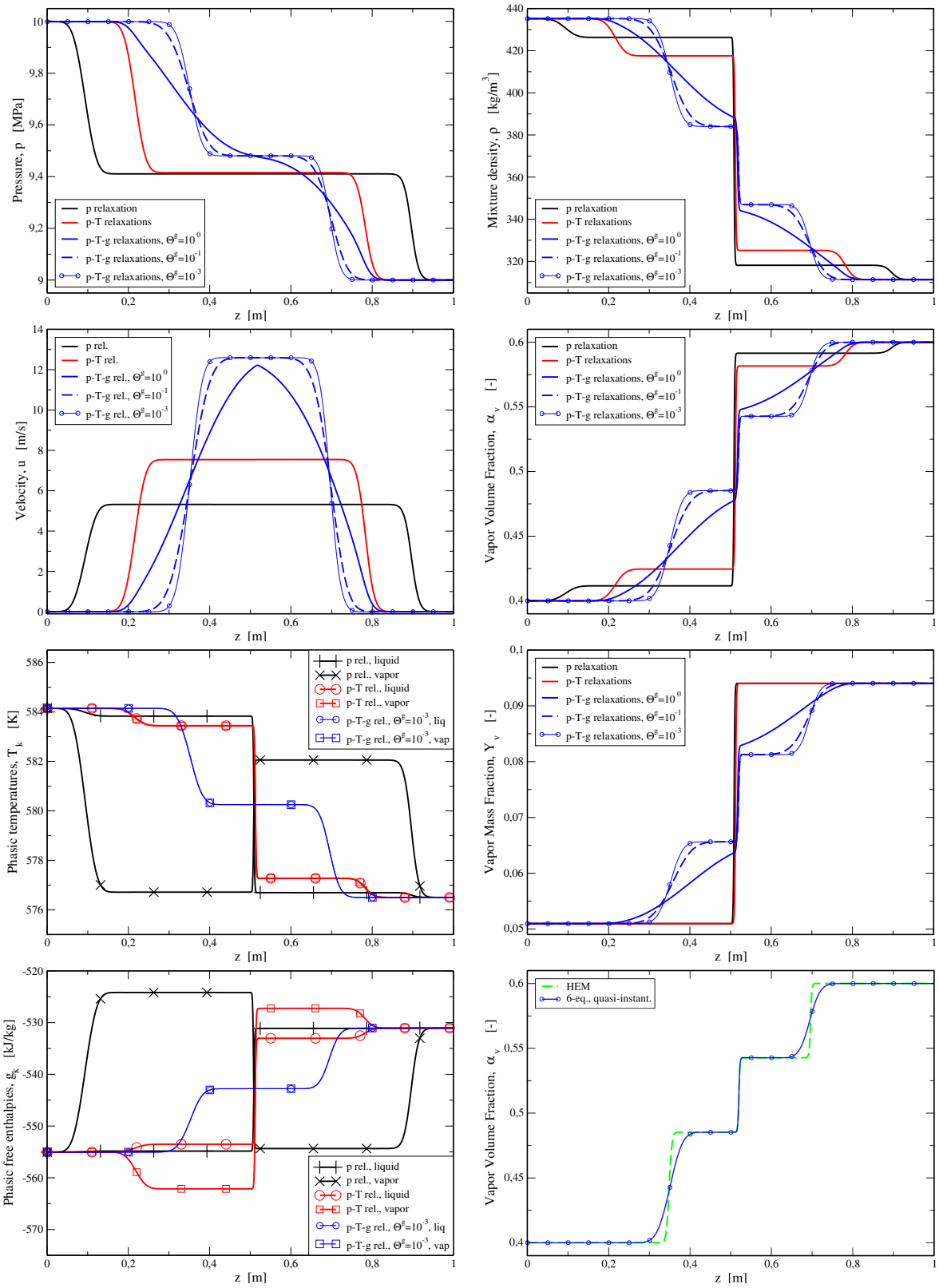

FIGURE 6.10. $t_{output} = 1.6\ ms$, 1000 cells, second order solver for the hyperbolic operator and Runge-Kutta 4-5 as ODE solver.

has a higher Gibbs free enthalpy, therefore, it is going to evaporate thanks to the mass transfer procedure. Conversely, in the post-shock plateau the vapor has a higher Gibbs free enthalpy, then a condensation occurs.

According to the characteristic time of the chemical equilibrium recovery, the 1-D profiles change. For values lower than $\Theta^g = 10^{-3}$, the results do not change anymore and, at the end of the relaxation processes, the disequilibria between the phases are practically extinguished. When these processes are fast, our code tends to the HEM as shown in Fig. 6.10. As for the previous case, the HEM is much less diffusive than the 6eq. model, however, for the contact discontinuity wave, the two-models are indistinguishable.

6.7.4 Evaporation shock tube test with the IAPWS-IF97 EoS

This shock tube test is to assess the capability of our code of dealing with quasi-vanishing phases and to approximate shock waves. A 1 m length pipe is filled by a mixture of liquid and steam water and a Riemann problem is located a 0.6 m. On the left the water is quasi-pure liquid (0.1% in volume of vapor) and on the right it is quasi-pure vapor (0.1% in volume of liquid), therefore the location of the Riemann problem is almost a liquid-vapor interface. The initial conditions are

$$\begin{cases} p = 10\ MPa,\ T_k = T_{sat}(p),\ u = 0\,m/s,\ \alpha_v = 10^{-3}, & for\ 0\,m \le z \le 0.6\,m, \\ p = \ 9\ MPa,\ T_k = T_{sat}(p),\ u = 0\,m/s,\ \alpha_v = 1 - 10^{-3}, & for\ 0.6\,m \le z \le 1\,m. \end{cases} \tag{6.83}$$

The Riemann problem generates a left-going rarefaction wave, a right going contact discontinuity and a right going shock. In Fig. 6.11 we show the effect of the different relaxation procedures. The pressure and temperature relaxations are quasi-instantaneous, i.e. we used $\Theta^p = \Delta t/10$ and $hA_{int}/V = 10^{11}\,W/(m^3\ K)$. The mass transfer is driven by the phasic Gibbs free enthalpy difference according three different characteristic times.

On the left side of the contact discontinuity, in the post-rarefaction *plateau*, the liquid assumes a temperature higher than the vapor phase. On the contrary, on the left side of the contact discontinuity, in the post-shock *plateau*, the liquid has a lower temperature than the vapor phase. Thanks to the temperature relaxation process, the two phases assume almost the same temperature ($|T_l - T_v| < 10^{-3}\ K$), however the liquid has a higher Gibbs free enthalpy therefore the mass transfer process provokes its evaporation on both sides of the contact wave.

In the post-shock *plateau* the liquid is almost vanishing: its volume fraction has varied from 10^{-3} to 10^{-6}. This is a very challenging condition for the relaxation procedures here proposed since the problem becomes bad conditioned for vanishing phases (cf. 6.12). Nevertheless our explicit ODE solver did not fail.

As in the previous case, the strength and the velocity of the waves are strongly affected by the relaxation processes, especially the one related to the mass transfer. The rapidity of the Gibbs free enthalpy relaxation deeply influences the wave pattern. The most impacted magnitudes are pressure and velocity.

For a very fast chemical relaxation ($\Theta^g = 10^{-3}$), the highest relative difference in terms of Gibbs free enthalpy is: $|g_l - g_v|/(\sum \alpha_k g_k) < 10^{-5},\ k = l, v$. For values lower than $\Theta^g = 10^{-3}$, the results do not change anymore.

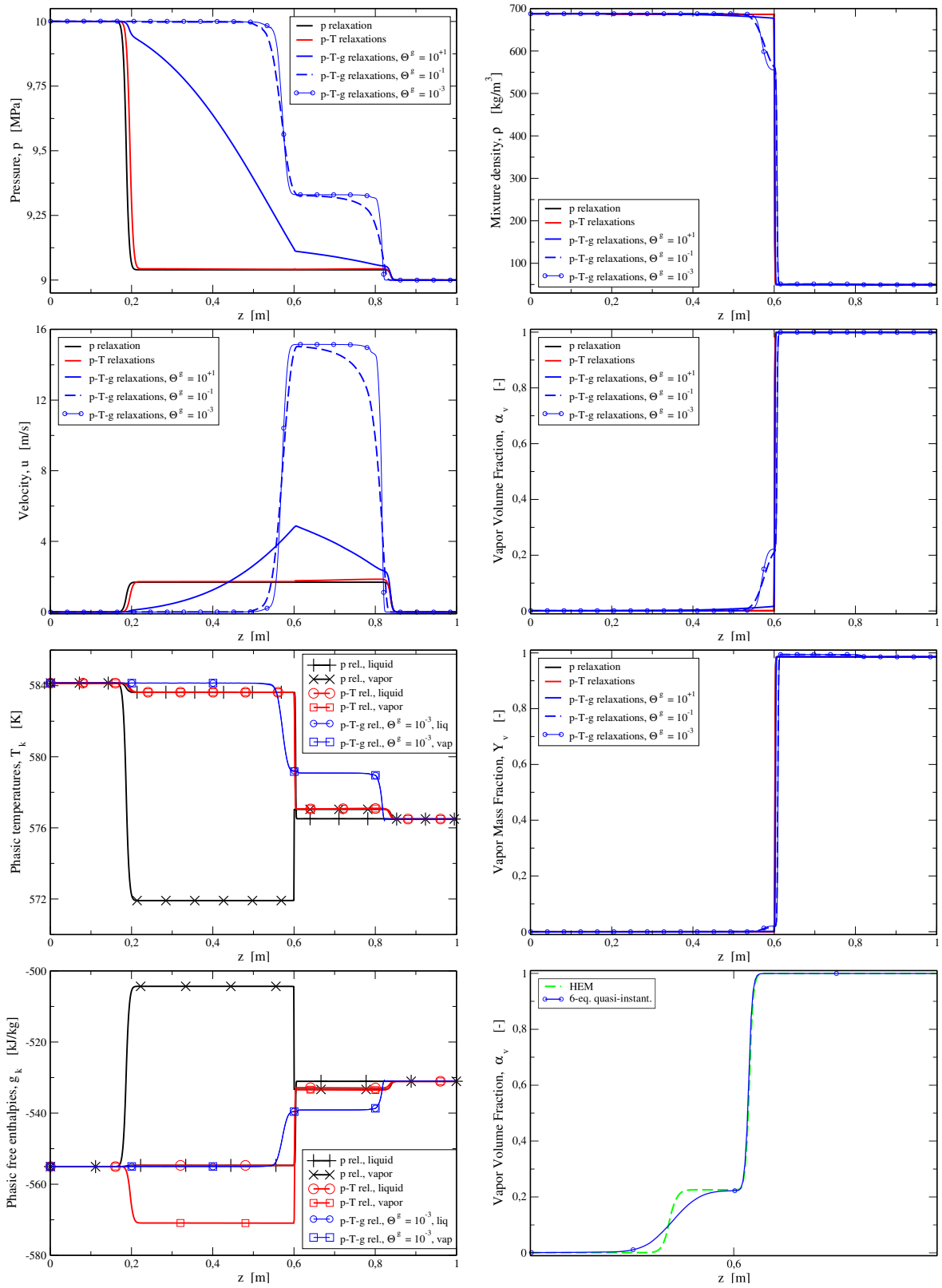

FIGURE 6.11. $t_{output} = 0.5\ ms$, 1000 cells, second order solver for the hyperbolic operator and Runge-Kutta 4-5 as ODE solver.

At the end of each time step, the two phases are almost at the full equilibrium in terms of pressure, temperature and Gibbs free enthalpy, hence our code tends to a HEM. In Fig. 6.11 we present also a comparison between the 6-eq. model with very fast relaxation procedures and the classic HEM. This is done in a magnified plot of the void fraction profile. As seen in the previous tests, the wave amplitudes are the same, however, the HEM is less diffusive than the 6-eq. model. Nonetheless, for the contact discontinuity wave, the two-models are indistinguishable.

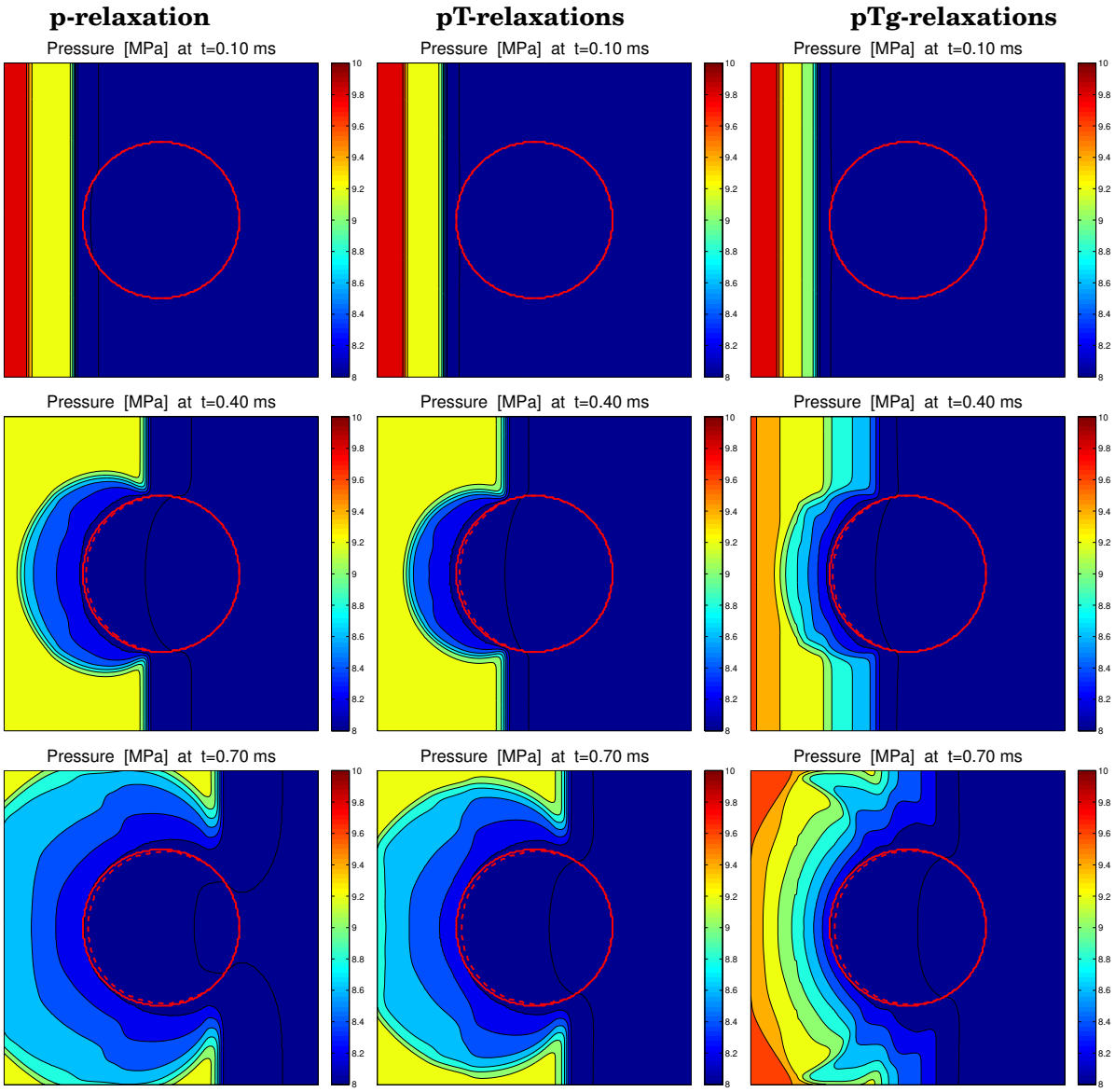

FIGURE 6.12. Pressure field, 200x200 cells, second order solver for the hyperbolic operator and Runge-Kutta 4-5 as ODE solver. The continuous red line represents the initial contour of the vapor bubble and the dashed red line indicates the interface at the displayed time.

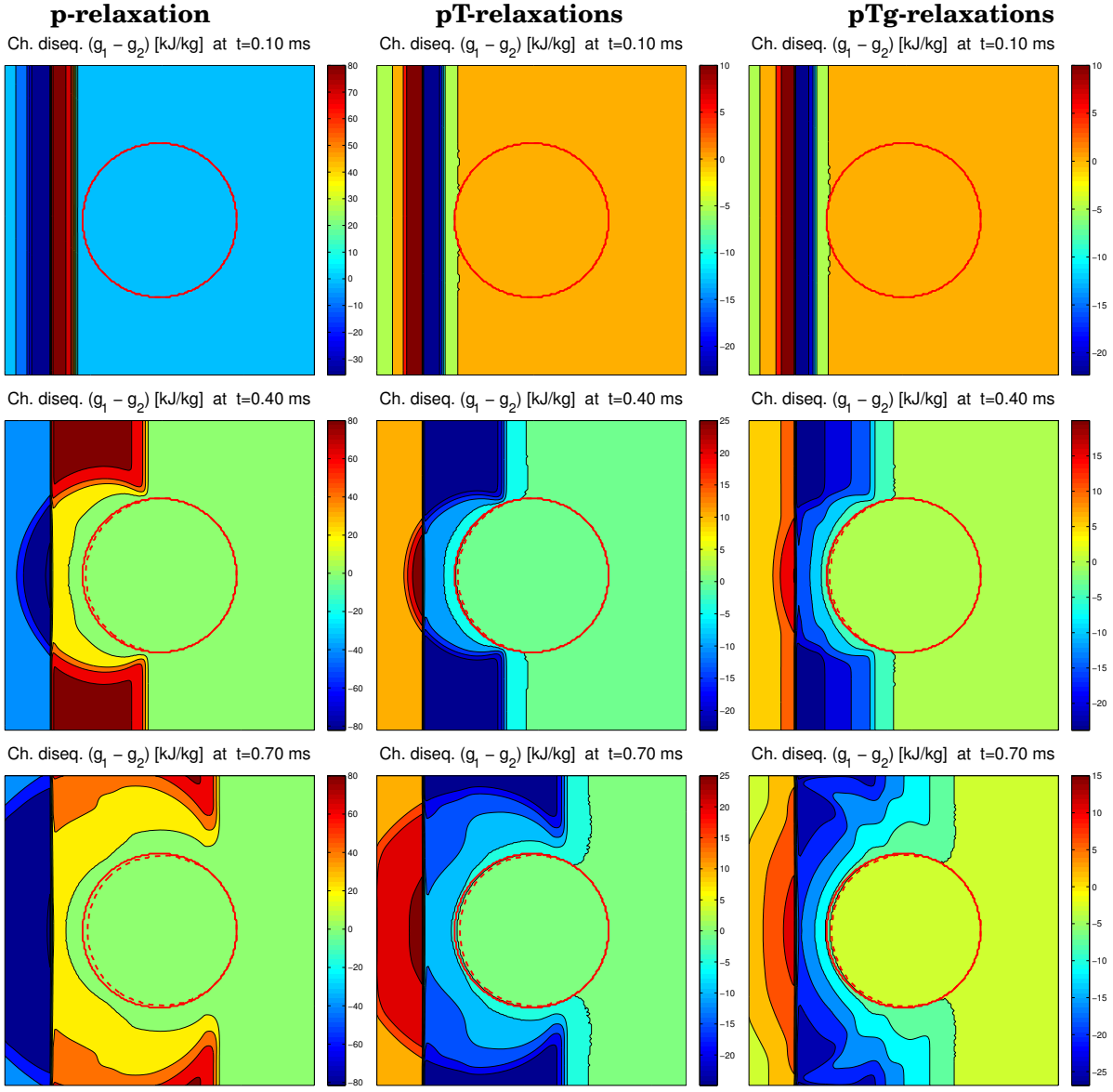

FIGURE 6.13. Chemical disequilibrium field, 200x200 cells, second order solver for the hyperbolic operator and Runge-Kutta 4-5 as ODE solver. The continuous red line represents the initial contour of the vapor bubble and the dashed red line indicates the interface at the displayed time.

6.8 2-D numerical test

As 2-D numerical test we are going to consider the interaction of a pressure wave in a liquid with a vapor bubble. In the industrial context, this test has many implications, for instance it can represent a portion of a waterhammer. That is, the compression of a vapor pocket originated close to a valve suddenly closed.

We consider a vapor bubble ($\alpha_v = 0.999$) contained in a two-phase media ($\alpha_v = 0.01$) that is compressed by a liquid ($\alpha_l = 0.999$) at higher pressure. This scenario is representative of the

compression of a two-phase *slug pattern* (see [43]) in which the slug is modeled as a vapor bubble that is surrounded by a mixture containing liquid and vapor at thermal and chemical equilibrium. In particular we are going to see the deformation of the vapor bubble and the propagation of the thermodynamic disequilibrium induced by the shock.

The geometric domain is a square of 1 m side containing a bubble located in the center of the domain $(0,0)$ that has a radius of 0.25 m. The high pressure liquid is located on the left side and is moving at 1 m/s towards the bubble.

At the vertical interface ($x = -0.35\ m$) between the liquid at higher pressure (10 MPa) and the mixture at lower pressure (8 MPa), the Riemann problem generates a right-going shock, a left-going shock and a contact discontinuity. These waves are visible on the first row of Fig. 6.12 where the pressure fields at $t = 0.1\ ms$ are reported. The shock is going to interact with the bubble, therefore, is partially reflected at the bubble interface due to the sudden change of acoustic impedance $Z = \rho c$ of the two media. The reflected wave is a rarefaction (see the second row of Fig. 6.12). Thus the shock front propagates right-wards on the top and the bottom of the bubble, instead, the new rarefaction wave spreads circularly towards the left of the bubble penetrating into the high pressure domain.

Let us focus now on the thermodynamic equilibrium between the phases, therefore, on Fig. 6.13. At $t = 0$, everywhere the phases are in thermodynamic equilibrium. Then, due to shock and rarefaction waves, those equilibria are lost and can be restored thanks to the relaxation procedures discuss above.

We now analyze the contribution of the relaxation processes on the high pressure domain on the left. This portion of the domain is crossed by two left-going rarefaction waves. The first is the one originating at $t = 0$ at the Riemann problem interface (see the first row of Fig. 6.13), the second is the result of the interaction of the right-going shock with the bubble surface (see the second row of Fig. 6.13). Both rarefaction waves make the liquid phase to be metastable at a higher temperature than vapor, however for the chemical disequilibrium, the liquid phase has a lower Gibbs free enthalpy than vapor. Thanks to the temperature relaxation, this discordance, between the thermal and the chemical disequilibrium, disappears. The phases are practically at the same temperature but the liquid has now a higher Gibbs free enthalpy than vapor. This chemical disequilibrium is reduced by the evaporation process guaranteed by the chemical relaxation.

Analyzing the right portion of the domain, the shock wave originating at $t = 0$ at the Riemann problem interface, moves rightwards and makes the vapor to be metastable at a higher temperature with respect to the liquid. But, in terms of the chemical disequilibrium, the vapor phase has a lower Gibbs free enthalpy than liquid. The temperature relaxation makes the phasic temperature to be almost equal and inverts the chemical disequilibrium. Thus, the vapor has a higher Gibbs free enthalpy than liquid. A condensation process occurs and reduces the chemical disequilibrium.

6.9 Conclusions

We have presented and tested three innovative procedures for the relaxation of the thermodynamical disequilibrium between two phases. This relaxation procedures are non-instantaneous but capable to reproduce instantaneous relaxation calculations (see Fig. 6.7 and Fig. 6.8). When the relaxation

processes between the phases are fast, this model can retrieve the classical HEM as shown in the 1D test using the IAPWS-IF97 EoS. Further, this relaxation procedures can use arbitrary EoS, that is a very important requirement in some particular industrial applications, for instance, nuclear safety.

The temperature and the mass transfer procedures contains explicitly the ratio A_{int}/V that will allow to adequate the strength of the transfer processes to the interface area of exchange. This feature has not been too much investigated in this paper but it will be considered in our future works.

The thermal and the chemical relaxations proposed in the core of the paper are not intended to be used for quasi-instantaneous processes. In that case, we propose two semi-analytic procedures for general EoS in 6.10. The latter have a greater numerical robustness when used in stiff contexts.

The perspectives of this work is to implement the complete model (6.65) in the EUROPLEXUS fast dynamic code for the analysis of fast transients that concern the safety of nuclear power plants, a domain in which the metastability of the phases plays a very important role. In order to use it for industrial applications, model (6.65) will be coupled with the steam-water tables presented in [79], that is, a look-up table technique with a globally continuous bicubic interpolating function.

6.10 Appendix 6.A: Semi-analytic relaxations

6.10.1 Appendix 6.A.1: Semi-analytic temperature relaxation

In case of a stiff temperature relaxation, a semi-analytic procedure may guarantee better numerical properties than system (6.48). The idea of this semi-analytic temperature relaxation is the same introduced in (6.32) for the phasic pressure relaxation. That is an exponential temporal decrease of the disequilibrium. For the temperature relaxation process, it reads

$$\frac{d(T_1 - T_2)}{dt} = -\frac{T_1 - T_2}{\Theta^T}. \tag{6.84}$$

Its analytical solution, for $\Theta^T \neq \Theta^T(t, T_k)$, is

$$(T_1 - T_2)(t) = (T_1 - T_2)_{t=0}\, e^{-t/\Theta^T}. \tag{6.85}$$

Coupling this driver to the pressure equilibrium of Eq. (6.44), the mass and the energy conservation laws, it comes out:

$$\begin{cases} \frac{d\rho_1}{dt} = -\frac{T_1 - T_2}{\Theta^T}\left(j_T - \frac{j_p}{k_p}k_T\right)^{-1}, \\ \frac{de_1}{dt} = +\frac{T_1 - T_2}{\Theta^T}\left(j_T - \frac{j_p}{k_p}k_T\right)^{-1}\frac{j_p}{k_p}, \end{cases} \tag{6.86}$$

where j_p, k_p, j_T and k_T are the one already expressed in (6.54) and (6.59). A robust numerical method is based on the semi-analytic system:

$$\begin{cases} \frac{d\rho_1}{dt} = -\frac{(T_1 - T_2)_{t=0}}{\Theta^T}\, e^{-t/\Theta^T}\left(j_T - \frac{j_p}{k_p}k_T\right)^{-1}, \\ \frac{de_1}{dt} = +\frac{(T_1 - T_2)_{t=0}}{\Theta^T}\, e^{-t/\Theta^T}\left(j_T - \frac{j_p}{k_p}k_T\right)^{-1}\frac{j_p}{k_p}. \end{cases} \tag{6.87}$$

6.10.2 Appendix 6.A.2: Semi-analytic Gibbs free enthalpy relaxation

In case of a Gibbs free enthalpy relaxation, a semi-analytic procedure may guarantee better numerical properties than system (6.62). The chemical disequilibrium is supposed to follow an exponential temporal decrease, that is:

$$\frac{d(g_1-g_2)}{dt} = -\frac{g_1-g_2}{\Theta^g}. \tag{6.88}$$

Its analytical solution, for $\Theta^g \neq \Theta^g(t,g_k)$, is similar to the one in (6.85) for the temperature disequilibrium. Using the rules of partial derivative and the mass and the energy conservation laws, Eq. (6.88) can be rewritten as

$$i_2\frac{dm_1}{dt} + j_2\frac{d\rho_1}{dt} + k_2\frac{de_1}{dt} = -\frac{g_1-g_2}{\Theta^g}, \tag{6.89}$$

where

$$\begin{aligned} i_g &= \left(\frac{\partial g_2}{\partial e_2}\right)_{\rho_2}\frac{e_1-e_2}{m_2} + \left(\frac{\partial g_2}{\partial \rho_2}\right)_{e_2}\frac{\rho_1-\rho_2}{\alpha_2\rho_1}, \\ j_g &= \left(\frac{\partial g_1}{\partial \rho_1}\right)_{e_1} + \left(\frac{\partial g_2}{\partial \rho_2}\right)_{e_2}\frac{\alpha_1\rho_2}{\alpha_2\rho_1}, \\ k_g &= \left(\frac{\partial g_1}{\partial e_1}\right)_{\rho_1} + \left(\frac{\partial g_2}{\partial e_2}\right)_{\rho_2}\frac{m_1}{m_2}. \end{aligned} \tag{6.90}$$

Coupling this driver to the pressure and temperature equilibria, as done in Sec. 6.4.3, it comes out:

$$\begin{cases} \frac{dm_1}{dt} = +\frac{g_1-g_2}{\Theta^g}\frac{j_Tk_p-j_pk_T}{\Delta}, \\ \frac{d\rho_1}{dt} = -\frac{g_1-g_2}{\Theta^g}\frac{i_Tk_p-i_pk_T}{\Delta}, \\ \frac{de_1}{dt} = +\frac{g_1-g_2}{\Theta^g}\frac{i_Tj_p-i_pj_T}{\Delta}, \end{cases} \tag{6.91}$$

where $\Delta = i_Tj_gk_p - i_Tj_pk_g - i_gj_Tk_p + i_gj_pk_T + i_pj_Tk_g - i_pj_gk_T$.

A robust numerical method is based on using the analytic solution of (6.88). In this case the system reads:

$$\begin{cases} \frac{dm_1}{dt} = +\frac{(g_1-g_2)_{t=0}}{\Theta^g}\,e^{-t/\Theta^g}\frac{j_Tk_p-j_pk_T}{\Delta}, \\ \frac{d\rho_1}{dt} = -\frac{(g_1-g_2)_{t=0}}{\Theta^g}\,e^{-t/\Theta^g}\frac{i_Tk_p-i_pk_T}{\Delta}, \\ \frac{de_1}{dt} = +\frac{(g_1-g_2)_{t=0}}{\Theta^g}\,e^{-t/\Theta^g}\frac{i_Tj_p-i_pj_T}{\Delta}. \end{cases} \tag{6.92}$$

6.11 Appendix 6.B: Irreversibility of the relaxation procedures

6.11.1 Appendix 6.B.1: Irreversibility of the pressure relaxation process

The pressure relaxation process is obviously an irreversible process. The physical irreversibility is not just due to the work made by the unavoidable friction forces, but persists even if friction forces are neglected as we have done here. Let us demonstrate it.

The time-evolution of the specific entropy $s_k = s_k(\rho_k, e_k)$ is

$$\frac{ds_k}{dt} = \left(\frac{\partial s_k}{\partial \rho_k}\right)_{e_k}\frac{d\rho_k}{dt} + \left(\frac{\partial s_k}{\partial e_k}\right)_{\rho_k}\frac{de_k}{dt}, \tag{6.93}$$

where $\left(\frac{\partial s_k}{\partial \rho_k}\right)_{e_k} = -\frac{p_k}{T_k \rho_k^2}$, and $\left(\frac{\partial s_k}{\partial e_k}\right)_{\rho_k} = \frac{1}{T_k}$. It corresponds to the Gibbs equation formulated in thermostatics and is based on the hypothesis of local equilibrium [154]. Inserting the Eq. (6.28) in the previous one:

$$\frac{ds_k}{dt} = \frac{p_{int} - p_k}{T_k \rho_k^2} \frac{d\rho_k}{dt}. \tag{6.94}$$

Thus, the mixture entropy evolution reads

$$\frac{dS}{dt} = \frac{\alpha_1}{T_1 T_2 \rho_1} [p_{int}(T_2 - T_1) + T_1 p_2 - T_2 p_1] \frac{d\rho_1}{dt}. \tag{6.95}$$

The time-evolution of ρ_1, considering what written in (6.94), is

$$\begin{aligned} \frac{d\rho_1}{dt} &= \left(\frac{\partial \rho_1}{\partial p_1}\right)_{s_1} \frac{dp_1}{dt} - \left(\frac{\partial \rho_1}{\partial p_1}\right)_{s_1} \left(\frac{\partial p_1}{\partial s_1}\right)_{\rho_1} \frac{ds_1}{dt} \\ &= \rho_1 K_{s,1} \frac{dp_1}{dt} - T_1 \rho_1^2 K_{s,1} \Gamma_1 \frac{ds_1}{dt} \\ &= \rho_1 K_{s,1} \frac{dp_1}{dt} - K_{s,1} \Gamma_1 (p_{int} - p_1) \frac{d\rho_1}{dt} \\ &= \frac{\rho_1 K_{s,1}}{1 + K_{s,1} \Gamma_1 (p_{int} - p_1)} \frac{dp_1}{dt}. \end{aligned} \tag{6.96}$$

Inserting this relation in (6.95):

$$\frac{dS}{dt} = \frac{\alpha_1 K_{s,1}}{T_1 T_2} \frac{[p_{int}(T_2 - T_1) + T_1 p_2 - T_2 p_1]}{1 + K_{s,1} \Gamma_1 (p_{int} - p_1)} \frac{dp_1}{dt}. \tag{6.97}$$

and taking the interface pressure as $p_{int} = (p_1 + p_2)/2$,

$$\frac{dS}{dt} = \frac{T_1 + T_2}{T_1 T_2} \frac{\alpha_1 K_{s,1} (p_2 - p_1)}{1 + \frac{1}{2} K_{s,1} \Gamma_1 (p_2 - p_1)} \frac{dp_1}{dt}. \tag{6.98}$$

since $K_{s,1} = 1/(p_1 \gamma_1) > 0$, if $p_2 > p_1$, the coefficient in front of the derivative is positive, and the $\frac{dp_1}{dt} > 0$ because it tends to re-equilibrate with p_2 thanks to Eq. (6.32). However, if $p_2 < p_1$ the mixture entropy will increase only if:

$$|p_2 - p_1| < \frac{2\gamma_1 p_1}{\Gamma_1} \tag{6.99}$$

therefore, this choice of p_{int} is not suitable if $p_2 \gg p_1$. A choice that guarantees that the mixture entropy will increase *unconditionally* during the pressure relaxation process is $p_{int} = max(p_1, p_2)$. We will use the latter when condition (6.99) is violated.

6.11.2 Appendix 6.B.2: Irreversibility of the temperature relaxation process

In physics, the sensible heat transfer is an irreversible process. Here we discuss the irreversibility of our temperature relaxation method.

Describing the time-evolution of the specific entropy $s_k = s_k(\rho_k, e_k)$ as done in Eq. (6.93), for phase 1:

$$\frac{ds_1}{dt} = \frac{1}{T_1} \frac{h A_{int}}{V} (T_2 - T_1) \left[\frac{1}{a \rho_1^2} \left(\frac{\Gamma_1}{\alpha_1} + \frac{\Gamma_2}{\alpha_2} \right) (p_1 - p_{int}) + \frac{1}{m_1} \right], \tag{6.100}$$

and for phase 2:

$$\frac{ds_2}{dt} = \frac{\alpha_1}{\alpha_2}\frac{1}{T_2}\frac{hA_{int}}{V}(T_2 - T_1)\left[\frac{1}{a\rho_1\rho_2}\left(\frac{\Gamma_1}{\alpha_1} + \frac{\Gamma_2}{\alpha_2}\right)(p_{int} - p_2) - \frac{1}{m_1}\frac{\rho_1}{\rho_2}\right]. \tag{6.101}$$

Finally, considering that the mixture entropy is $S = \alpha_1\rho_1 s_1 + \alpha_2\rho_2 s_2$, its time-derivative reads

$$\frac{dS}{dt} = \alpha_1\frac{hA_{int}}{V}(T_2 - T_1)\left[\frac{1}{a\rho_1}\left(\frac{\Gamma_1}{\alpha_1} + \frac{\Gamma_2}{\alpha_2}\right)\left(\frac{p_1 - p_{int}}{T_1} + \frac{p_{int} - p_2}{T_2}\right) + \frac{1}{\alpha_1}\left(\frac{1}{T_1} - \frac{1}{T_2}\right)\right]. \tag{6.102}$$

We have investigated the sign of this function, however, in the general case of $p_1 \neq p_2$, it seems to be too complex to demonstrate the irreversibility of the process. In order to check the physical consistency of our code, we calculate the mixture entropy at the beginning and at the end of this relaxation. So far we have never detected a decrease of the mixture entropy.

In the limit case of $p_1 = p_2$, (6.102) becomes

$$\frac{dS}{dt} = \frac{hA_{int}}{V}\frac{(T_1 - T_2)^2}{T_1 T_2} \geq 0, \tag{6.103}$$

hence, if the temperature relaxation occurs when phases are at pressure equilibrium, the process is irreversible.

6.11.3 Appendix 6.B.3: Irreversibility of the mass transfer process

In physics, the mass transfer is an irreversible process. Here we discuss the irreversibility of our mass transfer method.

Describing the time-evolution of the specific entropy $s_k = s_k(\rho_k, e_k)$, for phase 1:

$$\frac{ds_1}{dt} = \frac{1}{(k_p j_T - j_p k_T)T_1}\frac{dm_1}{dt}\left[-\frac{p_1}{\rho_1^2}(i_p k_T - k_p i_T) + (j_p i_T - i_p j_T)\right], \tag{6.104}$$

for phase 2:

$$\frac{ds_2}{dt} = -\frac{m_1}{m_2}\frac{1}{(k_p j_T - j_p k_T)T_2}\frac{dm_1}{dt}\left[-\frac{p_2}{\rho_1^2}(i_p k_T - k_p i_T) + (j_p i_T - i_p j_T)\right], \tag{6.105}$$

for the mixture:

$$\frac{dS}{dt} = \left\{\alpha_1\rho_1\frac{T_2 - T_1}{(k_p j_T - j_p k_T)T_1 T_2}\left[-\frac{p}{\rho_1^2}(i_p k_T - k_p i_T) + (j_p i_T - i_p j_T)\right] + (s_1 - s_2)\right\}\frac{dm_1}{dt}. \tag{6.106}$$

We have investigated the sign of this function, however, for the general case of $p_1 \neq p_2$ and $T_1 \neq T_2$, it seems to be too complex to demonstrate the irreversibility of the process. In order to check the physical consistency of our code, we calculate the mixture entropy at the beginning and at the end of the mass transfer process. So far we have never detected a decrease of the mixture entropy.

6.12 Appendix 6.C: Well-posedness of the relaxation procedures

In this section we want to discuss about the well-posedness of the relaxation procedures developed in the previous section. The dynamical systems that reproduce the disequilibrium relaxations have been written in the form

$$\mathbf{y}' = \mathbf{F}(\mathbf{y}). \tag{6.107}$$

This means that our relaxation procedures (6.41), (6.48) and (6.62), are autonomous ODE systems that do not depend explicitly on time. In the following we refer to them as $\mathbf{F}^p(\mathbf{y})$, $\mathbf{F}^T(\mathbf{y})$ and $\mathbf{F}^g(\mathbf{y})$.

According to Hadamard, a problem is well-posed if: (i) a solution exists, (ii) the solution is unique, (iii) the solution's behavior changes continuously with the initial conditions.

The existence of a solution of the problem (6.107) on a domain Ω is guaranteed by the Peano existence theorem [199], which requires only the continuity of the function $\mathbf{F}(\mathbf{y})$ (see (6.20)) on Ω. The uniqueness of the solution is ensured by Cauchy-Kowalevski theorem, which requires that $\mathbf{F}(\mathbf{y})$ be Lipschitz continuous. The latter condition guarantees also the continuously dependence of the solution by the data [42]. Lipschitz continuity requires

$$\sup_{(\mathbf{y}\in\Omega)} \left| \frac{\partial F_i}{\partial y_j}(\mathbf{y}) \right| < +\infty, \qquad 1 \le i,j \le m. \tag{6.108}$$

Before to proceed, let us precise that the relaxation procedures developed are senseless if just one phase is present, hence, we have a practical constraint, that is

$$\alpha_k \in (\epsilon, 1-\epsilon), \qquad \epsilon > 0, \tag{6.109}$$

where ϵ is a tolerance that allows to use the relaxation procedures just when both phases are present and their volume fraction is not negligible.

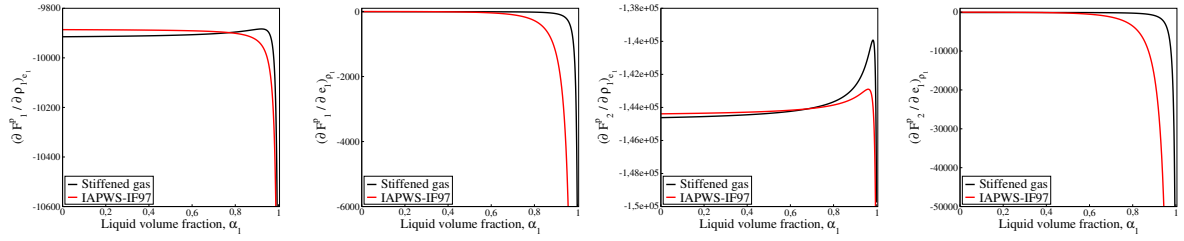

FIGURE 6.14. Trend of the partial derivatives $\frac{\partial F_i^p}{\partial y_j}(\mathbf{y})$ with respect to α_2 for two-phase water. The liquid is at 7 MPa and the vapor is at 6 MPa, close to their respective saturation temperatures. Both the stiffened gas and the IAPWS-IF97 EoS are considered and their trends are qualitatively similar. For this case $\Theta^p = 10^{-3}\,s$.

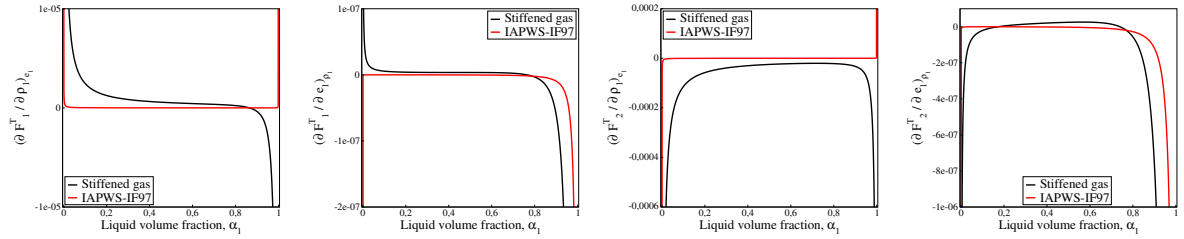

FIGURE 6.15. Trend of the partial derivatives $\frac{\partial F_i^T}{\partial y_j}(\mathbf{y})$ with respect to α_2 for two-phase water. Both the liquid and the vapor are at 7 MPa, the temperatures are $T_l = T_{sat} - 5K$ and $T_v = T_{sat} + 5K$. Both the stiffened gas and the IAPWS-IF97 EoS are considered. The different trends are due to the different sign of the partial derivatives of the thermodynamic quantities. For this case we considered $hA_{int}/V = 1\,W/m^3 \cdot K$.

As concerns the function $\mathbf{F}^p(\mathbf{y})$ of system (6.41), it is not defined for $a = 0$, however, as seen in (**??**), $a \neq 0$ for the physical domain defined by (6.14), (6.15), (6.109). Then $\mathbf{F}^p(\mathbf{y})$ is continuous in the domain of interest. For the first partial derivatives $\mathbf{F}^p(\mathbf{y})$ with respect to $\mathbf{y}$, it comes out that

$$\lim_{\alpha_1 \to 1} \frac{\partial F_i^p}{\partial y_j}(\mathbf{y}) = -\infty, \qquad 1 \leq i, j \leq 2. \tag{6.110}$$

Similarly, for the temperature relaxation, $\mathbf{F}^T(\mathbf{y})$ is continuous in the domain of interest. For its first partial derivatives, it comes out that

$$\lim_{\alpha_k \to 1} \frac{\partial F_i^T}{\partial y_j}(\mathbf{y}) = \pm\infty, \qquad 1 \leq i, j \leq 2. \tag{6.111}$$

The behavior of the partial derivatives of $\mathbf{F}^p(\mathbf{y})$ and $\mathbf{F}^T(\mathbf{y})$ throughout the two-phase domain is reported in Fig. 6.14 and 6.15 where we also compare, for two-phase water, the stiffened gas and the IAPWS-IF97 EoS. In the case of the pressure relaxation process, their trends are qualitatively similar, this means that the simple stiffened gas EoS is able to represent the physics of expanding/compressing fluids when no heat transfer occurs. On the other hand, as far as thermal properties are involved (see Fig. 6.15), the trends of the partial derivatives are different because the derivatives of the thermal properties have different sign for the two EoS.

For the mass transfer procedure, the second and the third components of (6.62) are not continuous in case

$$k_p j_T - j_p k_T = 0, \tag{6.112}$$

and for the partial derivatives of (6.62) we have

$$\lim_{\alpha_k \to 1} \frac{\partial F_i^g}{\partial y_j}(\mathbf{y}) = \pm\infty, \qquad 2 \leq i \leq 3, \qquad 1 \leq j \leq 3. \tag{6.113}$$

Summarizing, for systems (6.41), (6.48) and (6.62), it is required that $\alpha_k \in (\epsilon, 1-\epsilon)$ and that $k_p j_T - j_p k_T \neq 0$. In such a case, the functions are continuous and their partial derivatives are always bounded, independently from the adopted EoS. Therefore they are well-posed in the sense of Hadamard.

CHAPTER 7

A SIX-EQUATION SINGLE-VELOCITY MODEL WITH TABULATED EOS

The single-velocity six-equation model discussed in the previous two chapters is finally used here for the simulation of metastable two-phase flows of industrial concern. This is the last chapter of this work and involves most of the computational techniques developed throughout this Ph.D. thesis. It represents an ongoing research that will be submitted for publication in the *International Heat and Mass Transfer* journal.

The focus of this work is the merging of the single-velocity six-equation model with the novel relaxation procedures and the new steam-water tables. Its outcome is an accurate and time-efficient hyperbolic model for the analysis of metastable two-phase flows, that is the final product of this thesis.

The merging of the several contributions of this thesis is made possible by the work presented in Chapter 6. In fact, it allows to couple the complete single-velocity six-equation model to arbitrary equations of state. The final purpose of the work presented in Chapter 6 was, evidently, the coupling of the six-equation model to the steam-water tables developed in Chapter 4.

Although the steam-water tables and the look-up table technique worked remarkably in Chapter 4, the HEM and the HRM do not take into account the vapor metastable states. Instead the single-velocity six-equation model does. Hence the first step discussed in this chapter is the extension of the steam-water tables to the vapor metastable domain up to the vapor spinodal line.

Once the steam-water tables have been extended, the coupling to the six-equation model is described. Then, the final model is implemented in EUROPLEXUS code and is used for the simulation of metastable two-phase flows occurring due to a fast depressurization. It represents the industrial context of this work that is the numerical simulation of the metastable steam-water flows in the event of a Loss of Coolant Accident (LOCA) in nuclear power plants. The calculations are validated against experimental data available in the literature.

A hyperbolic phase-transition model coupled to direct steam-water tables for the analysis of metastable two-phase flows

In preparation for Computers & Fluids.

M. De Lorenzo[1], Ph. Lafon[1], M. Pelanti[1], A. Pantano[1,2,3], M. Di Matteo[4], Y. Bartosiewicz[4], J.-M. Seynhaeve[4].

7.1 Introduction

The last two decades have seen a great improvement in the modeling of the two-phase flows. Hyperbolic models have become more popular and their application domains are various. These advancements allowed to better take into account the disequilibria existing between the phases because the thermodynamic disequilibrium has been decomposed in mechanical, thermal and chemical ones.

In case of phase transition simulations of a one-component mixture, the presence of a thermodynamic disequilibrium leads to the presence of metastable states, that is, the persistence of a phase into the stability domain of another phase. Thanks to the contribution of the new hyperbolic techniques, the analysis of the metastable two-phase flows has greatly improved. Nonetheless, these improvements have not changed the numerical methodologies of common use in industry.

One of the reasons stems from the difficulty of using real equations of state in the new hyperbolic approaches, versus the necessity to accurately calculate the fluid properties in industrial applications. In fact, the numerical techniques recently proposed in the literature [64, 200, 233, 283] are often designed only for very simple EoS as the stiffened gas one.

In order to use such hyperbolic models for the simulation of metastable flows of industrial interest, our previous works have dealt, separately, with the calculation of fluid properties and the calculation of the transfer terms.

In [79], we have developed a fast and accurate technique for the calculation of steam-water properties for compressible two-phase flow models. This method is hundreds times faster than the direct use of the reference EoS, the IAPWS-IF97, with a negligible deviation with respect to the correct value.

In [81], we proposed a novel method for the relaxation of the thermodynamic disequilibrium for phases described by arbitrary EoS. Moreover, to correctly take into account the presence of metastable states, the equilibrium recovery process is not instantaneous. This method was coupled to a slow iterative algorithm implementing the IAPWS-IF97 EoS.

The purpose of the current work is to couple the two aforementioned techniques. The outcome of this work is a hyperbolic model for metastable two-phase flows that uses novel techniques for the

[1] IMSIA UMR EDF-CNRS-CEA-ENSTA, Palaiseau, France 91120.
[2] Politecnico di Torino, Torino, Italy 10129.
[3] INP Phelma, Grenoble, France 38000.
[4] Université Catholique de Louvain (UCL), Louvain la Neuve, Belgium 1348.

calculation of interfacial transfers and of steam-water properties. Moreover, it is computationally affordable for its use in industrial configurations.

In our previous works, the single-velocity six-equation model was numerically integrated using the basic Fortran libraries of the CLAWPACK software [168]. Due to its industrial interest, the single-velocity six-equation model has been implemented in EUROPLEXUS code for the simulation of metastable steam-water flows in the event of a Loss of Coolant Accident (LOCA), i.e. a Design Basis Accident (DBA) of nuclear power plants. Here we use our methodology for the simulation of fast depressurizations, validating it against experimental data available in the literature.

The plan of the article is the following. In Section 7.2 we briefly describe the six-equation single-velocity two-phase flow model together with its physical and mathematical properties. Here we discuss both the homogeneous hyperbolic portion of the model and the source terms necessary for the thermodynamic equilibrium recovery. Section 7.3 explains our strategy for the calculation of steam-water properties and the developments of the work done in [79] for the extension to the metastable vapor states. In Section 7.4 we show the numerical methods developed for the calculation of the complete model, focusing on the Riemann solver and the Runge-Kutta Ordinary Differential Equations (ODEs) solvers. These methods are used in Section 7.5 for the simulation of fast depressurizations occurring in steam-water systems. Finally, in Section 7.6, we give some conclusions and perspectives.

7.2 Six-equation single-velocity two-phase flow model

For the metastable two-phase flows simulation, we chose the six-equation single-velocity model in the form proposed in [200] to ensure *mixture-energy-consistency* at the discrete level. The six-equation model is a two-phase, two-pressure system modeling the dynamics of mixture fluids that can also deal with phase transition when the phases are the liquid and its vapor.

We introduce before the homogeneous hyperbolic portion of the model and, then, we describe the complete model.

7.2.1 Homogeneous hyperbolic portion of the model

The governing equations consist of mass and energy balance laws for each phase, the momentum balance for the mixture, plus an advection equation for one of the two phases. The velocity is assumed to be equal for the two phases. In 1D, the hyperbolic homogeneous portion of this model reads

$$\begin{cases} \partial_t \alpha_1 + u\partial_z \alpha_1 = 0, \\ \partial_t(\alpha_1\rho_1) + \partial_z(\alpha_1\rho_1 u) = 0, \\ \partial_t(\alpha_2\rho_2) + \partial_z(\alpha_2\rho_2 u) = 0, \\ \partial_t(\rho u) + \partial_z(\rho u^2 + \alpha_1 p_1 + \alpha_2 p_2) = 0, \\ \partial_t(\alpha_1\rho_1 E_1) + \partial_z[\alpha_1(\rho_1 E_1 + p_1)u] + \Sigma(\mathbf{U}, \partial_z \mathbf{U}) = 0, \\ \partial_t(\alpha_2\rho_2 E_2) + \partial_z[\alpha_2(\rho_2 E_2 + p_2)u] - \Sigma(\mathbf{U}, \partial_z \mathbf{U}) = 0. \end{cases} \tag{7.1}$$

At each phase is assigned a density ρ_k, a pressure p_k, a specific internal energy e_k and a volume fraction α_k, where $k = 1,2$. $E_k = e_k + \frac{1}{2}u^2$ are the specific total energies and $\rho = \alpha_1\rho_1 + \alpha_2\rho_2$ is the mixture density. Two other useful quantities are: the phasic mass fraction $Y_k = \alpha_k\rho_k/\rho$ and the phasic partial density $m_k = \alpha_k\rho_k$. The saturation condition $\alpha_1 + \alpha_2 = 1$ is obviously assumed.

The nonconservative terms that appear in the phasic total energy equations are

$$\Sigma(\mathbf{U}, \partial_z\mathbf{U}) = -u \cdot [Y_2\partial_z(\alpha_1 p_1) - Y_1\partial_z(\alpha_2 p_2)]. \tag{7.2}$$

These terms are non-zero if $u \neq 0$ and if $Y_1Y_2 \neq 0$, that is, if the fluid is a mixture containing both species moving at non-zero velocity.

The above system of partial differential equations is hyperbolic and its eigenvalues are

$$\lambda_1 = u - c_{hom}, \quad \lambda_{2,\dots,5} = u, \quad \lambda_6 = u + c_{hom}, \tag{7.3}$$

where the speed of sound of the associated homogeneous model is

$$c_{hom} = \sqrt{Y_1c_1^2 + Y_2c_2^2}, \tag{7.4}$$

and c_k are the phasic isentropic speeds of sound. In order to close the system, two equations of state (EoS) are needed, one per each phase. They are of the form of the *incomplete EoS* [63]:

$$p_k = p_k(\rho_k, e_k). \tag{7.5}$$

In this work, we do not use an analytic relation for (7.5), but, a look-up table algorithm for a fast and accurate evaluation of steam-water properties. This procedure provides bicubic spline functions globally continuous on the entire e-v domain. This technique is explained in Section 7.3.

7.2.2 The complete model for phase transition

The complete six-equation single-velocity two-phase flow model, proposed in [81], allows to simulate phase transition phenomena of metastable phases. The relaxation processes are non-instantaneous and are written for an arbitrary EoS.

Considering the contribution of the relaxation sources, the six-equation model reported in Eq. (7.1) reads:

$$\begin{cases} \partial_t\alpha_1 + u\partial_z\alpha_1 = \frac{\alpha_1}{a\rho_1\Theta^p}(p_1 - p_2) + \frac{\alpha_1}{a\rho_1}\frac{hA_{int}}{V}(T_1 - T_2) - \frac{1}{\rho_1}\left(1 - \alpha_1\frac{i_pk_T - k_pi_T}{k_pj_T - j_pk_T}\right)G_{1\to2}\frac{A_{int}}{V}, \\ \partial_t(\alpha_1\rho_1) + \partial_z(\alpha_1\rho_1u) = -G_{1\to2}\frac{A_{int}}{V}, \\ \partial_t(\alpha_2\rho_2) + \partial_z(\alpha_2\rho_2u) = +G_{1\to2}\frac{A_{int}}{V}, \\ \partial_t(\rho u) + \partial_z(\rho u^2 + \alpha_1p_1 + \alpha_2p_2) = 0, \\ \partial_t(\alpha_1\rho_1E_1) + \partial_z[\alpha_1(\rho_1E_1 + p_1)u] + \Sigma = -\frac{\alpha_1p_{int}}{a\rho_1\Theta^p}(p_1 - p_2) + b_T\frac{hA_{int}}{V}(T_1 - T_2) - b_gG_{1\to2}\frac{A_{int}}{V} \\ \partial_t(\alpha_2\rho_2E_2) + \partial_z[\alpha_2(\rho_2E_2 + p_2)u] - \Sigma = +\frac{\alpha_1p_{int}}{a\rho_1\Theta^p}(p_1 - p_2) - b_T\frac{hA_{int}}{V}(T_1 - T_2) + b_gG_{1\to2}\frac{A_{int}}{V} \end{cases} \tag{7.6}$$

where $b_T = \alpha_1\rho_1\left[\frac{p_{int}}{a\rho_1^2}\left(\frac{\Gamma_1}{\alpha_1} + \frac{\Gamma_2}{\alpha_2}\right) - \frac{1}{\alpha_1\rho_1}\right]$ and $b_g = \alpha_1\rho_1\frac{j_pi_T - i_pj_T}{k_pj_T - j_pk_T}$. h is the convection heat transfer coefficient, A_{int}/V is the interfacial area density per unit volume, Γ_k are the phasic Grüneisen coefficients, and Θ^p is the characteristic time for the pressure equilibrium recovery.

From (7.6) we can see that the pressure disequilibrium ($p_1 - p_2$) drives the compression-expansion energy transfer that leads to the pressure equilibrium. The term ($T_1 - T_2$) drives the sensible heat transfer and $G_{1\to 2}$ stands for the net mass flow rate per unit interfacial area due to phase transition phenomena.

7.3 Look-up table algorithm for liquid and vapor EoS

To correctly simulate phase transition phenomena, accurate equations of state should be used. For the steam-water properties, nowadays, the most reliable EoS for water is the IAPWS-95 [272]. This is an analytical equation based on experimental data and is used for general and scientific purposes. Given that the IAPWS-95 formulation is quite cumbersome and time consuming, IAPWS also provides a separate formulation recommended for industrial use, i.e. the IAPWS-IF97 [273]. The latter consists of a set of equations for five different regions, fitting the values resulting from the IAPWS-95. In this work we rely on the IAPWS-IF97 for the water properties calculation.

Generally, accurate EoS are expressed as:

$$f = f(\rho, T) \qquad \text{or} \qquad g = g(p, T), \tag{7.7}$$

where: $f = u - Ts$ and $g = h - Ts$ are, respectively, the Helmholtz free energy and the Gibbs free enthalpy. Such EoS are very accurate but extremely costly from a computational point of view. Therefore, replacing the incomplete EoS in (7.5) by an iterative algorithm that implements a complete EoS as (7.7) is feasible but too expensive for industrial calculations.

Based on the works of Kunick et al. [147], in [79] we proposed a strategy to calculate steam-water properties. In our previous work, it consisted in a look-up table method that calculates $p = p(\rho, e)$ by a bicubic interpolation on the e-v thermodynamic diagram.

Since it was used for HEM and HRM calculations, ρ and e referred to equilibrium single-phase states or to mixture ones. Whereas, for the current work, the look-up table technique is used for the calculation of phasic EoS, i.e. $p_k = p_k(\rho_k, e_k)$.

In the following we present the liquid and the vapor domains of water on the e-v diagram. Then we discuss the limits of these domains, showing the extension up to liquid and vapor spinodal curves. Finally, we recall the guidelines of our strategy for the bicubic interpolation of the thermodynamic properties.

7.3.1 The *e-v* diagram for water

The e-v diagram is quite uncommon in the literature. In [79] we have shown the behavior of thermodynamic properties in this plane, and the trend of isotherms, isobars and isoquality curves for single-phase water and mixtures at saturated conditions. Here, we make a different use of this diagram because we need one equation of state per phase.

Figure 7.1 depicts the liquid and the vapor domains on the e-v diagram. The water phase diagram is clearly subdivided into two portions. The liquid region, located on the left of the e-v diagram, is defined up to the critical point and the composition of the liquid spinodal and the $p = 0$ curves

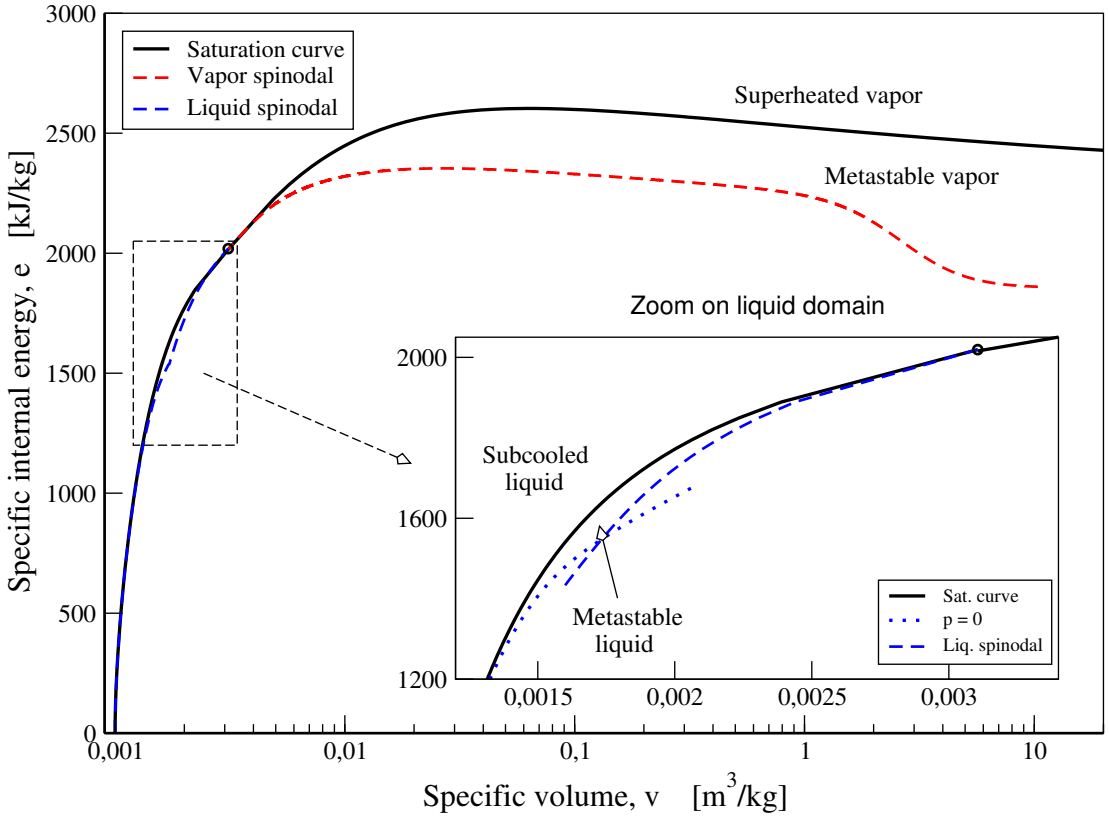

FIGURE 7.1. Liquid and vapor water on the e-v diagram. The critical point is indicated by circular markers ◯ in the main plot and its magnified view. Plot realized using the IAPWS-IF97 and the IAPWS-95.

(see [79] for further explanations). The vapor domain is the one located above of the critical point and the vapor spinodal line.

The area comprised between the two spinodal lines is not of interest because it refers to phasic unstable states.

In Fig. 7.2 we show the 2D trends of pressure, temperature and speed of sound on the whole e-v domain. Note that the 2D plots here reported are intended for phasic liquid and vapor, in stable and metastable conditions, then, their behaviors beyond the saturation curve do not correspond to the mixture plots shown in [79].

7.3.2 Extension to vapor metastable states

In fast transients of nuclear industry concerns, one or both phases can be metastable. The liquid can reach metastable states due to a rapid depressurization (see [79] or Section 7.5), and the vapor can depart from equilibrium conditions during the vapor pocket compression initiating a waterhammer. But, metastable vapor is also of concern in the expansion stages of the steam turbines, both in nuclear and in conventional steam power plants.

For these reasons, the novel steam-water tables have to take into account the metastable vapor states. For a prior work similar to the present one, refer to [148]. In this section we provide a method of determination of the thermodynamical states belonging to the vapor spinodal curve, which allows

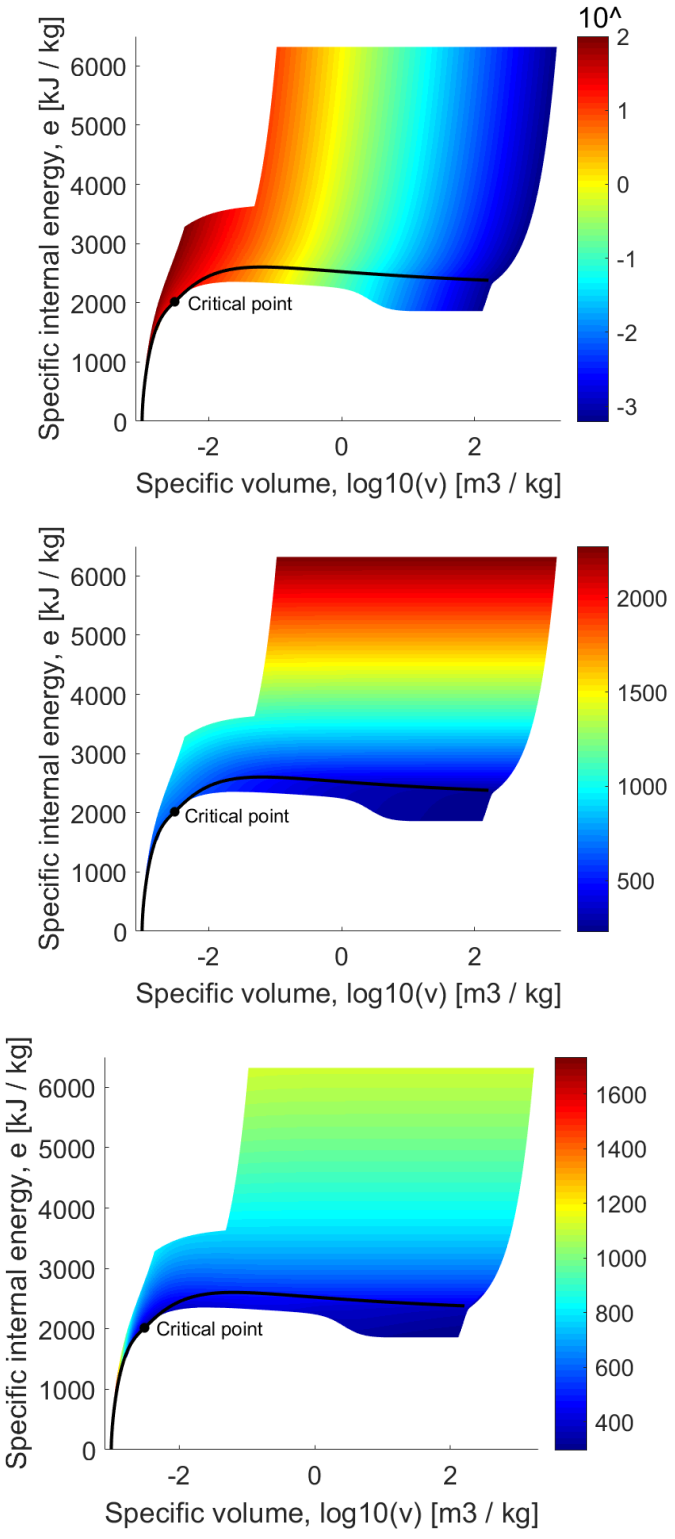

FIGURE 7.2. Phasic pressures (MPa), temperatures (K) and speeds of sound (m/s) on the e-v diagram. The results obtained using the IAPWS-IF97. The black line indicates the saturation curve.

the extension to the metastable vapor conditions included between the saturation curve and the spinodal one.

Contrary to the liquid spinodal curve shown in [79], the properties of the vapor spinodal have been determined using the IAPWS-95 Formulation. In fact, the IAPWS-95 expresses the thermodynamical variables as a function of $v = 1/\rho$ and T, therefore, it exists a function of the form

$$p = p(v, T), \tag{7.8}$$

that allows to define the loci at which

$$\left(\frac{\partial p}{\partial v}\right)_T = 0. \tag{7.9}$$

These correspond to the limit of thermodynamic stability for a pure phase, then, they define the spinodal curve [43, 73]. For the liquid domain, in [79], we used the IAPWS-IF97 to define this limit, however, this is not possible for the vapor phase.

The pure vapor boundary has been identified using the IAPWS-95, however, the metastable vapor properties are everywhere defined using the IAPWS-IF97. Even on the vapor spinodal line, once it has been identified by the IAPWS-95, the thermodynamic properties are recalculated using the IAPWS-IF97. In Fig. 7.3 we show the comparison between the pure vapor temperature and speed of sound on the vapor spinodal curves obtained by the IAPWS-95 and the IAPWS-IF97. The trends are very similar.

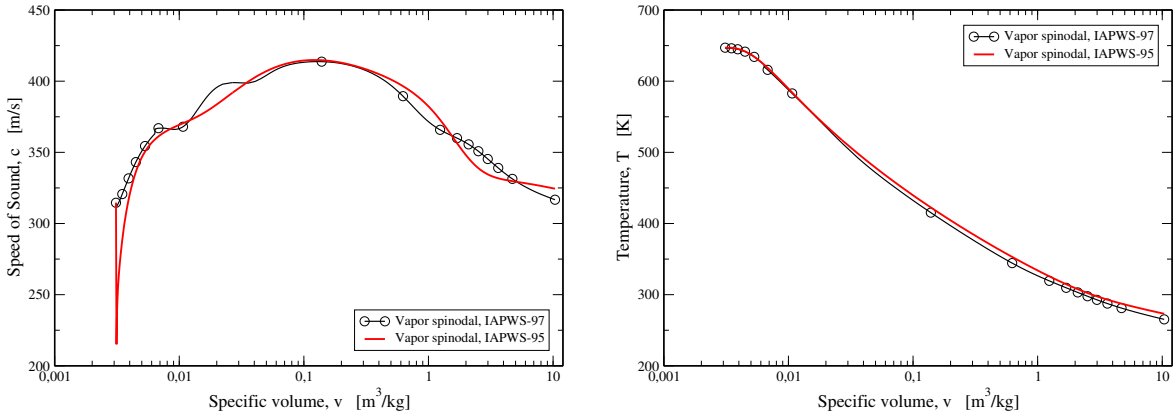

FIGURE 7.3. Speed of sound and temperature profiles on the vapor spinodal curve. The results obtained using the IAPWS-IF97 are compared to the ones obtained with the IAPWS-95.

Once the vapor spinodal curve has been identified, the domain of the steam-water tables can be extended up to this limit. Beyond this limit, the phase is unstable, then, non physical. That is the reason why the spinodal lines represent an impassable boundary in our work.

7.3.3 A bicubic interpolation method

For easiness, the irregular physical domain e-v, has been transposed in a Cartesian transformed domain, Y-X. This feature is depicted in Fig. 7.4.

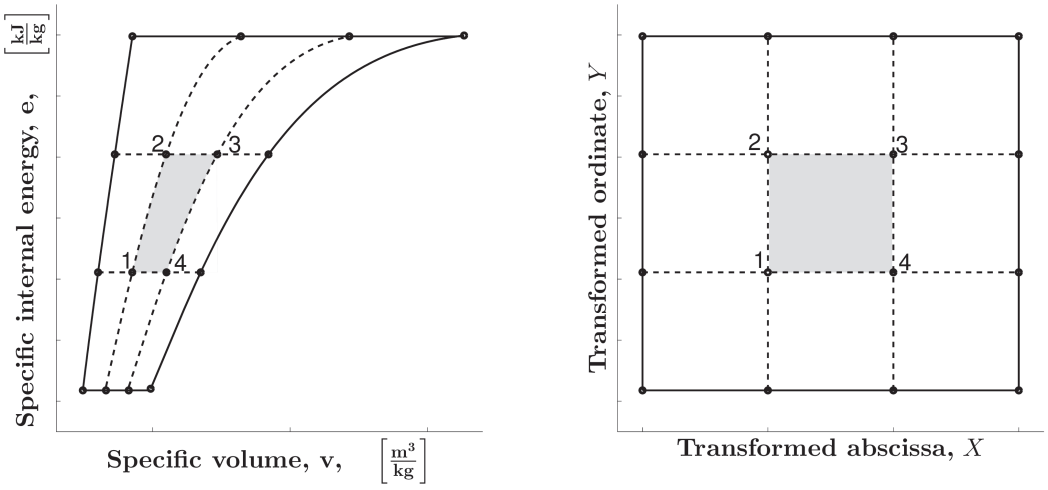

Figure 7.4: Grid of nodes in the physical domain and in the transformed one

As discussed in [79], in the liquid and supercritical domain we imposed an equidistant pattern of nodes, hence the distribution is linear, whereas, in the vapor domain the node distribution is logarithmic. Handling such a regular distribution of nodes ensures that, the cell containing the working point can be immediately found. Such a feature allows to strongly reduce the computational time of the cell identification.

Then, a *bicubic interpolation* is performed on the Cartesian diagram *Y-X*, using stored values on the *e-v* diagram.

To perform a bicubic interpolation, the cell must be square. A *bilinear mapping* is used to pass from the physical domain to the Cartesian one. The bilinear mapping functions are:

$$v = \alpha_1 + \alpha_2 X + \alpha_3 Y + \alpha_4 XY, \tag{7.10}$$

and

$$e = \beta_1 + \beta_2 X + \beta_3 Y + \beta_4 XY. \tag{7.11}$$

To identify α_i, β_i coefficients, one needs to set the vertices of the irregular quadrilateral cell on the *e-v* plane to be the vertices of the unit length square of the transformed space. In our particular case, the grid is formed by horizontal iso-e lines (see Fig. 7.4), then: $\beta_2, \beta_4 = 0$. Finally, it comes out:

$$\alpha_1 = v_1, \quad \alpha_2 = -v_1 + v_4, \quad \alpha_3 = -v_1 + v_2, \quad \alpha_4 = v_1 - v_2 + v_3 - v_4, \tag{7.12}$$

$$\beta_1 = e_1, \quad \beta_2 = 0, \quad \beta_3 = -e_1 + e_2, \quad \beta_4 = 0. \tag{7.13}$$

The bilinear mapping serves to identify the (X_0, Y_0) point corresponding to a phasic $(v_{k,0}, e_{k,0})$ value. Once the point is known, we can calculate the thermodynamic properties using a bicubic interpolation. Let us suppose to be interested in the phasic pressure calculation, thus:

$$p_k(v_{k,0}, e_{k,0}) = \tilde{p}_k(X_0, Y_0) = [1 \; X_0 \; X_0^2 \; X_0^3] \, \mathbf{A} \, [1 \; Y_0 \; Y_0^2 \; Y_0^3]^T \tag{7.14}$$

where $\mathbf{A}$ is the coefficient matrix and it describes the function p_k on the transformed space. Its elements are

$$\mathbf{A} = \begin{bmatrix} 1 & 0 & 0 & 0 \\ 0 & 0 & 1 & 0 \\ -3 & 3 & -2 & -1 \\ 2 & -2 & 1 & 1 \end{bmatrix} \begin{bmatrix} \tilde{p}_{k,1} & \tilde{p}_{k,2} & \partial_Y \tilde{p}_{k,1} & \partial_Y \tilde{p}_{k,2} \\ \tilde{p}_{k,4} & \tilde{p}_{k,3} & \partial_Y \tilde{p}_{k,4} & \partial_Y \tilde{p}_{k,3} \\ \partial_X \tilde{p}_{k,1} & \partial_X \tilde{p}_{k,2} & \partial_{X,Y} \tilde{p}_{k,1} & \partial_{X,Y} \tilde{p}_{k,2} \\ \partial_X \tilde{p}_{k,4} & \partial_X \tilde{p}_{k,3} & \partial_{X,Y} \tilde{p}_{k,4} & \partial_{X,Y} \tilde{p}_{k,3} \end{bmatrix} \begin{bmatrix} 1 & 0 & -3 & 2 \\ 0 & 0 & 3 & -2 \\ 0 & 1 & -2 & 1 \\ 0 & 0 & -1 & 1 \end{bmatrix}, \tag{7.15}$$

where, for instance, $\partial_X \tilde{p}_{k,1}$ indicates the derivative of the function p_k with respect to the coordinate X at node 1, that is, the node in the bottom left corner. One can refer to [79] for further information about the calculations of these derivatives.

The function $\tilde{p}_k(X,Y)$ refers to a Cartesian square grid and, by construction [212], has the following properties: i) the values of the function and the specified derivatives are reproduced exactly at the nodes, and, ii) the function and the specified derivatives change continuously at the edges of the square cells. Furthermore, these smoothness properties do not depend on the accuracy of the specified derivatives [212].

Due to the choice of the bilinear transformation, $p_k(v_k, e_k)$ is still a continuous function across the cell edges in the *e-v* diagram. However, not all the derivatives are continuous across the edges. Further details about derivatives calculation are given in [79].

7.4 Numerical solution methods

The numerical solution of system (7.6) can be obtained by a succession of operators [256] of first order,

$$\mathbf{U}_i^{n+1} = L_{source}^{\Delta t} \, L_{hyp}^{\Delta t} \, \mathbf{U}_i^n \tag{7.16}$$

or second order

$$\mathbf{U}_i^{n+1} = L_{source}^{\Delta t/2} \, L_{hyp}^{\Delta t} \, L_{source}^{\Delta t/2} \, \mathbf{U}_i^n, \tag{7.17}$$

where L_{hyp} and L_{source} denote, respectively, the hyperbolic and the source operator. The latter is composed by three operators: L_p, L_T, L_g that are, respectively, the operators for pressure, temperature and chemical potential relaxation procedures. The result of an operator is used as initial value for the following operator.

In this section, we describe the numerical techniques used for solving the hyperbolic homogeneous portion of the system and, then, the relaxation operators.

7.4.1 Hyperbolic operator

The hyperbolic homogeneous portion of the model, that is, Eq. (7.1), can be written as

$$\partial_t \mathbf{U} \; + \partial_z \mathbf{F}(\mathbf{U}) \; + \mathbf{B}_1(\mathbf{U}) \, \partial_z u \; + \mathbf{B}_2(\mathbf{U}) \, \partial_z(\alpha_1 p_1) \; + \mathbf{B}_3(\mathbf{U}) \, \partial_z(\alpha_2 p_2) \; = 0, \tag{7.18}$$

where:

$$\mathbf{U} = \begin{bmatrix} \alpha_1 \\ \alpha_1\rho_1 \\ \alpha_2\rho_2 \\ \rho u \\ \alpha_1\rho_1 E_1 \\ \alpha_2\rho_2 E_2 \end{bmatrix}, \quad \mathbf{F} = \begin{bmatrix} \alpha_1 u \\ \alpha_1\rho_1 u \\ \alpha_2\rho_2 u \\ \rho u^2 + \alpha_1 p_1 + \alpha_2 p_2 \\ \alpha_1(\rho_1 E_1 + p_1)u \\ \alpha_2(\rho_2 E_2 + p_2)u \end{bmatrix}, \quad \mathbf{B}_1 = \begin{bmatrix} -\alpha_1 \\ 0 \\ 0 \\ 0 \\ 0 \\ 0 \end{bmatrix}, \quad \mathbf{B}_2 = \begin{bmatrix} 0 \\ 0 \\ 0 \\ 0 \\ -uY_2 \\ +uY_2 \end{bmatrix}, \quad \mathbf{B}_3 = \begin{bmatrix} 0 \\ 0 \\ 0 \\ 0 \\ +uY_1 \\ -uY_1 \end{bmatrix}. \tag{7.19}$$

Considering a spatial domain decomposed in cells, we refer to $\mathbf{U}_i^n$ as the integral average of the calculation variables vector in the ith cell at the time step t^n. The evolution between t^n and t^{n+} is

$$\mathbf{U}_i^{n+} = \mathbf{U}_i^n - \frac{\Delta t}{\Delta z}\left(\mathbf{F}_{i+\frac{1}{2}}^n - \mathbf{F}_{i-\frac{1}{2}}^n\right) - \Delta t H_i \tag{7.20}$$

where $\mathbf{F}_{i\pm\frac{1}{2}}^n$ denote the fluxes at the boundaries of the mesh cell, and H_i groups all the contributions of nonconservative terms, that is

$$H_i = \int_{\Delta z} \mathbf{B}_1\, \partial_z u \; dz - \int_{\Delta z} \mathbf{B}_2\, \partial_z(\alpha_1 p_1)\, dz - \int_{\Delta z} \mathbf{B}_3\, \partial_z(\alpha_2 p_2)\, dz. \tag{7.21}$$

Equation (7.20) is exact, however we need an approximation method to evaluate both the fluxes and the integral of nonconservative terms. For the former, we adopt a HLLC-type method, then, the numerical approximation of flux is:

$$\mathbf{F}_{i+\frac{1}{2}}^{HLLC,n}(\mathbf{U}_i^n, \mathbf{U}_{i+1}^n) = \begin{cases} \mathbf{F}_\ell, & \text{if } S_\ell > 0, \\ \mathbf{F}_\ell^* = \mathbf{F}_\ell + S_\ell(\mathbf{U}_\ell^* - \mathbf{U}_\ell), & \text{if } S_\ell \le 0 < S^*, \\ \mathbf{F}_r^* = \mathbf{F}_r + S_r(\mathbf{U}_r^* - \mathbf{U}_r), & \text{if } S^* \le 0 < S_r, \\ \mathbf{F}_r, & \text{if } S_r \le 0. \end{cases} \tag{7.22}$$

This solver is *complete* because it assume as many waves as the ones of the system. In fact, three waves are present and move at speeds

$$s^1 = S_\ell\,, \qquad s^2 = S^*\,, \qquad s^3 = S_r. \tag{7.23}$$

They separate four constant states called: $\mathbf{U}_\ell$, $\mathbf{U}_\ell^*$, $\mathbf{U}_r^*$ and $\mathbf{U}_r$. We indicate with subscripts ${}^*\ell$, ${}^*r$ the quantities corresponding to the states $\mathbf{U}_\ell^*$ and $\mathbf{U}_r^*$ adjacent (respectively on the left and on the right) to the middle wave propagating at speed S^*. Following Davis [72] we define

$$S_\ell = \min(u_\ell - c_\ell, u_r - c_r), \qquad S_r = \max(u_\ell + c_\ell, u_r + c_r). \tag{7.24}$$

The speed S^* is then determined as in [264]:

$$S^* = u^* = \frac{p_r - p_\ell + \rho_\ell u_\ell(S_\ell - u_\ell) - \rho_r u_r(S_r - u_r)}{\rho_\ell(S_\ell - u_\ell) - \rho_r(S_r - u_r)}. \tag{7.25}$$

The completely upwind fluxes of Eq. (7.22) are: $\mathbf{F}_\ell = \mathbf{F}(\mathbf{U}_i^n)$ and $\mathbf{F}_r = \mathbf{F}(\mathbf{U}_{i+1}^n)$. The middle states are:

$$\mathbf{U}_{*\iota} = \begin{bmatrix} \alpha_{1,\iota} \\ (\alpha_1\rho_1)_\iota \frac{S_\iota - u_\iota}{S_\iota - S^*} \\ (\alpha_2\rho_2)_\iota \frac{S_\iota - u_\iota}{S_\iota - S^*} \\ \rho_\iota \frac{S_\iota - u_\iota}{S_\iota - S^*} S^* \\ (\alpha_1\rho_1)_\iota \frac{S_\iota - u_\iota}{S_\iota - S^*} \left(E_{1,\iota} + (S^* - u_\iota)\left(S^* + \frac{p_{1,\iota}}{\rho_{1,\iota}(S_\iota - u_\iota)} \right) \right) \\ (\alpha_2\rho_2)_\iota \frac{S_\iota - u_\iota}{S_\iota - S^*} \left(E_{2,\iota} + (S^* - u_\iota)\left(S^* + \frac{p_{2,\iota}}{\rho_{2,\iota}(S_\iota - u_\iota)} \right) \right) \end{bmatrix}, \tag{7.26}$$

with $\iota = \ell, r$.

Nonconservative terms are approximated using a first order approximation method, that is

$$\int_{\Delta z} \mathbf{B}_1(U)\, \partial_z u \; dz \approx \mathbf{B}_1(U_i^n)\left(u_{i+\frac{1}{2}} - u_{i-\frac{1}{2}} \right), \tag{7.27}$$

$$\int_{\Delta z} \mathbf{B}_2(U)\, \partial_z(\alpha_1 p_1) \; dz \approx \mathbf{B}_1(U_i^n)\left[(\alpha_1 p_1)_{i+\frac{1}{2}} - (\alpha_1 p_1)_{i-\frac{1}{2}} \right], \tag{7.28}$$

$$\int_{\Delta z} \mathbf{B}_3(U)\, \partial_z(\alpha_2 p_2) \; dz \approx \mathbf{B}_1(U_i^n)\left[(\alpha_2 p_2)_{i+\frac{1}{2}} - (\alpha_2 p_2)_{i-\frac{1}{2}} \right]. \tag{7.29}$$

In order to calculate the interfacial quantities, we use the wave pattern information coming from the HLLC solver. For the advection equation we use the method proposed in [153]:

$$u_{i+\frac{1}{2}}^{HLLC,n}(\mathbf{U}_i^n, \mathbf{U}_{i+1}^n) = \begin{cases} u_\ell, & \text{if } S_\ell > 0, \\ \frac{S_\ell - u_\ell}{S_\ell - S^*} S^*, & \text{if } S_\ell \le 0 < S^*, \\ \frac{S_r - u_r}{S_r - S^*} S^*, & \text{if } S^* \le 0 < S_r, \\ u_r, & \text{if } S_r \le 0. \end{cases} \tag{7.30}$$

For the nonconservative terms of the phasic energy equations, we propose:

$$(\alpha_k p_k)_{i+\frac{1}{2}}^{HLLC,n}(\mathbf{U}_i^n, \mathbf{U}_{i+1}^n) = \begin{cases} (\alpha_k p_k)_\ell, & \text{if } S_\ell > 0, \\ \alpha_{k,\ell}[p_{k,\ell} - \rho_{k,\ell}(S_\ell - u_\ell)(u_\ell - S^*)], & \text{if } S_\ell \le 0 < S^*, \\ \alpha_{k,r}[p_{k,r} - \rho_{k,r}(S_r - u_r)(u_r - S^*)], & \text{if } S^* \le 0 < S_r, \\ (\alpha_k p_k)_r, & \text{if } S_r \le 0. \end{cases} \tag{7.31}$$

7.4.2 Relaxation operators

In the literature, most of the works deal with instantaneous relaxation procedures to be used for very simple EoS as the stiffened gas one. In [81], authors proposed a novel method to describe the physics involved into the relaxation processes. They consist in dynamical systems of ODEs that allow the equilibrium recovery. The novelty of this work lies in the EoS independence of the numerical techniques.

These relaxation processes can be split into three systems of ODEs, each one modeling a different physical phenomenon. In this work the systems of ODEs are calculated using a high order explicit Runge-Kutta (RK) method with adaptive stepsize, that is, the so-called RK45 [108]. This method is

fourth order accurate with an error estimator of fifth order for the calculation of the variable time step.

The drawback of this explicit method is the loss of stability for stiff problems. However, one may refer to the appendix of [81] for alternative robust semi-analytical methods if needed.

At the end of the hyperbolic operator step, the phases are in full thermodynamic disequilibrium. This is attenuated using three relaxation operators that are used in series. First the pressure equilibrium step, then the temperature relaxation one and, finally, the mass transfer procedure. We introduce them in the following of this section.

7.4.2.1 Pressure relaxation operator

The pressure relaxation procedure is a system of ODEs composed of two equations. In the canonical form it writes

$$\begin{cases} \frac{d\rho_1}{dt} = -\frac{1}{a}\frac{p_1 - p_2}{\Theta^p}, \\ \frac{de_1}{dt} = -\frac{p_{int}}{a\rho_1^2}\frac{p_1 - p_2}{\Theta^p}, \end{cases} \tag{7.32}$$

where

$$a = \rho_1\Gamma_1\left[\frac{p_{int}}{\rho_1^2} - \left(\frac{\partial e_1}{\partial \rho_1}\right)_{p_1}\right] + \rho_2\Gamma_2\frac{\alpha_1\rho_2}{\alpha_2\rho_1}\left[\frac{p_{int}}{\rho_2^2} - \left(\frac{\partial e_2}{\partial \rho_2}\right)_{p_2}\right]. \tag{7.33}$$

p_{int} indicates the interfacial pressure. This technique is based on the first law of the thermodynamics and an exponential time-decay for the pressure disequilibrium. It allows a semi-analytical integration, then, it is very robust even for stiff cases ($\Theta^p \ll 1$). Since we use the six-equation model to integrate more easily the five-equation model of [139], the pressures equilibrium is required at the end of this pressure relaxation step. Hence, sufficiently small Θ^p must be used. For instance, for $\Theta^p = \Delta t^{conv}/9$, the final pressure disequilibrium is around the 0.01% of the initial one. As a result, phases may be considered roughly in pressure equilibrium.

7.4.2.2 Temperature relaxation operator

The temperature relaxation procedure is based on the first law of thermodynamics and the Newton's law for the convection. This step is the one responsible for the sensible heat transfer. In the canonical form, it is

$$\begin{cases} \frac{d\rho_1}{dt} = -\frac{hA_{int}}{V}(T_2 - T_1)\frac{1}{a}\left(\frac{\Gamma_1}{\alpha_1} + \frac{\Gamma_2}{\alpha_2}\right), \\ \frac{de_1}{dt} = -\frac{hA_{int}}{V}(T_2 - T_1)\left[\frac{p_{int}}{a\rho_1^2}\left(\frac{\Gamma_1}{\alpha_1} + \frac{\Gamma_2}{\alpha_2}\right) - \frac{1}{m_1}\right]. \end{cases} \tag{7.34}$$

h is the heat transfer coefficient expressed in $W/m^2 \cdot K$ and A_{int} is the interface area expressed in m^2 and flow pattern dependent. One can use some empirical correlations to estimate them or can use $\frac{hA_{int}}{V}$ as a parameter for speeding up or slowing down the sensible heat transfer process.

For very fast temperature relaxation processes, a more robust technique is reported in the appendix of [81]. It is a semi-analytical procedure based on an exponential time-decay for the temperature disequilibrium.

7.4.2.3 Mass transfer operator

The mass transfer procedure models the condensation and evaporation events. The procedure proposed in [81] is very flexible because it may incorporate various models present in the literature. For instance nucleation models (see [208, 214]), statistical mechanics theory (see [275]), or simpler relaxation models [28].

It is based on the pressure equilibrium between the phases, and, the phasic temperature difference invariance. This latter condition means that the heat transfer occurring in this processes is the latent one. No sensible heat transfer occurs. The canonical form of this relaxation process is

$$\begin{cases} \frac{dm_1}{dt} = -G_{1\to 2}\frac{A_{int}}{V}, \\ \frac{d\rho_1}{dt} = -G_{1\to 2}\frac{A_{int}}{V}\frac{i_p k_T - k_p i_T}{k_p j_T - j_p k_T}, \\ \frac{de_1}{dt} = -G_{1\to 2}\frac{A_{int}}{V}\frac{j_p i_T - i_p j_T}{k_p j_T - j_p k_T}. \end{cases} \tag{7.35}$$

To close the system, a closure law for the mass transfer term $G_{1\to 2}A_{int}$ is needed.

The mass transfer is due to a chemical disequilibrium, that is, a difference between the phasic Gibbs free enthalpy. For this reason, many authors in the literature assumes:

$$G_{1\to 2} \propto (g_1 - g_2). \tag{7.36}$$

In this work, we assume

$$G_{1\to 2}\frac{A_{int}}{V} = \frac{g_1 - g_2}{\Theta_g}, \tag{7.37}$$

where Θ_g is the characteristic time for the chemical equilibrium recovery. Such magnitude is not clearly known, then, we adopt a correlation inspired to [28, 79, 84], i.e.

$$\Theta_g = K_g\ \alpha_v^{-0.25}\left(\frac{p_{sat} - p}{p_{crit} - p_{sat}}\right)^{-1.8}. \tag{7.38}$$

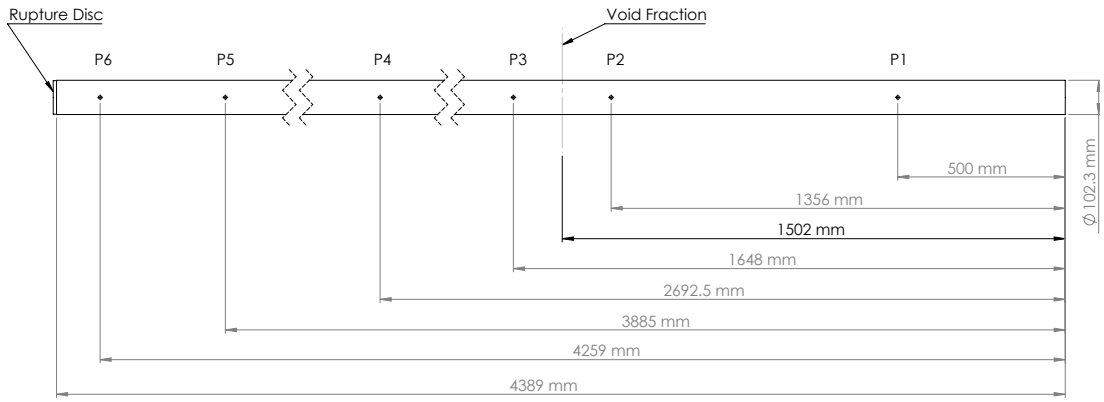

FIGURE 7.5. Schematic of Super Canon experimental facility and location of the measurement devices.

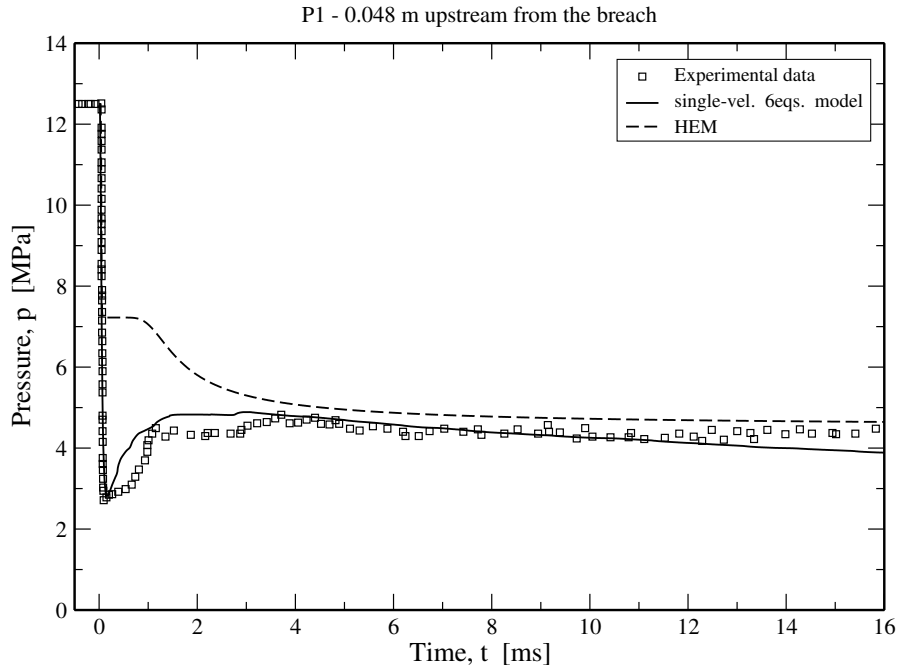

FIGURE 7.6. Pressure evolution in the first $16ms$ of the Bartak's experiment [16] ($12.5MPa$, $563.15K$). Assessment of the single-velocity six-equation model against the experimental data and the HEM results. For this calculation, the 1.7 m long tube has been discretized into a 1000 cells mesh and $K_g = 4$.

7.5 Numerical simulations of fast depressurizations

In the context of nuclear safety, the Loss of Coolant Accident (LOCA) is one of the Design Basis Accidents (DBA). It represents the sudden rupture of a primary system pipe of the nuclear power plants. When it occurs, a rarefaction wave originates at the breach and moves upstream in the primary circuit. The interaction of this wave with the reactor core may lead to the mechanical damage of core components. Then, for the fluid-structure analysis, the correct calculation of the rarefaction wave amplitude is of paramount importance.

The thermodynamic disequilibrium plays a crucial role on the rarefaction wave amplitude, thus, a simple HEM can not produce a correct simulation of these flows. Therefore, to improve the industrial simulation tools, the single-velocity six-equation model has been implemented in the fast dynamic code EUROPLEXUS.

Since the phenomena involving metastable states were not completely known, in the '70s-'80s, some experimental campaigns have been carried out. The experimental facilities for the industrial scenarios focused on the rapid depressurization of vessels or pipes containing water at subcooled conditions [16, 94, 223].

In this section we use these experiments for the validation of the methodology discussed above with EUROPLEXUS code. The benchmark is performed using the experimental data of Bartak [16], Edwards-O'Brien [94] and Super Canon test rig [223]. The schematic of the Super Canon facility and the measurement devices are shown in Fig. 7.5. The Bartak and Edwards-O'Brien test facilities

are very similar to Fig. 7.5. For further details about the test rigs geometry and the measurement techniques, one may refer to [16, 94, 223].

The initial pressure and temperature conditions are $12.5 MPa$ and $563.15 K$ for the Bartak test, $10.34 MPa$ and $557.59 K$ for the Edwards-O'Brien test, and $15 MPa$ and $593.15 K$ for the Super Canon test. Then, the corresponding subcooling degrees, i.e. $T_{sat}(p_{in}) - T_{in}$, are, respectively, $38 K$, $29 K$ and $22 K$.

The three experiments are triggered by the sudden opening of a rupture disc located at one extremity of the pipe. At that moment, a rarefaction wave originates at the break and moves backward. The very first part of the transient is well represented by the Bartak and Edwards-O'Brien data, whereas, the Super Canon experiments represent the global transient.

The depressurization is initially abrupt and fast, then pressure drops below the saturation pressure corresponding to the initial stagnation temperature ($7.4 MPa$ in Bartak experiment, $6.8 MPa$ in Edwards-O'Brien test, $11.2 MPa$ for Super Canon). The liquid water is then into the metastable domain.

Since the abrupt depressurization has led the liquid into a deep metastable condition, the fluid is driven from the thermodynamic disequilibrium towards the thermodynamic stability condition. Then, the depressurization is stopped by a quick vaporization, also called explosion-like nucleation. The system pressure is therefore driven towards the saturated conditions. Further discussions about the rate of depressurization, the pressure undershoot and the homogeneous nucleation phenomenon can be found in [3, 16, 43, 73, 246].

In Fig. 7.6, 7.7 and 7.8 we show the comparisons of the numerical simulations obtained with the single-velocity six-equation model and the experimental data. To underline the importance of the thermodynamic disequilibrium, we report as well the numerical results of the HEM. From these figures we can observe that the pressure undershoot just discussed is well reproduced by the six-equation model, whereas, for the HEM, the mixture always remains at saturated conditions. This means that a numerical simulation performed with a HEM leads to an underestimation of the amplitude of the rarefaction wave, then, for a fluid-structure interaction analysis, the HEM leads to an underestimation of the mechanical consequences on the structure.

By the experimental measurements we know that the velocity of propagation of the rarefaction wave compares well with the isentropic speed of sound of the liquid water initially present into the system. From Fig. 7.6, 7.7 we can see that this velocity is correctly simulated by both equilibrium and disequilibrium two-phase flow models.

For a HEM simulation, once the rarefaction wave has taken the fluid into the two-phase domain, the phase transition takes place in order to maintain the phases at the full thermodynamic equilibrium. In this case, the phase transition starts when the fluid reaches the saturated liquid curve.

For the single-velocity six-equation model, the rarefaction wave propagates into the liquid and takes it to metastable conditions. The phase transition does not take place immediately when the fluid reaches the saturated conditions, thus, the amplitude of the rarefaction wave is wider than in the HEM calculations. For the single-velocity six-equation model, the mass transfer that transforms the liquid into vapor is activated only when metastable conditions are detected. Once one of the two

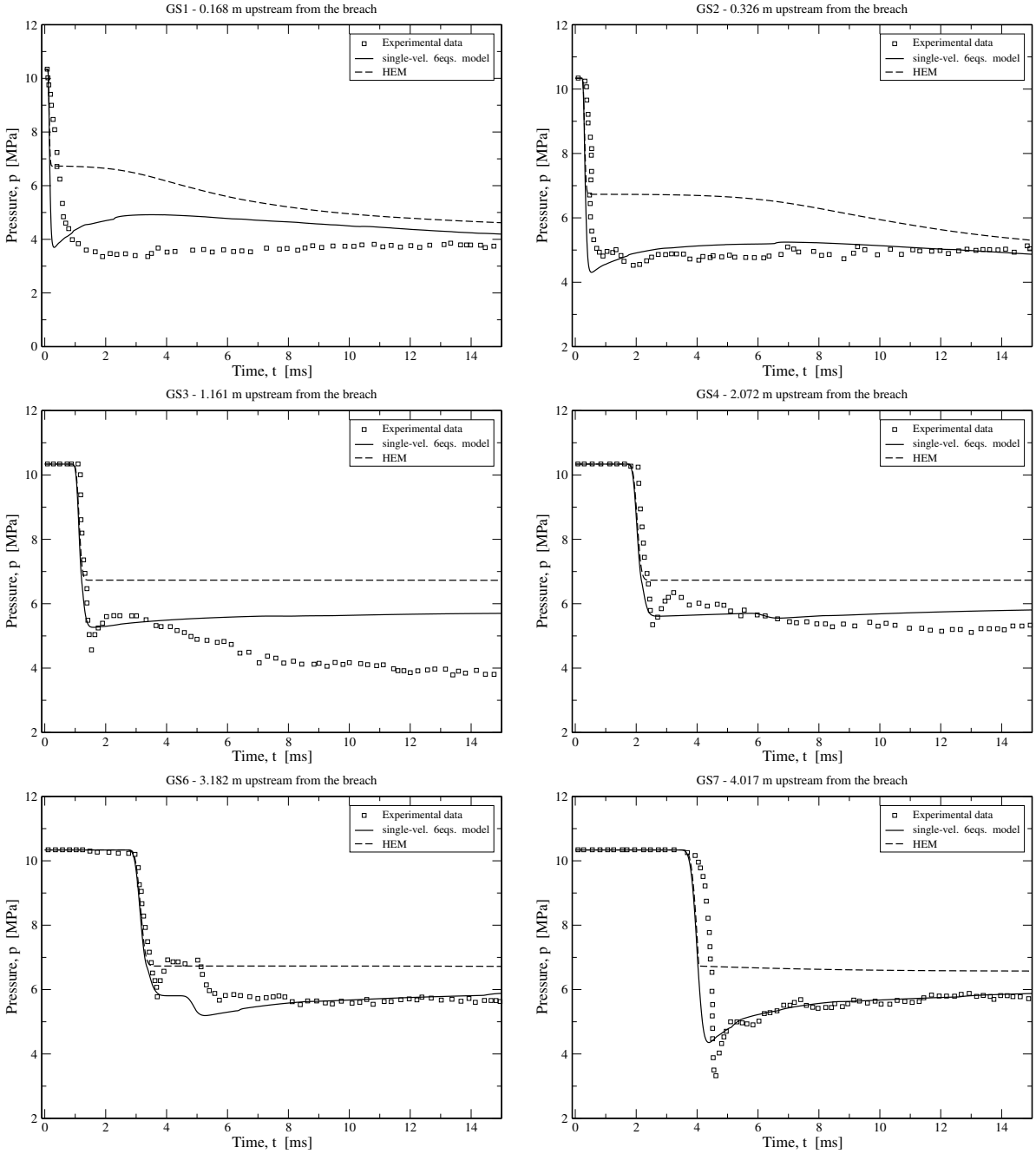

FIGURE 7.7. Assessment of the single-velocity six-equation model on a Edwards-O'Brien experiment. The initial stagnation conditions are 10.34 MPa and 557.59 K (1500 $psia$, 544^oF). For this calculation, the 4.096 m long tube has been discretized into a 1000 cells mesh and $K_g = 0.5$.

phases crosses the saturation curve, the mass transfer is activated and its intensity is proportional to the chemical disequilibrium (see Eq. (7.37)). This is coherent with the theory of thermodynamic stability according to which a deeper metastability condition leads to a faster mass transfer [43]. Summarizing, this modeling choice allows to well represent the two main physical features occurring in fast depressurizations: (i) the correct amplitude of the rarefaction wave, and (ii) the explosion-like

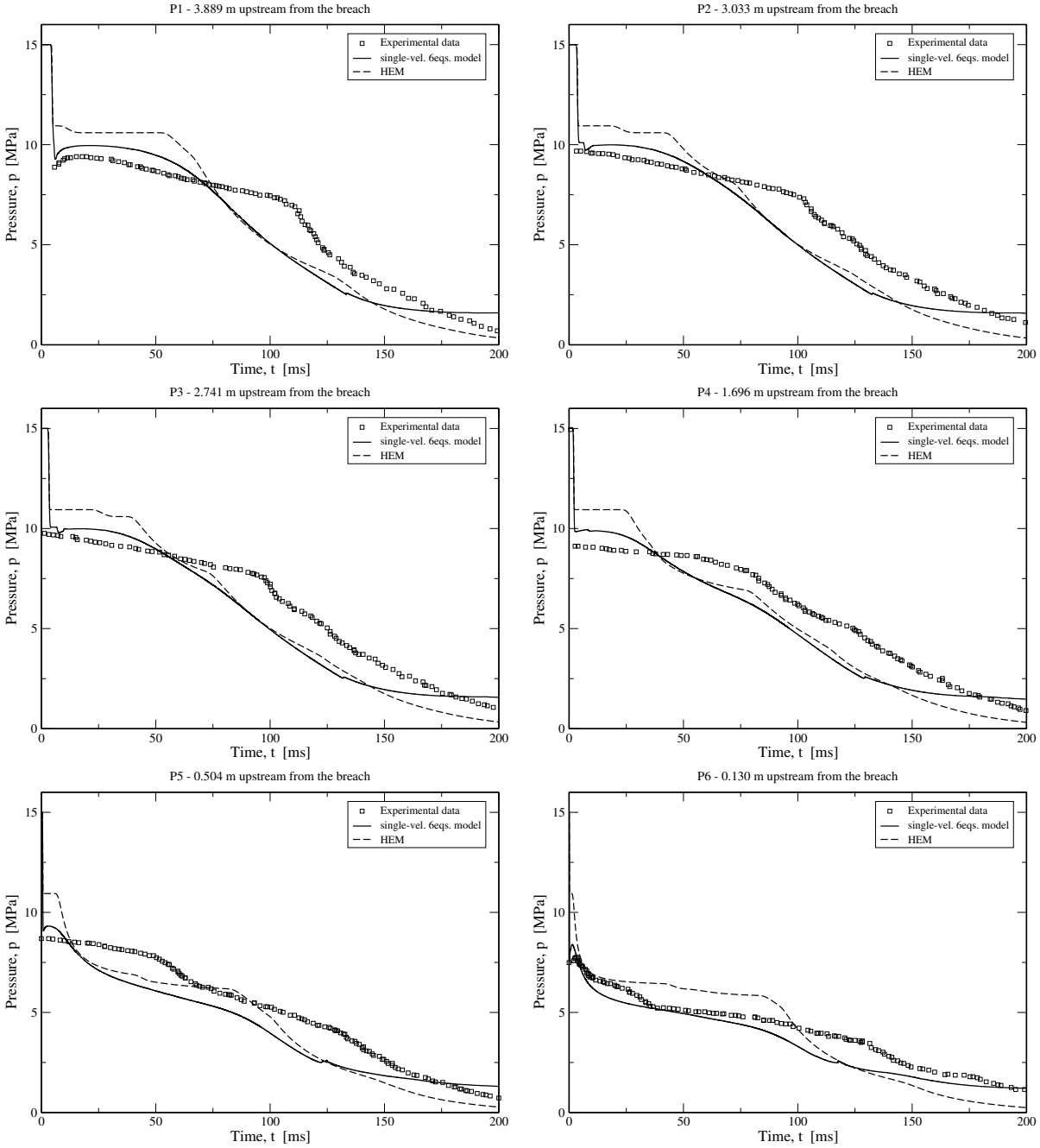

FIGURE 7.8. Assessment of the single-velocity six-equation model on a Super Canon experiment. The initial stagnation conditions are 15 MPa and 593.15 K. For this calculation, the 4.389 m long tube has been discretized into a 1000 cells mesh and $K_g = 0.5$.

nucleation phenomenon.

Considering the whole depressurization Super Canon experiment in Fig. 7.8, after the explosion-like nucleation, the pressure remains constant, but at values lower than the saturation one. Hence the liquid is still in metastable conditions. After 50 ms, the pressure decreases due to the emptying of the capacity. The emptying rate is imposed by the two-phase critical flow that sets at the breach [78].

7.6 Conclusions

In the present work we have developed a single-velocity six-equation model, for phase transition flows, in the EUROPLEXUS code. The industrial objective of this work was to provide EUROPLEXUS code of a hyperbolic model able to deal with thermal and chemical disequilibria to be used for the fluid-structure interaction analysis of hypothetical accidents in nuclear reactors.

This work is the merging of two techniques previously developed by the same authors. The first technique was about the fast and accurate calculation of steam-water properties [79]. The second technique introduced a method for solving the relaxation processes source terms using an EoS-independent numerical procedure [81].

The outcome of this work is a two-phase phase-transition model, based on the recent and more advanced hyperbolic models [64, 200, 233, 283], but improved thanks to the coupling with an accurate EoS. Here the process of equilibrium recovery is decomposed according to the physical disequilibria, then, it is closer to the physics than the more traditional bi-fluid models that are very popular in the nuclear safety field [24, 112, 220, 262].

The new methodology has been validated on experimental data of rapid depressurization tests available in the literature.

Conclusions and perspectives

This thesis focuses on the study of one-component two-phase flows with thermodynamic disequilibrium between the phases. Generally, in two-phase flows, phases can flow at different velocity, pressure, temperature and chemical potential. But, due to its crucial importance on the industrial applications of this thesis, the analysis of the thermodynamic disequilibrium is the focus of this work. Those metastable two-phase flows need to be numerically simulated in order to predict the mechanical behavior of the nuclear reactors components in case of accidental transients.

The purpose of this Ph.D. thesis was to develop modern and time-efficient models for the analysis of metastable two-phase flows, able to take into account the thermodynamic disequilibrium and to accurately calculate the water properties. The global time-efficiency of the numerical methods proposed is required for their use on industrial configurations.

To achieve the final goal of this thesis, a progressive path has been followed. On this path we can recognize three main milestones: the analysis of the stationary flashing metastable flows, the development of new steam-water tables for the transient metastable flows, and the work on the single-velocity six-equation two-phase flow model.

The first work, discussed in Chapter 3, was about the stationary choked metastable two-phase flows. These conditions may establish at the breach of the primary circuit of a PWR in the case of a LOCA. We compared four critical flow models against more than 400 experimental data to determine an appropriate benchmark for their capability to predict critical mass flux and critical pressure. The industrial outcome of this first work was the implementation in EUROPLEXUS of the Henry-Fauske (1971) critical flow model as boundary condition model of a circuit breach.

In the second work, reported in Chapter 4, the attention was drawn on the fast transient metastable two-phase flows as in rapid depressurizations, waterhammers and steam explosions. Based on the recent works of Kunick et al. [133], we developed an algorithm for the calculation of water properties as function of density and specific internal energy, i.e. a look-up table method in the e-v thermodynamic diagram. This algorithm is time-efficient and very accurate and was used to calculate water properties for two classical two-phase flow models in their conservative form. The two-phase flow models used for this work were the Homogeneous Equilibrium Model and the Homogeneous Relaxation Model.

The comparison between the numerical simulations of HEM and HRM and the experimental data was extremely positive and showed the importance of the thermodynamic disequilibrium for the fast depressurizations. The industrial outcome of this second work was the implementation in EUROPLEXUS of new steam-water tables and their coupling with HEM and HRM. A HEM

was already present in EUROPLEXUS, however, the new version is more robust and faster (30-70% in terms of CPU time). The previous version of the HRM was obsolete and did not provide reliable results anymore, while, the new one is accurate and coupled to the steam-water tables aforementioned. In EUROPLEXUS, these models have been named, respectively, *HTPM-EQUI* and *HTPM-META*.

The third work introduces further advancements and is discussed in the whole Part III. It focused on the single-velocity six-equation model for the simulation of transient metastable flows and is composed of three topics: the hyperbolic solver, the relaxation procedures and its industrial application.

For the hyperbolic solver, in Chapter 5, we made a comparison of five numerical schemes with different numerical treatments of the nonconservative terms to determine their influence on smooth and discontinuous solutions. Two out of the five Riemann solvers are a novel contribution of this thesis and are proven to be fast and accurate thanks to an efficiency study.

The relaxation procedures designed for this model are discussed in Chapter 6. The novelty of this work consists in the equation of state independence of the numerical techniques for the simulation of the mechanical and thermodynamic relaxation processes. Further, these new relaxation procedures are non-instantaneous, then, the metastable states can be correctly taken into account. This work represents the core scientific contribution of this Ph.D. thesis.

Finally, in Chapter 7, the main developments done so far have been merged for the simulation of fast depressurizations of initially subcooled water. The domain of the steam-water tables has been extended so to include also the domain of the metastable vapor. Then, the single-velocity six-equation model has been coupled to the new steam-water tables thanks to the EoS-independent relaxation procedures. This method allows a good simulation of the rarefaction waves in metastable liquid water as shown by the comparison with the experimental data.

The single-velocity six-equation model has been implemented in EUROPLEXUS where it is labeled as *HTP6*.

Ultimately, the work done in this Ph.D. thesis is a further step towards the unification of the today *mathematical and numerical modeling state-of-art* of the two-phase flow domain to the *up-to-date thermodynamics for real fluids*. Then, it has been proven to be adequate for the industrial simulation of compressible metastable two-phase flows that may arise in many circumstances.

Industrial perspectives

Most of the work carried out for this thesis is already at the industrial grade, i.e. robust and computationally inexpensive.

The steam-water tables have been tested on more than 5 million points, showing to be robust and accurate. The HEM and the HRM have been tested on many scenarios and proven to be accurate on the whole validity domain of the steam-water tables. The HEM is intrinsically robust because iteration-free, while, the HRM is based on an iterative algorithm that may not converge during

severe transient simulations. Then, for some severe industrial simulations as steam explosions, a feature to be improved is the iterative algorithm for the pressure calculation of the HRM.

Similarly, the robustness of the single-velocity six-equation model can be still improved. The methodology developed is iteration-free and numerically robust, especially when the semi-analytic relaxation procedures are used. However the weakness of the methodology stems in the existence of a validity domain for the pure phase properties. This validity domain is bounded by the liquid and vapor spinodal curves and the $p = 0$ line for the liquid. At low pressures, the metastable domain is very narrow because the $p = 0$ line lies close to the liquid saturation curve, then the liquid phase may cross this line provoking the end of the numerical simulation. To overcome these difficulties, one may extend the liquid metastable domain to the tensile water ($p < 0$), as done in [148], or design a more robust numerical technique for the equilibrium recovery of the liquid phase, forcing the liquid to follow an attractive trajectory to the saturated equilibrium conditions. The drawback of the latter strategy is that the relaxation processes can no longer be decomposed according to physical phenomena as done in Chapter 6 (compression, sensible heat and latent heat) and the equilibrium recovery would just be driven by a mathematical law unable to decouple the different physical phenomena.

Further, a medium-term perspective of this work could be the adjustment of the relaxation techniques to the velocity disequilibrium case and their coupling with the seven-equation model already present in EUROPLEXUS [64, 174]. In that case, no adjustments would be necessary for using the steam-water tables within the seven-equation model.

Academical perspectives

For academical purposes, the main contributions of this thesis stem in the novel relaxation procedures of Chapter 6. They provide new tools for the simulation and the understanding of the phase transition phenomena.

From the small scale point of view, thanks to the decoupling of the physical phenomena effects (compression, sensible heat and latent heat transfers), one can conduct a finer analysis of equilibrium recovery mechanisms. Using these techniques, it could be possible to increment the physical understanding of some phenomena, simulating vapor bubbles cavitation or liquid droplets vaporizations. This analysis of the thermal and chemical disequilibria can be useful to extrapolate new macroscopic correlations, etc. A preliminary step towards this goal has been already done by the *IMSIA*, joint lab EDF-CNRS-ENSTA-CEA. The single-velocity six-equation model together with the steam-water tables have been implemented on the high-order code called *Code_Safari* [69, 100].

From the macroscopic point of view, the novel relaxation procedures allow to study same physical phenomena at different flow pattern regimes. It could be interesting to study the dependency of some phenomena on the topological magnitudes (interfacial area).

Moreover, the mass transfer procedure proposed in Chapter 6 allows to take into account different phase transition models using the same numerical framework. This could be used to conduct a benchmark of the different phase transition models (nucleation models, relaxations models, etc.)

against experimental data.

Another perspective of this work is the simulation of fluids other than water. Together with *Université catholique de Louvain* (*UCL*, Belgium) and *Sherbrooke University* (Canada), we participated to a work on the CO2 properties tabulation for the simulation of challenging two-phase flow phenomena [103] in ejectors. A further advancement could be the use of the single-velocity six-equation model for the analysis of such nonequilibrium flows.

BIBLIOGRAPHY

[1] Abgrall R., Karni S., 2010, A comment on the computation of non-conservative products. J. Comput. Phys., Vol. 229, 2759-63.

[2] Abgrall R., Kumar H., 2014, Numerical approximation of a compressible multiphase system. Commun. Comput. Phys., Vol. 15, 1237-65.

[3] Alamgir M., Lienhard J.H., 1981, Correlation of pressure undershoot during hot water depressurization. J. Heat Transfer, Vol. 103, 52-55.

[4] Alberty R.A., 2001, Use of Legendre transforms in chemical thermodynamics. Pure Appl. Chem., Vol. 73, No. 8, 1349-80.

[5] Allievi L., 1913, Teoria del colpo d'ariete. Atti Collegio Ing. Arch., (English translation by Halmos E.E., 1929, The theory of waterhammer, Trans. ASME).

[6] Ambroso A., Hérard J.-M., Hurisse O., 2009, A method to couple HEM and HRM two-phase flow models. Comput. Fluids, Vol. 38, 738-56.

[7] Amos C.N., Schrock V.E., 1983, Critical discharge of initially subcooled water through slits. Report NUREG/CR-3475.

[8] Apfel R.E., 1972, The tensile strength of liquids. Sci. Amer. Vol. 227, 58-71.

[9] Ardron K.H., 1978, A two-fluid model for critical vapor-liquid flow. Int. J. Multhiphase Flow, 4, 323-337.

[10] Ardron K.A., Ackerman M.C., 1978, Studies of the critical flow of subcooled water in a pipe, CSNI, Paris, France.

[11] Attou A., Bolle L., Seynhaeve J.M., 2000, Experimental study of the critical flashing flow through a relief line: evidence of the double-choked flow phenomenon. Int. J. Multiphase Flow, 26, 921-947.

[12] Baer M.R., Nunziato J.W., 1986, A two-phase mixture theory for the deflagration-to-detonation transition (ddt) in reactive granular materials. Int. J. Multiphase Flow, Vol. 12, 861–89.

[13] Baiti P., LeFloch P.G., Piccoli B., 2001, Uniqueness of Classical and Nonclassical Solutions for Nonlinear Hyperbolic Systems. J. Differential Equations, Vol. 172, 59-82.

[14] Balsara D.S., 2012, Self-adjusting, positivity preserving high order schemes for hydrodynamics and magnetohydrodynamics. J. Comput. Phys., Vol. 231, 7504-17.

[15] Barois, 1969, Etude expérimentale de l'autovaporisation d'un écoulement ascendant adiabatique d'eau dans un canal de section uniforme, PhD thesis, Université Scientifique et Médicale de Grenoble.

[16] Bartak J., 1990, A study of the rapid depressurization of hot water and the dynamics of vapour bubble generation in superheated water. Int. J. Multiphase Flow, Vol. 16, 789-98.

[17] Bartosiewicz Y., Seynhaeve J.M., 2013, Delayed equilibrium model (DEM) of flashing choked flows relevant to LOCA. Multiphase Science & Technology, 25, 117-131.

[18] Bartosiewicz Y., Seynhaeve J.-M., 2014, Delayed Equilibrium Model (DEM) of flashing choked flows relevant to LOCA and implementation in system codes. ICONE22-30957, Prague, Czech Republic.

[19] Babitskiy A.F., 1975, Concerning the discharge of boiling fluids.

[20] Bendiksen K.H. et al., 1991, The dynamic two-fluid model OLGA: Theory and application. SPE

Prod. Eng., 171-80.

[21] Bereux F., Sainsaulieu L., 1997, A roe-type Riemann solver for hyperbolic systems with relaxation based on time-dependent wave decomposition. Numer. Math., Vol. 77, 143-185.

[22] Berry R.A., Zou L., Zhao H., Zhang H., Peterson J.W., Martineau R.C., Kadioglu S.Y., Andrs D., 2016, RELAP-7 Theory Manual, Idaho National Laboratory technical report INL/EXT-14-31366(Revision 2).

[23] Berthoud G., 2000, Heat transfer modeling during a vapor explosion, Nuclear Technology, Vol. 130, 39-58.

[24] Bestion D., 1990, The physical closure laws in the CATHARE code. NED, 124, 229-245.

[25] Bethe H., 1942, The theory of shock waves for an arbitrary equation of state, Clearinghouse for Federal Scientific and Technical Information, Report PB-32189.

[26] Bianchini S., Bressan A., 2005, Vanishing viscosity solutions of nonlinear hyperbolic systems. Ann. of Math., Vol. 161, 223-342.

[27] Bilicki Z., Dafermos C., Kestin J., Majda G., Zeng D.L., 1987, Trajectories and singular points in steady-state models of the two-phase flows. Int. J. Multiphase Flow, 13, 511-533.

[28] Bilicki Z., Kestin J., 1990, Physical aspects of the relaxation model in two-phase flow, Proceedings of the Royal Society A, Math. Phy. Sciences, Vol. 428, 379-97.

[29] Bilicki Z., Kestin J., Pratt M.M., 1990, A reinterpretation of the results of the Moby Dick experiments in terms on the nonequilibrium model, ASME J. Fluids Engineering, 112, 212-17.

[30] Bilicki Z., Kwidzinski R., Mohammadein S.A., 1996, Evaluation of th relaxation time of heat and mass exchange in the liquid-vapour bubble flow. Int. J. Heat and Mass Transfer, Vol. 39, 753-59.

[31] Birkhoff G., Zarantonello E.H., 1957, Jets. Wakes, and Cavities, Academic Press, New York.

[32] Blander M., Katz J.L., 1975, Bubble nucleation in liquids. AIChE Journal Vol. 21, 833-48.

[33] Board S.J., Hall R.W., Hall R.S., 1975, Detonation of Fuel Coolant Explosions, Nature, Vol. 254, 319.

[34] Boivin J.Y., 1979, Two-phase critical flow in long nozzles. Nuclear Technologies, 46, 540-545.

[35] Bouchut F., 2004, Nonlinear stability of finite volume methods for hyperbolic conservation laws and well-balanced schemes for sources. Frontiers in Mathematics, Birkhäuser Verlag.

[36] Bouré J.A., 1973, Dynamique des écoulements diphasique: propagation de petites perturbations. Commissariat à l'Energie Atomique, Report CEA-R-4456.

[37] Bouré J.A., Fritte A.A., Giot M.M., Réocreux M.L., 1976, Highlights of two-phase critical flow: On the links between maximum flow rates, sonic velocities, propagation and transfer phenomena in single and two-phase flows. Int. J. Multiphase Flow, 3, 1-22.

[38] Bourgine et al., 1979, Rapport preliminaire des essais Super Moby Dick. Report TT-621, CEA, Grenoble.

[39] Brennen C.E., 2005, Fundamentals of multiphase flows, Cambridge University Press.

[40] Burnell J.G., 1947, Flow of boiling water, through nozzles orifices and pipes. Engineering, 164, 572-576.

[41] Callen H.B., 1985, Thermodynamics and an Introduction to Thermostatistics. John Wiley & sons.

[42] Canuto C., Tabacco A., 2015, Mathematical Analysis II. Springer International Publishing.

[43] Carey V.P., Liquid-Vapor Phase-Change Phenomena. Francis & Taylor, New York, USA.

[44] Carpenter J.H., Belcourt N., Nourgaliev R., 2013, General Purpose Steam Table Library. Report SAND2013-7328, Sandia National Laboratories, USA.

[45] Castro M.J., LeFloch P.G., Muñoz-Ruiz M.L., Parés C., 2008, Why many theories of shock waves are necessary: convergence error in formally path-consistent schemes. J. Comput. Phys., Vol. 227, 8107-29.

[46] Castro-Diaz M.J., Fernández-Nieto E.D., Morales de Luna T., Narbona-Reina G., Parés C., 2013, A HLLC scheme for nonconservative hyperbolic problems. Application to turbidity currents with sediment transport. ESAIM: Math. Model. Numer. Anal., Vol. 47, 1–32.

[47] Castro-Diaz M.J., Fernandez-Nieto E.D., 2012, A class of computationally fast first order finite volume solvers: PVM methods. SIAM J. Sci. Comput., Vol. 34, A2173-96.

[48] Caupin F., Herbert E., 2006, Cavitation in water: a review. Comptes Rendus Physique 7(9-10): 1000.

[49] Caupin F., Stroock A.D., 2013, The stability limit and other open questions on water at negative pressure. Liquid Polymorphism: Advances in Chemical Physics, ed Stanley HE (Wiley, New York), Vol. 152, 51-80.

[50] Celata G.P., Cumo M., D'Annibale F., Farello G.E., 1988, The influence on non-condensable gas on two-phase critical flow. Int. J. Multiphase Flow, 14, 175-187.

[51] Chalmers N., Lorin E., 2009, Approximation of non-conservative hyperbolic systems based on different shock curve definitions. Canad. Appl. Math. Quart., Vol. 17, 447.

[52] Chalons C., Coquel F., 2016, A new comment on the computation of non conservative products using Roe-type path conservative schemes. Preprint version.

[53] Chang J.S., 1998, Fracture probability and leak before break analysis for the cold neutron source moderator vessel. ASME PVP, San Diego, California.

[54] Chen G., Levermore C., Liu T., 1994, Hyperbolic conservation laws with stiff relaxation terms and entropy. Communications on Pure & Applied Mathematics, Vol. 47, 787-830.

[55] Chiapolino A., Saurel R., Nkonga B., 2017, Sharpening diffuse interfaces with compressible fluids on unstructured meshes. J. Comput. Phys., Vol. 340, 389-417.

[56] Clerc S., 2000, Numerical Simulation of the Homogeneous Equilibrium Model for Two-Phase Flows. J. Comput. Phys. Vol. 161, 354-75.

[57] Colella P., 1982, Glimm's method for gas dynamics. SIAM J. Sci. Stat. Comput., Vol. 3, 76-110.

[58] Collier R.P., Liu J.S., Mayfield M.E., Stuben F.B., 1980, Study of critical two-phase flow through simulated cracks. Report BCL-EPRI-80-1.

[59] Collier J.C., Thome J.R., 1994, Convective boiling and condensation, Oxford University Press.

[60] Colombeau J.F., Le Roux A.Y., 1986, Numerical techniques in elastoplasticity. Proceeding on Nonlinear Hyperbolic Problems, St Etienne eds. Carasso, Raviart, Serre, Lect. Notes in Maths. 1270, Springer-Verlag.

[61] Coquel F., Gallouet T., Hérard J.-M., Seguin N., 2002, Closure laws for a two-fluid two-pressure model. C. R. Math. Acad. Sci. Paris, Vol. 334, 927-32.

[62] Cordier F., Degond P., Kumbaro A., 2014, Phase appearance or disappearance in two-phase flows. Journal of Scientific Computing.

[63] Cowperthwaite M., 1969, Relationships between Incomplete Equations of State, J. Franklin Institute, Vol. 285, 379-87.

[64] Crouzet F., Daude F., Galon P., Hérard J.-M., Hurisse O., Liu Y., 2015, Validation of a two-fluid model on unsteady liquid–vapor water flows. Computers & Fluids, Vol. 119, 131-42.

[65] D'Arcy D.F., 1971, On acoustic wave propagation and critical mass flux in two-phase flow. J. Heat Transfer 93 No. 4, 413-421.

[66] D'Auria F., Vigni P., 1980, Two-phase critical flow models. Comitato nazionale per l'energia nucleare, No. 49, Rome, Italy.

[67] Dagan R., Elias E., Wacholder E., Olek S., 1993, A two-fluid model for critical flashing flows in pipes. Int. J. Multhiphase Flow, 19, 15-25.

[68] Dal Maso G., LeFloch P.G., Murat F., 1995, Definition and weak stability of nonconservative products. J. Math. Pures Appl., Vol. 74, 483-548.

[69] Daude F., Berland J., Emmert T., Lafon Ph., Crouzet F., Bailly C., 2012, A high-order finite-difference algorithm for direct computation of aerodynamic sound. Comput. Fluids, Vol. 61,

46-63.

[70] Daude F., Galon P., Gao Z., Blaud E., 2014, Numerical experiments using a HLLC-type scheme with ALE formulation for compressible two-phase flows five-equation models with phase transition. Comput. Fluids, Vol. 94, 112-38.

[71] Daude F., Galon P., 2016, On the computation of the Baer-Nunziato model using ALE formulation with HLL- and HLLC-type solvers towards fluid-structure interactions. J. Comput. Phys., Vol. 304, 189-230.

[72] Davis S.F., 1988, Simplified second-order Godunov-type methods. SIAM J. Sci. Stat. Comput., Vol. 9, 445-73.

[73] Debenedetti P.G., 1996, Metastable Liquids: Concepts and Principles. Princeton University Press, Princeton, NJ.

[74] Delchini M.O., Ragusa J.C., Berry R.A., 2016, Viscous regularization for the non-equilibrium seven-equation two-phase flow model. J. Sci. Comput., Vol. 69, 764-804.

[75] Delchini M.O., Ragusa J.C., Berry R.A., 2017, Simulations of single- and two-phase shock tubes and gravity-driven wave problems with the RELAP-7 nuclear reactor system analysis code. Nucl. Engng. Des., Vol. 319, 106-16.

[76] Delhaye J.M., Boure J.A., 1982, General equations and two-phase flow modeling. In: Handbook of multiphase systems, Hemisphere Publishing Corp., New-York, USA.

[77] De Lorenzo M., Lafon Ph., Bartosiewicz Y., Seynhaeve J.-M., 2016, Physical and Numerical Investigations for the Development of a New Experimental Facility for Studying Blowdown Phenomena, Proc. ICONE24, Charlotte, North Carolina.

[78] De Lorenzo M., Lafon Ph., Seynhaeve J.-M., Bartosiewicz Y., 2017, Benchmark of Delayed Equilibrium Model (DEM) and Classic Two-Phase Critical Flow Models against Experimental Data. Int. J. Multiphase Flow, Vol. 92, 112-30.

[79] De Lorenzo M., Lafon Ph., Di Matteo M., Pelanti M., Seynhaeve J.-M., Bartosiewicz Y., 2017, Homogeneous Two-Phase Flow Models and Accurate Steam-Water Table Look-up Method for Fast Transient Simulations. Int. J. Multiphase Flow, Vol. 95, 199-219.

[80] De Lorenzo M., Pelanti M., Lafon Ph., 2018, HLLC-type and path-conservative schemes for a single-velocity six-equation two-phase flow model: a comparative study. Applied Mathematics and Computation, Vol. 333C, 95-117.

[81] De Lorenzo M., Lafon Ph., Pelanti M., 2018, A hyperbolic phase-transition model with non-instantaneous EoS-independent relaxation procedures. Submitted to J. Comput. Phys.

[82] De Vuyst F., Ghidaglia J.-M., Le Coq G., 2005, On the numerical simulation of multiphase water flows with changes of phase and strong gradients using the Homogeneous Equilibrium Model. Int. J. Finite Volume, Vol. 2.

[83] Di Matteo M., 2014, Overview of Equations of State for real gases and their application. Thesis, Politecnico di Torino, Turin (in Italian).

[84] Downar-Zapolski P., Bilicki Z., Bolle L., Franco J., 1996, The non-equilibrium relaxation model for one-dimensional flashing liquid flow. Int. J. Multiphase Flow, 22, 473-83.

[85] Drew D., Cheng L., LaHey R. T., 1979, The analysis of virtual mass effects in two-phase flow. Int. J. Multiphase Flow.

[86] Drew D.A., 1983, Mathematical modeling of two-phase flow. Ann. Rev. Fluid. Mech., Vol. 15, 261-91.

[87] Drew D.A., Segel L.A., 1971, Averaged equations for two-phase flows. Stud. appl. Math., Vol. 1, 205-31.

[88] Dumbser M., Balsara D.S., 2016, A new efficient formulation of the HLLEM Riemann solver for general conservative and non-conservative hyperbolic systems. J. Comput. Phys., Vol. 304, 275-319.

[89] Dumbser M., Castro M., Parés C., Toro E.F., 2009, ADER schemes on unstructured meshes for

non-conservative hyperbolic systems: applications to geophysical flows. Comput. Fluids 38, Vol. 94, 1731-48.

[90] Dumbser M., Toro E.F., 2011, A Simple Extension of the Osher Riemann Solver to Non-conservative Hyperbolic Systems. J. Sci. Comput., Vol. 48, 70-88.

[91] Dumbser M., Toro E.F., 2011, On universal Osher-type schemes for general nonlinear hyperbolic conservation laws. Commun. Comput. Phys., Vol. 10, 635-71.

[92] Duponcheel M., Seynhaeve J.-M., Bartosiewicz Y., 2013, Implementation and validation of the DEM model in NEPTUNE_CFD and its application to the simulation of double-choked flows. NURESAFE, report D31.22.12a-b.

[93] Eberhart J.G., 2009, A New Four-Parameter Equation of State and Its Application in Predicting the Spinodal Temperature of Water. Water Journal, Vol. 1, 85-91.

[94] Edwards A.R., O'Brien T.P., 1970, Studies of Phenomena Connected with the Depressurization of Water Reactors. J. British Nuclear Society, Vol. 9, 125-35.

[95] Einfeldt B., 1988, On Godunov-type methods for gas dynamics. SIAM J. Numer. Anal., Vol. 25, 294-318.

[96] Elias E., Chambré P.L., 1993, Flashing inception in water during rapid decompression. ASME J. Heat Transfer, 115, 231-238.

[97] Elias E., Chambré P.L., 2000, Bubble transport in flashing flow. Int. J. Multhiphase Flow, 26, 191-206.

[98] Elias E., Lellouche G.S., 1994, Two-Phase Critical Flow. Int. J. Multiphase Flow, 20, 91-168.

[99] El Mekki-Azouzi M., 2010, Étude éxpérimentale de l'eau et de solutions aqueuses mètastables. PhD thesis, Université d'Orléans, France.

[100] Emmert T., Lafon Ph., Bailly C., 2009, Numerical study of self-induced transonic flow oscillations behind a sudden duct enlargement. Physics of Fluids, Vol. 21, 106105.

[101] EUROPLEXUS user manual: http://europlexus.jrc.ec.europa.eu/public/manual_html/index.html.

[102] Evans N.A., Mitchell D.E., Nelson L.S., Corradini M.L., 1982, Recent results form the SANDIA steam explosion program, SAND82-2269C.

[103] Fang Y., De Lorenzo M., Lafon Ph., Poncet S., Bartosiewicz Y., 2018, An Accurate and Efficient Look-up Table Equation of State for Two-phase Compressible Flow Simulations of Carbon Dioxide. Submitted to Industrial & Engineering Chemistry Research.

[104] Faucher E., Hérard J.M., Barret M., Toulemonde C., 2000, Computation of flashing flows in variable cross section ducts. Int. J. of Comp. Fluid Dynamics, Vol. 13, 365-91.

[105] Faucher V., Crouzet F., Debaud F., 2014, Mechanical consequences of LOCA in PWR: Full scale coupled 1D/3Dsimulations with fluid–structure interaction. Nucl. Engng. Des., Vol. 270, 359-78.

[106] Fauske H.K., 1962, Contribution to the theory two phase one component critical flow. ANL6633.

[107] Feburie V., Giot J.M., Granger S., Seynhaeve J.M., 1993, A model for choked flow through cracks with inlet subcooling. Int. J. Multiphase Flow, 19, 541-562.

[108] Fehlberg E., 1969, Low-order classical Runge-Kutta formulas with step size control and their application to some heat transfer problems. NASA Technical Report 315.

[109] Flåtten T., Lund H., 2012, Relaxation two-phase flow models and the subcharacteristic conditions. Math. Models Methods Appl. Sci., Vol. 21, 2374-2407.

[110] Flinta J., 1984, Calculation equation which gives the critical flow in an explicit form for reactor safety analysis. European Two-Phase Flow Group Meeting, Rome, Italy.

[111] Fraser D.W.H., Abdelmessih A.H., 2002, A study of the effects of the location of flashing inception on maximum and minimum critical two-phase flow rates: Part II: analysis and modelling. NED, 213, 11-30.

[112] Gale J., Tiselj I., Horvat A., 2008, Two-fluid model of the WAHA code for simulations of water

hammer transients. Multiphase Science and Technology, Vol. 20, 291-322.

[113] Germain P., Lee E.H., 1973, On shock waves in elastic-plastic solids. J. Mech. Phys. Solids, Vol. 21, 359-82.

[114] Ghiaasiaan S.M., 2007,Two-Phase Flow, Boiling, and Condensation: In Conventional and Miniature Systems. Cambridge University Press.

[115] Gidaspow D., Li'czkowski R.W., Solbrig C.W., Hughes E.D., Mortensen G.A., Amer. Nuclear Sot. Trans., Vol. 17, 249.

[116] Godlewski E., Raviart P.-A., 1996, Numerical Approximation of Hyperbolic Systems of Conservation Laws. Springer-Verlag, New York.

[117] Goncalvès E., Patella R.F., Constraints on equation of state for cavitating flows with thermodynamic effects. Appl. Math. Comput., Vol. 217, 5095-102.

[118] Gouse S.W., Brown G.A., 1964, A survey of the velocity of sound in two-phase mixtures. ASME Paper 64-WA/FE-35.

[119] Guillemaud V., 2007, Modélisation et simulation des écoulements diphasique par une approche bifluide à deux pressions. PhD thesis, Université de Provence - Aix Marseille I.

[120] Ha C.-T., Park W.-G., Jung C.-M., 2015, Numerical simulations of compressible flows using multi-fluid models. Int. J. of Multiphase Flow, Vol. 74, 5-18.

[121] Haar L., Gallagher J.S., Kell G.S., 1984, NBS/NRC Steam Tables. Hemisphere, Washington, DC.

[122] Hadamard J., 1923, Lectures on Cauchy's Problem in Linear Partial Differential Equations. Yale Univ. Press, New Haven, Conn.

[123] Hardy Ph., Mali P., 1983, Validation and development of a model describing subcooled critical flow through long tubes. Energie Primarie, 18, 5-23.

[124] Henry R.E., 1968, A Study of One-and-Two Component, Two-Phase Critical Flows at Low Qualities, ANL-7430.

[125] Henry R.E., Fauske H.K., 1971, The Two-Phase Critical Flow of One-Component Mixtures in Nozzles, Orifices, and Short Tubes. J. Heat Transfer, 93, 179-187

[126] Hou T.Y., LeFloch P.G., 1994, Why nonconservative schemes converge to wrong solutions: error analysis. Math. Comput., Vol. 62, 497-530.

[127] Huhtiniemi I., Magallon D., Hohmann H., 1999, Results of recent KROTOS FCI tests: alumina versus corium melts. Nucl. Engng. Des., Vol. 189, 379-89.

[128] Hughes T.J.R., 2000, The Finite Element Method, Dover Publications.

[129] Hurisse O., 2017, Numerical simulations of steady and unsteady two-phase flows using a homogeneous model. Comput. Fluids , Vol. 152, 88-103.

[130] Ilic V. et al., 1986, A qualified data base for critical flow of water. Report 4556 EPRI.

[131] Imre A., Martinas K., Rebelo L.P.N., 1998, Thermodynamics of negative pressures in liquids. J. Non-Equilib. Thermodyn., Vol. 23, 351-75.

[132] Imre A.L. et al., 2013, Estimation of the Thermodynamic Limit of Overheating for Bulk Water from Interfacial Properties. Int. J. of Thermophysics, Vol. 34, 2053-64.

[133] International Association for the Properties of Water and Steam, 2015, Guideline on the Fast Calculation of Steam and Water Properties with the Spline-Based Table Look-Up Method (SBTL).

[134] International Association for the Properties of Water and Steam, 2007, Revised Release on the IAPWS Industrial Formulation 1997 for the Thermodynamic Properties of Water and Steam, Lucerne, Switzerland.

[135] International Formulation Committee of the 6th International Conference on the Properties of Steam, 1967, The 1967 Formulation for Industrial Use, Verein Deutscher Ingenieure, Dusseldorf.

[136] Ishii M., 1975, Thermo Fluid Dynamic Theory of Two Phase-Flow. Eyrolles, Paris, France.

[137] Ishii M., Hibiki T., 2011, Thermo-Fluid Dynamics of Two-Phase Flow. Springer.

[138] Kanno H., Speedy R.J., et al., 1975, Supercooling of water to -92^{o}C under pressure. Science 189: 880-881.

[139] Kapila A.K., Menikoff R., Bdzil J.B., Son S.F., Stewart D.S., 2001, Two-phase modeling of deflagration-to-detonation transition in granular materials: reduced equations. Phys Fluids, Vol. 13, 3002–25.

[140] Karplus H.B, 1958,The velocity of sound in a liquid containing gas bubbles. Illinois Inst. Tech. Rep. COO-248.

[141] Kieffer S.W., 1977, Sound speed in liquid-gas mixtures: water-air and water-steam. J. Geophys. Res., Vol. 82, 2895-2904.

[142] Kim S.-M., Mudawar I., 2015, Review of two-phase critical flow models and investigation of the relationship between choking, premature CHF, and CHF in micro-channel heat sinks. Int. J. Heat and Mass Transfer, 87, 497-511.

[143] Kiselev S.B., Ely J.F., 2001, Curvature effect on the physical boundary of metastable states in liquids. Physica A, 299, 357-370.

[144] Kolev N.I., 1986, Transiente Zweiphasenstromung. Springer, Berlin.

[145] Kolev N.I., 2005, Multiphase flow dynamics I-II-III. Springer, Berlin.

[146] Kreeft J.J., Koren B., 2010, A new formulation of Kapila's five-equation model for compressible two-fluid flow, and its numerical treatment. J. Comput. Phys., Vol. 229, 6220-42.

[147] Kunick M. et al., 2015, CFD Analysis of steam turbines with the IAPWS standard on the Spline-Based Table Look-Up Method (SBTL) for the fast calculation of real fluid properties. Turbine Technical Conference and Exposition: Proceedings of ASME Turbo Expo 2015.

[148] Kunick M., Berry R.A., Martineau R.C., Kretzschmar H.-J., Gampe U., 2017, Application of the new IAPWS Guideline on the fast and accurate calculation of steam and water properties with the Spline-Based Table Look-Up Method (SBTL) in RELAP-7. Kerntechnik, Vol. 82, 1-16.

[149] Jeandey C., Gros D'Aillon L., Bourgine R., Barriere G., 1981, Auto vaporisation d'écoulements eau/vapeur. Report TT-163, CEA, Grenoble.

[150] Jeandey C., Gros D'Aillon L., 1983, Débit critique en tuyere courte, Super Moby Dick. Report TT-71, CEA, Grenoble.

[151] Jin J.S., Xin Z.P., 1995, The relaxation schemes for systems of conservation laws in arbitrary space dimensions. Comm. Pure Appl. Math. Vol. 48, 235-276, 1995.

[152] John H., Reimann J., Westphal F., Friedel L., 1988, Critical two-phase flow through rough slits. Int. J. Multhiphase Flow, 14, 155-174.

[153] Johnsen E., Colonius T., 2006, Implementation of WENO schemes in compressible multicomponent flow problems. J. Comput. Phys., Vol. 219, 715-32.

[154] Jou D., Casas-Vázquez J., Lebon G., 1988, Extended irreversible thermodynamics. Rep. Prog. Phys., 51, 1105-79.

[155] Labois M., 2008, Modélisation des désequilibres mécaniques pour les écoulements diphasiques: approches par relaxation et par modèle réduit. PhD thesis, Université de Provence.

[156] Labourdette C., Ghidaglia J.-M., Redford J.A., Faure S., 2017,Accurate state variables for fluid flow simulation using Quicksteam and Quickmethane. European Journal of Mechanics - B/Fluids , Vol. 65, 132-40.

[157] Lackmé C., 1979, Autovaporisation dans une conduite d'un liquide saturé ou sous-refroidi a l'entrée. Report R-4957, CEA, Grenoble.

[158] Lackmé C., 1979, Incompleteness of the flashing of a supersaturated liquid and sonic ejection of the produced phases. Int. J. Multhiphase Flow, 5, 131-141.

[159] Lackmé C., 1981, Cinetique de la vaporisation de l'eau chaude qui se détand dans un tube. Report CEA-R-5108, CEA, Grenoble.

[160] Lafon P., Essadki M. Bartosiewicz Y., Seynhaeve J.-M., 2015, Assessment of two phase critical flow models and implementation in fast transient flow dynamics software. Proc. of the ASME, PVP2015, Boston, USA

[161] Larsen M. et al., 1997, PeTra: a novel computer code for simulation of slug flow. Paper 3884 1, SPE Annual Technical Conference and Exhibition, San Antonio, Texas.

[162] Le Floch P.G., 1989, Shock Waves for Nonlinear Hyperbolic Systems in Nonconservative Form. IMA series, University of Minnesota, USA.

[163] Le Floch P.G., 1993, Propagating phase boundaries. Formulation of the problem and existence via the Glimm method. Arch. Rational Mech. Anal., Vol. 123, 153-97.

[164] Le Metayer O., Massoni J., Saurel R., 2004, Elaborating equations of state of a liquid and its vapor for two-phase flow models. Int. J. Thermal Sciences, Vol. 43, 265-76.

[165] Lemonnier H., 2002, An Attempt to Apply the Homogeneous Relaxation Model to the Wahaloads Benchmark Tests with Interaction with the Mechanical Structure. CEA-T3.3-D61-200302, WAHALoads project deliverable D61.

[166] Lepareux M., 1994, Materiau EAU, Report DMT 94/398, CEA Saclay, France.

[167] Lepareux M., 1997, Programme-Plexus, les modèls de débit critique. Report CEA-DMT-97/029, CEA, Saclay.

[168] LeVeque R., 2002, Finite Volume Methods for Hyperbolic Problems. Cambridge University Press, UK.

[169] LeVeque R.J., Pelanti M., 2001, A class of approximate Riemann solvers and their relation to relaxation schemes. J. Comput. Phys., Vol. 172, 572-591.

[170] Lienhard J.H., Shamsundar N., Biney P.O., 1986, Spinodal lines and equations of state - a review. Nucl. Engng. Des., Vol. 95, 297-313.

[171] Linga G., 2015, A Hierarchy of Non-Equilibrium Two-Phase Flow Models. Not published. See: https://www.researchgate.net/publication/273950348.

[172] Liu T.-P., 1987, Hyperbolic conservation laws with relaxation. Commun. Math. Phys., Vol. 108, 153-75.

[173] Lochon H., Daude F., Galon P., Hérard J.M., 2016, Comparison of two-fluid models on steam-water transients. ESAIM, Vol. 50, 1631-57.

[174] Lochon H., 2016, Modélisation et simulation d'écoulements transitoires eau-vapeur. PhD thesis, Aix-Marseille.

[175] Lochon H., Daude F., Galon P., Hérard J.M., 2018, Computation of fast depressurization of water using a two-fluid model: revisiting Bilicki modelling of mass transfer. Computers & Fluids, Vol. 156, 162-74.

[176] Lund H., 2012, A hierarchy of relaxation models for two-phase flow. SIAM J. Appl. Math., Vol. 72, 1713-41.

[177] Lund H., Aursand P., 2012, Two-Phase Flow of CO2 with Phase Transfer. Energy Procedia, Vol. 23, 246-55

[178] Martínez Ferrer P.J., Flåtten T., Munkejord S.T., 2012, On the effect of temperature and velocity relaxation in two-phase flow models. ESAIM: Math. Model. Numer. Anal., Vol. 46 , 411-42.

[179] Maxwell J.C., 1875, On the dynamical evidence of the molecular constitution of bodies. Nature, Vol. 11, 357-59.

[180] McFadden J. H. et al., 1984, RETRAN-02 - A Program for Transient Thermal-Hydraulic Analysis of Complex Fluid Flow Systems, Vol. 1. Electric Power Research Institute.

[181] Menikoff R., Plohr B.J., 1989, The Riemann problem for fluid flow of real materials. Rev. Mod. Phys., Vol. 61, 75-130.

[182] Meslin P.Y. et al., 2006, Evidence of 210Po on martian dust at meridiani planum. J. Geophys. Res. 111, art. E09012.

[183] Milliken R.E. et al., 2007, Hydratation state of the Martian surface as seen by Mars Express OMEGA: 2H2O content of surface. J. Geophys. Res. 112, art. E08507.

[184] Moody F.J., 1965, Maximum flow-rate of a single component two-phase mixture. J. Heat Transfer, 87, 134-141.

[185] Moody F.J., 1969, A pressure pulse model for two-phase critical flow and sonic velocity. J. Heat Transfer, 91, 371-381.

[186] Moody F.J., 1975, Maximum discharge rate of liquid-vapor mixtures from vessels, Non equilibrium two-phase flows. Ed. Lahey-Wallis, ASME.

[187] Murrone A., Guillard H., 2005, A five equation reduced model for compressible two phase flow problems. J. Comput. Phys., Vol. 202, 664-98.

[188] Nakagawa M., Harada A., Berana M.S., 2009, Analysis of expansion waves appearing in the outlets of two-phase flow nozzles, HVAC&R Res., Vol. 15, 1065-79.

[189] Natalini R., 1999, Recent mathematical results on hyperbolic relaxation problems, in Chapman & Hall/CRC Monogr. Surv. Pure Appl. Math., Vol. 99, Chapman & Hall/CRC, Boca Raton, FL, 128-98.

[190] Nunziato J.W., Walsh E.K., 1980, On ideal multiphase mixtures with chemical reactions and diffusion. Archs Rational Mech. Analysis, Vol. 73, 285-311.

[191] Ogasawara H., 1969, A theoretical approach to two-phase critical flow. Bull. JSME.

[192] Pana P., 1976, Berechnung der station/iren Massenstromdichte von Wasserdampfgemischen und der auftretenden RfickstoBkr/ifte. Report IRS-W-24.

[193] Parés C., 2006, Numerical methods for nonconservative hyperbolic systems: a theoretical framework. SIAM J. Numer. Anal., Vol. 44, 300-21.

[194] Park C.K, Park J.W., Chung M.K., Chung M.H., 1977, An Empirical Correlation for Critical Flow Rates of Subcooled Water Through Short Pipes with Small Diameters. J. of the Korean Nuclear Society, 29, 35-44.

[195] Park H.-S. et al., 2007, Experimental study on a two-phase critical flow with a non-condensable gas at high pressure conditions. Int. J. Multiphase Flow, 33, 1222-1236.

[196] Passman S.L., 1977, Mixtures of granular materials. Int. J. Engng Sci, Vol. 15, 117-29.

[197] Passman S.L., Nunziato J.W., Walsh E.K., 1984, A theory of multiphase mixtures. In Rational Thermodynamics, 286-325, McGraw-Hill, New York.

[198] Patankar S.V., 1980, Numerical heat transfer and fluid flow. Comput. Fluids, London, Taylor & Francis.

[199] Peano, G., 1890, Demonstration de l'intégrabilité des équations différentielles ordinaires. Mathematische Annalen., Vol. 37, 182-228.

[200] Pelanti M., Shyue K.-M., 2014, A mixture-energy-consistent six-equation two-phase numerical model for fluids with interfaces, cavitation and evaporation waves. J. Comput. Phys., Vol. 259, 331-57.

[201] Pelanti M., Shyue K.-M., 2014, A mixture-energy-consistent numerical approximation of a two-phase flow model for fluids with interfaces and cavitation. In: Hyperbolic Problems: Theory, Numerics, Applications, Proceedings of the Fourteenth International Conference on Hyperbolic Problems, 839-46, F. Ancona, A. Bressan, P. Marcati, and A. Marson Eds., AIMS.

[202] Pelanti M., 2017, Low Mach number preconditioning techniques for Roe-type and HLLC-type methods for a two-phase compressible flow model. Appl. Math. Comput., Vol. 310, 112-33.

[203] Pérez Manes J. et al., 2014, Validation of NEPTUNE-CFD Two-Phase Flow Models Using Experimental Data, Hindawi Publishing Corporation, Science and Technology of Nuclear Installations, Article ID 185950, 19 pages.

[204] Petitpas F., Franquet E., Saurel R., Le Metayer O., 2007, A relaxation-projection method for compressible flows. Part II: Artificial heat exchanges for multiphase shocks. Journal of Computational Physics, 225, 2214-48.

[205] Petitpas F., Saurel R., Franquet E., A. Chinnayya, 2009, Modelling detonation waves in condensed energetic materials: Multiphase CJ conditions and multidimensional computations. Shock Waves, 19, 377-401.

[206] Pettenati M., Mercury L., Azaroual M., 2008, Capillary geochemistry in non-saturated zone of soils. Water content and geochemical signatures. Applied Geochem. 23, 3799-3818.

[207] Pinhasi G.A., Ullmann A., Dayan A., 2005, Modeling of flashing two-phase flow. Reviews in Chemical Eng., 21, 133-264.

[208] Plesset M.S., Zwick S.A., 1954, The growth of vapor bubbles in superheated liquids. J. Appl. Phys., Vol. 25, 493-500.

[209] Pokharna H., Mori M., Ransom V.H., 1997, Regularization of Two-Phase Flow Models: A Comparison of Numerical and Differential Approaches. J. Comput. Phys., Vol. 134, 282-95.

[210] Poole P.H., Sciortino F., Essmann U., Stanley H.E., 1992, Phase behaviour of metastable water. Nature 360, 324-28.

[211] Porsching T.A., 1977, A finite difference method for thermally expandable fluid transients. Nucl. Sci. Eng. Vol. 64, 177.

[212] Press W.H., Teukolsy S.A., Vetterling W.T., Flannery B.P., 1997, Numerical Recipes. Cambridge University Press, USA.

[213] Prosperetti A., Tryggvason, 2009, Computational methods dor multiphase flow. Cambridge University Press, UK.

[214] Prosperetti A., Plesset M.S., 1978, Vapour-bubble growth in a superheated liquid. J. Fluid Mech., Vol. 85, 349-368.

[215] Ramboz C., Danis M., 1990, Superheating in the Red Sea? The heat-mass balance of the Atlantis II Deep revisited. Earth Planet. Sci. Lett., Vol. 97, 190-210.

[216] Ransom V.H., Trapp J.A, 1978, Relap5 progress summary analytical choking criterion for two-phase flow. Idaho Report CDAP-TR-013.

[217] Ransom V.H., Hicks D.L., 1984, Hyperbolic two-pressure models for two-phase flow. Journal of Computational Physics, Vol. 53, 124-151.

[218] Rascle P., Morvant O., 1994, Spécifications fonctionnelles de THETIS: Calcul par interpolation des fonctions thermodynamiques de fluides diphasiques. Electricité de France, Rapport HT-13/94/014 B, 150 pages (in French).

[219] Raviart P.A., Sainsaulieu L., 1995, A nonconservative hyperbolic system modeling spray dynamics. I. Solution of the Riemann problem. Math. Models Methods Appl. Sci., Vol. 5, 297-333.

[220] RELAP5/MOD3.3, 2001, code manual, Vol. I. Idaho Falls, USA

[221] RELAP-7 Progress Report: FY-2015 Optimization Activities Summary. Report INL/EXT-15-36771, Idaho Falls, USA.

[222] Rhebergen S., Bokhov O.e, van der Vegt J.J.W., 2009, Discontinuous Galerkin finite element method for shallow two-phase flows. Comput. Methods in Appl. Mech. Eng., Vol. 198, 819-30.

[223] Riegel B., 1978, Contribution à l'étude de la décompression d'une capacité en régime diphasique. PhD thesis, Institut National Polytechnique de Grenoble.

[224] Robbe M.F., Lepareux M., 1996, Programme PLEXUS, matériau EAU, modèle homogène non equilibré. Rapport DMT 96/142, CEA Saclay, France.

[225] Roth G.A., Aydogan F., 2014, Theory and implementation of nuclear safety system codes - part I: Conservation equations, flow regimes, numerics and significant assumptions. Progress in Nuclear Energy, 76, 160-82.

[226] Reocreux M., 1974, Contribution à l'étude des débits critiques en écoulement diphasique eau-vapeur. PhD thesis, Université Scientifique et Médicale de Grenoble.

[227] Romstedt P., Werner W., 1986, Numerical analysis of critical two-phase flow in a convergent-divergent nozzle. NED, 92, 71-83.

[228] Ruas V., 2016, Numerical Methods for Partial Differential Equations: An Introduction. Wiley, New York.

[229] Sainsaulieu L., 1995, Finite Volume Approximation of Two Phase-Fluid Flows Based on an Approximate Roe-Type Riemann Solver. J. Comput. Phys. Vol. 121, 1-28.

[230] Sánchez-Linares C., Morales de Luna T., Castro Diaz M.J., 2016, A HLLC scheme for Ripa model. Appl. Math. Comput., Vol. 272, 369-84.

[231] Saurel R., Abgrall R., 1999, A Multiphase Godunov Method for Compressible Multifluid and Multiphase Flows. J. Comput. Phys. Vol. 150, 425-67.

[232] Saurel R., Le Metayer O., Massoni J., Gavrilyuk S., 2007, Shock jump relations for multiphase mixtures with stiff mechanical relaxation. Shock Waves, Vol. 16, 209-32.

[233] Saurel R., Petitpas F., Abgrall R., 2008, Modelling phase transition in metastable liquids. Application to cavitating and flashing flows. J. Fluid Mech., Vol. 607, 313-50.

[234] Saurel R., Petitpas F., Berry R.A., 2009, Simple and efficient relaxation methods for interfaces separating compressible fluids, cavitating flows and shocks in multiphase mixture. J. Comput. Phys., Vol. 228, 1678-1712.

[235] Saurel R., Fraysse F., Furfaro D., Lapedie E., 2017, Multiscale multiphase modeling of detonations in condensed energetic materials. Computers and Fluids, Vol. 159, 95-111

[236] Schoch S., Nikiforakis N., Lee B., Saurel R., 2013, Multi-phase simulation of ammonium nitrate emulsion detonations. Combustion and Flame, 160, 1883-99.

[237] Schrock V.E., Amos C.N., 1984, Two-phase critical flow, in Two-Phase Flow and Heat Transfer, China US Progress, Hemisphere, Washington, USA.

[238] Schrock V.E., Starkman E.S., Brown R.A., 1977, Flashing flow of initially subcooled water in convergent-divergent nozzles. J. Heat Transfer, 99, 263.

[239] Schwartz L., 1954, Sur l'impossibilité de la multiplication des distributions. C. R. Acad. Sci. Paris, Vol. 239, 847-48.

[240] Seynhaeve J.-M., 1980, Etude experimèntale des écoulements diphasiques critiques a faible titre. PhD thesis, Université Catholique de Louvain.

[241] Seynhaeve J.-M., De Crécy A., Bartosiewicz Y., 2015, Uncertainty Analysis of Delayed Equilibrium Model (DEM) using the CIRCE Methodology. NURETH16, Chicago, USA.

[242] Shapiro A., 1954, The Dynamics and Thermodynamics of Compressible Fluid Flow. McGraw-Hill, New York, USA.

[243] Shmulovich K.I. and Graham C.M. (2004). An experimental study of phase equilibria in the systems H2O-CO2-CaCl2 and H2O-CO2-NaCl at high pressures and temperatures (500-800^{o}C, 0.5-0.9 GPa): geological and geophysical applications. Contr. Mineral. Petrol., Vol. 146, 450-62.

[244] Simpson A.R., 1989, Large Water-Hammer Pressures for Column Separation in Pipelines. J. Hydraul. Eng., Vol. 117, 1310-16.

[245] Skripov V.P., 1972, Metastable Liquids. Wiley, New York.

[246] Skripov V.P., Sinicyn P.A. et al., 1980, Teplofizicheskyie Svoyistva Zhidkostey v Metastabil'nom Sostoyanyii. Atomizdat, Moskva.

[247] Smith L.L. et al, 1980, SIMMER-II: a computer program for LMFBR disrupted core analysis. Technical report LA-7515-M, NUREG/CR-0453, Rev. 1, Los Alamos National Laboratory.

[248] Stadtke H., 2006, Gasdynamic aspects of the two-phase flow, Wiley-VCH Verlag GmbH & CO. KGaA, Weinheim, Germany.

[249] Sokolowski L., Kozlowsk T., 2012, Assessment of Two-Phase Critical Flow Models Performance in RELAP5 and TRACE Against Marviken Critical Flow Tests. NUREG/IA-0401.

[250] Sozzi G.L., Sutherland W.A., 1975, Critical flow of saturated and subcooled water at high pressure. Report NEDO-13418, General Electric Company, San Jose, USA.

[251] Span R., Wagner W., 1996, A New Equation of State for Carbon Dioxide Covering the Fluid

Region from the Triple-Point Temperature to 1100 K at Pressures up to 800 MPa. J. Phys. Chem. Ref. Data 1996, 25, 1509-96.

[252] Spore J.W. et al., 2001, TRAC-M/FORTRAN 90 Theory Manual. Los Alamos National Laboratory, Los Alamos, NM. NUREG/CR-6724.

[253] Starkman E.S., Schrock V.E., Neusen K.F., 1964, Expansion of a very low quality two-phase fluid through a convergent-divergent nozzle. J. of Basic Engineering, No. 86.

[254] Stewart H.B., Wendroff B., 1984, Two-phase flow: models and methods. J. Comput. Phys., Vol. 56, 363-409.

[255] Stillinger F.H., 1980, Water Revisited. Science, Vol. 209, 4455.

[256] Strang, 1968, On the construction and comparison of difference schemes. SIAM J. Numer. Anal., Vol. 5, 506-17.

[257] Takeda T., Ohtsu I., 2017, ROSA/LSTF Test and RELAP5 Analyses on PWR Cold Leg Small-Break LOCA with Accident Management Measure and PKL Counterpart Test. Nuclear Engineering and Technology, Vol. 49, 928-40.

[258] Tenter A., Weisman J., 1978, The Use of the Method of Characteristics for Examination of Two-Phase Flow Behavior. Nuclear Technology, 37, 19-28.

[259] Thièry R., Mercury L., 2009, Explosive properties of water in volcanic and hydrothermal systems. J. Geophys. Res., Vol. 114.

[260] Thomas P., 1998, Extension des table de l'eau utilisées dans le code CATHARE 2. EDF-CEA-FRAMATOME, France.

[261] Tian B., Toro E.F., Castro C.E., 2011, A path-conservative method for a five-equation model of two-phase flow with an HLLC-type Riemann solver. Comput. Fluids, Vol. 46, 122-32.

[262] Tiselj I., Petelin S., 1997, Modelling of Two-Phase Flow with Second-Order Accurate Scheme. J. Comput. Phys. Vol. 136, 503-21.

[263] Tiselj I., Horvat A., Gale J., 2008, Numerical scheme of the WAHA code. Multiphase Science and Technology, Vol. 20, 323-54.

[264] Toro E.F., 1997, Riemann Solvers and Numerical Methods for Fluid Dynamics. Springer-Verlag, Berlin, Heidelberg.

[265] Toro E.F., Spruce M., Speares W., 1994, Restoration of the contact surface in the HLL-Riemann solver. Shock Waves, Vol. 4, 25-34.

[266] Toumi I., 1992, A weak formulation of Roe's approximate Riemann solver. J. Comput. Phys., Vol. 102, 360-73.

[267] Trapp J.A., Ransom V.H., 1982, A choked-flow calculation criterion from non-homogeneous non-equilibrium two-phase flows. Int. J. Multiphase Flow, 8, 669-681.

[268] Tremble G.T., Turner W.J., 1977, Characteristics of two-phase one-component flow with slip. NED, 42, 287-295.

[269] Valero E., Parra I.E., 2002, The role of thermal disequilibrium in critical two-phase flow. Int. J. Multiphase Flow, 28, 21-50.

[270] Vogrin J.A., 1963, An Experimental Investigation of Two-Phase, Two-components Flow in a Horizontal Converging-Diverging Nozzle. ANL-6754.

[271] Volpert A.I., 1967, Spaces BV and quasilinear equations. Math. USSR Sbornik, Vol. 73, 255-302.

[272] Wagner W., Pruß A., 2002, The IAPWS Formulation 1995 for the Thermodynamic Properties of Ordinary Water Substance for General and Scientific Use, J. Phys. Chem. Ref. Data , Vol. 31, 387-535.

[273] Wagner W. et al., 2000, The IAPWS Industrial Formulation 1997 for the Thermodynamic Properties of Water and Steam, ASME J. Eng. Gas Turbines and Power, Vol. 122, 150-182.

[274] Wallis G.B., 1980, Critical two-phase flow. Int. J. Multiphase Flow, 6, 97-112.

[275] Ward C.A., 1977, The rate of gas absorption at a liquid interface. The Journal of Chemical

Physics, Vol. 67, 229-35.

[276] Ward C.A., Findlay R. D., Rizk M., 1982, Statistical rate theory of interfacial transport. I. Theoretical development. The Journal of Chemical Physics, Vol. 76, 5599-605.

[277] Ward C.A., Fang G., 1999, Expression for predicting liquid evaporation flux: Statistical rate theory approach. Phys. Rev., 59, 429-40.

[278] Whalley P.B., 1996, Two-Phase Flow and Heat Transfer. Oxford University Press.

[279] Wood A.B., 1930, A textbook of sound. G. Bell and Sons Ltd, London, UK.

[280] Wang X.-D., Wang Z.-X., Duan Y.-Y., An B., Lee D.-J., 2014, Efficient evaluation of thermodynamic properties of water and steam on p–h surface. Journal of the Taiwan Institute of Chemical Engineers, Vol. 45, 372-79.

[281] Yoon H.J., Ishii M., Revankar S.T., 2006, Choking flow modeling with mechanical and thermal non-equilibrium. Int. J. Heat and Mass Transfer, 49, 171-186.

[282] Zaloudek F.R., 1963, The critical flow of hot water through short tubes, Handford Atomics Products Operations. HW77594.

[283] Zein A., Hantke M., Warnecke G., 2010, Modeling phase transition for compressible two-phase flows applied to metastable liquids. J. Comput. Phys., Vol. 229, 2964-98.

[284] Zheng Q., Durben D.J., Wolf G.H., Angell C.A., 1991, Liquids at large negative pressures: water at the homogeneous nucleation limit. Science, 254(5033), 829–832.

[285] Zia R.K.P., Redish E.F., McKay S.R., 2007, Making Sense of the Legendre Transform. American Journal of Physics, Vol. 77, 614-22.

[286] Zhokov V.V. et al., 1992, Criteria of leakage occurrence and pressure vessels failure as applied to reactors. Trans. ASME, J. Pres. Ves. Technology, 114, 378-380

université PARIS-SACLAY

ÉCOLE DOCTORALE
Sciences mécaniques et énergétiques, matériaux et géosciences (SMEMAG)

Titre : Modélisation et simulation numérique des écoulements diphasiques métastables

Mots clés : diphasique, métastable, instationnaire, solveur de Riemann, lois d'état

Résumé : Cette thèse de doctorat s'intéresse aux écoulements diphasiques métastables typiques de certains transitoires accidentels qui pourraient intervenir dans les centrales nucléaires. Ces phénomènes sont difficiles à traiter en raison de la complexité topologique de l'écoulement, des transferts entre phases et du couplage fort entre les caractéristiques thermodynamiques et les aspects mathématiques.
Les méthodes classiques utilisées dans l'industrie ne décrivent pas complétement la complexité de ces écoulements. En fait, si ces méthodes prennent en compte un certain déséquilibre thermodynamique entre l'eau liquide et sa vapeur, elles pêchent par contre au niveau de la consistance mathématique. Par ailleurs, les méthodes hyperboliques qui ont été proposées pour pallier ce défaut tardent à être appliquées dans l'industrie car elles utilisent pour la plupart des lois d'état simples qui ne sont pas adaptées pour les calculs industriels. Le but de cette thèse est de perfectionner ces nouvelles approches en couplant des méthodes hyperboliques modernes à des équations d'état précises. Le produit final de ce travail est un nouveau modèle pour l'analyse industrielle des écoulements diphasiques métastables qui associe de nouvelles méthodes pour le calcul des transferts interfaciaux et les techniques les plus récentes pour l'estimation des propriétés de l'eau et de sa vapeur. De plus, cette approche est d'un coût abordable pour les configurations industrielles.
Les méthodes développées dans cette thèse ont été systématiquement vérifiées avec des solutions exactes et validées en utilisant des données expérimentales de la littérature.

Title : Modelling and numerical simulation of metastable two-phase flows

Keywords : two-phase, metastable, transient, Riemann solver, equation of state

Abstract : This Ph.D. thesis deals with the metastable two-phase flows typical of accidental transients that could occur in nuclear power plants. Those phenomena are of difficult treatment due to the topological difficulty of the flow, the interphase transfers and the strong coupling between thermodynamic features and mathematical aspects.
The methods today in use in industry do not fully describe the complexity of these flows. In fact, if these methods take into account a certain thermodynamic disequilibrium between liquid and vapor water, they lack mathematical consistency. On the other hand, the hyperbolic methods that have been proposed for overcoming this problem are slow to spread in the industry because most of them use simple equations of state that are not adequate for industrial calculations. The purpose of this Ph.D. thesis is to improve these new approaches by coupling modern hyperbolic methods to accurate equations of state. The final product of this work is a new model for the industrial analysis of metastable two-phase flows that incorporates novel techniques for the calculation of interfacial transfers and up-to-date techniques for the estimation of steam-water properties. Moreover, it is computationally affordable for its use in industrial configurations.
The methods developed in this thesis have been sistematically verified against exact solutions and validated using experimental data of the literature.

Université Paris-Saclay
Espace Technologique / Immeuble Discovery
Route de l'Orme aux Merisiers RD 128 / 91190 Saint-Aubin, France